

Spintronic Operations Driven by Terahertz Electromagnetic Pulses

Dissertation

zur Erlangung des Grades eines
Doktors (Dr. rer. nat.)

am Fachbereich Physik
der Freien Universität Berlin

vorgelegt von

Johan Julius Frederick Heitz

Berlin, September 2021

Erstgutachter: Prof. Dr. Tobias Kampfrath

Zweitgutachter: Prof. Dr. Wolfgang Kuch

Tag der Disputation: 12. Januar 2022

Abstract

Spintronic devices, supplementing and surpassing charge-based electronics by including the electron spin, have recently begun to reach the market. Information carriers such as electrons (in field-effect transistors) and photons (in optical fibers) have already reached the terahertz range (THz, 10^{12} Hz). To make the electron spin compatible and competitive, spintronic operations need to be pushed to THz frequencies. So far, it is unclear whether fundamental spintronic effects such as spin accumulation or spin-orbit torque can be transferred to THz frequencies. In this respect, it is also important to note that the THz range coincides with many fundamental excitations, for instance phonons, magnons, and the relaxation of electronic currents. Strong THz electromagnetic pulses can be used to study such fundamental excitations, making use of both the electric and magnetic fields of the electromagnetic pulse.

In this thesis, strong THz electromagnetic pulses are applied to spintronic thin-film stacks to drive charge and spin currents, apply torque and manipulate magnetic order. A short optical probe pulse or a resistance probe interrogate the transient magnetic response.

First, a measurement strategy is developed to simultaneously detect all components of the vector magnetization of thin film magnets in optical transmission probe experiments at normal incidence, requiring only a variation in the initial probe polarization. To this end, the magnetic circular and linear birefringence (MCB, MLB) effects are measured simultaneously and a calibration strategy for the often neglected MLB effect is presented.

Second, using this detection scheme, we study the THz frequency operation of spintronic effects in ferromagnetic(FM)/non-magnetic (NM) heavy metal stacks. We find signatures of THz spin accumulation at the FM/NM interface. The spins injected into a ferromagnet relax within ~ 100 fs, in line with electron-spin equilibration times measured by ultrafast optically induced demagnetization. Indications of the field-like spin-orbit torque (FL-SOT) are found.

Third, an effective method to modulate the relative THz electric and magnetic field amplitudes in thin film samples is presented, enabling one to disentangle effects driven by the electric or the magnetic component of the THz electromagnetic pulse. A near-perfect conductor (THz mirror) quenches the THz electric field in a region close to the mirror, while doubling the THz magnetic field. Measurements with a ferromagnetic thin film confirmed a THz magnetic field increase of 1.97 ± 0.06 and a suppression of the THz electric field in the sample.

Finally, we utilize the electric-field suppression effect close to metals to optically gate the THz electric field driven resistance modulation of an antiferromagnet (AFM) grown on a semiconducting substrate. An optically induced transient substrate conductance depletes the THz electric field in the AFM layer, while not perturbing the AFM magnetic order directly. A simple model of parallel conductances is presented, confirming the experimental observations.

In conclusion, this thesis is an important contribution to push fundamental spintronic effects such as spin accumulation and spin-orbit torque to the THz range. The developed methodologies are helpful to advance nonlinear THz spectroscopy of magnetic materials.

Kurzfassung

Da die ersten auf spintronischen Prinzipien erbauten Speicher den Markt erreichen und gleichzeitig Informationsträger wie Elektronen (in Feldeffekttransistoren) und Photonen (in Glasfaserkabeln) in den Terahertz-Frequenzbereich (THz, 10^{12} Hz) vordringen, stellt sich die Frage, ob die Spintronik, welche die Elektronik um den Elektronenspin erweitert, mit solch hohen Frequenzen kompatibel ist. Gleichzeitig ist der THz-Frequenzbereich, welcher elementare Anregungen wie Phononen und Magnonen enthält, auch für die Grundlagenforschung interessant. Um diese Anregungen zu untersuchen bieten sich elektromagnetische THz-Pulse mit hohen Feldstärken an, denn sie können direkt an elektrische und magnetische Resonanzen koppeln. Diese Arbeit untersucht mit THz-Lichtpulsen, die in spintronischen Dünnschichtproben Spin- und Ladungsströme induzieren, ob elementare spintronische Effekte, wie die Spin-Akkumulation oder das Spin-Bahn-Drehmoment, auch bei THz-Frequenzen aktiv sind. Die magnetische Antwort wird mit kurzen optischen Pulsen oder mittels elektrischer Messungen zeitaufgelöst abgefragt.

Die spintronischen Effekte werden in ferromagnetischen (FM)/nichtmagnetischen (NM) Dünnschicht-Metallmultilagenn untersucht, wobei zuerst eine Messmethode erarbeitet wird, um alle räumlichen Anteile der Probenmagnetisierung gleichzeitig zu bestimmen. Hierzu werden die magnetische zirkuläre Doppelbrechung (MCB) und die, oft vernachlässigte, magnetische lineare Doppelbrechung (MLB), welche der Abfragepuls beim Durchdringen der Probe entlang der Probennormale erfährt, gleichzeitig bestimmt. Ein besonderes Augenmerk liegt auf der Normierung des MLB-Signals. Mithilfe dieser neuartigen Messmethode werden Indizien für eine THz Spin-Akkumulation und das feldartige Spin-Bahn-Drehmoment (FL-SOT) an der FM/NM Grenzfläche gefunden, welche auf einen Spinaustausch zwischen dem nichtmagnetischen Schwermetall und dem FM zurückgeführt werden. Die in den FM eindringenden Spins relaxieren auf einer Zeitskala von ~ 100 fs, was mit Ergebnissen aus ultraschnellen optischen Demagnetisierungsstudien übereinstimmt.

Zusätzlich wird die nichtlineare THz-Spektroskopie dahingehend erweitert, vom elektrischen oder magnetischen THz-Feld getriebene Signale unterscheiden zu können, indem die relativen Stärken der elektromagnetischen Felder im Inneren einer Dünnschichtprobe beeinflusst werden. Hierbei unterdrückt ein elektrisch leitender THz Spiegel das THz elektrische Feld in der Probe, während das THz magnetische Feld um einen Faktor 1.97 ± 0.06 verstärkt wird. Diese Unterdrückung des THz elektrischen Feldes in der Nähe eines Leiters wird genutzt, um die vom THz elektrischen Feld getriebene Widerstandsmodulation in einem, auf einem (optisch angeregten) halbleitenden Substrat gewachsenen, Antiferromagneten (AFM) zu steuern. Dabei wird die Wirkung des THz elektrischen Feldes im AFM unterdrückt ohne den magnetischen Zustand des AFM zu stören. Ein einfaches Modell stützt die Interpretation der Beobachtungen.

Zusammenfassend leistet diese Arbeit einen wichtigen Beitrag, um spintronische Effekte wie die Spin-Akkumulation und das Spin-Bahn-Drehmoment im THz-Frequenzbereich zu etablieren und erweitert zusätzlich die Möglichkeiten der nichtlinearen THz-Spektroskopie an Magneten.

Contents

Abstract	III
Deutsche Kurzfassung	V
Contents	VII
1. Introduction	1
2. Theoretical background	7
2.1. Overview	7
2.2. Solid-state magnetism	7
2.2.1. Subsystems of a solid	7
2.2.2. Crystalline solid: the lattice	8
2.2.3. Electrons in a periodic crystal potential	9
2.2.4. The electron spin	10
2.2.5. Spin couplings	12
2.2.6. Magnetically ordered solids	13
2.2.7. Magnetic solids	16
2.2.8. Magnons and phonons	19
2.2.9. Temperature Dependence of Magnetic Order	20
2.2.10. Magnetic anisotropy	21
2.3. Light-matter coupling and dynamics	22
2.3.1. Light-electron coupling	22
2.3.2. Light-spin coupling	23
2.3.3. Spin-orbit torques	25
2.3.4. Spin currents in ferromagnets	26
2.3.5. Spin detection by magnetoresistive and magneto-optic effects	30
2.4. Light propagation in matter	33
2.4.1. The electromagnetic wave	33
2.4.2. Frequency Domain	35
2.4.3. Refractive index and polarization	35
2.4.4. Transmission and reflection at normal incidence	36
2.5. Nonlinear light-matter interaction	37
2.5.1. Second order (quadratic) nonlinearity	38
2.5.2. Third order (cubic) nonlinearity	38
2.6. Context of this work	39
2.6.1. Low frequency studies	39
2.6.2. THz frequency studies and this work	41
3. Experimental methods	45
3.1. Introduction: the pump-probe technique	45
3.2. The (pulsed) laser	46

3.3.	Tabletop THz spectrometer	49
3.3.1.	THz generation	51
3.3.2.	Optional optical pump	54
3.3.3.	Optical probe	55
3.4.	Computer controlled data acquisition	56
4.	Determining the magneto-optic sample response for MLB and MLD	61
4.1.	Motivation	61
4.1.1.	Magneto-optic normal incidence transmission probing	63
4.2.	Concept of the experiment	65
4.2.1.	Saturated magnetization with time-dependent orientation	65
4.2.2.	The M_{\parallel} and $M_{\mathbf{k}}$ signals	66
4.2.3.	Separation of MCB and MLB	68
4.3.	Experiment	68
4.4.	Data and discussion	70
4.4.1.	Samples	70
4.4.2.	Hysteresis loops: the $M_{\mathbf{k}}$ signal	71
4.4.3.	$S \propto M^2$: the M_{\parallel} signal	72
4.4.4.	Fitting to extract b	74
4.5.	Conclusion	76
5.	THz Frequency Spin Accumulation	79
5.1.	Motivation	79
5.2.	The probing mechanism	80
5.3.	Microscopic scenarios of transient ΔM	82
5.3.1.	Effects linear in E_{THz}	82
5.3.2.	Effects quadratic in E_{THz}	85
5.3.3.	Consequences for setup parameters	85
5.4.	Experiment	86
5.4.1.	Setup	86
5.4.2.	Time drift correction	87
5.4.3.	Data pre-treatment	89
5.5.	Preliminary results and discussion	90
5.5.1.	Out-of-plane magnetization change ΔM_{\perp}	91
5.5.2.	In-plane magnetization change along M_0	96
5.5.3.	THz spin accumulation: outlook	103
5.6.	Conclusion	107
6.	Separated actions of B_{THz} and E_{THz}	109
6.1.	Motivation	109
6.2.	Principle	110
6.3.	Experiment	112
6.4.	Data and Discussion	115
6.5.	Outlook and Conclusion	119

7. Optical suppression of THz writing in antiferromagnetic CuMnAs	123
7.1. Introduction	123
7.2. CuMnAs samples	125
7.3. Experiment	128
7.4. Data and discussion	131
7.4.1. Data analysis procedure	131
7.4.2. Role of the optical pump	133
7.4.3. Two resistor model	138
7.4.4. Tentative comparison to existing technology	142
7.5. Conclusion	143
8. Summary	145
A. Appendix: Fit procedure to extract b	149
B. Appendix: Auxiliary calculations for THz writing suppression	151
Bibliography	153
Publications	171
Acknowledgments	175

1 Introduction

Spintronics: the future of computation?

The field of spintronics aims to supplement and surpass conventional information technology by employing the electron spin for computation. Working towards application, spintronic research focuses on fundamental operations such as the generation and control of spin(-polarized) currents, the manipulation of spin orientations, controlled spin accumulation at interfaces and the efficient transfer of spins across material interfaces [Mae06, Sei18b, Sin15]. These necessary fundamental operations have been researched both theoretically [Tak08, Man19] and experimentally [Jed01, Avc19, Che19, Wad16, Fan16, Dew18, Sei18b] at sub-THz frequencies. Recently, the *spin-transfer random access memory* (ST-MRAM) was unveiled as the first commercial ferromagnetic memory based on spintronic principles [Gar18].

Conventional electronics operate with mostly gigahertz ($\text{GHz} = 10^9 \text{ Hz}$) clock rates [Mar14a], with the first forays to terahertz ($\text{THz} = 10^{12} \text{ Hz}$) frequencies. A field-effect transistor with a $\sim 1 \text{ THz}$ cutoff frequency has already been demonstrated [dA11]. Other notable examples include work towards 6G [Xin21] and THz frequency networking [Gha20, Gha21]. The goal is to have spintronic functionality at THz frequencies. Thus, it is necessary to investigate the spintronic principles known from sub-THz frequency studies, at THz frequencies. However, THz spintronic experiments to date have been limited by the lack of THz frequency alternating current sources and suitable experiments.

Fundamental importance of the THz frequency range

The THz frequency range is especially interesting for fundamental research as many materials in all thermodynamic phases have important resonances in the THz frequency range. For example, in solid state systems THz frequency light is sensitive to conduction electrons near the Fermi surface, while optical radiation is mostly sensitive to states deeper in the electronic structure [Kam06]. Many fundamental excitations of crystals, namely phonons [Zha19] and magnons [Qin15], are observed in THz probe spectroscopy. Additionally, fundamental effects such as the exchange interaction [Mey17] are on the meV energy scale ($1 \text{ THz} \approx 300 \mu\text{m} \approx 1 \text{ ps} \approx 4 \text{ meV}$). Importantly, the propagation of electrons in solid state systems can emit THz frequency radiation [Sha04, Sei16].

The development of reliable sources for THz frequency radiation allowed for optical pump-THz probe experiments. Indeed, THz probe spectroscopy has applications for sensing gases [You20] and rapidly characterize materials [Zie96], spintronics research [Gue21], possibly interesting for security [Kaw04, Che07] and quality control [Naf19, Fit05], and even the study of historic artworks [SM13, Cos16].

THz pump - optical probe spectroscopy

The development of THz sources with large field strengths has enabled another mode of THz spectroscopy: *nonlinear THz spectroscopy*. Instead of being an observer, THz radiation could now be used to (selectively) excite resonances in the THz regime [Mae17, Mae18, Hof09, Zha20]. Experiments are performed in a stroboscopic pump-probe manner, where the sample properties are investigated either optically or electrically a certain delay time τ after the THz pump pulse. Repeating the measurement for many different pump-probe delays yields the time resolved sample response.

A THz pump-optical probe spectrometer has marked benefits over, for example, optical pump- optical probe spectrometers. The long wavelength THz radiation appears quasi static in a sample when interrogated simultaneously with a few femtosecond long optical pulse. Thus, THz pump-optical probe spectroscopy has the unique ability to detect both the amplitude and phase of the material response, leading to deeper insight than from optically pumped experiments [Kam06].

While large THz field strengths are also accessible from large facilities and accelerators like FLASH in Hamburg, it is both cost effective and technologically less challenging to remain in local laboratories with table-top THz sources [Fue19]. Modern laser based table-top THz radiation sources produce few cycle THz pulses with peak fields in the order of 1 MV/cm or more [Mae17]. Such strong THz fields have been employed to investigate liquid molecules [Saj17, Ham17], selectively excite phonons [Koz19, vH18, Mae18] and magnons [Bai16, Kam10], as well as to drive currents in metals [Kam13].

In this thesis we rely mostly on the ability of THz electric fields to drive currents in metals, acting like THz frequency alternating current sources. Large THz frequency pump fields thus allow for THz speed exploration of known DC electrical spintronic effects. THz frequency currents have successfully modulated the magnetic state of an antiferromagnet [Ole18]. It remains to be shown, for example, if THz speed spintronic charge-to-spin conversion leads to a spin accumulation at sample interfaces or if this process is intrinsically limited to lower frequencies.

The THz magnetic field is known to interact with the magnetic order of ferromagnets directly, like an external magnetic field via the Zeeman effect, with potential importance for THz speed magnetic switching applications [Pol18, Vic13]. However, since both fields of an electromagnetic wave are necessarily intertwined, is there a chance to isolate the effects of either of the fields?

As mentioned above, the sample response is investigated with an optical probe pulse. Additional to THz pump induced sample transmission changes, an optical probe pulse undergoes a polarization state change proportional to the transient sample properties either through electro-optical [Kei16] or magneto-optical effects [Kam02, Zve97]. Importantly, magneto-optical probing has been used successfully for the study of sub-THz spin-orbit torques [Fan16, Cel19, Mon15, Tsa18] and sub-THz spin accumulation [Hir18, Sta17].

In this thesis we will focus on magneto-optical probing with a probe pulse that traverses (transmission geometry) the sample. To date, these transmission probe experiments mostly

resolve the magnetization projection along the propagation direction of the probe pulse via the Faraday effect, or magnetic circular birefringence (MCB) [Zve97]. Measuring magnetic dynamics in the plane of a thin film sample requires tilting the sample to project the in-plane magnetization on to the probe propagation direction, requiring measurements for multiple sample tilt angles to reconstruct the vector magnetization. Alternatively, the magnetic linear birefringence (MLB), also called Voigt effect, [Rog16, Sai17, Kal08, Pyr19] or the quadratic magneto-optical intensity change [Ign21] are employed to probe in-plane magnetization. However, a transmission geometry magneto-optical probing experiment that reveals all (pump-induced) vector components of the magnetization simultaneously, without significant setup changes during the measurement and without the need for involved data analysis, is still lacking. In reflection probe experiments, such a simultaneous detection of all components of the vector magnetization has been demonstrated [Fan16, Cel19]. However, as transmission probe experiments have intrinsic advantages over reflection probe experiments (chapter 4) a measurement scheme for a simultaneous detection of all vector magnetization components in transmission geometry is desirable.

This thesis

Chapter 2 presents the theory and chapter 3 presents the methods necessary for the understanding and interpretation of the results of this thesis.

In chapter 4 we address the current limitations to transmission probe magneto-optical detection. We extend the conventional MCB detection scheme with a measurement strategy for magneto-linear birefringence (MLB), aiming towards functionality similar to that of existing reflection probe methods [Fan16, Cel19]. We demonstrate a method to calibrate the MLB signal.

In chapter 5 we investigate if the spin accumulation in a material with strong spin orbit coupling forms at THz speeds. We combine a non-magnetic heavy metal (NM) with large spin-orbit coupling with a ferromagnetic (FM) layer acting as a detector. In these sample systems we perform THz field driven experiments. We determine the origin of the observed signals and draw conclusions on the role of the NM/FM interface and the interaction of spins injected into a FM with the magnetization. We also apply the results from chapter 4 and attempt to quantify the amount of spin magnetic moment injected into the FM.

Chapter 6 focuses on the separate actions of the THz magnetic and electric fields. An experimental strategy is presented to manipulate the relative strength of both inseparable fields in the sample. We investigate the effectiveness of the proposed addition to standard THz pump-optical probe experiments and highlight advantages and limitations, as well as possible applications. For example, while the presented method is only effective in thin film (thickness $< \lambda_{\text{THz}}/4$) samples that do not perturb the THz pulse significantly, it may aid THz magnetic field driven magnetic switching and could be used to determine the nature (THz magnetic or electric field drive) of previously uncharacterized signals.

Finally, in chapter 7, we control the previously demonstrated THz electric field driven resistance modulation of an AFM [Ole18] by optically exciting the semiconducting substrate.

We propose a simple model to explain the write protection and demonstrate that the AFMs magnetic orientation is indeed protected from manipulation. The results presented may be of importance for all-optical control of magnetic memories in the future.

2 Theoretical background

This chapter introduces the basic concepts necessary to understand the context and novelty of the results presented later in this work. The information presented is based on the textbooks [Ash05], [Kit04], [Sto06],[Dem16], [Boy08], and [Hec16] as well as the very concise presentations of similar material by T.S. Seifert [Sei18b], and S.M. Maehrlein [Mae17], with permission of the authors.

2.1 Overview

This work investigates ultrafast magnetic dynamics in metals. To this end, the spintronic metal samples are excited with ultrashort light pulses from state-of-the-art fs pulse laser systems. The excited dynamics are investigated with weaker fs laser pulses from the same laser systems. In this chapter we will discuss a selection of basic principles and effects that will be needed to understand the experimental data later. At the heart of this work lies the electron with both its charge and its intrinsic spin magnetic moment. These two properties lead to a variety of couplings between the spin-carrying electrons amongst themselves, with the atoms in their environment, and with the light fields involved in the experiments.

First, we will discuss magnetic solids, including the emergence of the spin, the couplings of spins amongst themselves leading to magnetic order, and the coupling of the magnetic order to the crystal lattice of the material. Thereafter, we will discuss the various coupling mechanisms of light with the spin and charge properties of the electrons. We will discover that light is an excellent tool to excite charge and spin currents, interact with the spin orientation directly, as well as interact with and even modify the crystal lattice at sufficient field strengths. Additionally, we will discuss the ability to interrogate charge and spin dynamics in the system through their interaction with light fields. Finally, we will summarize how the individual interactions come together in the experiments of this thesis.

2.2 Solid-state magnetism

2.2.1 Subsystems of a solid

A solid is made of atomic cores that are surrounded by electrons, each of which carries a spin magnetic moment. Making some assumptions, the atomic lattice including bound core electrons, the valence electrons and the electron spins are considered as three separate energetic baths [Ash05, Mae17]. The three energetic subsystems are sketched in figure 2.1. Typically, an external stimulus will deposit energy in one of the energetic subsystems, thereafter the subsystems exchange energy and angular momentum among each other until thermal equilibrium is restored. The different energy and angular momentum exchange mechanisms occur on different characteristic timescales [Sei16, Ash05]. Observing this

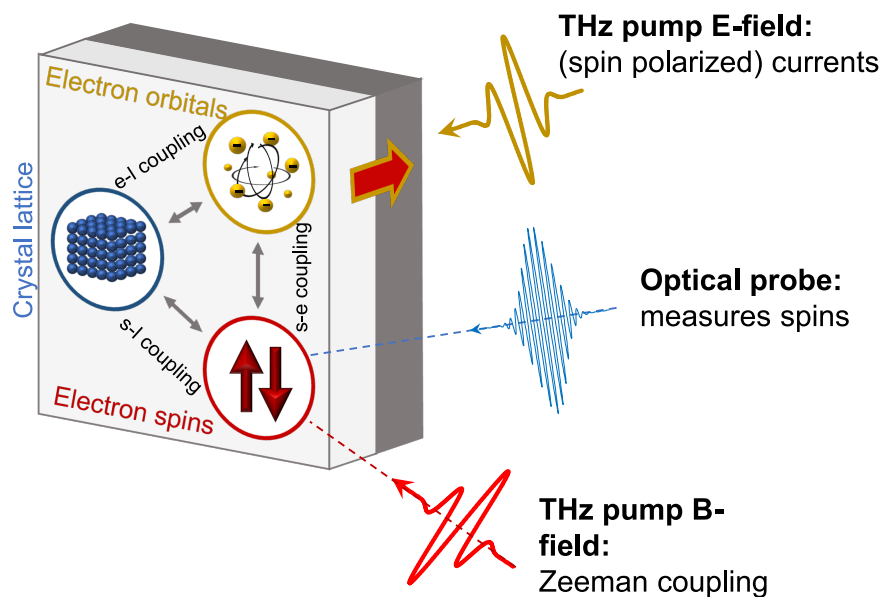


Figure 2.1.: Energy baths of a solid Within this thesis we assume that solids are composed of a lattice of atomic cores including bound electrons (blue circle), conduction electrons that are free to move (yellow circle) and the electrons spins which are the intrinsic magnetic angular momentum of the electrons (red circle). These three groups store energy and angular momentum and are able to exchange them among each other through various coupling mechanisms. External stimuli couple to the subsystems of the solid. For example, the THz magnetic (B) field (red pulse) couples to the spin system via the Zeeman interaction. The THz electric (E) field (yellow pulse) can, for example, accelerate electrons. The interaction of the electronic orbitals (yellow) and the electron spins (red) through spin-orbit coupling (section 2.2.5) can lead to the generation of spin polarized currents into the depth of the sample (red and yellow arrow). The optical probe couples to the spin system via magneto-optical effects (section 2.3.5) and measures the spin orientation. Figure adapted from T. Kampfrath.

energy redistribution and the associated pathways is the goal of pump-probe spectroscopy [Sto06].

2.2.2 Crystalline solid: the lattice

A crystal is characterized by the order of its member atoms. The spatial relationships of the atoms involved are defined within the basic building block of a crystal, the unit cell [Kit04]. The unit cell atom arrangement captures many important qualities of the crystal. It is convenient to categorize the unit cell arrangement in terms of crystal classes with shared symmetries and properties. Examples of such crystal classes are cubic, face-centered cubic, or hexagonal unit cells. To form a crystal, the unit cell is repeated in all spacial directions. A detailed discussion of crystal symmetries and an introduction to the notation is presented in chapter 1 of [Kit04].

The crystal lattice is a regular arrangement of atomic positions. The atoms may fluctuate around their equilibrium positions (lattice sites) within the crystal potential. Coordinated,

long-range harmonic vibrations of the atoms are the elementary excitations of the lattice, called phonons [Dem16]. We will discuss them in more detail below.

2.2.3 Electrons in a periodic crystal potential

The periodicity of the lattice has crucial consequences for the electrical properties of a crystal. To understand the connection, we will assume what is known as the independent-electron approximation [Ash05, Sei18b]. The independent-electron approximation considers a single electron in the periodic potential of lattice nuclei and other electrons. This periodic potential has the same periodicity as the lattice in the direction along the wavevector \mathbf{k} [Kit04]. Thus, the electron can be represented as plane waves $e^{i\mathbf{k}\cdot\mathbf{r}}$ multiplied with a lattice-periodic factor $u_{\mathbf{k}}(\mathbf{r})$. The resulting Eigenfunctions of such plane wave electrons in a periodic potential are called Bloch waves [Kit04, Sei18b]

$$\Psi_{n,\mathbf{k}}(\mathbf{r}) = e^{i\mathbf{k}\cdot\mathbf{r}} u_{n,\mathbf{k}}(\mathbf{r}). \quad (2.1)$$

These wavefunctions are classified by the wavevector \mathbf{k} and the integer band index n .

The Bloch waves constitute a complete basis of the Hilbert space and have the eigenenergies $\varepsilon_{n,\mathbf{k}}$ with respect to the Hamiltonian of a single electron [Kit04, Sei18b]. The wavevector dependence of the eigenenergies $\varepsilon_{n,\mathbf{k}}$ express, that only electrons with certain energies are allowed to propagate in certain directions of the crystal [Dem16]. When the allowed energies of the electron are considered as a function in momentum space, they form continuous bands. The combination of all allowed electron bands is called the band structure (see figure 2.2a), from which the electronic properties of the crystal can be determined [Dem16, Kit04].

The electron in the crystal is restricted to energies allowed by the band structure. The group velocity of electrons in a crystal lattice depends on the band curvature [Kit04, Sei18b]

$$\mathbf{v} = \frac{1}{\hbar} \frac{d\varepsilon_{n,\mathbf{k}}}{d\mathbf{k}} \quad (2.2)$$

with the reduced Planck's constant $\hbar = h/2\pi$.

Electrons are fermions, thus the electron distribution in a solid is determined by Fermi-Dirac statistics [Kit04, Sei18b]. The Fermi-Dirac distribution function is

$$f(\varepsilon, \mu, T) = \frac{1}{1 + e^{\left[\frac{\varepsilon - \mu}{k_B T}\right]}} \quad (2.3)$$

with electron energy ε , temperature T , Boltzmann constant k_B and chemical potential μ . The chemical potential μ determines the mean number of electrons in the system [Sto06, Sei18b]. As fermions, electrons obey the Pauli exclusion principle. In consequence

two electrons will not occupy the same state together. At $T = 0$ this leads to a complete filling of the electron bands up to the Fermi Energy ε_F [Sto06]. Depending on the band structure of the material there may be an energy range containing no electron bands over the entire crystal momentum space (see figure 2.2a). Such a lack of states is called a *bandgap* [Dem16]. If the Fermi energy lies within the bandgap, the bandgap can separate the lower energy, usually filled, *valence band* from the higher energy *conduction band*. Such a material is called an insulator as the unpopulated bands above the bandgap are responsible for the electronic transport. In metals, however, the valence and conduction bands are not energetically separated by a bandgap and thus the thermal energy $k_B T$ may promote some electrons from the valence band into the conduction band around ε_F [Kit04, Sei18b], see figure 2.2b.

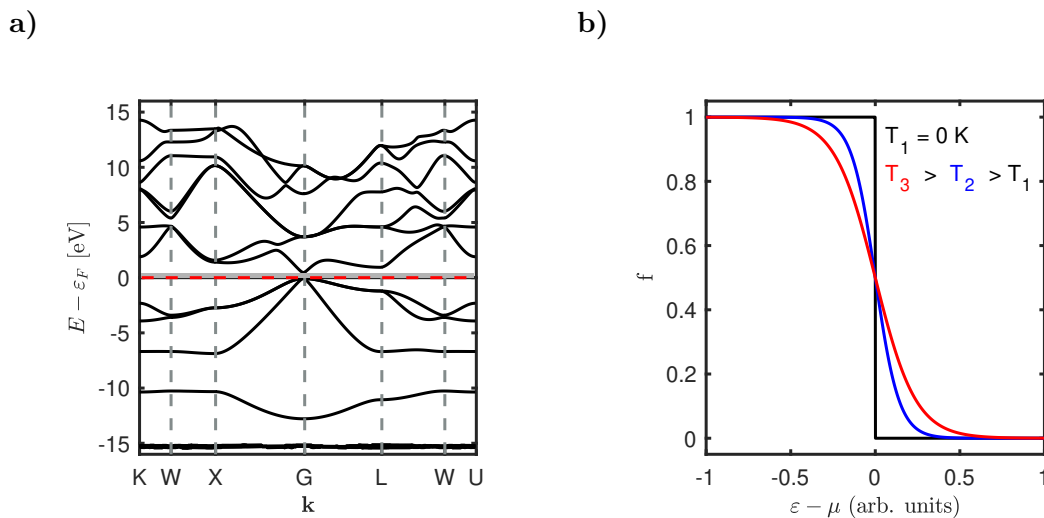


Figure 2.2.: The electron in a crystal a) Calculated bandstructure of the semiconductor GaAs. The Fermi level ε_F (red dashed line) separates the filled valence band states below from the vacant conduction band states above. The gray shaded area indicates the bandgap, a region of momentum space without electronic states. The bottom axis letter labels correspond to high symmetry directions in the crystal. The simulation was performed in *Quantum Espresso* by F. Meyer, the data was taken from the TU Graz website of P. Hadley (http://lampx.tugraz.at/~hadley/ss1/bands/bandstructures/GaAs/gaas_bands.html, 7. August 2021) b) The Fermi distribution at three different temperatures. At $T = 0$ all states up to ε_F are filled, all states above are empty. Thermal excitation with the energy $k_B T$ may promote electrons into the conduction band in the absence of a bandgap (in metals) for $T > 0$. Figure redrawn from [Sei18b]

2.2.4 The electron spin

Every electron possesses two contributions to its total angular momentum. The orbital angular momentum relates to the electrons path around an atomic core. Additionally, it has an intrinsic angular momentum called the electron spin \mathbf{s} [Sto06], which (much oversimplified) can be imagined as a rotation of a sphere-like electron about a symmetry axis of the sphere. In such an oversimplified classical picture, this rotation about itself gives rise to a magnetic field around each electron. This spin magnetic moment can be oriented in space and will be drawn as an arrow in figures throughout this thesis. The

electron spin is central to the discussion of magnetism and its existence well established experimentally [Mot29, Com12, Dem16].

Quantum-mechanically, the properties of the electron spin \mathbf{s} are captured by a relativistic, linearized version of Schrödinger's equation called the Dirac equation [Nol15, Mae17]. The Dirac equation is second order in the time derivative and expands the Schrödinger equation to include the electron spin \mathbf{s} by treating the wavefunctions as vectors of complex functions of time and space and the coefficients consequently as matrices [Nol09, Sei18b]. The components of the spin angular momentum operator $\hat{\mathbf{s}}$ fulfil the same commutation relations as the familiar orbital angular momentum $\hat{\mathbf{l}}$ (with the Levi-Civita permutation symbol ϵ_{ijk}) [Nol09, Sei18b]

$$[\hat{s}_i, \hat{s}_j] = i\hbar\epsilon_{ijk}\hat{s}_k \quad (2.4)$$

$$[\hat{s}_i, \mathbf{s}^2] = 0 \quad (2.5)$$

which identify the components of the spin angular momentum operator as subject to an uncertainty principle [Sto06]. The simultaneous precise determination of more than one component is not possible. The two orientations of the spin, typically called 'spin up' and 'spin down', are eigenstates of \hat{s}_z and \mathbf{s}^2 . In fact, these two orientations are the (angular momentum of the rotating electron) eigenstates $\pm\hbar s$ of the operator \hat{s}_z with a spin quantum number $s = 1/2$ [Sei18b, Dem16]. Throughout this work we will occasionally refer to the two spin orientations as the two 'flavors' of spin. It should be noted that the spin angular momentum and the orbital angular momentum are not conserved quantities in a central field. Instead, in a central field, the sum of spin and angular orbital momentum, the total angular momentum, is conserved. This is important for the spin-orbit interaction, below, which can transfer angular momentum in between the spin and orbit degree of freedom without a change in the total angular momentum [Sto06, Nol15, Mae17].

The electron spin magnetic moment $\hat{\boldsymbol{\mu}}_s$ is related to the Bohr magneton $\mu_B = e\hbar/2m_e$ with the electron mass and elementary charge m_e and $e = |e|$ respectively. Considering the electron gyromagnetic ratio (g-factor) $g_e \approx 2$, one arrives at [Nol15, Sei18b]

$$\hat{\boldsymbol{\mu}}_s = -\frac{g_e\mu_B}{\hbar}\hat{\mathbf{s}}. \quad (2.6)$$

It is worth mentioning, that the Bloch functions $\Psi_{n,\mathbf{k}}$ implicitly consider the spin in the band index n [Kit04, Sei18b]. It will be important later that they can factor into spin and orbital components if the Hamiltonian of the system is independent of the electron spin [Sto06]. Now we will consider the interaction of the spin magnetic moment with external fields.

2.2.5 Spin couplings

Spins can couple to external magnetic and electric fields. Like the spin itself, these couplings are relativistic effects and can be classified by the Lorentz factor γ [Sto06]

$$\gamma = \left(\sqrt{1 - \frac{v^2}{c^2}} \right)^{-1} \quad (2.7)$$

Even though the velocities v are typically much smaller than the speed of light c and γ is not significantly different from 1, relativistic effects occur. These relativistic effects are of fundamental significance for the existence of a spontaneous magnetic direction in a solid-state system. With $\gamma \approx 1$, it is sufficient to consider the lowest order expansion with respect to v/c only [Sto06]. The two most important lowest order effects are the *Zeeman interaction* and the *Spin-Orbit interaction* (SOI). Together with the *exchange interaction*, these three interactions determine the magnetic properties of a material [Sto06, Mae17]. Typically, the exchange interaction is strongest, followed by SOI and the weakest, the Zeeman interaction [Sto06, Sei18b].

Zeeman interaction

For an electron in a crystal, the Zeeman interaction with an associated Hamiltonian $\hat{H}_z = -\hat{\boldsymbol{\mu}}_e \cdot \hat{\mathbf{B}}^{\text{tot}}$ arises from the interaction of a single electron magnetic moment $\hat{\boldsymbol{\mu}}_e$ with a (small) magnetic field $\hat{\mathbf{B}}^{\text{tot}}$ [Nol09, Sei18b]. This magnetic field is the sum of all external fields at the location of the electron in the solid [Sto06].

The electron magnetic moment $\hat{\boldsymbol{\mu}}_e$ is the sum of both the spin magnetic moment $\hat{\boldsymbol{\mu}}_s$, discussed before, and the orbital magnetic momentum $\hat{\boldsymbol{\mu}}_{\text{orb}} = \frac{\mu_B}{\hbar} \hat{\mathbf{l}}$ [Nol09, Sei18b]

$$\hat{\boldsymbol{\mu}}_e = \hat{\boldsymbol{\mu}}_{\text{orb}} + \hat{\boldsymbol{\mu}}_s \quad (2.8)$$

The Zeeman interaction can lift the degeneracy of electronic states depending on the spin orientation. As a result, the band-structure becomes spin-dependent. In the ferromagnets considered here, the mean magnetic moment is dominated by the spin ($\hat{\boldsymbol{\mu}}_s$) [Nol09, Sei18b].

Macroscopically, the Zeeman interaction aligns the spin to an applied magnetic field. When a spin magnetic moment interacts with an external magnetic field \mathbf{B} , it experiences a Zeeman Torque \mathbf{T}_Z [Gui20]

$$\mathbf{T}_Z = \hat{\boldsymbol{\mu}}_s \times \mathbf{B} \quad (2.9)$$

that will start a spin precession around the magnetic field. An additional damping torque acts towards the applied field. Gradually, the precessing spin will lose angular momentum and eventually align with the applied field [Sto06]. We will discuss this in section 2.3.2.

Spin-orbit interaction

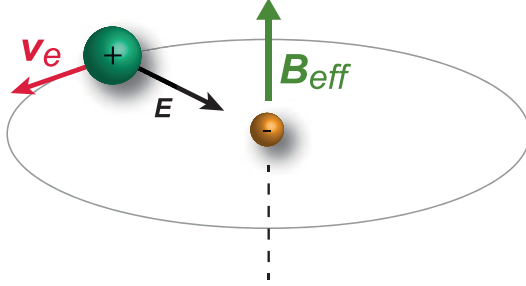


Figure 2.3.: Spin-orbit coupling (SOC) The classical picture of spin-orbit coupling from the point of view of an electron (yellow) moving in a crystal. Through relativistic effects, the Coulomb field of the charged nucleus (green) gains a magnetic component that can interact with the electron spin magnetic moment μ_s . This is the *spin-orbit field* $\mathbf{B}_{\text{eff}}^{\text{so}} \propto (\mathbf{v} \times \mathbf{E}_{\text{pr}})/c^2$. This figure was reproduced from [Mae17] with permission from S. M. Mährlein.

The spin can also interact with the fields of the atoms around it. The spin-orbit interaction (SOI) arises when the relativistic electron travels past the atomic cores and the other electrons in the lattice. An atomic core at rest has a central electric (Coulomb) field $\mathbf{E}(r)$ depending on the distance r from the nucleus and no magnetic field \mathbf{B} . However, from the point of view of the relativistic electron the magnetic field \mathbf{B}' of the nucleus (which is 0) gains an effective magnetic field $\propto \mathbf{v} \times \mathbf{E}$ [Sto06, Mae17, Sei18b]

$$\mathbf{B}'_{\perp} = \gamma \left(\mathbf{B}_{\perp} - \frac{\mathbf{v} \times \mathbf{E}(r)}{c^2} \right) \approx -\frac{\mathbf{v} \times \mathbf{E}(r)}{c^2} = \mathbf{B}_{\text{eff}}^{\text{so}}. \quad (2.10)$$

The Lorentz factor $\gamma \approx 1$ as stated before. Thus, the orbital motion of the electron generates an effective magnetic field, known as the spin-orbit magnetic field $\mathbf{B}_{\text{eff}}^{\text{so}}$. In fact, if $\mathbf{E}(r)$ arises from a spherically symmetric potential, there is a connection of $\mathbf{B}_{\text{eff}}^{\text{so}}$ and the orbital angular momentum $\hat{\mathbf{l}}$ [Sei18b, Sto06]

$$\mathbf{B}_{\text{eff}}^{\text{so}} \propto \lambda \hat{\mathbf{l}} \quad (2.11)$$

where λ is the spin-orbit parameter.

The spin-orbit field $\mathbf{B}_{\text{eff}}^{\text{so}}$ also interacts with the spin magnetic moment $\hat{\mu}_s$ of the electron in a Zeeman interaction-like manner $\hat{\mathbf{H}}_z = \frac{g_e \mu_B}{\hbar} \hat{\mathbf{s}} \cdot \mathbf{B}_{\text{eff}}^{\text{so}}$. As a result, the SOI gives rise to a spin-orbit torque (SOT) [Sei18b, Žel18, Wad16]. We will discuss the spin-orbit torque further in section 2.3.3 of this chapter.

2.2.6 Magnetically ordered solids

The combination of Coulomb interaction and Pauli principle with the properties of the crystal lattice leads to the emergence of spontaneous magnetic order. In the following we will consider the coupling of spins amongst themselves first, before considering the implications of coupling the spin system with the lattice.

Exchange coupling and the Heisenberg Model

The magnetic order of solid-state systems is generally a quantum mechanical effect [Sto06]. The interaction of multiple magnetic moments within a solid is best approached by investigating the direct interaction of two electron spins. Electrons, being spin 1/2 fermions, obey Pauli's exclusion principle: two such particles may not share the same state [Dem16, Kit04]. Let us consider the combined wavefunction for two electrons and compare it to the wavefunction if the particles trade places. The wavefunction $\Psi(r_1, s_1; r_2, s_2)$, for two electrons with position r and spin s , is antisymmetric with respect to particle exchange $\Psi(r_1, s_1; r_2, s_2) = -\Psi(r_2, s_2; r_1, s_1)$. Therefore, two electrons with the same spin $s_1 = s_2$ have vanishing probability to be at the same $r_1 = r_2$ [Kit04, Sei18b]. This is Pauli's exclusion principle in action, the two electrons will avoid each other.

When two electrons of the same spin avoid each other, it reduces their Coulomb interaction energy. The reduction in Coulomb energy suggests spins prefer to align parallel, that is ferromagnetically. However, the curvature of the electron wavefunction may increase due to the node at $r_1 = r_2$. The wavefunction curvature is related to the total kinetic energy of the system. The gain in total kinetic energy may overcompensate the lowered Coulomb energy, favoring antiparallel (antiferromagnetic) spin order. Whether the total energy is larger or smaller for $s_1 = s_2$ than for $s_1 \neq s_2$ depends on the details of the electron wavefunctions [Kit04, Sei18b]. Most atoms have many electrons distributed over many electron shells. In such atoms the spin configuration is given by Hund's phenomenological rules [Sto06, Ral08].

As an example, we will construct a fully antisymmetric many-electron wavefunction based on single-electron wavefunctions. Initially we regard a two-electron system while considering the interactions of the spins ($|S, m_s\rangle$) separately from the electrons in their orbitals ($|q\rangle$) [Nol09, Sei18b]. This is allowed because the Hamiltonian has no explicit spin dependence [Nol09]. To construct a fully antisymmetric two electron wavefunction from two parts, one part needs to be antisymmetric while the other is symmetric [Nol09, Mae17].

$$|\Psi\rangle^\mp = |q\rangle^\pm |S, m_s\rangle^\mp \quad (2.12)$$

where the superscript '+' denotes a symmetric, '-' an antisymmetric wavefunction. Adhering to Pauli's principle limits the possible spin component wavefunctions and leaves the electron wavefunction with three antisymmetric ('-') and one symmetric ('+') solutions of the form $|q\rangle = \Phi_q(r_1)\Phi_q(r_2) \pm \Phi_q(r_2)\Phi_q(r_1)$. Here, $\Phi_q(r)$ are the individual electron spatial waveform components [Nol09]. These combine into the well-known singlet and triplet states with antiparallel and parallel spin alignment, respectively

$$|\Psi_1\rangle = \frac{|q\rangle^+ (|\uparrow\downarrow\rangle - |\downarrow\uparrow\rangle)}{\sqrt{2}} \quad (2.13)$$

$$|\Psi_2\rangle = |q\rangle^- \begin{cases} |\downarrow\downarrow\rangle \\ \frac{|\uparrow\downarrow\rangle + |\downarrow\uparrow\rangle}{\sqrt{2}} \\ |\uparrow\uparrow\rangle \end{cases} \quad (2.14)$$

The spin part of the wavefunctions $|\Psi_1\rangle$ and $|\Psi_2\rangle$ is $|0, 0\rangle$ and $|S, m_s\rangle$ with $m_s = -1, 0, 1$ respectively, as indicated by the arrows [Nol09].

The Hamiltonian of the system is constructed from a spacial and a spin part in a similar fashion. The four solutions $|\Psi_1\rangle$ and $|\Psi_2\rangle$ have two energy eigenvalues E_{\pm} of the spin independent (spatial) Hamiltonian H_q [Nol09]

$$H_q|q\rangle^{\pm} = E_{\pm}|q\rangle^{\pm} \quad (2.15)$$

Spontaneous magnetic order arises if $E_+ \neq E_-$ and the singlet and triplet states are no longer degenerate. The energetically lower state corresponds to a reduced electron-electron Coulomb interaction and, therefore, a preferred spin orientation [Sto06].

We treat the spin ordering with another (spin) Hamiltonian H_s with the same energy eigenvalues E_{\pm} of the spatial Hamiltonian H_q [Sei18b]

$$H_s|0, 0\rangle = E_+|0, 0\rangle \quad (2.16)$$

$$H_s|1, m_s\rangle = E_-|1, m_s\rangle \quad (2.17)$$

A solution that lends itself is the molecular Heisenberg model Hamiltonian [Sei18b]

$$H_s = J_0 - J_{12}S_1 \cdot S_2 \quad (2.18)$$

with the *exchange constant* [Sei18b]

$$J_{12} = \frac{1}{\hbar}(E_+ - E_-) \quad (2.19)$$

Importantly: this is called the *exchange interaction* as the spin ordering arises purely from the wavefunction symmetry under particle exchange and scales with the overlap of the single-particle wavefunctions [Sto06]. The presence of spin-orbit coupling is not required. Additional to the interaction strength, the exchange constant J_{12} determines the preferred spin orientation. If $J_{12} < 0$ the spin system prefers antiparallel alignment called antiferromagnetism while $J_{12} > 0$ indicates parallel, ferromagnetic spin ordering[Sei18b, Sto06].

Atomic magnetism

To approach magnetic solids, we consider the interaction of two magnetic ions. The Heitler-London Model applies the spin Hamiltonian, above, to the interaction of two ions with one electron each. Here the two cores and the two particles all interact via the Coulomb interaction. Importantly, this model emphasizes the association of electrons with individual atomic cores, that is the localized nature of the electrons [Sto06]. The two atoms are close enough for the electron waveforms to overlap but not close enough for the waveforms to encompass both cores at once [Hei27, Mae17]. This is the typical situation in insulators.

The Heitler-London Hamiltonian may even be extended to atoms carrying multiple electrons and can, therefore, describe the exchange interaction in model magnetic solids. Within the ‘macrospin approximation’, the individual electron spins per atom are combined to form a total effective atomic spin S [Nol09, Mae17, Sto06].

$$H = - \sum_{i,j} J_{ij} \mathbf{S}_i \cdot \mathbf{S}_j \quad (2.20)$$

In Chemistry the Heitler-London model is a justification for Lewis’ electron-pair bond concept [Sto06]. It must be stressed that J_{ij} is very dependent on boundary conditions and the inherent assumptions of the model. J_{ij} can be determined in ab-initio calculations or from experiments [Hei27, Mae17].

Essentially, the exchange interaction is mediated by the direct or indirect overlap of electron wavefunctions. In certain cases, a suitable diamagnetic intermediate atom may have an electron orbital overlapped with those of two other magnetic atoms such like Fe – O – Fe in Yttrium Iron Garnets. This oxygen atom electron orbital ‘extends’ the reach of the Fe orbitals, a process called *super exchange*. Other manifestations of exchange are the *double exchange* and the *RKKY interaction* [Mae17, Sto06, Nol09].

2.2.7 Magnetic solids

The preferred orientation of spins has consequences for magnetic order in macroscopic solids, categorized by the sign of the *exchange constant* J_{ij} .

Ferromagnets ($J_{ij} > 0$)

As discussed above, a positive exchange coupling constant indicates that spins in the material choose to align parallel to each other (figure 2.4a). This means that macroscopically these individual moments m_i create a large magnetic moment – the magnetic order parameter, magnetization, $\mathbf{M} = \sum_i \mathbf{m}_i$ [Sto06]. A macroscopic magnetization will be accompanied by a magnetic field extending beyond the material. Upholding an extended magnetic field is energetically very costly. Magnets typically form randomly oriented domains to reduce their magnetic field. Magnetic domains are small regions of space in which

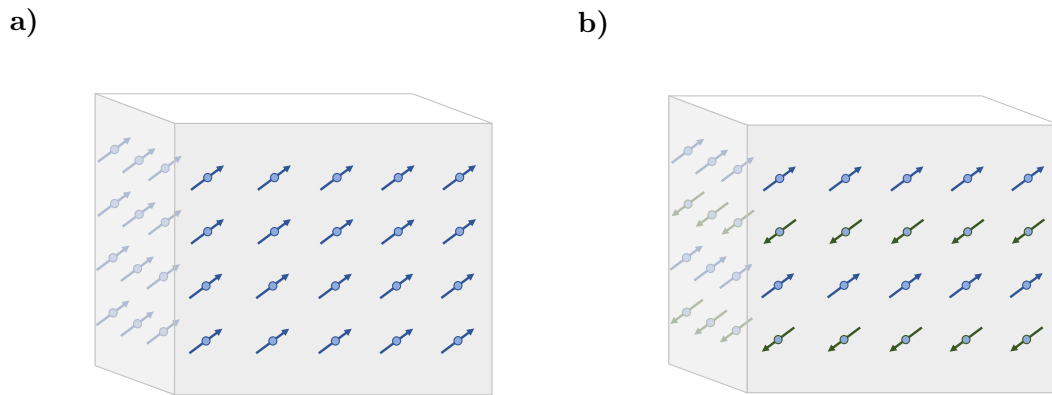


Figure 2.4.: Magnetic order **a)** *Model ferromagnet*: a positive exchange constant ($J_{ij} > 0$) favors parallel spin magnetic moment m alignment. The magnetic order parameter is the magnetization $M = \sum_i m_i$. **b)** *Model antiferromagnet*: antiferromagnetic coupling ($J_{ij} < 0$) favors antiparallel spin magnetic moment m alignment. The magnetic lattice can be decomposed into two ferromagnetically coupled magnetic sublattices M_1 (blue) and M_2 (green). The magnetic order parameter is the Néel vector $L = M_1 - M_2$. Ferrimagnets occur when the antiferromagnetic sublattices are not perfectly compensated. Note that the exchange coupling is isotropic, the direction in which the magnetic order parameter points is determined by the *anisotropy* (see section 2.2.10).

the atomic moments are in ferromagnetic, parallel, alignment [Kit04, Sei18b].

These domains remain randomly aligned, unless an externally applied magnetic field supplies the necessary energy to align all domains the same way (figure 2.5). When all domains are oriented identically the magnet is said to have a saturated magnetization [Kit04]. When the external field is removed, the magnet returns to multidomain state, minimizing the external field. However, the magnetization will not be quenched completely, and the small remainder is called the remanence magnetization. It will resist an oppositely applied external magnetic field. The field needed to return the magnetization to zero is the coercivity. Consequentially, ferromagnets exhibit hysteresis. Hysteresis loop measurements characterize remanence and saturation magnetization [Kit04]. The sample magnetization is monitored while the external field is swept in between oppositely oriented maximal values.

The speed at which the magnetization can adjust to an external field is intrinsically limited in ferromagnets. The Zeeman interaction couples the magnetization to an external magnetic field. The Zeeman torque tilts the magnetization in a direction orthogonal to both. Thereafter, the magnetization precesses around the external field at the Larmor frequency. The damping like torque slowly transfers angular momentum from the precessing magnetization to the lattice until $\mathbf{M} \parallel \mathbf{B}_{\text{ext}}$. The angular momentum exchange with the lattice limits ferromagnetic switching to the GHz regime [Sto06]. More details of this process are discussed in section 2.3.2. Typical example ferromagnets are Fe, $\text{Co}_{20}\text{Fe}_{60}\text{B}_{20}$, and $\text{Ni}_{81}\text{Fe}_{19}$ also called permalloy (Py).

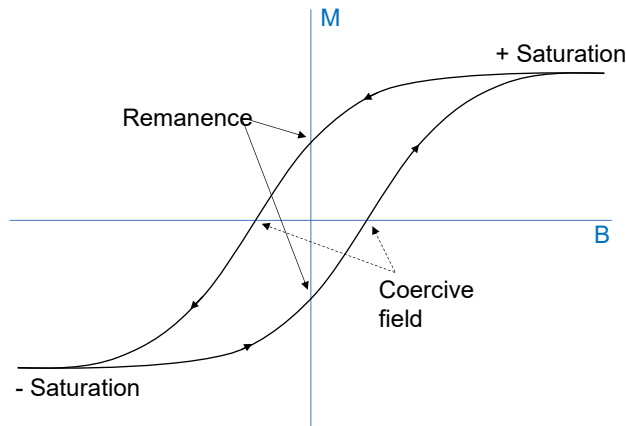


Figure 2.5.: Hysteresis Ferromagnets exhibit hysteresis. Without an external magnetic field the a ferromagnet minimizes its external field by forming randomly oriented magnetic domains. This remaining field at $B_{\text{ext}} = 0$ is the *remanence*. To counteract the remanence magnetization a *coercive field* has to be applied. At sufficient external field all magnetic moments are oriented along B_{ext} , the sample magnetization is *saturated*. In a hysteresis measurement the sample is taken from one saturated orientation to the other and back. Hysteresis measurements are essential to determine the properties of ferromagnetic samples. Figure adapted from [Kit04].

Antiferromagnets ($J_{ij} < 0$)

A negative exchange constant favors antiparallel spin alignment. Antiferromagnets (AFM) consist of equal numbers of oppositely aligned spins, thus they are magnetically ordered solids without an external Magnetization $\mathbf{M} = \sum_i \mathbf{m}_i = 0$ [Sto06].

The model AFM lattice can be broken into two oppositely oriented ferromagnetic sublattices $M_{1,2}$ (figure 2.4b). Those sublattices contain equal numbers of spins and their magnetization cancels: $\mathbf{M} = \mathbf{M}_1 + \mathbf{M}_2 = 0$. The magnetization is not a good order parameter for antiferromagnets. Instead, a staggered order parameter, the Néel vector $\mathbf{L} = \mathbf{M}_1 - \mathbf{M}_2$, indicates an axis along which the sublattices orient [Bai20]. Lacking a magnetization, and therefore a stray field, the AFM order cannot be reoriented by external magnetic field [Sto06]. An external magnetic field would align both sublattices in the same direction and must overcome the typically large exchange field [Mar14b]. The lack of a magnetization makes working with AFMs more difficult than working with ferromagnets. However, the AFM imperviousness to manipulation through external fields can be a great technological boon. For example, it is expected that AFM data storage bits can possibly be in closer proximity than ferromagnetic bits, whose stray fields interact [Jun18].

Additionally, if data is encoded in the Néel vector \mathbf{L} , AFM memories are expected to switch significantly faster than their ferromagnetic counterparts. The reorientation of \mathbf{L} is not limited by angular momentum exchange with the lattice as in ferromagnets. To reorient \mathbf{L} both sublattices $\mathbf{M}_1 = -\mathbf{M}_2$ require equal and opposite torque, creating an equal and opposite angular momentum change. This lifts the need to transfer angular momentum to the lattice. In consequence, \mathbf{L} may be reoriented without precession at speeds well in the THz regime [Jun18, Yan20], motivating the study in chapter 7.

For completeness we mention the existence of ferrimagnets. Ferrimagnets are imperfect AFMs with a slight canting or imbalance of the two sublattice magnetizations, resulting in a small macroscopic magnetization. These materials are of interest for researchers, for example, because the presence of a small magnetization provides a handle for measurements of the magnetic state [Mae18]. In this work however, only ferromagnets and antiferromagnets are researched.

2.2.8 Magnons and phonons

Phonons

In section 2.2.2 we have mentioned that long range coordinated fluctuations of the atomic positions around the lattice points are called phonons. Phonons are the elementary excitation of the lattice and represent bosonic quasi-particles with energy and momentum associated with the phonon frequency Ω and wavevector \mathbf{K} [Dem16]. Typically, these collective motions within the crystal are reduced to a single chain of atoms with the spacing of atoms in the corresponding direction in the crystal [Kit04]. The atoms of such a chain can either oscillate along \mathbf{K} (longitudinal) or perpendicular to \mathbf{K} (transversal).

The phonon wavevector is related to the oscillation wavelength $\lambda = 2\pi/K$ which imposes constraints on the possible oscillations a finite crystal lattice can support. The longest wavelength phonon occurs when all atoms along the direction of \mathbf{K} oscillate in phase. The shortest wavelength corresponds to twice the interatomic spacing a in that direction in the lattice [Dem16]. Since the lattice is a periodic reproduction of the unit cell, all phonons can be investigated within one unit cell. In momentum space the *first Brillouin Zone*, reaches from $K = -\pi/a$ to $K = \pi/a$. The relationship of energy (frequency Ω) and momentum (wavevector \mathbf{K}) in the first Brillouin zone is called the *phonon dispersion relation* [Kit04]. Such phonon dispersion relations can be visualized similar to the electronic bandstructure in figure 2.2a.

A special feature arises when the unit cell contains two (or more) atoms. In this case the vibrational modes are separated into an *acoustic* (when both atoms move in phase) and an *optical* (when the two atoms move out of phase) *branch*. The optical branch is named after the special case when the vibration is associated with an oscillating electric dipole that can couple to light [Dem16].

Most phonons are in the infrared ($0.8 \mu\text{m} - 1 \text{mm}$ or correspondingly $375 \text{THz} - 0.3 \text{THz}$) spectrum of light [Dem16]. In contrast to the acoustic branch phonons, the optical phonons have a non-zero frequency at the center of the Brillouin Zone. If optical phonons create an electric dipole moment, they are said to be *IR-active* and can be seen in IR spectroscopy. If the phonons create a changing polarizability instead, they are called *Raman active* and can be accessed with inelastic scattering processes. If the medium is inversion-symmetric, phonons can only be IR or Raman active, not both. Raman active phonons of the optical branch are accessed with *Raman scattering*, the acoustic phonon branch is accessed with *Brillouin scattering*. Importantly, since the wavevector range of light associated with

optical frequencies is usually small, light is only able to excite phonons from the center of the Brillouin Zone [Dem16].

Within this work phonons are relevant for the thermalization processes after sample excitation.

Magnons

The magnetic atoms of a crystal form a magnetic (sub-)lattice of their own. This magnetic lattice can be considered the magnetic system of the crystal and can act as an angular momentum bath [Sto06, Mae17]. The individual magnetic moments of the lattice are coupled by the exchange interaction. If one of the perfectly aligned spins is impulsively deflected, this perturbation propagates in all directions. Analogous to phonons, spin waves (or magnons) are quantized and characterized by wavevector \mathbf{k} , frequency ω and their polarization (left- or right-handed circular precession). Magnons also have a dispersion relation similar to that of phonons [Kit04]. In a ferromagnet, the lowest energy magnon is uniform precession of the magnetic lattice with the energy needed to flip a single spin. Magnons in systems of multiple magnetic sublattices, such as antiferromagnets and ferrimagnets, are much more involved [Dem16].

Spin-waves can also carry spin currents [Wan04]. As the magnon energy corresponds to an integer number of flipped spins, magnons lower the local magnetization. As we shall discuss in the next section, thermally excited magnons can quench the magnetization completely [Sto06].

2.2.9 Temperature Dependence of Magnetic Order

The magnetization of a ferromagnet is the sum of all the individual spins it contains. As we have seen in the last section, the magnetic lattice can act as an energy bath. At nonzero temperatures, the individual spins are supplied with thermal energy and begin to precess randomly. This corresponds to the incoherent excitation (or population) of magnons, lowering the average magnetization of the ferromagnet [Sto06]. With increasing temperature, more magnons are excited. The magnetization is further suppressed until it vanishes at the critical temperature T_C . This critical temperature is known as Curie temperature in ferromagnets and as Néel temperature in antiferromagnets. At this critical temperature, the solid undergoes a phase transition from spontaneous magnetic order to paramagnetism [Kit04].

The temperature dependence of a ferromagnet is often calculated analytically in a mean-field approach. One considers a single spin exposed to an average (mean-field) of its interactions in the crystal. Typical mean field theories to determine the magnetic temperature dependence are the Weiss-Heisenberg Theory and the Stoner model [Sto06]. It is found that the magnetization has a temperature dependence of the form $M(T) \propto (T_{\text{crit}} - T)^\alpha$ with a critical exponent α [Kit04, Sei18b].

In the context of this work, we will encounter small temperature induced decreases of the

magnetization but otherwise remain far from the critical temperature of the samples.

2.2.10 Magnetic anisotropy

The exchange interaction discussed above aligns magnetic moments with respect to each other but is otherwise completely isotropic: the axis along which magnetic moments align is not inherently determined. However, the magnetic moments reside within a complicated environment of effective magnetic fields that may impose an anisotropy on the magnetization. These effects make some spatial directions in the solid energetically favorable for the Magnetization (easy axis) and others unfavorable (hard axis) [Sto06].

The magnetic anisotropy has multiple contributions, most prominently the competition of *magneto-crystalline anisotropy* (MCA) and *shape anisotropy*.

Magneto-crystalline anisotropy

The magneto-crystalline anisotropy arises when the spin coupling imposes the anisotropies of the lattice on the magnetization. Microscopically, this is done by spin-orbit coupling (section 2.2.5) [Kit04]. The spin-orbit field is determined by the crystal potential and thus subject to the crystal structure. In a simple picture, the orbital motion of electrons may prefer to lie in a certain plane within the complex electronic structures of the neighboring atoms. The corresponding spin-orbit field then aligns all spins in this particular direction [Sto06].

Shape anisotropy

The shape anisotropy is caused by the spin-spin magnetic dipole interaction (SSMD) [Sto06, Sei18b]. In a simple picture, each spin is surrounded by magnetic field lines similar to those of a bar magnet: arising from the short ends and bulging out along the long ends. Two spins (magnets) in close contact will align in the energetically most favorable configuration: in line and head to tail. The macroscopic shape of the magnetic material may impose restrictions on the magnetic orientation of the outermost spins. The SSMD interaction will make all other spins in the material ‘feel’ these restrictions to varying degrees as well [Sto06].

Treatment

The MCA in the bulk of the sample and the shape anisotropy at the surface compete. For thin film samples, the shape anisotropy can reach a sizeable influence. Anisotropy is typically treated phenomenologically by expanding the anisotropy energy E in terms of the magnetization direction up to the fourth order. A symmetry analysis considering the crystal structure of the sample will reduce this to an energy surface of the magnetization

orientation. This energy surface depends on a relatively small number of phenomenological parameters [Sei18b, Sto06].

Within this work, the anisotropy is either present as the AFM switching barrier encountered in chapter 7 or within the ferromagnetic samples of chapters 4, 5, and 6. The ferromagnetic samples were magnetized with an external magnetic field many times stronger than the anisotropy to saturate the sample magnetization and ensure reliably interpretable results.

2.3 Light-matter coupling and dynamics

2.3.1 Light-electron coupling

This work considers the interaction of metals with light in the near-IR and low frequency THz regime. In these conditions the primary light-matter interaction is dominated by the Coulomb interaction between the electron charge and the electric field of the light wave. Macroscopically, the total electric field E drives charge currents j . For low enough field strengths, the linear response is the well known Ohm's law in frequency space [Hec16, Sei18b]

$$\mathbf{j}(\omega) = \boldsymbol{\sigma}(\omega)\mathbf{E}(\omega) \quad (2.21)$$

where σ is the sample conductivity. Thus, the light field does work on the sample, which scales $\propto E^2$. The energy transferred to the metal is given by [Hec16]

$$P = E^2 \operatorname{Re}(\sigma) \quad (2.22)$$

The energy transferred to the metal manifests in the form of heat and can transiently demagnetize a ferromagnet as discussed in section 2.2.9.

Quantum-mechanically, the absorption of light can be understood as light-driven optical transitions from an initial electron state $|i\rangle$ to a final state $|j\rangle$. A light field with frequency ω and photon energy $E = \hbar\omega$ can match the transition energy and be absorbed. The transition rate in between the two states is evaluated by Fermi's golden rule within linear-response theory [Sei18b]

$$\omega_{i,j} = \frac{2\pi}{\hbar} |M_{i,j}|^2 \delta(\varepsilon_j - \varepsilon_i - \hbar\omega). \quad (2.23)$$

The electron-dipole operator matrix element $M_{i,j}$ and the delta distribution conserve energy.

Energy redistribution

Following an optical transition, the energy is distributed in the system by a number of relaxation processes such as electron-electron, electron-phonon and electron-magnon scattering [Sto06].

Typically, the fastest relaxation mechanism is electron-electron scattering on a sub-picosecond timescale, causing rapid carrier multiplication. Carrier multiplication broadens the initial electron distribution of a few highly excited electrons. Eventually this will lead to a thermalized electronic system, well described by the elevated temperature Fermi-Dirac distribution. [Sei18b]

Electron-phonon and electron-magnon interactions, coupling the electron bath to the lattice and magnetic subsystems respectively, occur on longer timescales in the order of 0.1 – 10 ps. When energy is evenly distributed among the three subsystems a few ps after excitation, heat diffusion will need another few nanoseconds typically before the entire system is in equilibrium with its environment again. [Sto06, Sei18b]

In typical optical pump-probe experiments the electrons are excited into high lying states by photons with typically > 1 eV energy. In this thesis however we will be mostly dealing with charge currents involving electrons just above the Fermi level because of the comparatively small photon energy (~ 4 meV) of THz frequency photons.

2.3.2 Light-spin coupling

To a smaller extent, which is nonetheless important here, the electron spins can directly couple to EM fields: to the magnetic field of light through Zeeman coupling, and to the electric field of light through spin-orbit torque.

Zeeman coupling: magnetization and magnetic fields

As mentioned in section 2.2.5, a magnetic field \mathbf{B} acting on the spin magnetic moment \mathbf{m} will cause a Zeeman Torque \mathbf{T}_Z

$$\mathbf{T}_Z = \mathbf{m} \times \mathbf{B} \quad (2.24)$$

which tilts the spin out of the \mathbf{m}, \mathbf{B} plane. The spin begins precessing around the applied magnetic field B at the Larmor frequency $\boldsymbol{\omega} = \gamma \mathbf{B}$. Here, the gyromagnetic ratio $\gamma = \frac{g\mu_0}{2m_e}$ relates the angular momentum \mathbf{L} and the magnetic moment $\mathbf{m} = \gamma \mathbf{L}$. Interestingly, the Larmor frequency does not depend on the angle enclosed by \mathbf{m} and \mathbf{B} and the precession motion does not lose energy on its own [Sto06].

Relaxation processes can be modeled by a phenomenological damping torque \mathbf{T}_D on \mathbf{m} acting towards the equilibrium magnetization

$$\mathbf{T}_D = \frac{\alpha}{m} \left[\mathbf{m} \times \frac{d\mathbf{m}}{dt} \right] \quad (2.25)$$

where α is the Gilbert damping parameter. It is a phenomenological constant determined by the rate of energy and angular momentum transfer to the lattice. Essentially, the precessing moment exerts a force on the environment and the back-action damps the precession. Combining both torques yields the Landau-Lifshitz-Gilbert (LLG) equation [Sto06, Sei18b]

$$\frac{d\mathbf{m}}{dt} = \gamma [\mathbf{m} \times \mathbf{B}] + \frac{\alpha}{m} \left[\mathbf{m} \times \frac{d\mathbf{m}}{dt} \right] \quad (2.26)$$

The timescale on which the precession is damped out is captured by the spin-lattice relaxation time. The spin-lattice relaxation time is typically ~ 100 ps in transition metal films. The precessing spin may also lose angular momentum by launching spin waves (magnons) [Sto06, Sei18b].

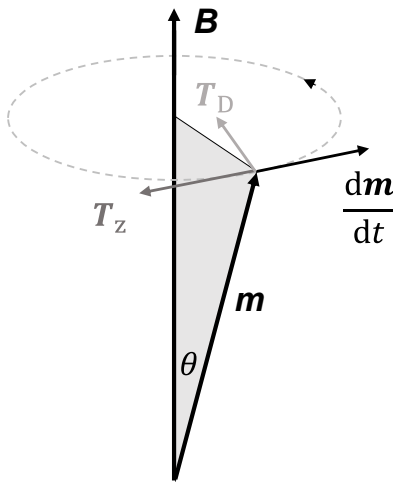


Figure 2.6.: Torques on \mathbf{M} Under the influence of an external magnetic field \mathbf{B} the magnetization \mathbf{m} experiences a Zeeman torque \mathbf{T}_Z that initiates precession motion. This precession will be damped by the damping torque \mathbf{T}_D that transfers angular momentum to the lattice. The processes are described by the LLG equation (eq. 2.26). This figure was redrawn and adapted from [Sto06]

Within the macrospin approximation the sum of all individual spins \mathbf{m} are combined in one average spin, the magnetization \mathbf{M} of the ferromagnet. The discussion above is just as valid for $\mathbf{m} = \mathbf{M}$ [Sto06].

A special case arises if the applied magnetic field evolves on timescales much shorter than the spin-lattice relaxation time and for a sample with a Larmor frequency outside the THz pump spectrum. In this work we will encounter a Zeeman torque on a magnetization caused by the magnetic field of a THz light pulse with ~ 1 ps period. Naturally, if the time-dependent magnetic field $\mathbf{B}_{\text{THz}}(t)$ has a component perpendicular to the magnetization, it will cause the time-dependent Zeeman torque $\mathbf{T}_z(t)$. Since the spin-lattice relaxation time is much longer than the action of $\mathbf{B}_{\text{THz}}(t)$, negligible amounts of energy and angular momentum can be exchanged with the lattice during the interaction with the light pulse. The effective torque on the magnetization will be the cumulative action (temporal integral) of the applied B-field [Vic13]. We will precisely measure $\mathbf{M}(t)$ with fs resolution and reconstruct the temporal shape of the applied field $\mathbf{B}_{\text{THz}}(t)$ in the following chapters.

Spintronic transport and torque

Even more interesting than the magnetic dynamics of stationary spins is the multitude of effects arising when spins are transported through space. The aim of this work is to understand the properties of such itinerant magnetic moments and the resulting magnetic dynamics, especially at THz frequencies, for further use in Spintronic applications.

Generally, spin transport may happen in three ways: 1) Spin carrying itinerant electrons may be spin polarized resulting in a coexistence of spin and charge currents (mainly in metals). 2) A spatial separation of equal numbers of spin carrying electrons by spin flavor will transport magnetic angular momentum in space while preserving charge neutrality: a pure spin current (also in metals). 3) Magnons may also mediate the exchange of magnetic moments creating effective magnon spin currents (even in insulators) [Sin15, Wan04, Sei18b].

The magnetic moment of a spin μ_s has two basic motion components: rotation and translation. In the nonrelativistic limit both can be expressed in the context of a continuity equation for local spin density. In its full form, the spin current is represented by a rank 2 tensor with direction of flow and polarization. Importantly, only the spin magnitude $\hbar/2$, not the spin itself is conserved. In terms of the linear velocity \mathbf{v} , the angular velocity $\boldsymbol{\omega}$, and the local magnetization \mathbf{M} , one can write [Sun05, Sei18b]

$$\frac{d\mathbf{M}}{dt} = -\nabla \cdot \mathbf{v} \otimes \mathbf{M} + \boldsymbol{\omega} \times \mathbf{M} \quad (2.27)$$

where $v_i M_j = (\mathbf{v} \otimes \mathbf{M})_{ij}$ are the tensor elements of $\mathbf{v} \otimes \mathbf{M}$. The first term is an expression for spin currents while the second describes spin torques (rotational motion). A torque due to field $\boldsymbol{\omega}$ is therefore an angular current density $\mathbf{j}_\omega := \boldsymbol{\omega} \times \mathbf{M}$. The other term describes the linear spin current density is $\mathbf{j}_s := \mathbf{v} \times \mathbf{M}$. This condenses the continuity equation into [Sun05, Sei18b]

$$\frac{d\mathbf{M}}{dt} = -\nabla \cdot \mathbf{j}_s + \mathbf{j}_\omega \quad (2.28)$$

It should be noted that linear current density is not conserved in this equation. The torques \mathbf{j}_ω on local magnetic moments can therefore act as sinks and sources of current density in the steady state $\nabla \cdot \mathbf{j}_s = \mathbf{j}_\omega$ [Sun05, Sei18b].

2.3.3 Spin-orbit torques

One possible contribution to \mathbf{j}_ω is the spin-orbit torque (SOT), the torque that a spin s experiences when interacting with the spin-orbit field $H = \mathbf{s} \cdot \mathbf{B}_{\text{eff}}^{\text{so},s}$. The superscript ‘so,s’ indicates that this is the interaction of the spin-orbit field with the orientational dynamics of the spin, in contrast to orbital motion in which the SO field will be labelled ‘so,orb’. [Man09, Sei18b]

$$\mathbf{j}_\omega \propto \mathbf{s} \times \mathbf{B}_{\text{eff}}^{\text{so,s}} \propto \mathbf{s} \times \left(\mathbf{E} \times \frac{\mathbf{v}}{c} \right) \quad (2.29)$$

in the following we will consider a relevant selection of the different manifestations of spin currents \mathbf{j}_s and their consequences.

2.3.4 Spin currents in ferromagnets

The magnetization is the sum of all spins in a ferromagnet. In remanence not all spins are aligned parallel with the magnetization. However, the remaining magnetization indicates that significantly more electrons are spin polarized one way and fewer opposite to it. The more numerous are referred to as the majority spins (on majority carrier electrons), the others as minority spins. Therefore, charge currents inside and originating from a ferromagnet are automatically spin polarized [Sto06]. Also, electrons with spins oriented along the magnetization direction will have a higher probability of entering a ferromagnet from outside than oppositely oriented spins [Sto06]. This spin filtering effect of ferromagnets is highly relevant in technological applications like magnetic tunnel junctions and spin valves. It also manifests in the giant magnetoresistance (GMR) and tunnel magnetoresistance effects ubiquitous in modern data storage and magnetic sensing technology [Dey21, Sto06, Ral08].

Spin dependent Hall effects

The spin-dependent Hall effects are very similar to the ordinary Hall effect. The ordinary Hall effect describes the deflection of charges in a conductor subject to a magnetic field. The Lorentz force perpendicular to both an external field and the charge current direction is responsible for the deflection [Dem13]. The spin-Hall effects also deflect electrons, instead of the electron charge it is the spin orientation with respect to an intrinsic spin-orbit field that determines the deviation [Sin15].

Like SOT, which acts on the spin, the electron motion will be affected by a spin-orbit force. The spin-orbit force \mathbf{F} is analogous to a Lorentz force due to a spin-orbit field $\mathbf{B}_{\text{eff}}^{\text{so,orb}} \propto \nabla \times \mathbf{s} \times \mathbf{E}$, resulting in [Chu07]

$$\mathbf{F} \propto \frac{e}{c} \mathbf{v} \times \mathbf{B}_{\text{eff}}^{\text{so,orb}} \quad (2.30)$$

which will cause a spin dependent deflection of the electrons. e is the electron charge, c the speed of light and \mathbf{v} the velocity of the electrons. The spin-orbit force deviates spin polarized electrons from their path, giving rise to a spin current \mathbf{j}_s perpendicular to the original driving field \mathbf{E} [Chu07, Sei18b]

$$j_{s,ij} = \sum_k \sigma_{ijk}^{\text{SHE}} E_k \quad (2.31)$$

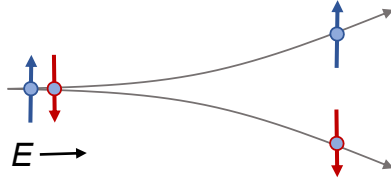
This spin current is characterized by the spin Hall conductivity tensor $\underline{\sigma}^{\text{SHE}}$. The spin Hall conductivity tensor consists of three microscopic contributions: [Sin15]

$$\underline{\sigma}^{\text{SHE}} = \underline{\sigma}^{\text{INT}} + \underline{\sigma}^{\text{SS}} + \underline{\sigma}^{\text{SJ}} \quad (2.32)$$

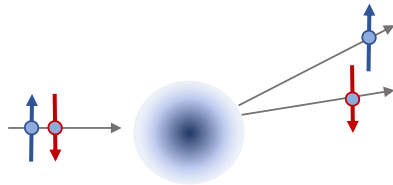
The first term $\underline{\sigma}^{\text{INT}}$ is the intrinsic contribution, and directly related to the interaction with the intrinsic spin-orbit field. As $\underline{\sigma}^{\text{INT}}$ is not disorder related and thus not dependent on the electron momentum scattering time τ [Sin15].

The second and third terms, on the other hand, depend on the electron momentum scattering time τ as they are disorder related. The second term $\underline{\sigma}^{\text{SS}}$ is the skew scattering contribution, describing (a Mott like) inelastic scattering process in which the spin carrying electron undergoes a spin dependent momentum change. A second contribution to $\underline{\sigma}^{\text{SS}}$ exists from scattering of electrons off impurities without SOI when traveling in a spin-orbit-coupled band structure. The third and last term $\underline{\sigma}^{\text{SJ}}$ is related to side-jump scattering, an elastic scattering process historically related to the scattering of a gaussian wave-packet off a spherical impurity. Opposite spins will be deflected equally into opposite directions which conserves the total momentum, in contrast to the skew scattering process [Sei18b, Sin15].

a) Intrinsic deflection



b) Skew scattering



c) Side-jump scattering

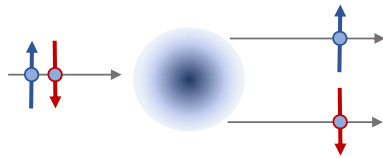


Figure 2.7.: Contributions to $\underline{\sigma}^{\text{SHE}}$ The terms of equation 2.32 are **a)** the intrinsic contribution to the Spin Hall effect $\underline{\sigma}^{\text{INT}}$ that is directly related to the interaction of the spin with the spin-orbit field. **b)** The skew scattering contribution $\underline{\sigma}^{\text{SS}}$ is related to an inelastic, Mott-like spin-dependent scattering off impurities. It is dependent on the electron momentum scattering time τ . **c)** The side jump scattering term $\underline{\sigma}^{\text{SJ}}$ describes an elastic scattering process which displaces the electrons depending on their spins without altering the propagation direction. It is historically related to the scattering of gaussian wavepackets off a spherical impurity. Figure redrawn from [Nag10]

Examples of spin-dependent Hall effects are the spin Hall effect (SHE) and the inverse spin Hall effect (ISHE). Both SHE and ISHE occur in metals with SOI but lacking magnetic order (such as Pt, Co, W). The spin Hall effect sorts a non-spin-polarized charge current

depending on the spin orientation, creating a spin current perpendicular to the driving charge current. Statistically, charge currents in metals without spontaneous magnetization involve the same number of charges for each spin orientation. Therefore, the pure charge current is converted into a pure transversal spin current. As the name suggests the ISHE does the inverse, it converts a spin current into a charge current [Sei18b, Sin15].

Spin accumulation at ferromagnet/normal metal interfaces

Spins can accumulate at sample interfaces either through spin transport from the bulk of the sample or because of spin dependent band alignment when a charge current flows across a ferromagnet/nonmagnetic metal (FM/NM) interface [Sei18b, Sto06].

Spin dependent band alignment at a FM/NM interface arises because of the intrinsic imbalance between spin up and spin down electron populations in a ferromagnet. A charge current emitted from a ferromagnet will be spin polarized, reflecting the ratio of majority and minority spin polarizations inside the ferromagnet. In contrast, a charge current emitted from a nonmagnetic metal will have equal numbers of spin-up and spin-down electrons [Sin15, Sei18b]. This has consequences for spin carrying electrons transitioning across an FM/NM interface.

A spin carrying charge attempting to move from a nonmagnetic metal to a ferromagnet will have a high probability of success if its spin is polarized in the minority carrier direction (along the magnetization) because it finds empty states to scatter into [Sto06]. Spins of the opposite orientation will more likely be rejected because the majority spin bands are filled first. Because the spontaneous spin flip length is about ten times longer than the spin averaged electron mean free path, these rejected spins will accumulate at the FM/NM interface. On the other hand, a spin carrying charge attempting to pass the FM/NM interface from the ferromagnetic side will inherit a spin polarization from the intrinsic spin imbalance in the ferromagnet. This imbalance will remain for at least the spin flip length in the nonmagnetic metal until the spin polarization difference has equilibrated. Again, a spin accumulation (population imbalance) close to the interface is observed [Sto06].

More interesting, within the context of the results presented in this work, are spin accumulations at sample interfaces due to the bulk SOI as discussed above. In contrast to the spin-dependent band alignment which require an out-of-sample plane charge current, the spin-dependent Hall effects are driven by in-plane charge currents and appear even in single layer samples [Sin15]. The spin Hall effect will generate an out-of-sample spin current from an in-plane charge current in a nonmagnetic metal [Liu11]. This out-of-plane spin current leads to a spin accumulation at the sample interface, with identical numbers of oppositely oriented spins at opposite sample edges. The alignment of the spins accumulated by SHE is always perpendicular to the driving current direction [Sei18b, Sin15]. This is experimentally interesting, as the angle between the spin orientation on the non-magnet side of the FM/NM interface and the magnetization of the ferromagnet can be varied. However, the SHE is not the only effect that produces a spin accumulation with a spin orientation perpendicular to the driving current direction [Sin15]. Additionally, at FM/NM interfaces, there can be inbuilt interfacial fields. These inbuilt interface fields can

lead to current driven spin accumulations by the Rashba effect [Les16], for example.

The Rashba effect

The spin dependent Hall effects discussed above are bulk charge-to-spin conversion effects with a conversion efficiency rarely exceeding ten percent. In contrast, the Rashba effect is an interface dependent spin-orbit coupling mechanism that may reach comparatively large charge to spin conversion efficiencies [Les16]. The Rashba effect arises due to inversion symmetry breaking at material interfaces. This change from the bulk crystal structure of either layer material gives rise to an electric field normal to the interface and lifts the spin degeneracy [Sin15]. In this environment, very close to the interface, a charge current flow can cause a non-zero spin accumulation. The efficiency of the Rashba effect is extremely sensitive to the properties of the normal-to-the-interface electric field and as such is very dependent on the interface properties such as roughness and material intermixing.

The Rashba effect is also not the only interface dependent, spin selective process [Gue21, Fan14]. In realistic multilayer samples the control of the interface quality during growth is all but simple. Indeed, nominally similar samples must not have identical interfaces depending on the growth conditions. One aim of this work is to study the interaction of spin accumulations at FM/NM interfaces and the interaction of this accumulated magnetic moment on the ferromagnets magnetization.

Spin current mediated torques

Up until now we have considered torques arising from the interaction of external or spin-orbit fields with the spin. Now we shall consider the spin as a carrier of magnetic moment perturbing an existing magnetic order. Such a situation can occur when a ferromagnet and a nonmagnetic metal with large spin-orbit coupling (and thus a strong spin-dependent Hall effect) are in contact [Liu11, Liu12, Sin15, Gui20] as will be discussed in results chapter 5. It can also occur within an antiferromagnet if the spin-orbit interaction orients some itinerant spins into a direction different from the magnetic order parameter [Wad16, Gom10, Zho19], as presented in results chapter 7.

Consider a spin \mathbf{s}_{in} entering a ferromagnet with magnetization \mathbf{M} from the outside. The injected spin can be interpreted as a weak external field acting on the magnetization and creating a torque analogous to the Zeeman torque. This is called the field-like torque [Wad16]

$$\mathbf{T}_{\text{FL}} \propto \mathbf{M} \times \mathbf{s}_{\text{in}} \quad (2.33)$$

This Zeeman like torque will tilt the magnetization out of its equilibrium position and initiate a magnetization precession. However, since the magnetization also looks like an external field to the spin, both will precess together around a common axis $\mathbf{s}_{\text{in}} + \mathbf{M}$. Since the magnetic moment of a single spin is very small compared to that of the magnetization,

this precession only lasts for as long as \mathbf{s}_{in} and \mathbf{M} interact and leaves both \mathbf{M} and \mathbf{s}_{in} in a different orientation than before [Ral08, Han08].

In typical experiments many spins are injected at once, with slightly different speeds and directions. Even if the injected spin current is perfectly spin polarized (all spins aligned) the velocity distribution causes a range of interaction times of the spins \mathbf{s}_{in} and \mathbf{M} . Different interaction times for each of the spins results in a different final orientation for each spin, reducing (dephasing) the injected spin polarization. When this dephasing process is complete, the average of the injected spins and the magnetization will be aligned along a common average axis that is the new magnetization direction [Ral08, Han08]. This process is described by the (anti-)damping or spin-transfer (STT) torque [Wad16]

$$\mathbf{T}_{\text{in}} \propto \mathbf{M} \times \mathbf{M} \times \mathbf{s}_{\text{in}} \quad (2.34)$$

In special cases the action of the (anti-)damping torque due to spin injection can counteract the damping torque \mathbf{T}_{D} that a precessing magnetization naturally experiences, hence the optional ‘anti’ prefix. In extreme cases the anti-damping torque can increase angle between magnetization and the precession axis beyond the tipping point. Beyond the tipping point the damping torque \mathbf{T}_{D} will act towards the applied field axis again, but towards the opposite direction as before. Spin-orbit torques are expected to be major players in modern spintronic applications and have been already used successfully to switch the magnetization in ferromagnets [Jhu20, Das18].

So far, we have discussed means to control spin dynamics both by torque and by transport effects. The next section will introduce the principles of spin detection with magnetoresistive and magneto optic effects.

2.3.5 Spin detection by magnetoresistive and magneto-optic effects

The magnetic state of a sample is often interrogated with optical (magneto optic) or electrical (magnetoelectric) methods. In both cases a probe current $\mathbf{j} = \underline{\sigma}\mathbf{E}$ interrogates the sample conductivity $\underline{\sigma}$ which depends on the sample magnetization. Such a probe current can be either applied via electrical contacts (where \mathbf{E} is the associated voltage) or through the action of the electric field of light (figure 2.8).

We shall write the magnetic dependent components of the conductivity in terms of the sample magnetization $\underline{\sigma}(\mathbf{M}) = \mathbf{M}$. In an isotropic material, the probe current driven by an electric field (either from an electro-magnetic wave or through contacts) is given by [Nád21]

$$\mathbf{j}_{\text{pr}} = \underline{\sigma}\mathbf{E}_{\text{pr}} = \underbrace{\sigma_0\mathbf{E}_{\text{pr}}}_{\text{nonmagnetic}} + \underbrace{a(\mathbf{M} \times \mathbf{E}_{\text{pr}})}_{\text{AHE}} + \underbrace{b(\mathbf{M} \cdot (\mathbf{M} \cdot \mathbf{E}_{\text{pr}}))}_{\text{AMR}} + \underbrace{c\mathbf{M}^2\mathbf{E}_{\text{pr}}}_{\text{isotropic MR}} \quad (2.35)$$

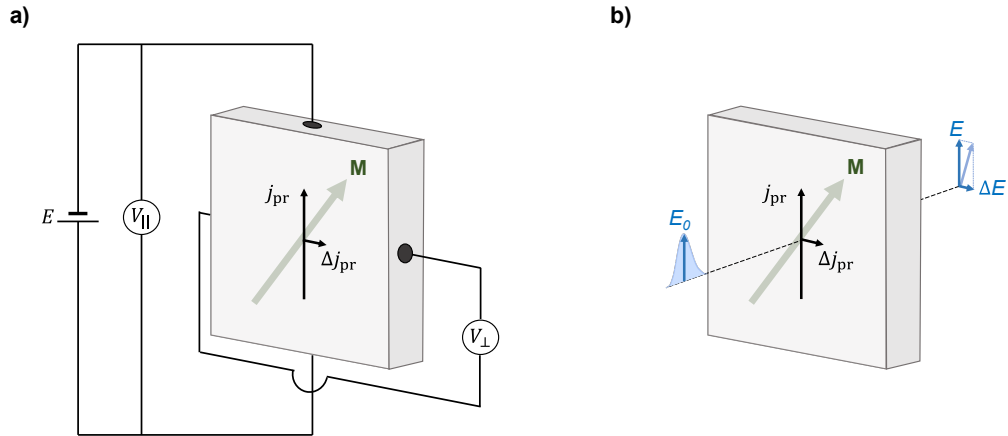


Figure 2.8.: Probing the magnetic state The magnetization can be probed either with contact electrodes or with light. **a)** A voltage (electric field \mathbf{E}) applied to a sample will drive a probing current $\mathbf{j}_{\text{pr}} = \underline{\sigma}\mathbf{E}$. $\underline{\sigma}$ depends on the relative orientation of \mathbf{j} and the magnetization \mathbf{M} and the probing current will experience alterations according to equation 2.35. A change in the longitudinal voltage V_{\parallel} arises due to the AMR term while the AHE term produces $\Delta\mathbf{j}_{\text{pr}}$ and thus V_{\perp} . **b)** Similarly, the electric field \mathbf{E}_0 of a probe light pulse generates a probe current \mathbf{j}_{pr} . Again there will be a magnetization dependent alteration of \mathbf{j}_{pr} and a perpendicular current component $\Delta\mathbf{j}_{\text{pr}}$. Both these current components re-radiate (dark blue \mathbf{E} and $\Delta\mathbf{E}$), causing an apparent polarization rotation (light blue arrow) of the probe light. This polarization change can be detected as outlined in chapter 3.3.3.

with the material dependent coefficients a, b, c . A pump induced change of the magnetization will alter the current and cause re-emission of light with an altered polarization state, proportional to the magnetic change of $\underline{\sigma}$. For instance, if $\underline{\sigma}$ gives rise to a current contribution perpendicular to the original probe current, current applied to a sample with contact electrodes will cause a perpendicular voltage that can be measured (figure 2.8a). Alternatively, if the probe current is due to a probing light field \mathbf{E}_0 , a small electric field $\Delta\mathbf{E}$ is emitted perpendicular to the reemitted field from the original probe current. Such an additional perpendicular light field component is observed as a polarization plane rotation proportional to $\Delta\mathbf{E}/E_0$ (figure 2.8b).

The magnetization independent conductivity σ_0 produces a *magnetization independent current contribution*. As the work in this thesis involves detecting changes in the sample magnetization, the second and third terms of equation 2.35 are more relevant. The second term gives rise to the *anomalous Hall effect* (AHE) which is referred to as *magnetic circular birefringence* (MCB) at optical frequencies. MCB can be measured as so-called *Faraday effect* (FE, in transmission) or *magneto-optical Kerr effect* (MOKE, in reflection) [Sto06, Zve97, Nád21]. The third term is related to the *anisotropic magnetoresistance* (AMR) and gives rise to the *magnetic linear birefringence* (MLB) magneto-optical probing effect [Sto06, Zve97, Nád21]. The AMR can be measured in the so-called planar Hall effect geometry. MLB is the transmission probe counterpart to the quadratic MOKE effect [Fan16]. The MLB can be measured in transmission and reflection probing and is sometimes called the *Cotton-Mouton effect* [Zve97]. The fourth term of equation 2.35 is the isotropic magnetoresistance.

In summary, we can relate AHE with MCB and AMR with MLB. The other terms (FE, MOKE, planar Hall, Cotton-Mounton) refer to special measurement geometries and are often intermixed, causing confusion. We will briefly discuss the AHE and AMR terms here and again, in further detail, when discussing the experimental details in chapter (section 4).

Anomalous Hall Effect

The second term of equation 2.35 describes a current contribution due to the anomalous Hall effect (AHE). The AHE can be understood as the consequence of the SHE (section 2.3.4) in a ferromagnet but much more complex intrinsically, as treated by Nagaosa *et al.* [Nag10]. The spin-orbit field adds a magnetization (spin) dependent velocity component perpendicular to both the propagation direction of the carriers (\mathbf{E}) and the magnetization \mathbf{M} . In ferromagnets one spin flavor is dominant and a spin dependent deflection of carriers creates a perpendicular spin polarized charge current. If the initial current is due to the electric field of light, the perpendicular current component will re-radiate together with the original current, adding an electric field $\Delta\mathbf{E}$ perpendicular to \mathbf{E} (figure 2.8). At optical frequencies, the AHE is known as magnetic circular birefringence (MCB) and is sensitive to magnetization changes along the propagation direction of the probing light [Zve97]. In this thesis, the samples are probed at normal incidence and the AHE/MCB effect probes the out-of-sample plane magnetization component.

Anisotropic Magnetoresistance and differential measurement

The third term of equation 2.35 describes a current contribution due to the anisotropic magnetoresistance (AMR). Phenomenologically, the AMR manifests as a magnetization dependent resistance that a probe current \mathbf{j}_c in a magnetically ordered solid experiences. The conductivity σ_{\parallel} (σ_{\perp}) is smaller (larger) for a parallel (perpendicular) orientation of charge current and magnetic order parameter [McG75]. The same effect creates a similarly orientation dependent charge current perpendicular to the initial current direction, confusingly called the planar Hall effect for historical regions. The effect is even in Magnetization: in ferromagnets it does not distinguish in between two 180° rotated magnetizations (chapter 5) and is therefore also active in antiferromagnets with oppositely oriented magnetic sublattices (chapter 7) [Fin14, Mar14b, Wad16].

It is a consequence of spin-orbit coupling and depends on intrinsic components and extrinsic, disorder related, spin dependent scattering. The dominant mechanism depends both on temperature and the material properties [Nád21].

In general, the AMR effect can be understood as a current \mathbf{j}_{AMR} created by the interaction of, and depending on the angle θ between, the initial charge current \mathbf{j}_c and the magnetization \mathbf{M} [Nád21].

$$\mathbf{j}_{\text{AMR}} = -\alpha_{\text{AMR}}\mathbf{M} \cdot (\mathbf{M} \cdot \mathbf{j}_c) \quad (2.36)$$

with the coefficient (AMR angle) α_{AMR} . The AMR effect is the (in-plane) projection of \mathbf{j}_{AMR} onto the driving field E

$$\mathbf{j}_{AMR||M} = -\frac{\alpha_{AMR}}{2}M^2\mathbf{j}_c(\cos 2\theta + 1) \quad (2.37)$$

The observed resistance change can be understood as the increase or decrease of \mathbf{j}_c by $\mathbf{j}_{AMR||M}$. The perpendicular planar Hall current is the (in-plane) projection of \mathbf{j}_{AMR} perpendicular to the driving field E

$$\mathbf{j}_{AMR\perp M} = -\frac{\alpha_{AMR}}{2}M^2\mathbf{j}_c \sin 2\theta \quad (2.38)$$

The AMR will play a central role in the detection of the magnitude and direction of magnetic order in this work.

Isotropic magnetoresistance

The last term of equation 2.35 describes a current contribution proportional to the magnitude of the magnetization but without orientational dependence. It is mentioned for completeness [Nád21].

2.4 Light propagation in matter

All experiments performed in this work depend on the interaction of short (laser-) light pulses and matter. Strong optical (near-IR) pulses from an amplified laser system are converted to THz radiation with concepts from nonlinear optics. The THz frequency light acts as a pump pulse in pump-probe experiments. Both the THz electric and magnetic fields will perturb the energetic subsystems of the solid. The dielectric response and possible magnetic dynamics, arising from these perturbations, are interrogated with a weaker, optical probe light pulse. A selection of the core optical principles necessary for this work is presented here.

Within the context of this work, a full treatment with Maxwells' equations is not necessary and it is sufficient to discuss light in the semi-classical framework. However, where necessary we will state some results arising from the application of Maxwells equations, especially when discussing the propagation of light waves in transparent media.

2.4.1 The electromagnetic wave

Initially, we will consider light as a plane wave in the z direction at normal incidence on the sample. The time dependence of the electrical light field $\mathbf{E}(t)$ is determined by the wave vector \mathbf{k} defining spatial periodicity and propagation direction z , the angular frequency ω

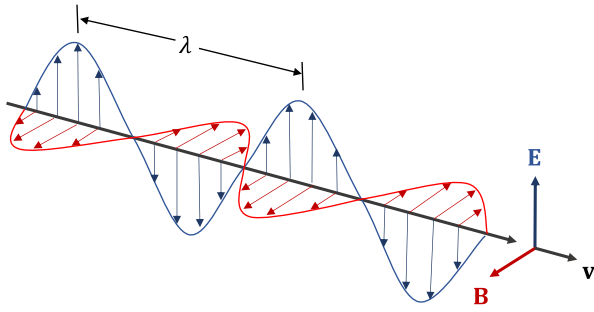


Figure 2.9.: The EM wave Light is composed of an electric E and a magnetic B field which oscillate in phase and orthogonal to one another. The wavelength λ is related to the wavevector $\mathbf{k} = 2\pi/\lambda$, defining the propagation direction \mathbf{v} , and the frequency $\omega = 2\pi c/\lambda$. Figure redrawn from [Hec16].

related to oscillation in time t , and the amplitude E_0 of the oscillation linearly polarized in the direction of the unit vector $\hat{\mathbf{x}}$ [Hec16]

$$\mathbf{E}(z, t) = E_0 e^{i(\mathbf{k}z - \omega t)} \hat{\mathbf{x}} \quad (2.39)$$

where the speed of light c relates $\omega = c\mathbf{k}$ and \mathbf{k} is related to the wavelength $\lambda = 2\pi/\mathbf{k}$. To describe propagation direction along an arbitrary wave vector \mathbf{k} one would exchange $\mathbf{k}_z z$ with $\mathbf{k} \cdot \mathbf{r}$. The energy carried by a photon of frequency ω is $\hbar\omega$. In addition to the electric field of light, the light wave has an additional magnetic field $\mathbf{B}(t)$ with the same temporal evolution and phase (figure 2.9) [Hec16]

$$\mathbf{B}(z, t) = B_0 e^{i(\mathbf{k}z - \omega t)} \hat{\mathbf{y}} \quad (2.40)$$

which is in phase and perpendicular to $\mathbf{E}(z, t)$ to fulfill

$$\mathbf{B}_{0,\hat{\mathbf{y}}} \propto \frac{\mathbf{k}}{\omega} (\hat{\mathbf{z}} \times \mathbf{E}_{0,\hat{\mathbf{x}}}). \quad (2.41)$$

The power transported across a unit area is given by the Poynting vector \mathbf{S} in the propagation direction $\hat{\mathbf{z}}$ [Hec16]

$$\mathbf{S} = c^2 \varepsilon_0 \mathbf{E} \times \mathbf{B} \quad (2.42)$$

which in more relevant terms is described by the intensity I (thus also power deposited) and scales with the square of the electric field $I \propto |E|^2$ [Hec16]. Additionally, light waves adhere to the superposition principle. The superposition principle states that the fields from multiple light waves occupying the same space at the same time will add up locally, but not hinder or modify each other [Hec16]. However, if the sum of the fields is strong enough to elicit a nonlinear response from the medium, the induced nonlinear polarization will allow multiple light fields to interact [Boy08]. Such nonlinear interactions are discussed in section 2.5.1.

2.4.2 Frequency Domain

In this work all light sources are pulsed, and light pulses contain a spectrum of frequencies. The frequency bandwidth of a light pulse is related to the temporal pulse duration by an uncertainty relation [Hec16]. Signals can be converted from time domain to frequency domain and back by the Fourier Transformation [Wer11].

$$\mathbf{E}(\omega) = \int E(t)e^{-i\omega t} dt \quad (2.43)$$

where the result is a complex valued function of the frequency ω . In typical optical experiments one is only sensitive to the intensity envelope of the pump pulse and the phase must be inferred from Kramers-Kronig relations [Mae17, Boy08]. A special feature of THz spectroscopy is that the electro-optic detection of $\mathbf{E}_{\text{THz}}(t)$ provides access to both the amplitude and phase of the THz electric field. THz spectroscopy combined with electro-optic and magneto-optic detection provides direct access to the dielectric functions of materials in THz probe spectroscopy [Mae17].

2.4.3 Refractive index and polarization

For propagation through linear and homogeneous (the permittivity ε and the permeability μ are constants) media the refractive index n is [Hec16]

$$n = \sqrt{1 - \frac{\sigma(\omega)}{i\varepsilon_0\omega}} \quad (2.44)$$

where ε_0 is the vacuum permittivity, ω the frequency and σ the conductivity. The refractive index of the material dictates the velocity of light v [Hec16]

$$v = \frac{c}{\sqrt{\varepsilon\mu}} = \frac{c}{n} \quad (2.45)$$

This has direct consequences for measurements. The electric field of light can be decomposed into two mutually perpendicular waves with complex amplitude. The complex nature of the component amplitudes allows for a phase shift between the two component waves. If both components oscillate in phase, the resulting electric field vector will oscillate in a plane. This is called linear polarization. If the two components oscillate with a finite phase relationship the resulting field vector will trace out an ellipse in the plane perpendicular to the propagation. At a $\pi/4 \times \lambda$ phase shift the polarization becomes circular. The light is said to have elliptical or circular polarization. A similar decomposition may be done in terms of a left- and right-handed circular polarization basis [Hec16].

In a medium the complex refractive index can be directionally dependent (birefringence). The directionally dependent refractive index will change the polarization state of light

traveling through the medium since it acts differently on the two components of the wave [Hec16]. The refractive index will react to perturbations of the medium via ε, μ and thus n .

2.4.4 Transmission and reflection at normal incidence

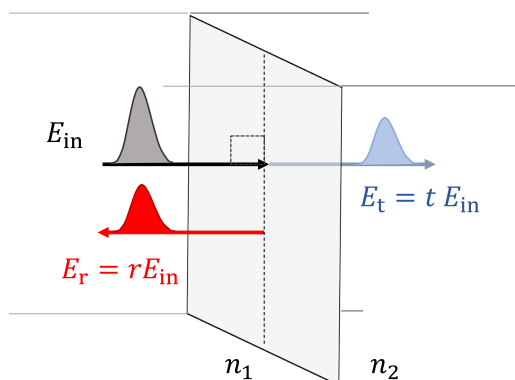


Figure 2.10.: Reflection at normal incidence A light beam encountering the interface between two materials with refractive indices $n_{1,2}$ will split into a transmitted and a reflected beam. At the interface, the transmitted and reflected fields must add up to the incident field. We consider the special case of normal incidence, when the Fresnel reflection and transmission coefficients r, t (eq. 2.46 and 2.47) have no polarization dependence.

A plane wave, coming from material one with refractive index n_1 , encountering an interface to medium two with refractive index n_2 will split into a transmitted and a reflected part (figure 2.10). At the interface the incoming intensity amplitude must equal the sum of the two outgoing amplitudes. The reflection (R) and transmission (T) coefficients are defined as ratios of intensity $I_{t,r}/I_{in}$ with $I \propto E^2$. However, we want to make a claim about the phase relationship of the initial and reflected electric fields at normal incidence to the interface, thus we consider [Hec16]

$$r = \frac{E_r}{E_i} = \frac{n_1 - n_2}{n_1 + n_2} \quad (2.46)$$

and

$$t = \frac{E_t}{E_i} = \frac{2n_1}{n_1 + n_2} \quad (2.47)$$

where $r^2 = R, t^2 = T$ and energy conservation requires $r^2 + t^2 = R + T = 1$.

Considering the case of $n_1 = n_{\text{air}} \approx 1$ and $n_2 = n_{\text{glass}} \approx 1.5$, r becomes negative. This corresponds to a π phase shift (reversed polarity) of the reflected field E_r with respect to incident field E_i because of the well-known identity $e^{i\pi} = -1$ [Con96]. Therefore, the field amplitude reflected at the air/glass interface will be 20% of the incident field amplitude with reversed polarity. The magnetic fields associated with the incident and reflected waves undergo the same amplitude changes. The reflected waves do not reverse their polarity due to the cross product in equation 2.41 ($\mathbf{B}_{0,\hat{y}} \propto \frac{\mathbf{k}}{\omega}(\hat{\mathbf{z}} \times \mathbf{E}_{0,\hat{x}})$) and the opposite propagation directions $\pm \hat{\mathbf{z}}$ of the incident and reflected waves. We will make use of this consideration in results chapter 6. There we will employ the reflection from a nearly perfectly conducting metal surface. Such a metal has a mostly imaginary (lossy) refractive index and nearly all the field amplitude is reflected, $r \approx -1$ [Hec16].

The more general case of reflection at an incidence angle θ with the sample normal will incur an angle dependence of transmission and reflection coefficient. Additionally, the transmission and reflection will be different for polarization components parallel (p - polarized) and perpendicular (s-polarized) to the plane in which incident and reflected ray lie. It is noteworthy, that at Brewsters' angle θ_{Br} the reflection for p-polarized light vanishes. At Brewster's angle the reflected light will be linearly s-polarized [Hec16].

The THz B field

Typically, the time-varying magnetic field $B(t)$ takes a subordinate role in discussions of optics. However, it should be noted that the magnetic field of a light pulse can interact with magnetic moments in the sample directly via the Zeeman effect discussed in section 2.3.2. This interaction is linear in the driving B field.

In the following we will consider the interaction of the time-varying electric field $E(t)$ of the light wave as it interacts with the electrons and competes with the other electric fields in the solid.

2.5 Nonlinear light-matter interaction

So far, we have discussed the linear response of matter to EM fields. We have seen that an applied electric field \mathbf{E} will generate a charge current \mathbf{j} due to Ohm's law [Hec16, Sei18b]

$$\mathbf{j}(\omega) = \underline{\sigma}(\omega)\mathbf{E}(\omega) = -i\varepsilon_0\omega(\epsilon - 1)\mathbf{E}(\omega) \quad (2.48)$$

which depends on the material properties through the structure and magnetic dependences of the conductivity tensor $\underline{\sigma}$. The conductivity can be related to the dielectric function ϵ , and thus to the susceptibility χ : $\underline{\sigma} \propto \epsilon - 1 = n^2 - 1 = \chi$. The electro-optic and magneto-optic probing mechanisms discussed above are transient measurements of the sample conductivity tensor [Hec16, Sei18b].

However, if the light fields are strong enough, they will compete with the fields inside the crystal. Macroscopic, this is expressed as the formation of an induced charge-current density \mathbf{j}_{ind} that may become nonlinear for large intensities $I(t) = n\varepsilon_0c|\mathbf{E}(t)|^2/2$ [Rab07, Sei18b, Mae17]

In a compressed, symbolic form one can write

$$\mathbf{j}_{\text{ind}} = \sum_{i=1}^{\infty} \underline{\sigma}^{(i)} \mathbf{E}^i \quad (2.49)$$

the conductivity $\underline{\sigma}^{(i)}$ is a tensor of rank $i + 1$. An even order conductivity would require that an electric field E that causes a charge-current density \mathbf{j}_{ind} would cause $-\mathbf{j}_{\text{ind}}$ under space inversion. This is impossible in crystals with inversion symmetry. Thus, nonlinear

effects of even order only appear in the absence of inversion symmetry. [Mae17, Boy08]

$$\mathbf{j}_{\text{ind},k} = \left(\sum_{l=1}^3 \underline{\sigma}_{kl}^{(1)} \mathbf{E}_l + \sum_{l,m=1}^3 \underline{\sigma}_{klm}^{(2)} \mathbf{E}_l \mathbf{E}_m + \sum_{l,m,n=1}^3 \underline{\sigma}_{klmn}^{(3)} \mathbf{E}_l \mathbf{E}_m \mathbf{E}_n \right) \quad (2.50)$$

We will consider nonlinear effects up to third order that are relevant for this thesis. The induced charge-current density will re-radiate. Importantly, the higher order charge-current densities allow electric fields with multiple frequencies to interact, adding sum and difference frequency components to the re-radiated light for example.

2.5.1 Second order (quadratic) nonlinearity

A second order susceptibility only appears in media without inversion symmetry. $\underline{\sigma}^{(2)}$ will combine the influence of two light fields with ω_1 and ω_2 in the induced charge-current density. This polarization will contain four frequency components [Boy08, Mae17]

$$\begin{aligned} \omega_{\text{DFG}} &= \omega_1 - \omega_2 \\ \omega_{\text{SFG}} &= \omega_1 + \omega_2 \\ \omega_{\text{SHG}} &= 2\omega_{1,2} \\ \omega_{\text{OR}} &= \omega_{1,2} - \omega_{1,2} = 0 \end{aligned} \quad (2.51)$$

The most important for this thesis are the last three. The second harmonic generation ω_{SHG} will occur in terms of frequency doubling in chapter 3.3.2. Optical rectification ω_{OR} , the difference frequency process with frequencies from the same pulse spectrum, will convert optical laser light into THz radiation (chapter 3.3.1). The electro-optical detection used to characterize the temporal evolution of the THz electric field (chapter 3.3.3) can be viewed as a sum frequency generation ω_{SFG} process [Kam06, Gal99].

2.5.2 Third order (cubic) nonlinearity

This term also appears in media with inversion symmetry. The optical Kerr effect used in Kerr lensing (section 3.2) is part of this group. The induced birefringence (refractive index difference along and perpendicular to the linear probe polarization) is dependent on intensity envelope $I \propto E^2$ [Boy08, Mae17, Sei18b]

$$\Delta n(\omega) = n_2(\omega) c \varepsilon_0 E^2(\omega) \quad (2.52)$$

where n_2 describes the nonlinear response of the refractive index to a time averaged Intensity $\langle E^2 \rangle$, additional to the weak field response n_0 [Boy08, Mae17]

$$n = n_0 + n_2 \langle E^2 \rangle \quad (2.53)$$

2.6 Context of this work

In this thesis, we investigate the THz speed properties of effects previously investigated only up to GHz speeds. As conventional AC current sources do not reach THz speeds, we utilize the electric and magnetic field of THz frequency light pulses. Typical material systems are pure ferromagnets (F), combinations of ferromagnetic and normal metal layers (FM/NM), as well as antiferromagnets (AFM). Typically, we investigate thin films of less than a few hundred nanometers thickness, but with larger lateral extent. We use the magnetic field of light to directly interact with the magnetization. We use strong THz electric fields to drive currents in the sample and weaker probe fields (both DC and at optical frequencies) to determine the sample conductivity and, thus, the spin dynamics (figure 2.8).

At this point we will take a step back and review some example experiments that make use of the above before highlighting how those concepts come together in this thesis. The experimental details of this thesis are presented in the next chapter.

2.6.1 Low frequency studies

First we will present a few examples of typical low frequency studies and methods. These do not represent a comprehensive overview of the field but rather are chosen for their relevance to the studies performed in this work.

External magnetic fields

A magnetization experiences a Zeeman torque (section 2.2.5) in the presence of an external B field. The ensuing damped precession as captured by the LLG equation (section 2.3.2) and studied in ferromagnetic resonance (FMR) experiments. In FMR experiments, a ferromagnet is saturated and oriented by a static (=no time dependence) magnetic field. An alternating (=time dependent) B field with frequency ω_B is applied at an angle to the magnetization, creating an additional time dependent torque. ω_B is chosen close to the Larmor resonance frequency (section 2.3.2). This frequency depends on the material properties and the static magnetic field [Sto06, Yos20]. The precession behaves like a driven oscillator and the magnetic properties of the sample can be determined in the resonance conditions (thus Ferromagnetic Resonance) [Man18]. The two important timescales are the oscillation period in resonance τ_1 and damping time τ_2 . τ_2 relates to the angular momentum transfer from the spin to the lattice, it is the spin-lattice relaxation time [Sto06]. Precessional motion of the magnetization in FM/NM stacks may also launch spin wave mediated spin currents in adjacent layers and is employed in spin-pumping experiments [Sto06, Yan16].

A short ~ 200 ps external magnetic field pulse can cause an overshoot of the magnetization M over the 90° angle of M with the original axis [Ger02], a process called precessional switching [Tud04]. In this case, M decays into a state antiparallel with its original direction. This is an example of magnetic switching and very important conceptually for magnetic storage. Magnetic switching with optical pulses has been demonstrated experimentally as well [Lam14], but is debated [Wan20a]. Recently, the external field has been replaced with injected spin magnetic moment in the form of a spin-transfer torque [Jhu20, Das18].

The symmetry and magnitude of magnetic effects (also the magneto-optical detection) is investigated by saturating the sample magnetization with an external magnetic field and then observing maximal signal variation for opposite external fields. Such a characterization of the signal variation due to the maximum possible (saturated) magnetization change provides a reference against which the typical small, induced variations in measurements can be compared [Mae17, Bea96].

External electric fields

An applied electric field E will cause a charge current j_c in a sample, depending on the conductivity σ . In low frequency electronics one conventionally thinks of the voltage U applied to a sample with resistance $R = 1/\sigma$ creates a charge current $j_c = \frac{U}{R} = \sigma E$. In the presence of spin-orbit coupling, a transient magnetization arises from a charge current either directly at suitable sample interfaces or due to charge to spin conversion effects like, for example, the Rashba effect (section 2.3.4) [Gam11] or spin-dependent Hall effects (section 2.3.4). Such current generated magnetic accumulations can transfer magnetic moment to neighboring magnets (in FM/NM stacks) and can even cause spin-transfer-torques and magnetization reversal [Ral08, Han08]. In suitable AFM crystal structures, the charge to spin conversion processes may even create opposite torques on both sublattices and act like a *staggered field* [Wad16, Žel18]. This staggered field achieves what no external magnetic field can: a reorientation of the Néel vector L perpendicular to the current flow direction [Ole17].

Additionally, in ferromagnets, the intensity gradient of an optical pulse has been employed to reverse the magnetization and cause domain wall motion [Sho19].

Magneto-transport effects in the presence of spin-orbit coupling, e.g. spin-dependent Hall effects, have been studied extensively with both electrical and optical detection [Sei18b]. The electrical detection with AMR investigates the magnetization dependent conductivity tensor $\underline{\sigma}$ experienced by a probing current and is especially useful for the study of ferro-, ferri-, and antiferromagnets [Ole17, Wad16, Nád21]. Optically, the magnetic properties of a sample are often characterized in reflection geometry with a magneto-optical Kerr effect (MOKE) geometry [Fan16, Urs16].

2.6.2 THz frequency studies and this work

It is yet unclear if all the interactions known for low frequency excitation are active at THz speeds (picosecond timescales) or if they encounter intrinsic speed limits. The work in this thesis relies on a pump-probe scheme with THz light excitation (both E_{THz} and B_{THz}) and either optical or electrical detection of the resulting ps dynamics. We will highlight effects that appear within the work in response to external fields before discussing the explicit experimental basics in the next chapter.

Promising work along this line has been done, for example, by I. Radu *et al.* who studied magnetization reversal of antiferromagnetic GdFeCo in response to a fs duration optical pulse via a transient ferromagnetic state [Rad11]. O. J. Lee *et al.* demonstrated ballistic precessional ferromagnetic switching with spin-orbit torques driven by 50 ps current pulses [Lee11]. K. Jhuria *et al.* studied ferromagnetic switching due to spin-orbit torque from 6 ps long current pulses. [Jhu20]. T. S. Seifert *et al.* demonstrated the THz switching speed (1 ps driving current pulse) in antiferromagnetic CuMnAs [Ole18] which we will build on in chapter 7.

THz E field pump

In this thesis, the spin accumulation due to spin-dependent Hall effects in FM/NM bilayers is investigated at THz speeds (chapter 5). The alternating, THz frequency charge current $\mathbf{j}_{c,THz}$ is generated by the electric field of a THz pump light pulse $\mathbf{j}_{c,THz} = \boldsymbol{\sigma} \mathbf{E}_{THz}$. The interaction of the transient spin populations with the spontaneous magnetization in the F layer is observed on fs timescales. In AFMs, the THz speed charge current creates, magnetic sublattice dependent, staggered magnetic fields. THz speed reorientation of AFM domains is quenched by functionalizing the semiconducting substrate in chapter 7. In ferromagnets, ohmic heating from a THz charge current leads to demagnetization [Wil17, Sha18] (chapter 6).

THz B field pump

The THz magnetic field will interact with the magnetization of a ferromagnetic layer via the Zeeman interaction (section 2.3.2). The Zeeman interaction gives rise to a Zeeman torque and subsequent magnetization dynamics. Importantly, the THz B field evolves quicker than the damping rate of the magnetization precession in typical ferromagnets. The torque response integrates over the duration of the applied magnetic field. Consequently, the Zeeman torque signal provides a measure for the time dependent magnetic field in the sample [Vic13] (chapter 5). The THz magnetic fields in this study are ≤ 1 T while the spin-orbit field is often ~ 4 T. The THz magnetic field will thus not disturb SOI generated spin polarizations strongly [Sei18b].

Additionally, a scheme is presented to distinguish the simultaneous actions of the THz E and B fields in chapter 6.

E field probe

The sample response is probed by a weaker charge current induced by an optical probe pulse along the polarization direction of \mathbf{E}_{pr} in chapters 4, 5, and 6. The probing field E is supplied via electrical contacts in chapter 7.

3 Experimental methods

In this work, we will study the magnetic dynamics of magnetically ordered thin film samples upon excitation with intense THz frequency light pulses. The transient magnetization will be interrogated either contact-less by short optical frequency light pulses, or by contacted electrical resistance measurements. Repeated measurements with different pump-probe delays allow us to reconstruct the magnetic dynamics. We will exploit the versatility of this technique to investigate light field driven magnetization dynamics, THz light field induced spin currents and the interaction of these spin currents with existing magnetic order. We will also extend the capabilities of this experimental technique, adding the ability to determine whether the THz electric or magnetic light field is driving the observed sample response. Eventually, we will also investigate the suppression of THz light field induced resistance modulation in an antiferromagnet.

In this chapter we will discuss the basic implementation of the THz pump – optical/electrical probe experiment. First, we will give a brief overview over the amplified laser system and the THz generation process in a tilted-pulse front Lithium Niobate source. We will discuss the basic experimental setup and introduce the concepts necessary to adapt it to the needs of the individual experiments. The individual customization of the basic setup will be described in each of the results chapters. Finally, we will discuss the detection mechanisms and the physical implementation of the detection. This chapter forms a repository of the basic experimental concepts that the results chapters will refer to, in order to avoid repetition.

While we discuss only those principles necessary for the interpretation of the results of this thesis, the field of magnetism research has brought forth a plethora of experimental techniques. For an overview of many experimental techniques to investigate magnetism we suggest [Sto06]. For a detailed discussion of pulsed lasers please refer to [Mil10, Rul05]

3.1 Introduction: the pump-probe technique

The pump-probe principle provides the experimental basis for the time domain spectroscopy performed in this work. It is a ubiquitous technique that, for example, enables the study of elementary solid-state excitations such as phonons, magnons and ultrafast relativistic transport effects by recording the temporal response of the solid-state sample on a femtosecond timescale [Kam13, Kam10, Mae18]. A strong light pulse (‘pump’) excites the sample and the ensuing dynamics are interrogated with a second, weaker light pulse (‘probe’) at a certain delay time later. The probe pulse is weak, such that it does not influence the previously generated excitation. Typically, the probe pulse is linearly polarized initially, and experiences a change of the polarization state (rotation or ellipticity) depending on the interaction with the excited sample. The time resolution of such a measurement is determined by the time that the probe pulse interacts with the sample, i.e. the probe pulse duration. The pump-probe process is repeated in a stroboscopic manner

with various pump-probe time delays, thus recording the temporal evolution of the sample response [Rul05].

The (transient) sample magnetization is interrogated with magneto-optic and magneto-electric effects, which have different names depending of the probe geometry as discussed in the previous chapter 2.3.5. In this thesis, the optical pulse will probe the sample response in transmission and at normal incidence. However, the pump-probe principle is not limited to optical excitation and detection. One study presented in this work (chapter 7) will interrogate the system response to optical stimulus with a contacted measurement of the anisotropic magnetoresistance (AMR, section 2.3.5).

We will first discuss the laser system that provides both a weak probe and a strong pump beam in the near infrared spectral region. However, we will only briefly touch upon laser technology, for a comprehensive discussion please refer to [Mil10, Rul05]. Afterwards, we will discuss the THz source that will convert the strong near-IR pump beam into THz frequency radiation. The THz generation is performed in a high field, table-top THz tilted pulse front lithium niobate source. These THz pulses in turn are used as pump pulses for THz pump – optical probe spectroscopy of magnetic samples. Finally, we will discuss the various probing mechanisms available to interrogate the system response. Together with the discussion of various details of the experimental apparatus, this chapter serves as a reference guide to avoid repetition of the experimental basics throughout the thesis. The detailed customization of the fundamental setup is discussed in the corresponding results chapters.

3.2 The (pulsed) laser

A typical laser consists of three components: a gain medium, a cavity and an energy source typically called pump. Very powerful light pulses are generated by daisy-chaining multiple amplification units [Rul05].

MHz Oscillator

The oscillator and fundamental ‘clock’ of the laser is a *COHERENT VITARA-T* Oscillator. This is a turn-key laser system with a self-aligning cavity and excellent long-term stability. At 80 MHz repetition rate it is tunable in spectral bandwidth and central wavelength, in our case it produces 25 fs pulses at 790 nm central wavelength. A synchronized 80 MHz electrical trigger informs the timing of further active laser components. A principle sketch of such a laser system is presented in figure 3.1.

Even though it is a company secret how the cavity is designed exactly, the laser properties sheet suggests a titanium-doped sapphire (Ti:Al₂O₃ or Ti:Sa) gain medium in a tunable cavity. Ti:Sa is a 4-level electronic system that supports the necessary population inversion for stimulated emission. The gain medium is pumped with another 532 nm laser. The cavity, acting as a linear optical resonator of length l , supports optical modes with frequencies $f_j = j\Delta f$, where $j \in \mathbb{N}$ and the mode spacing $\Delta f = c/2l$ [Rul05]. For pulsed

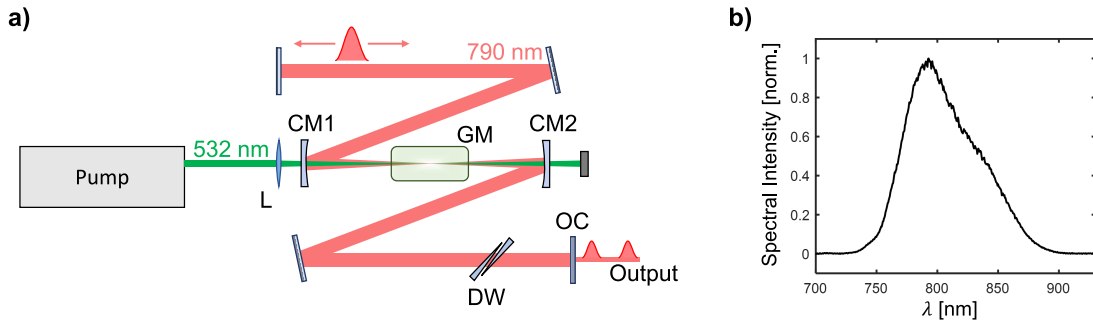


Figure 3.1.: The MHz Oscillator concept a) As the exact schematics of the *COHERENT VITARA-T* 80 MHz Oscillator are confidential, we here provide a simplified schematic of a laser with comparable output, as described by [Mae17]. The gain medium (GM) is a titanium-doped sapphire (Ti:Sa) that forms a population inversion upon excitation with a 532 nm pump laser (green). The cavity around the GM supports a light pulse that is amplified on every pass through the GM. The curved mirrors (CM1, CM2) focus the light into the crystal for a better interaction with the excited crystal region. For pulsed operation, the laser must be in mode-locked operation, relying on the mode-locking properties of the GM. The dispersion introduced by the GM is compensated for with the double wedges (DW) for stable operation. On every pass, part of the pulse in the cavity is transmitted through the output coupler (OC) and becomes available for experiments. The cavity round-trip length is matched to the desired 80 MHz repetition rate of the laser. The *COHERENT VITARA-T* is a self-aligning turn key system that optimizes the cavity autonomously. Both the output central wavelength and spectral width can be tuned. b) The output spectrum of the *COHERENT VITARA-T* used throughout this work.

operation, the different modes of the cavity must be phase-locked. Such mode-locked operation is achieved by periodic modulation of the cavity properties. A modulation of the cavity is achieved, for example, by exploiting the Kerr-lens forming in the gain medium in response to the light pulse in the cavity [Mil10]. Kerr lensing is a χ^3 effect, thus the refractive index of the gain medium depends on the instantaneous intensity of the light traversing it (section 2.5.2). As the typical laser mode has a gaussian intensity profile both across the beam and in time, the transient refractive index in the gain medium will act like a time-dependent lens, modulating the cavity at the correct interval for mode-locked operation [Bra92]. Upon each round-trip in the laser, part of the light pulse is coupled out for use in the experiment.

The output beam is split into two components: one component of approximately 130 mW power used to interrogate the material response in the measurement (‘probe’), and another component roughly 3 times more powerful that seeds the kHz amplifier, discussed next.

kHz Amplifier

To reach the large laser pulse powers required in this work, single pulses from the oscillator pulse train must be amplified. Single pulses are picked for amplification, reducing the repetition rate from 80 MHz to 1 kHz. Two Faraday insulators prevent back-scattering from the amplifier into the Oscillator. The seed pulses are temporally stretched with a spectral chirp. This lowers their peak field and protects the laser optics from damage.

Chirped pulse amplification (CPA) [Str85] of this type was honored with the 2018 Nobel Prize in Physics as strong field laser pulses are ubiquitous in modern physics research. After amplification the chirp is corrected and the original pulse duration is restored for the amplified pulse. An additional benefit of a *compressor* that controls the final chirp is that it can preempt the chirp experienced by the laser pulse while propagating to the experiment, ensuring the shortest pulses and highest fields directly at the sample.

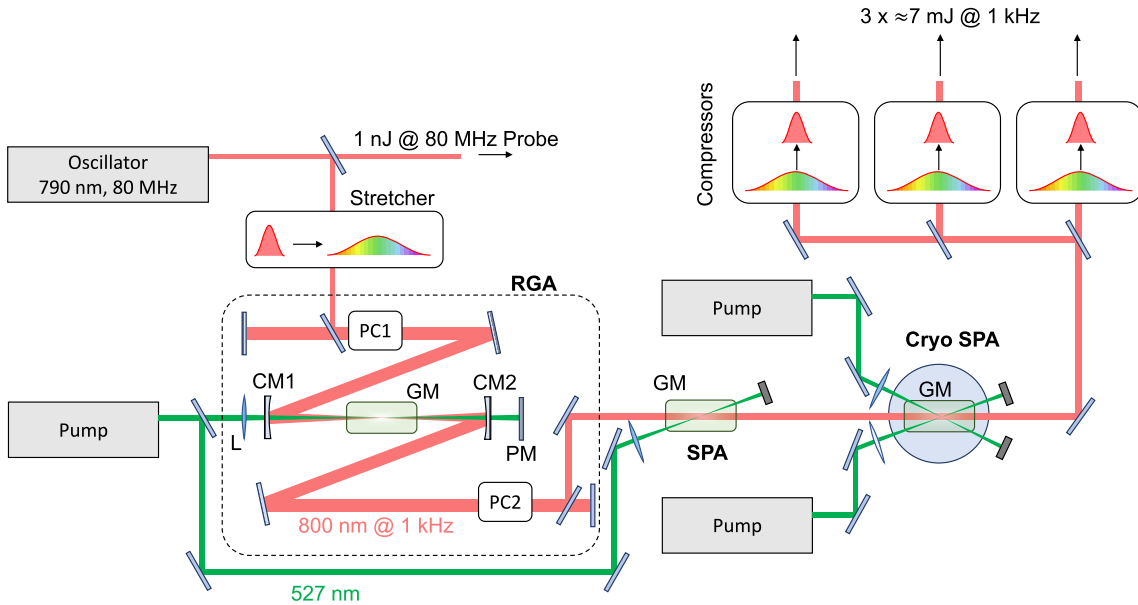


Figure 3.2.: Principle of the kHz amplifier While the laser system used in this work is a custom conglomerate of a *COHERENT Legend Elite Duo* and a *COHERENT Cryo-PA*, we here present the strongly simplified amplification scheme. The fundamental 'clock' of the laser is the oscillator in the top left corner. The 80 MHz oscillator pulse train is split in a rough 1:3 ratio, transmitting ≈ 1 nJ pulse energy for optical probing while using the rest to 'seed' the amplifier. The seed pulses are chirped for efficient amplification, increasing the pulse duration and lowering the peak field. Chirping pulses for amplification is known as *chirped pulse amplification* (CPA). The first amplification stage is called the *regenerative amplifier* (RGA, black dotted box) because the gain medium (GM) is located in a cavity. The Ti:Sa gain medium is pumped with 527 nm laser light. To maximize the output the pump light is reflected back into the GM for a second pass (PM). Contrary to the oscillator, the RGA cavity does not require mode-locking as the seed light is pulsed already. Each pulse must complete tens of round-trips in the cavity for optimal amplification, thus not every pulse from the oscillator pulse train is amplified. Pockels cell 1 (PC1) couples 1 in every 80 000 oscillator pulses into the cavity for amplification, reducing the laser repetition rate to 1 kHz. After sufficient round-trips the amplified pulse is coupled out by PC2. The next amplification step is a *single pass amplifier* (SPA) where the pulse makes only one pass through the GM. The third amplification stage is a *cryogenically cooled single pass amplifier* (Cryo-SPA). For heat load control the laser crystal is cooled to 80 K in a recirculating Helium cryostat. As a result the Cryo-SPA is able to sustain pumping with two pump lasers depositing ~ 70 W of pump power. Finally, the amplified pulse train is separated into three output beams with an average pulse energy of ≈ 7 mJ. Each output is separately compressed, compensating for the stretchers action and returning the laser pulses to short temporal duration and large peak fields. An additional benefit of the compressors is the ability to preemptively account for later dispersion along the beam path, ensuring the required pulse length and chirp directly at the experiment. The multiple amplification processes gradually shift the laser central wavelength to 800 nm.

The amplifier stages in this work are a custom combination of a *COHERENT Legend Elite Duo* and a *COHERENT Cryo-PA*. Together, they combine three amplification stages that are pumped by *COHERENT Evolution HE* or *COHERENT Revolution* pump lasers (Nd:YLF, 527 nm, 45mJ at 1kHz repetition rate, 150 ns pulse length, two generations of essentially the same laser) as seen in figure 3.2. Initially, one pulse is picked from the oscillator pulse train by a pockels cell and allowed to propagate in the *regenerative amplifier* (RGA) cavity. The gain medium in the cavity is pumped twice as the pump beam is folded back on itself after the first pass through the crystal. After multiple round trips, the second pockels cell extracts the amplified pulse. The RGA boosts the pulse power from a few hundred mW to 6 W. From there, the pulse traverses two more *single pass amplifiers* (SPA). Noticeably, the last laser crystal is held at 80 K in a recirculated Helium cryostat for efficient cooling and amplification. It is also pumped by two pump lasers totaling ≈ 60 W of pump power incident on the crystal. This very powerful amplification unit is a custom design from *COHERENT*. Finally, the amplified beam is split into three beams with approximately 7 mJ, 35 fs pulses centered at 800 nm and with a repetition rate of 1 kHz. Each of the three outputs has a separate pulse compressor unit, thus the output pulse duration (chirp) can be adjusted for each output separately.

This system has been upgraded since the last thesis was completed at this system by S. F. Mährlein [Mae17]. Thus his description differs slightly from the one presented here, while referring to the same laser system.

3.3 Tabletop THz spectrometer

There are many different methods to generate radiation in the THz frequency range. Please refer to [Bru12, Fue19] for a general overview of the state-of-the-art. A particularly promising broad-band THz emitter is the spintronic emitter demonstrated by T. S. Seifert [Sei16]. We will discuss the inverse process to the spintronic emitter in chapter 5. This thesis makes use of a tilted pulse front Lithium Niobate source to generate strong field THz pump pulses for magnetism research. The sample response is detected by electro-optic and magneto-optic sampling.

The basic principle of electro-optic and magneto-optic sampling relies on the vastly different timescales on which the pump and probe fields evolve. The THz pump pulse has a period of ≈ 1 ps while the probe pulse envelope is only 25 fs long. For a fs probe pulse co-propagating with a THz pulse the THz field in the sample is quasi-static [Kam13]. Many repetitions of the experiment with different pump-probe delays reconstruct the sample response to the THz field. Naturally, as the probe pulse must be shorter than the sample property evolution, the probe pulse duration limits the temporal and frequency resolution of the pump-probe experiment.

A schematic overview of the experiment is presented in figure 3.3 and will be referred to throughout the following discussion.

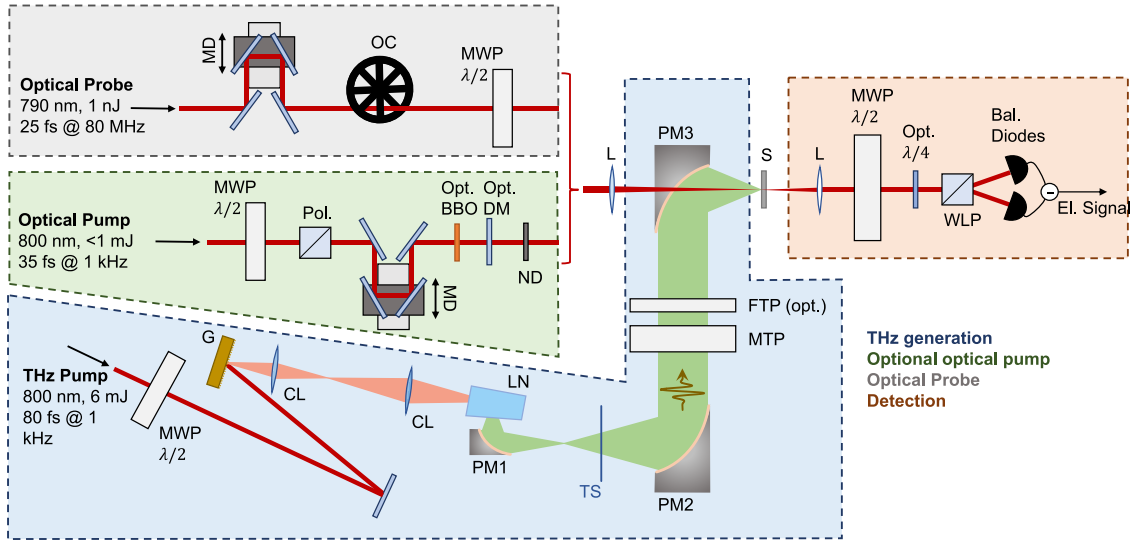


Figure 3.3.: Setup Schematic The base setup is identical for all results presented in this chapter. A THz source (blue region) provides THz pulses at the sample (S) location. Typically, an optical probe beam (grey region) is focussed through a hole in the last parabolic mirror (PM3) to interrogate the sample response. The modulated probe beam properties are translated into an electrical signal by the detection (orange region). Chapter 7 does not require the probe beam, but a second optical pump (green region) instead. **Step-by-step: THz pump (blue region)** 6 mJ pulses stretched to ≈ 80 fs with 800 nm central wavelength are taken from one laser output to pump the Lithium Niobate (LN) crystal. The special tilted pulse front phase matching is achieved by imaging the laser spot on a grating (G) with two cylindrical lenses (CL) into the crystal. The motorized $\lambda/2$ waveplate (MWP) tunes the grating efficiency and controls the pump power supplied to the LN crystal. The THz radiation (green area) is caught by a short focal length parabolic mirror (PM1) and cleaned from remaining 800 nm pump light with a *Teflon* scatterer (TS). A second 2-inch parabolic mirror (PM2) collimates the THz radiation. A motorized THz polarizer (MTP) and an optional fixed orientation THz polarizer (FTP) control the THz radiation power and polarization plane as described in figure 3.5. The THz radiation is focussed onto the sample by another parabolic mirror (PM3). **Optical probe (grey region)** ≈ 1 nJ, 25 fs pulses from the 80 MHz oscillator pulse train are mechanically delayed (MD) with respect to the THz pump pulse with a motorized linear translation stage. To reduce the accumulated heat in the sample, the probe beam can be blocked in between the THz pulses with an optical chopper (OC). A motorized $\lambda/2$ waveplate (MWP) controls the probe polarization plane. **Detection (orange region)** A motorized $\lambda/2$ waveplate (MWP) compensates the initial probe polarization rotation plus any polarization rotation from the static sample properties to balance the detection. To measure polarization ellipticity changes, an optional $\lambda/4$ waveplate (Opt. $\lambda/4$) turns an elliptical polarization into a polarization rotation. A polarization rotation is translated into an intensity balance of the two orthogonally polarized beams leaving the Wollaston prism (WLP) and detected as a difference signal voltage from the balanced Si photodiodes (Bal. Diodes). **Optical pump (green region)** < 1 mJ of 800 nm light is taken from another 1 kHz laser output and compressed to 35 fs duration. A combination of a motorized $\lambda/2$ waveplate (MWP) and a polarizer (Pol.) allow for automated power control. The optical pump is mechanically delayed (MD) with respect to the THz pump pulse with a motorized linear translation stage. Optionally, the 800 nm (1.55 eV) pulses can be frequency doubled in BBO (Opt. BBO) to 400 nm (3.1 eV). Remaining pump light is removed with a dielectric mirror (Opt. DM). Further power reduction is achieved with neutral density (ND) filters, as explained in the main text.

3.3.1 THz generation

Many tabletop THz sources rely on optical rectification (section 2.5.1) to convert strong laser pulses to the THz frequency range. The simultaneous interaction of two intense light waves of frequencies ω_1, ω_2 with a large second order nonlinear susceptibility χ^2 will generate a nonlinear polarization response P_{NL}^2 containing, among others, a non-oscillating term $\omega = \omega_{1,2} - \omega_{1,2} = 0$ which is commonly referred to as ‘rectified’ [Boy08, Fue19]. Ultrashort laser pulses, however, contain a spectrum of frequencies, broadening the initial spectral line $\omega = 0$ to reach finite frequencies, up to the THz frequency range.

Optical rectification in Lithium Niobate is more complicated than in other typical generation crystals (GaSe, ZnTe, etc.). The special complication arises from the rather difficult phase matching conditions. For efficient THz generation it is necessary to match the pump light phase to the THz radiation phase in the crystal. Typically, the frequency dependent refractive index of a generation crystal will match for the two frequencies along a certain crystal direction. The phase matching in Lithium Niobate is more complicated and described in detail in [Heb02, Heb04, Heb08]. For this thesis, it is sufficient to understand that efficient THz generation in Lithium Niobate requires a pulse front tilt of the pump light. A pulse-front tilt is achieved when light is scattered from a grating, such as the one in figure 3.3. A pulse-front tilt means that the pulse front experiences a delay across the cross section of the beam, while the phase front of the NIR beam remains perpendicular to the travel direction. This is as if the beam was segmented laterally and the segments were continuously delayed in time. A combination of a reflective grating and a 4f telescope are used to create a beam with tilted pulse front, imaging the laser spot on the grating on the generation crystal. Additionally, the crystal itself has one side face cut in the same angle, emitting THz radiation in plane waves at an angle to the direction of the laser pump light.

One important feature of the OR process is that it generates identical, thus *carrier envelope phase* (CEP) stable THz pulses from non-CEP-stable pump laser pulses. CEP stable THz pulses are a necessary requirement for the stroboscopic pump-probe technique, as a fluctuating CEP would ‘wash out’ the sample response over many pulses [Mae17, Kam06].

The THz pump pulses of this work are generated in a tilted pulse front Lithium Niobate source that is described in detail in [Saj15]. We use a 1.3 mol-% MgO doped stoichiometric LiNbO₃ crystal. The 800 nm wavelength pump pulse from the amplified laser system is stretched from 35 fs to ≈ 80 fs with the output compressor (see above). The pump pulse front tilt of 62° inside the crystal generates a THz spectrum centered at ≈ 1 THz [Saj15]. The pulse front tilt is generated with a 2000 lines/mm grating and a 4f telescope made up of one 250 mm and one 150 mm cylindrical lens. The Lithium Niobate source generates 1 ps duration, near single cycle pulses with a spectrum from 0.1 – 2.5 THz peaked at 1 THz and field strengths of up to 1 MV/cm at the sample. The electric field of the THz pulse and the corresponding power spectrum of our source is presented in figure 3.4. The typical THz spot size on the sample is $\approx 1100 \mu\text{m}$ (gaussian 1/e diameter), this value will be used throughout the thesis. The electric field evolution was determined with *electro-optic sampling* (EOS) in a 50 μm z-cut quartz and deconvolved with a detector response function,

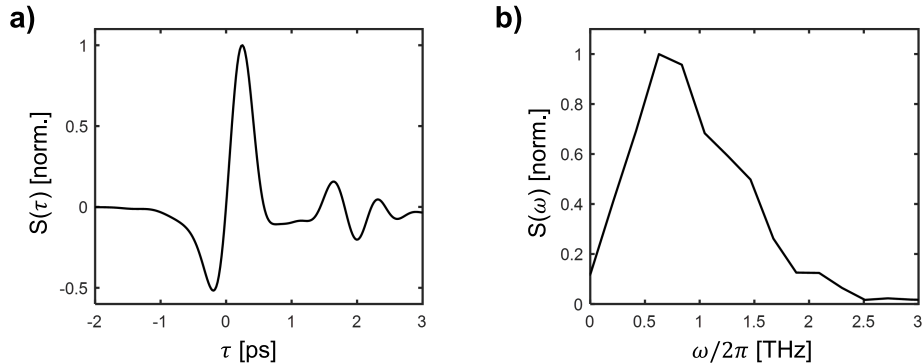


Figure 3.4.: The THz source properties a) The THz electric field detected with electro-optic sampling in 50 μm z-cut quartz. The trace was deconvolved with a response function measured by A. L. Chekhov, Y. Behovits and B. Rosinus Serrano. The main pulse ($\tau < 1$ ps) is followed by multiple echoes that are due to the response of air. b) The intensity spectrum associated with the THz pulse of panel a. The LN source emits pulses with a spectral range of 0.1-2.5 THz, centered at 1 THz.

experimentally determined by A. L. Chekhov, Y. Behovits and B. Rosinus Serrano.

The THz radiation is collected by a short focal length off-axis parabolic mirror. Remaining mid-IR pump light is removed from the beam with teflon sheet scatterers that are transparent to the THz radiation. The THz radiation is collimated with a 2-inch off-axis parabolic mirror. After collimation, the THz radiation polarization is conditioned as described below. Finally, the THz radiation is focused on the sample with another 2-inch off-axis parabolic mirror. This last parabolic mirror has an additional hole along the axis of the focus, providing access to the sample for the probe beam.

Polarization and power control

The THz radiation generated in the lithium niobate source has a fixed polarization direction along the crystal c-axis. However, the experiments often require the comparison of THz stimuli with different polarization planes and even completely opposite field polarity. Rotating the entire generation assembly to change the polarization plane is unfeasible. Broadband waveplates in the appropriate frequency range are yet unavailable, thus we resort to variable polarization plane projections using *TYDEX HDPE* and *PP THz* polarizers.

A polarizer is an optical element that rejects one linear polarization component of light while transmitting the orthogonal polarization component. The transmitted field component of an ideal polarizer is the projection of the incident light field into the transmission plane of the polarizer, at an angle γ to the incident linear polarization direction. Considering $I \propto E^2$, the transmitted intensity is given by Malus' Law [Hec16]

$$I_t = I_0 \cos^2(\gamma) \quad (3.1)$$

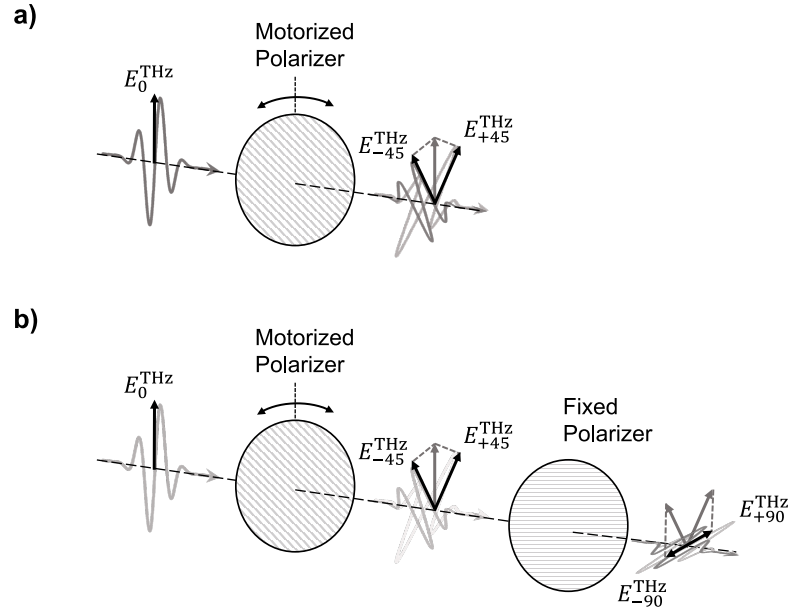


Figure 3.5.: Polarization projection a) A THz polarizer mounted in a home-built motorized rotation mount projects the incident THz field E_0^{THz} into one of two new, mutually orthogonal polarization directions $E_{\pm 45}^{\text{THz}}$, at an angle $\gamma = \pm 45^\circ$ from the polarization of E_0^{THz} . According to Malus' Law (equation 3.1) $E_{\pm 45}^{\text{THz}} = \frac{1}{\sqrt{2}}E_0$. b) A further THz polarizer with fixed orientation can project the two $E_{\pm 45}^{\text{THz}}$ into the direction orthogonal to the initial THz polarization direction E_0^{THz} to create two THz pulses with flipped polarity $E_{\pm 90}^{\text{THz}}$. The new maximum field value is still achieved when the motorized polarizer is set to $\gamma = \pm 45^\circ$, however the double projection leaves the maximum available THz field at $E_{\pm 90}^{\text{THz}} = \frac{1}{2}E_0$. Importantly, the second polarizer fixes the final polarization and ensures the flipped polarity, thus choices of $\gamma = \pm(< 45^\circ)$ can be used as a THz power control. To ensure a clean final polarization, the fixed polarizer is doubled in the experiment.

Chapter 7 requires two orthogonal THz polarities, thus a THz polarizer mounted in a home-built rotation stage projects the THz light into two orientations $\gamma = \pm 45^\circ$, with electric field $E_{\pm 45} = \sqrt{\frac{1}{2}I_0} = \frac{1}{\sqrt{2}}E_0$ (figure 3.5a). In this case, the 800 nm pump power incident on the generation crystal is varied to control E_0 , with a maximum $E_0 \sim 700$ kV/cm. A straightforward option to vary the 800 nm pump power is to employ the polarizing properties of the grating used for pulse-front tilting (figure 3.3). The intensity of light diffracted from the grating also depends on the incident polarization plane with Malus' Law above. Thus, in chapter 7, the 800 nm polarization plane is controlled with a motorized *THORLABS* $\lambda/2$ waveplate mounted in a *NEWPORT PR50CC* motorized rotation mount and controlled with a *NEWPORT ESP301*.

Chapters 5 and 6 require THz radiation with opposite polarity, corresponding to a polarization rotation by 180° . However, equation 3.1 shows that $I_0 \cos^2(\pm 90^\circ) = 0$. A work-around is to subdivide the process into two projections of 45° each, as shown in figure 3.5b. The first polarizer is again motorized with a home-built rotation stage, while the second polarizer is fixed in the direction orthogonal to the initial THz polarization direction. The maximum possible field transmitted through the polarizer assembly is achieved at $\gamma = \pm 45^\circ$ (first polarizer), yielding $E_{\pm 90} = \sqrt{\frac{1}{4}I_0} = \frac{1}{2}E_0$ (~ 500 kV/cm). However,

depending on $\pm\gamma$ of the first polarizer, the field strength of the final THz radiation can be controlled. This power control is preferable over varying the pump power to the Lithium Niobate crystal as it does not influence the thermal equilibrium in the generation crystal. It must be noted that the extinction ratio of the THz polarizers is limited, thus the final polarizer was doubled to ensure a clean THz polarization for the experiment.

3.3.2 Optional optical pump

The measurement in chapter 7 interrogates the sample response through contacted electrical measurements, thus it does not require an optical probe pulse. However, it requires an optical pump pulse, additional and time delayed to the THz pump pulse. The additional optical pump is indicated in figure 3.3 as one of the two options to be focused on the sample through the hole in the final parabolic mirror.

The additional optical pump pulse is provided from another, separately compressed, output of the laser amplifier. This laser output provides a 1 kHz repetition rate pulse train with ≈ 7 mJ, 35 fs pulses centered at 800 nm. Roughly 4% of the laser output intensity are picked off with a pick-off mirror for further use. A combination of a motorized (*NEWPORT PR50CC*) $\lambda/2$ waveplate (*THORLABS*) and a polarizing beamsplitter (*ALTECHNA*) provide power control, according to the polarization sensitive transmission of a polarizing beamsplitter (Malus' Law equation 3.1). The $\propto \cos^2$ transmission dependence provides a near linear power control for a narrow region of angles, saturating both for high and low powers. In practice, the limited polarizer extinction ratio also limits the lowest possible powers, accompanied with a loss of beam polarization when the transmitted (intentional) and leaked (unintentional, polarized perpendicular to the transmitted) components become equal. To remain in the linear region, the variable power control is followed with *neutral density* (ND filters) that provide a frequency independent fixed attenuation of the beam. The typical 1.55 eV optical pump spot size on the sample was determined with the pinhole method to be $\approx 85 \mu\text{m}$ (gaussian 1/e diameter), this value will be used throughout the thesis.

Optionally, the optical pump frequency is doubled (wavelength halved to 400 nm) in a beta barium borate ($\text{Ba}(\text{BO}_2)_2$, BBO) crystal. Frequency doubling is a nonlinear *sum frequency generation* (SFG) process involving two photons of identical photon energy mixing to produce one photon of twice the energy (section 2.5.1). The intensity of the second harmonic wave I_2 scales quadratically with the intensity of the initial wave $I_2 \propto I_1^2$, before saturating at high powers [Boy08]. Remaining 800 nm pump light is removed with a dichroic mirror. The very low 400 nm powers made beam characterization with the pinhole method impossible, thus from gaussian optics (considering the beam narrowing in the frequency doubling process) we estimate a spot size of approximately $(\sqrt{(2)/2}) \cdot 85 \mu\text{m} \approx 60 \mu\text{m}$ (gaussian 1/e diameter).

Finally, the optical pump path length can be changed with a motorized linear translation stage (*NEWPORT GTS-150* controlled by a *NEWPORT XPS* controller), allowing for a pulse-pulse delay with respect to the THz pump pulse.

3.3.3 Optical probe

Chapters 4, 5, and 6 require an optical probe to interrogate the sample properties. Additionally, EOS in quartz allows us to characterize the THz pulse as presented in figure 3.4. As mentioned in section 3.2 above, a fraction of the 80 MHz oscillator pulse train are reserved to act as probe beam. Thus, ≈ 1 nJ, 25 fs linearly polarized pulses with 790 nm central wavelength interrogate the sample properties. The probe path length can be modified with a motorized linear translation stage (*NEWPORT GTS-150* controlled by a *NEWPORT XPS* controller), allowing for a pump-probe delay τ with respect to the THz pump pulse. Additionally, the probe polarization can be controlled with a motorized (*NEWPORT PR50CC*) *B. HALLE* broadband $\lambda/2$ waveplate. The typical optical probe spot size on the sample was determined with the pinhole method to be $\approx 60 \mu\text{m}$ (gaussian $1/e$ diameter), this value will be used throughout the thesis.

Upon interaction with the sample (or detection crystal) the linearly polarized probe beam may acquire a polarization rotation θ or ellipticity change η proportional to the transient sample parameters. A polarization change is detected with a balanced detection or optical bridge. The optical bridge is a combination of a Wollaston prism (WP) and a balanced photodiode (figure 3.3). The Wollaston prism splits an incoming beam into two orthogonally polarized component beams that are recorded on two coupled *HAMAMATSU* Si photodiodes, fast enough to resolve the 80 MHz pulse train. The two photodiodes are wired to record the difference in the two component beams, having no output when both component beams have equal intensity. Another motorized (*NEWPORT PR50CC*) *B. HALLE* broadband $\lambda/2$ waveplate compensates for an underlying polarization rotation from the sample and the initially rotated probe polarization, balancing the intensities on the photodiodes in the absence of a pump induced polarization change.

A probe beam polarization rotation θ leads to an imbalance of the two component beam intensities and thus to a finite signal from the Si photodiodes. The probe ellipticity change η is converted to a polarization rotation with an optional *B. HALLE* broadband $\lambda/4$ waveplate in front of the Wollaston prism. To recover the time-dependent material properties we vary the pump-probe delay τ and repeat the measurement, reconstructing the signal $S(\tau)$. The motorized translation stage controlling τ is operated in *fast scan mode*: it scans the entire pump-probe delay range in one continuous motion and records the position whenever an electrical trigger signal arrives, synchronized with the 1 kHz laser repetition rate. As a consequence $S(\tau)$ is not sampled on an equi-spaced τ grid and each pump-probe trace must be interpolated before further processing, such as averaging multiple pump-probe traces.

While the probe intensity is chosen to be weak enough not to perturb the sample itself, we protected the sample in chapter 5 from accumulated heat from the probe beam by blocking the 80 MHz pulse train with a *THORLABS* optical chopper in between the 1 kHz repetition rate pump pulses.

3.4 Computer controlled data acquisition

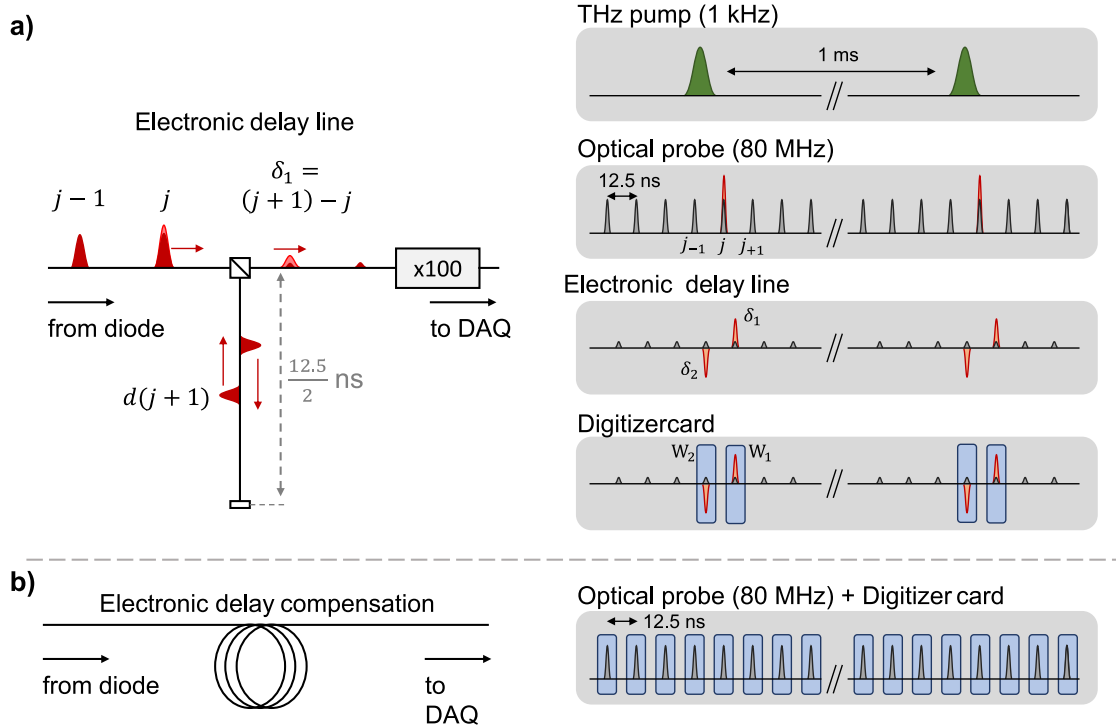


Figure 3.6.: Detection on ps and ms timescales **a)** The electrical delay line is an electrical interferometer performing a background subtraction. An appropriately dimensioned voltage divider (indicated as beamsplitter) separates incoming pulses into a transmitted and a deviated part. The deviated component $d(j+1)$ of the pulse preceding the signal carrying pulse j reverses sign upon reflection at the end of the delay line and is superimposed with the transmitted component of pulse j . The delay line length is matched to the pulse separation of 12.5 ns. The signal carried by pulse j remains as $\delta_1 = (j+1) - j$ and is amplified $\times 100$ before continuing to the data acquisition (DAQ). The superposition of j with the following pulse $j-1$ will also isolate the signal $\delta_2 = -\delta_1$. The process is also displayed as signal pulse trains in the grey boxes on the right. The two signal components are detected with the digitizer card (blue measurement windows) and combined in LabVIEW. **b)** To record the sample response on a ms timescale every oscillator pulse is recorded, sampling the sample properties at 12.5 ns intervals for 1 ms duration. Recording longer timescale data is necessary for calibration measurements like hysteresis loops. Recording every MHz pulse requires that the electronic delay line and the signal amplifier are removed. The change in signal propagation delay through these components is compensated by adding signal cable (indicated as wire coils), ensuring a good overlap of the detection windows (blue) with the 80 MHz pulses. Figure partially redrawn from [Mae17].

The repetition rate mismatch of the pump (1 kHz, 1 ms period) and probe (80 MHz, 12.5 ns period) pulses means that only 1 in 80 000 oscillator pulses carries a pump induced modulation. The entire oscillator pulse train is sensitive to material property changes on times up to 1 ms. We will employ these two separate regimes to determine the sample response to the THz pump pulse (ps timescale, chapters 5, 6) and to calibrate the sample detection with measurements on the ms timescale (chapter 4). In contrast, in chapter 7 we detect pump dependent sample changes electrically on the second timescale.

Picosecond timescale optical detection

Each oscillator pulse will generate an electrical signal pulse, ideally due to a pump induced modulation but also due to inherent diode property mismatch or imperfect detection balancing. As seen in figure 3.6a the pump induced signal carrying pulse j is preceded and followed by non-signal carrying pulses $j \pm 1$. To isolate the pump-induced change, we first perform an electrical background subtraction with an *electronic delay line*. A similar description of the electronic delay line is presented in [Mae17].

Essentially, the electronic delay line acts similar to a hard-wired lock-in amplifier. The electrical signal pulses are split into a *transmitted* and *deviated* components by a voltage divider with appropriate resistances, indicated by the beamsplitter in figure 3.6a in analogy to an optical interferometer. The *deviated* component of the electrical pulse $j + 1$ will travel down the delay line and be reflected at the (short-circuited) end. Upon reflection, the electrical pulse changes sign and travels back to the electrical beamsplitter. The delay line length is chosen such that the pulse propagation time matches the 12.5 ns period of the 80MHz pulse train. Back at the beamsplitter, the now inverted *deviated* component of pulse $j + 1$ is superimposed with the *transmitted* component of the signal carrying pulse j on its way to the digitizer card. This superposition subtracts the pulse $j + 1$ from the pulse j , leaving only the pump induced signal change δ_1 . However, the *deviated* component of the signal carrying pulse j will also be subtracted from the *transmitted* component of the following pulse $j - 1$, leading to a second signal copy $-\delta_2$ with opposite sign. The electronic signal is amplified in a broadband signal amplifier by ~ 100 before traveling to the digitizer card in the measurement computer. The entire measurement is controlled with *LabVIEW*.

The signal pulse train is recorded by a *NATIONAL INSTRUMENTS PCI-5122* digitizer card. The digitizer card integrates for a certain time window around the arrival of the 80 MHz synchronized electrical trigger signal from the oscillator laser. It is crucial that the electrical trigger delay time is matched to the arrival time of the signal pulses from the detection. To adjust timing the trigger cable length can be modified, as electrical signal propagate at roughly 2/3 of the speed of light in typical coaxial laboratory cables. The digitizer card will record both δ_1 and δ_2 separately. As $\delta_1 = -\delta_2$ subtracting the two signals from one another increases the signal to noise ratio further.

Millisecond timescale optical detection

Determining the static sample properties for calibration in chapter 4 requires a measurement of the milli- and microsecond evolution of the sample properties, for example to record hysteresis loops. Each THz pulse is associated with 80 000 oscillator probe pulses, arriving every 12.5 ns over a 1 millisecond interval. Each of these 80 000 pulses is recorded to reconstruct the longer timescale signal (figure 3.6b). Realistically, the sampling rate (100 MS/s) and the onboard buffer size (32 MB) of the digitizer card limit the detection to ≈ 79.500 pulses for every kHz trigger from the laser before the onboard memory is filled.

The electrical delay line and the signal amplifier necessary for ps dynamics measurements

are removed to record the entire oscillator pulse train. The electrical delay change associated with removing components from the signal path is compensated with an appropriate length of BNC signal cable, such that the digitizer card measurement windows remain overlapped with the electrical pulses. Without the electrical delay line the signal to noise ratio is generally lower, however this technique is only necessary for the detection of comparatively large signals.

Second timescale electrical detection

In chapter 7 the orientation of the magnetic order parameter is investigated with a contacted 4-point resistance measurement scheme. The sample resistance is measured while the THz excitation beam changes the magnetic order. The resistance changes depending on the relative orientation of magnetic order parameter \mathbf{O} (magnetization \mathbf{M} in ferromagnets, Néel Vector \mathbf{L} in antiferromagnets) and current direction. This effect is known as the anisotropic magnetoresistance (AMR) and discussed in section 2.3.5. The resistance (conductance) experienced by a probe current \mathbf{j}_{pr} is typically lower (larger) for $\mathbf{j}_{\text{pr}} \perp \mathbf{O}$ and larger (lower) for $\mathbf{j}_{\text{pr}} \parallel \mathbf{O}$.

The samples in chapter 7 have a cross shape with electrical contacts on each bar end. A *KEITHLEY 2400 SourceMeter* provides a constant current along one cross beam I_x while recording the accompanying voltage drop across the same contacts U_x , yielding the *longitudinal resistance* $R_{xx} = U_x/I_x$ measurement. A second voltmeter (*KEITHLEY 2000 Multimeter*) measures the voltage drop U_y perpendicular to the current direction, yielding the *transversal resistance* $R_{xy} = U_y/I_x$.

4 Determining the magneto-optic sample response for MLB and MLD

Ultrafast changes of the magnetic state of a material can be measured in a pump-probe experiment using magneto-optical effects for detection. Within this thesis, the focus lies on the detection of THz light induced dynamics of the magnetization vector in a thin film. The magneto-optical effects lead to a probe polarization rotation or ellipticity change that can be detected experimentally. The normal incidence transmission probe (the probe light traverses the sample before being detected) reduces the complexity of magneto-optical probing, allowing for a straightforward separation of signals dependent on in- and out-of-plane magnetization changes. The active magneto-optical effects are the magnetic circular birefringence (MCB), also called the Faraday effect, and magnetic linear birefringence (MLB). MCB detects the magnetization projection onto the probe propagation direction. Magnetization changes in the sample plane may be detected by MLB. MLB is not part of the standard magneto-optical toolbox for THz pump - optical transmission probe experiments yet, limiting the sensitivity of typical transmission probe experiments to magnetization change along the probe propagation direction.

The MLB has an additional benefit for the study of thin film multilayer samples as it depends on the existence of a magnetization in the sample, imposing a spatial filter that ignores all nonmagnetic layers. In the next chapter (5) we demonstrate a measurement prescription to detect both the MCB and MLB in a THz pump - optical transmission probe experiment simultaneously. We will utilize the spatial filter property for the study of THz frequency spin pumping of a ferromagnet. In this chapter we lay the foundation for detection with MLB and present a calibration method for quantitative in-plane magnetization change measurements. A crucial ingredient of this study is the fast variation of the sample magnetization with an external magnet, thereby allowing for low-noise probing of the typically small magneto-optical effects. This thesis partially aims to add the MLB effect to the table-top THz frequency magnetic spectroscopy toolbox.

A manuscript, containing parts of this chapter, is in preparation.

4.1 Motivation

Magnetism is at the heart of most technological applications that govern our everyday life. Examples include sensors and consumer electronics. A classic example for consumer electronics is data storage on ferromagnetic hard drives. Magnetic data storage especially motivates research into ultrafast magnetism. Current clock rates of computer storage are reaching their limit in the GHz regime [Mar14a], while data transmission via fiber-optic link has cracked the 1 Tb/s barrier already [Buc19]. To bridge this data bottleneck, it is necessary to investigate the fundamental magnetic effects in the THz frequency range. In this thesis we use THz frequency light fields (chapter 5) to drive magnetic dynamics

in thin film magnetic samples. These ps timescale magnetic dynamics are probed optically on a fs timescale in a pump-probe scheme (chapter 3). The optical probe beam is sensitive to the samples' transient magnetic order (e.g. magnetization) because of various magneto-optical effects. The magneto-optical effects alter the polarization state of the probe light interacting with the magnetic solid, depending on the magnetic order in the sample (chapter 2.3.5). Over the years, many experimental geometries have emerged ranging from time-resolved magnetic spectroscopy to magnetic imaging capabilities, spanning almost the entire spectrum of light, from X-rays to mm waves [Sto06].

Our goal is to determine the vectorial changes of the magnetization optically and in transmission without the usual necessity of changing the sample or the laser beam orientations [Din01, Kus11]. Such a measurements have been demonstrated for a reflection probe measurement at normal incidence [Fan16, Cel19]. However, both the complexity of the experiment and the data interpretation can be simplified by choosing to probe the magnetic dynamics in transmission. Investigating the sample magnetization with probe light that traverses the entire sample yields an integrated response over the entire film thickness. In contrast, reflection probes have a sensitivity depth profile. Experimentally, achieving normal incidence is also simpler than adhering to a specific incident angle. Thus, it is clearly advantageous to study sufficiently transparent thin film magnetic samples in a normal incidence transmission probe geometry.

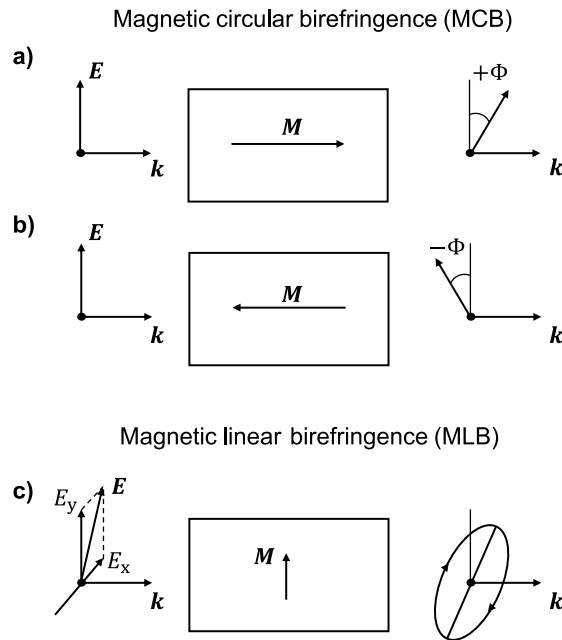


Figure 4.1.: The magneto-optical effects for probe transmission The magneto-optical probing effects for probe transmission through the sample. The boxes represent the material with magnetization direction M . The initial polarization state of the probe light is indicated to the left of each sample. The probe polarization state after the interaction with the sample is indicated to the right of each material box. **a) + b)** Magnetic circular birefringence (MCB), also called Faraday effect, sensitive to $\Delta M \parallel \mathbf{k}$. **c)** Magnetic linear birefringence (MLB) sensitive to $\Delta M \perp \mathbf{k}$. This figure was adapted from [Zve97]

Typically, two complex-valued magneto-optical effects are considered for a transmission

probe, namely magnetic circular birefringence (MCB) and magnetic linear birefringence (MLB). These magneto-optical effects are categorized depending on the relative orientation of the magnetization \mathbf{M} and the propagation direction of light \mathbf{k} , and whether they cause a rotation or ellipticity polarization change. The relative orientation of \mathbf{M} and \mathbf{k} and the polarization change are schematically depicted in figure 4.1.

While the MCB probes only the magnetization parallel to \mathbf{k} , it is linearly proportional to \mathbf{M} . The linear dependence on \mathbf{M} makes the Faraday effect a staple of magnetism research, being easily discriminated from other sources of polarization change by comparing measurements with oppositely magnetized sample. However, to measure an in-plane magnetization change with the MCB effect requires a projection of \mathbf{M} onto \mathbf{k} , that is a canting of the sample with respect to the probe beam. The transmission probe magneto-optic effect directly sensitive to the in-plane magnetization is the magnetic linear birefringence (MLB). The MLB effect is $\propto \mathbf{M}^2$ and in reflection probing it is probed by quadratic MOKE [Fan16, Buc09, Mon15]. A quadratic dependence on the magnetization conventionally poses a significant disadvantage experimentally, as a magnetization reversal is not sufficient to discriminate from non-magnetic effects on the probe polarization. However, the $\propto \mathbf{M}^2$ dependence even allows the MLB (AMR) to detect magnetic order in collinear antiferromagnets [Wad16].

To achieve our goal and detect the vectorial magnetization in transmission and at normal incidence we can use a simultaneous measurement of the in-plane magnetization sensitive MLB and the out-of-plane magnetization sensitive MCB. Indeed, we will see that the two effects have a different dependence on the angle between initial probe polarization direction and the sample magnetization. Disentangling the in and out-of-plane magnetization requires no more than three measurements with three different initial probe polarizations.

To date, the lack of a measurement and calibration scheme has kept the MLB effect (in transmission) out of experimentalists' arsenal. However, in this chapter we will present a novel calibration method for the MLB signal which will allow us to successfully separate in-plane and out-of-plane THz speed magnetization dynamics in the next chapter (5). The aim of this calibration method is to determine the maximal achievable signal change due to an in-the-sample-plane variation of the magnetization \mathbf{M} .

4.1.1 Magneto-optic normal incidence transmission probing

As discussed in section 2.3.5, and illustrated in figure 2.8, magneto-optical probing can be understood as the interaction of the probing light field \mathbf{E}_{pr} with the sample conductivity σ . If the sample is magnetic, σ will gain contributions that depend on the magnetization \mathbf{M} . As a consequence, the incident light field \mathbf{E}_{pr} will induce an additional \mathbf{M} -dependent current density $\Delta\mathbf{j}_{\text{pr}}$, with components either parallel or perpendicular to the current in the absence of \mathbf{M} ($\mathbf{M} = 0$) \mathbf{j}_0 . Eventually, the modified probe current will re-radiate, and the resulting electric field will have gained an additional component $\Delta\mathbf{E}_{\text{pr}}$. From equation 2.35, as derived in [Nád21], we can write the contribution $\Delta\mathbf{E}_{\text{pr}}$ due to $\mathbf{M} \neq 0$ as

$$\Delta \mathbf{E}_{\text{pr}} \propto \Delta \mathbf{j}_{\text{pr}} \propto \underbrace{a(\mathbf{u}_{\perp} \cdot \mathbf{M})\mathbf{u}_{\perp} \times \mathbf{E}_{\text{pr}}}_{\text{AHE/MCB}} + \underbrace{b(\mathbf{M} \cdot (\mathbf{M} \cdot \mathbf{E}_{\text{pr}}))}_{\text{AMR/MLB}} + \underbrace{c\mathbf{M}^2\mathbf{E}_{\text{pr}}}_{\text{isotropic MR}} \quad (4.1)$$

For simplicity we assume normal incidence, with the sample in the x, y-plane and the probe beam propagating along the z direction, along the sample normal \mathbf{u}_{\perp} . The relative strength of the linear and quadratic (in \mathbf{M}) conductivities is contained in the factors a, b . The last term, corresponding to the isotropic magnetoresistance, is shown only for completeness.

The detection of the experiment probes the change in \mathbf{E}_{pr} perpendicular to the direction $\mathbf{E}_{\text{pr}0}$ obtained for $\mathbf{M} = 0$. More precisely, we obtain the birefringence signal [Azz87]

$$S \propto \left(\frac{\Delta \mathbf{E}_{\text{pr}} \times \mathbf{E}_{\text{pr}0}^*}{|\mathbf{E}_{\text{pr}0}|^2} \right) \cdot \mathbf{u}_{\perp} \quad (4.2)$$

where the vector product yields

$$\Delta \mathbf{E}_{\text{pr}} \times \mathbf{E}_{\text{pr}0}^* \propto -a|\mathbf{E}_{\text{pr}0}|^2 \mathbf{M}_{\perp} + b(\mathbf{M}_{\parallel} \times \mathbf{E}_{\text{pr}0}^*)(\mathbf{M}_{\parallel} \cdot \mathbf{E}_{\text{pr}0}^*) \quad (4.3)$$

where \mathbf{M}_{\parallel} and \mathbf{M}_{\perp} refer to the components of the magnetization parallel and perpendicular to the sample surface. Equation 4.2 is plausible, as it only yields a signal if $\Delta \mathbf{E}_{\text{pr}}$ is perpendicular to $\mathbf{E}_{\text{pr}0}^*$. We can define the angle θ in between in plane magnetization \mathbf{M}_{\parallel} and initial probe polarization direction \mathbf{E}_{pr} , which are both parameters of the experiment (figure 4.2a), and arrive at magnetic signals

$$S = -2a\mathbf{u}_{\perp} \cdot \mathbf{M}_{\perp} + b\mathbf{M}_{\parallel}^2 \sin(2\theta) \quad (4.4)$$

Here, the term $\mathbf{u}_{\perp} \cdot \mathbf{M}_{\perp}$ expresses the scalar magnitude of the out of sample plane magnetization component. The first term indeed probes the magnetization change along the probe propagation direction $\mathbf{k} \parallel \mathbf{u}_{\perp}$ normal to the sample, consistent with MCB (the Faraday effect). Note that the first term has no θ dependence (figure 4.2b). The second term is proportional to the in plane magnetization \mathbf{M}_{\parallel} . This \mathbf{M}_{\parallel} term is even in magnetization ($\propto \mathbf{M}^2$) and also $\propto \sin(2\theta)$ (figure 4.2b), it is the MLB contribution.

The different θ dependence of MCB and MLB provide us with an experimental handle to distinguish the two terms experimentally. Note that the quantities a, b are complex-valued, giving rise to both a polarization rotation and ellipticity change for the probe beam [Zve97].

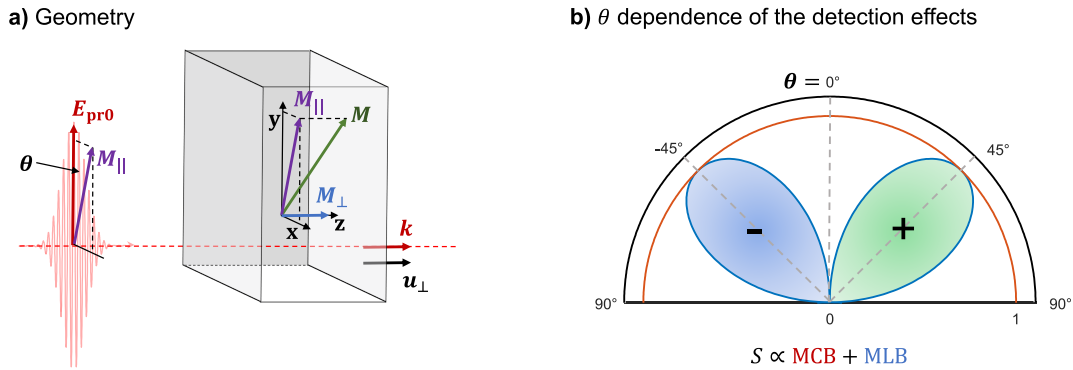


Figure 4.2.: Geometry and θ dependence a) The sample magnetization \mathbf{M} has a projection in the sample plane (x,y-plane) \mathbf{M}_{\parallel} and a component \mathbf{M}_{\perp} along the sample normal \mathbf{u}_{\perp} (along z). The probe pulse passes through the sample at normal incidence, that is $\mathbf{k} \parallel \mathbf{u}_{\perp}$. θ is the in-plane angle between the magnetization projection \mathbf{M}_{\parallel} and the probe pulse electric field direction $\mathbf{E}_{\text{pr}0}$. b) The magnetic dependent signal (equation 4.4) has two terms: the MCB (red line, $\propto \mathbf{M}$, sensitive to \mathbf{M}_{\perp} , independent of θ) and the MLB term (blue line, $\propto \mathbf{M}^2$, sensitive to \mathbf{M}_{\parallel} , $\propto \sin(2\theta)$). The MLB term is negative for $\theta < 0$ (blue lobe) and positive for $\theta > 0$ (green lobe).

4.2 Concept of the experiment

4.2.1 Saturated magnetization with time-dependent orientation

In principle our normal incidence transmission probe measurement is sensitive to both in- and out-of-plane magnetization in a thin film magnetic sample. Our aim here is to determine the material specific weights a, b for MCB and MLB, respectively. We are primarily interested in b because MLB measurements are less common. a, b capture the maximum signal strength of each magnetization component and must be determined when the magnetization is saturated in the correct orientation. To determine a one would apply a strong external field in the out-of-plane direction to saturate \mathbf{M}_{\perp} . However, the in-plane magnetic anisotropy of thin film samples is strongly opposed to an out-of-plane magnetization and such an external field would have to exceed the ~ 1 T anisotropy field to saturate \mathbf{M}_{\perp} . These field strengths are not available to us, thus we will focus on the determination of b relating to MLB and MLD in this chapter.

Saturating \mathbf{M}_{\parallel} is aided by the in-plane magnetic anisotropy and only requires ~ 10 mT. Magnetic fields on the order of ~ 100 mT are readily supplied by both static DC ('fridge') magnets and AC electromagnets. Electromagnets with AC driver generate a time dependent field, proportional to the driving current. To determine the maximum signal strength for the MLB term of equation 4.4, we keep the probe field \mathbf{E}_{pr} polarization fixed and modulate the in-plane orientation of the magnetization. As seen in figure 4.2b, the MLB signal (blue line) has its positive (green lobe) maximum at $\theta = 45$ and its negative maximum (blue lobe) at $\theta = -45$, where θ is the angle between \mathbf{M} and \mathbf{E}_{pr} .

A superposition of an AC magnetic field and an orthogonal DC magnetic field (both in the sample plane) is a convenient strategy to modulate the orientation of \mathbf{M}_{\parallel} (figure 4.3a). The DC magnetic field must be strong enough to saturate \mathbf{M}_{\parallel} , ensuring $(\mathbf{B}_{AC} + \mathbf{B}_{DC})$ saturates the in-plane magnetization at all times. The AC field has a sinusoidal time dependence, oscillating between two oppositely oriented maximal field B_{AC} . The superposition of both fields inherits the AC field time dependence to the angle θ between the probe polarization \mathbf{E}_{pr0} and the in-plane magnetization \mathbf{M}_{\parallel} .

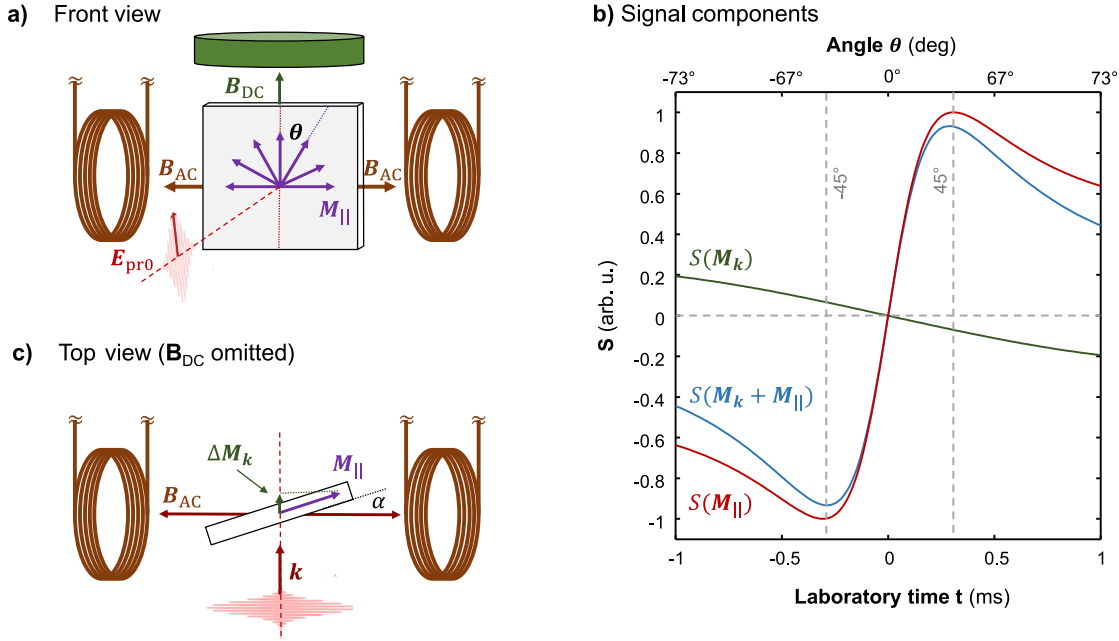


Figure 4.3.: Experimental Concept **a)** The sample (gray box) magnetization \mathbf{M}_{\parallel} is saturated in-plane by a superposition of an AC (\mathbf{B}_{AC} , brown coils and double arrow) and a DC (\mathbf{B}_{DC} , green disk and arrow) magnetic field. The sample is interrogated by an optical probe pulse with electric field direction \mathbf{E}_{pr0} (red). θ is the angle between \mathbf{E}_{pr0} and \mathbf{M}_{\parallel} . **b)** The expected signal $S(\mathbf{M}_k + \mathbf{M}_{\parallel})$ (blue curve, equation 4.8) is a superposition of the MLB term $S(\mathbf{M}_{\parallel})$ that is sensitive to the in-plane magnetization (red curve) and the MCB term \mathbf{M}_k (green curve) that is sensitive to the component of \mathbf{M} projected onto \mathbf{k} . The angle θ (top axis) between \mathbf{E}_{pr0} and \mathbf{M}_{\parallel} inherits a time dependence (laboratory time, bottom axis) from \mathbf{B}_{AC} . Notice that the $S(\mathbf{M}_{\parallel})$ components peaks at $\theta = \pm 45$ (top axis) as expected from a $\propto \sin(2\theta)$ dependence. **c)** Top view of the sample in the AC magnetic field. The DC magnet lies in the paper plane and is omitted for clarity. \mathbf{M}_k arises if the sample is tilted by α away from normal incidence. The in-plane magnetic anisotropy is much stronger than the peak B_{AC} field (~ 50 mT) and \mathbf{M} is not significantly pulled out of the sample plane.

The data in panel **b)** was plotted for $B_{AC}/B_{DC} = 3.3$, $\alpha = 2^\circ$, and $a, b = 1$.

4.2.2 The M_{\parallel} and M_k signals

As mentioned above, we are physically unable to saturate \mathbf{M}_{\perp} and thus cannot determine a properly. Therefore we will focus on b associated with the $\propto \mathbf{M}^2$ effects MLB and MLD (the second term of equation 4.4).

Signal $\propto M^2$

With the superposition of external magnetic fields shown in figure 4.3a we sweep the magnetization back and forth in between $\sim \pm 90^\circ$ from the direction of $\mathbf{E}_{\text{pr}0}$. The expected MLB signal $S(\mathbf{M}_{\parallel}) \propto \sin(2\theta)$ is plotted as the red curve of figure 4.3b. Notice that the bottom axis of figure 4.3b is laboratory time, as the measurement later will sample the magnetization at regular time intervals. The AC magnetic field has a sinusoidal time dependence, however. The angle θ is determined by the ratio of the AC and DC external magnetic fields. Since the amplitude of $B_{\text{AC}} = B_{\text{AC}0} \sin(t)$ is easier controlled than that of B_{DC} we set $b_{\text{DC}} = 1$ and retain $B_{\text{AC}0}$ as a fit parameter in the next section.

$$\theta = \tan^{-1} \left(\frac{B_{\text{AC}}}{B_{\text{DC}}} \right) = \tan^{-1} \left(\frac{B_{\text{AC}0} \sin(t)}{b_{\text{DC}}} \right) \quad (4.5)$$

and the top axis of figure 4.3b shows the corresponding values of θ for $B_{\text{AC}}/B_{\text{DC}} = 3.3$. Notice the vertical dashed lines in figure 4.3b indicating $\theta = \pm 45^\circ$. At these points $|\sin(2\theta)| = 1$ and $|S(\mathbf{M}_{\parallel})| = a$. Thus, to determine b in an ideal scenario (sample tilt $\alpha = 0$), it is sufficient to determine half the peak-to-peak distance of $S(\mathbf{M}_{\parallel})$ (red curve of figure 4.3b)

$$S(\mathbf{M}_{\parallel}) = bM_{\parallel}^2 \sin(2\theta) \quad (4.6)$$

where $M_{\parallel}^2 = 1$ is saturated. Beyond $|\theta| = 45^\circ$ the $\sin(2\theta)$ term (figure 4.2b) decreases again, and therefore $S(\mathbf{M}_{\parallel})$ decreases also.

Signal $\propto M$

Note that, there are experimental tolerances and the samples are not always perfectly normal to the probe beam direction. Small tilts α (figure 4.3c) away from normal incidence give rise to a signal in the MCB term (the first term of equation 4.4). The large in-plane magnetic anisotropy of thin film samples will prevent the magnetization to be pulled out of the sample plane significantly ($|B_{\text{AC}}| \leq 50$ mT). However, the sample tilt allows an α -dependent projection of \mathbf{M}_{\parallel} onto \mathbf{k} (figure 4.3c), fulfilling the condition for a MCB signal $S(\mathbf{M}_{\mathbf{k}})$ (section 4.3b, green curve)

$$S(\mathbf{M}_{\mathbf{k}}) = -2a|B_{\text{AC}}| \sin(t) \tan(\alpha). \quad (4.7)$$

Importantly, $\mathbf{M}_{\mathbf{k}}$ does not depend on θ . In practice, we can only measure the superposition of both components (equations 4.6 and 4.7) as $S(\mathbf{M}_{\mathbf{k}} + \mathbf{M}_{\parallel})$ with an additional θ dependent constant measurement offset $O_{\text{const.}}(\theta)$ (and $M_{\parallel}^2 = 1$)

$$S(\mathbf{M}_{\mathbf{k}} + \mathbf{M}_{\parallel}) = -2a|B_{\text{AC}}| \sin(t) \tan(\alpha) + b \sin(2\theta) + O_{\text{const.}}(\theta) \quad (4.8)$$

4.2.3 Separation of MCB and MLB

Equation 4.8 highlights that there are three components to the measured signal: the term $\propto \mathbf{M}$ being independent of θ , the term $\propto \mathbf{M}^2$ depending θ , and a constant offset. The aim is to separate MCB and MLB contributions.

A straightforward approach to disentangling the terms of equation 4.8 is to fit the measurement with the predicted curve shape. Up to now we have assumed that the polarization direction of the probe pulse $\mathbf{E}_{\text{pr}0}$ remains oriented along the direction of \mathbf{B}_{DC} . A well determined fit with multiple parameters requires a set of measurements. We generate multiple measurements by changing the initial orientation of $\mathbf{E}_{\text{pr}0}$ with respect to the direction of \mathbf{B}_{DC} , captured by the angle Θ_0 . Note that, contrary to θ , Θ_0 is not dependent on the time evolution of \mathbf{B}_{AC} but rather a separate experimental parameter (see section 4.3). Thus we replace $\theta \rightarrow \theta + \Theta_0$ in equation 4.8.

In section 4.3 we will also determine that the constant offset of equation 4.8, $O_{\text{const.}}$, does indeed not depend on t but has a strong Θ_0 dependence. Additionally, when we actually apply this technique in chapter 5 the angle Θ_0 will acquire a measurement uncertainty Θ_0^{off} . Finally, the last measurement uncertainty to account for is the perpendicular alignment of \mathbf{B}_{AC} and \mathbf{B}_{DC} . Phenomenologically, a slight deviation from perpendicular alignment manifests as a small timeshift t^{off} along t in the measurement. We thus have

$$\begin{aligned}
 S_{\text{F}}(\Theta_0) = & -2a|B_{\text{AC}}| \sin(t + t^{\text{off}}) \tan(\alpha) \\
 & + b \sin\left(2 \tan^{-1}\left[|B|_{\text{AC}} \sin(t + t^{\text{off}})\right] + \Theta_0 + \Theta_0^{\text{off}}\right) \\
 & + O_{\text{const.}}(\Theta_0)
 \end{aligned} \tag{4.9}$$

To describe the measured data, we use $a, b, B_{\text{AC}}, t^{\text{off}}, \alpha$, and Θ_0^{off} as fit parameters. Here, the B independent offset $O_{\text{const.}}(\Theta_0)$ is best left as a free parameter for all Θ_0 . The fit routine is implemented in MATLAB and described in detail in Appendix A

4.3 Experiment

Different from the other studies presented in this thesis, the determination of b does not rely on the pump-probe technique. Here, the oscillators' 80 MHz pulse train with 1 nJ pulse energy and a spectrum centered at 790 nm central wavelength is used as a probe (section 3.3.3). The probe spot on the sample has a diameter of $\approx 60 \mu\text{m}$. As shown in figure 4.4, the ferromagnetic sample was interrogated at normal incidence to the probe beam. To orient the sample for normal incidence, the incident and reflected probe beam were overlapped $\approx 4 \text{ cm}$ away from the sample. At that distance, the probe beam had a diameter of $\approx 2 \text{ mm}$. Assuming one beam diameter read-off error, the sample tilt angle α has an upper limit uncertainty of $\pm 3^\circ$.

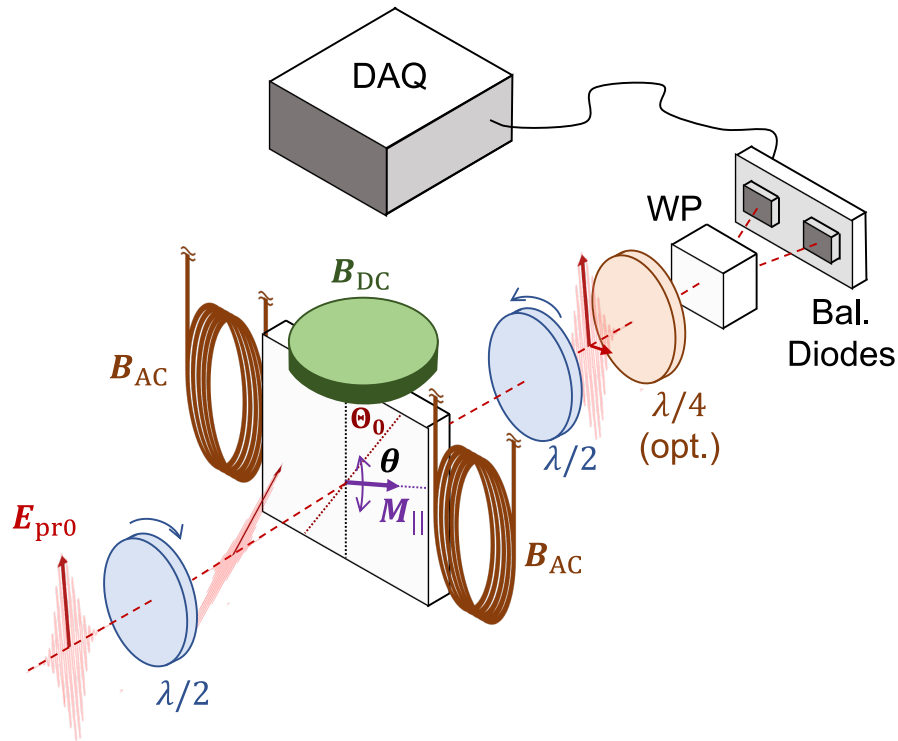


Figure 4.4.: Experimental Setup The sample is placed in the superposition of an AC (brown coils) and a perpendicular DC (green disk) magnetic field. The vector addition of both magnetic fields allows the time dependent orientation of the magnetization \mathbf{M} . The sample magnetization is interrogated with linearly polarized optical pulses (red pulse) from the 80 MHz oscillator pulse train. The polarization direction is given by $\mathbf{E}_{\text{pr}0}$ (red arrow). A motorized $\lambda/2$ waveplate rotates the probe polarization by an angle Θ_0 away from the \mathbf{B}_{DC} direction. The angle between the probe polarization direction (red dashed line on the sample) and the time dependent magnetization (purple dashed line on the sample) is given by the time dependent angle θ . After the sample the probe pulse has picked up a magnetization dependent orthogonal change $\Delta\mathbf{E}_{\text{pr}}$ and a second motorized $\lambda/2$ waveplate compensates for Θ_0 . An optional $\lambda/4$ waveplate can translate elliptical polarization into polarization rotation. The probe beam is split into two orthogonal polarization component beams by the Wollaston Prism (WP). The component beams are separately detected in a balanced diode and the difference signal recorded in a data acquisition system (DAQ). The exact details can be found in chapter 3.

The probe polarization ($\mathbf{E}_{\text{pr}0}$ in figure 4.4) was initially defined with a *NEWPORT polarcor 05P109AR.16* polarizer. A motorized *B. HALLE* broadband $\lambda/2$ waveplate (blue disk in figure 4.4) determined the angle Θ_0 between $\mathbf{E}_{\text{pr}0}$ and the DC magnetic field direction. A second, identical, motorized waveplate compensated for the combination of Θ_0 and a possible base birefringence of the sample. For probe ellipticity change measurements an optional *B. HALLE* broadband QWP could be added with a fixed orientation (orange disk in figure 4.4). One important source of systematic error arose from the slightly different properties of the two nominally identical $\lambda/2$ waveplates. The resulting Θ_0 dependent unbalancing of the balanced detection (chapter 3.3.3) manifested as the offset $O_{\text{const.}}(\Theta_0)$ to every measured curve.

The AC magnet (represented by coils in figure 4.4) was oriented in the sample plane, centered on the sample. A *RIGOL DG1062* signal generator generated the sinusoidal

control voltage. The amplitude of the sinusoidal control voltage determines the maximum field strength of the AC magnetic field. The control voltage oscillated at 510 Hz, slightly faster than half the system repetition rate $1 \text{ kHz}/2 = 500 \text{ Hz}$ for trigger stability. The signal generator generated one period of the control voltage whenever a kHz trigger arrived. The trigger frequency division was performed by a *NEW FOCUS 3501* optical chopper driver.

A DC magnet (green disc in figure 4.4) was oriented in the sample plane, orthogonal to the AC magnetic field, and centered on the sample. The sample–DC magnet distance determined the DC field in the sample and, thus, the AC magnetic field strength at which $\theta = 45^\circ$. The strength of the magnetic field at the sample was determined with 2 V control voltage and found to be $36 \pm 1 \text{ mT}$ along \mathbf{B}_{AC} , and $1 \pm 1 \text{ mT}$ along the probe propagation direction $\mathbf{k} = \mathbf{u}_\perp$. The large uncertainty in the magnetic field strength measurement (with a *PROJEKT ELEKTRONIK FM302* hand held tesla meter with *AS-NTP-0,6* Hall sensor) is due to the limited access to the sample position. The AC magnetic field strength scales linearly with the control voltage. The DC magnet component depends strongly on the position of the magnet. The DC magnet is removed for the corresponding pump-probe measurements, thus the \mathbf{B}_{DC} value is only an order of magnitude reference. \mathbf{B}_{DC} must be large enough to saturate the sample, but smaller than \mathbf{B}_{AC} to achieve the signal shape presented in figure 4.3b. \mathbf{B}_{DC} can be inferred from the peak positions in $S(\mathbf{M}_\parallel)$ as discussed in section 4.2.2.

The 500 Hz AC magnetic field typically ensures that each THz pulse (1 kHz repetition rate) experiences an opposite orientation of \mathbf{M} . In this study, however, we were interested in the response of \mathbf{M} to the external field, in the absence of THz pump pulses. For this reason the *National Instruments NI-PCI 5122* digitizer card was set to record as many oscillator pulses as possible in the 1 ms interval between kHz triggers. The oscillator pulse train contains 80 000 pulses/ms of which the digitizer card could record 79 500 before running out of on-board memory. This procedure is described in more detail in the experimental basics chapter, section 3.4. The 79 500 pulses sample \mathbf{M} in time steps of 12.5 ns while the AC magnetic field evolves from one maximum to the oppositely oriented maximum field strength. To increase the signal to noise ratio each 79 500 point trace is binned (averaged) into groups of 100 pulses, yielding a $\mathbf{M}(t)$ curve of 795 points for a half cycle of \mathbf{B}_{AC} with improved signal to noise ratio.

4.4 Data and discussion

4.4.1 Samples

The data presented here were recorded as part of the characterization efforts for the pump-probe experiments in the next chapter (5). The thin film samples were magnetic monolayers or bilayers comprised of a magnetic and a nonmagnetic layer with film thicknesses of 3–6 nm. All samples have been grown on 500 μm thick glass substrates with $5 \times 5 \text{ mm}$ lateral dimensions. The samples were protected from corrosion by 10–20 nm cap layers

of MgO and glass. The ferromagnet was $\text{Co}_{20}\text{Fe}_{60}\text{B}_{20}$ in all cases. More information on the samples is presented in the next chapter (5). The samples were grown by Samridh Jaiswal and Maria-Andromachi Syskaki from the group of Professor Mathias Kläui at the Johannes Gutenberg University, Mainz (Germany).

4.4.2 Hysteresis loops: the M_k signal

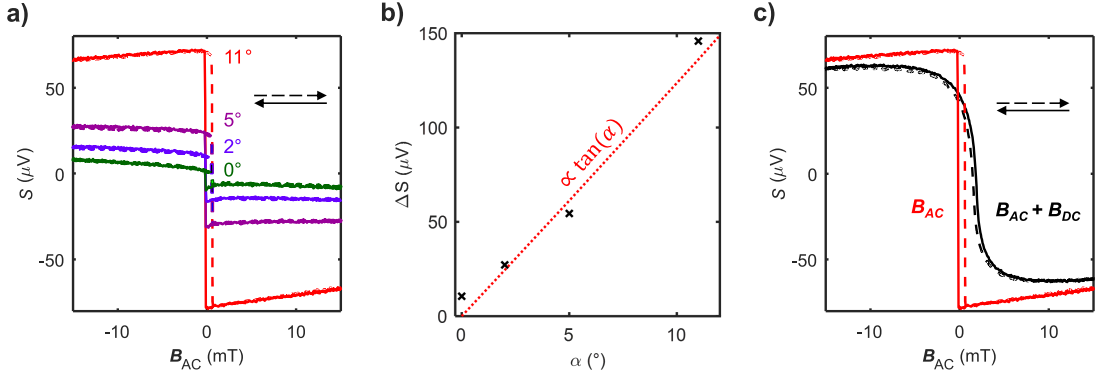


Figure 4.5.: $S(M_k)$. The $S(M_k)$ signal contribution measured in a ferromagnet/nonmagnetic metal bilayer (3 nm $\text{Co}_{20}\text{Fe}_{60}\text{B}_{20}$ + 3 nm Pt). **a)** $S(M_k)$ measured for sample tilt angles $\alpha = 0^\circ, 2^\circ, 5^\circ,$ and 11° . Without B_{DC} the magnetization remains on the B_{AC} axis and traces out a step-like hysteresis loop. The in-plane magnetic anisotropy is overcome by $|B_{AC}| \ll 10$ mT. The projection of $M_{||}$ onto k increases $\propto \alpha$. At 11° tilt and large magnetic field the saturated magnetization appears to be decreasing. Possibly, M is pulled slightly out of the sample plane towards B_{AC} , decreasing the projection on k . Notice that the nominally 0° (normal incidence) curve produces a sizeable signal. **b)** The difference of the saturated states ΔS , averaged in the regions $3 \text{ mT} < |B_{AC}| < 4.5 \text{ mT}$, indeed evolve $\propto \tan(\alpha)$ (red dashed line, $7 \cdot 10^{-4} \cdot \tan(\alpha)$). **c)** The red curve is an identical copy of the red curve in panel a), measured for $\alpha = 11^\circ$. Introducing B_{DC} perpendicular to B_{AC} (black curve) ensures that M is always saturated, tracing out an arc in the sample plane. Therefore, the sudden step and the hysteresis are not observable anymore. At large angles α the $\propto M$ term of equation 4.4 dominates the $\propto M^2$ term. The DC magnetic field prevents a full orientation along B_{AC} , reducing S compared to the red curve. The apparent lateral shift of the black curve is due to a component of B_{DC} acting along B_{AC} if the DC magnet is not situated equidistant from both poles of the AC magnet (t^{off} accounts for this shift in equation 4.9). A constant offset, determined from the end points of each curve, was removed in panels a and c.

During the discussion of figure 4.3 panels b and c (section 4.2.2), we determined that the $S(M_k)$ component is due to a projection of $M_{||}$ onto the probe propagation direction k . We thus expect the $S(M_k)$ projection to depend $\propto \tan(\alpha)$ (equation 4.7). The sample under consideration is a ferromagnet/nonmagnetic metal bilayer (3 nm $\text{Co}_{20}\text{Fe}_{60}\text{B}_{20}$ + 3 nm Pt). First we will consider data recorded with only an AC magnetic field in the sample (figure 4.3a without the green DC magnet). The AC magnetic field strength oscillates between two opposite maxima but remains on the same axis. Therefore, the magnetization reverses direction rather abruptly instead of tracing out an arc. This is a typical hysteresis measurement (section 2.2.7).

Figure 4.5a displays the hysteresis curves recorded in the absence of B_{DC} for multiple sample tilt angles α . A constant offset has been removed from each curve, determined

from the end points of each curve. The signal saturates for external magnetic fields larger than a few mT. At very low external fields the magnetization resists reversing, displaying hysteresis. From this data it is evident that the in-plane anisotropy field of the sample is $\ll 10$ mT. For the largest tilt angle $\alpha = 11^\circ$, the saturated signals decrease at larger external fields. This may be an indication for a slight out-of-plane magnetization tilt towards \mathbf{B}_{AC} that would reduce the in-plane component \mathbf{M}_{\parallel} and thus $\mathbf{M}_{\mathbf{k}}$. Notice that the signal amplitude for nominally $\alpha = 0^\circ$ is still significant (green curve). This indicates that the $\propto \mathbf{M}$ effect is hard to suppress completely within the experimental uncertainty of the sample tilt angle.

Figure 4.5b displays the signal amplitudes ΔS (black crosses) as a function of the sample tilt angle α . ΔS is extracted as the difference of data averaged in the regions $3 \text{ mT} < |\mathbf{B}_{AC}| < 4.5 \text{ mT}$. The red dashed line is a guide to the eye ($7 \cdot 10^{-4} \cdot \tan(\alpha)$), confirming the $\propto \tan(\alpha)$ dependence of the $\mathbf{M}_{\mathbf{k}}$ term (equation 4.7).

In figure 4.5c the red curve is a copy of the largest angle ($\alpha = 11^\circ$) measurement in panel a). The signal shape changes significantly as \mathbf{B}_{DC} is introduced perpendicular to the AC magnetic field. The step-like hysteresis curve turns into a smooth transition from one saturated state to the other, with no hysteresis. This is the signal shape expected from the considerations in section 4.2.2 above (green curve in figure 4.3b). In fact, the superposition of \mathbf{B}_{AC} and \mathbf{B}_{DC} saturates \mathbf{M} at all times, causing a time dependent orientation of \mathbf{M} . As indicated by the purple arrows in figure 4.3a, the magnetization traces out a half-circle as the AC field evolves. Therefore the $\mathbf{M}_{\mathbf{k}}$ projection changes smoothly with the AC field also. Notice that the saturated state in the presence of the DC magnet is smaller than without it. The DC magnet prevents \mathbf{M} from completely aligning with \mathbf{B}_{AC} and therefore limits the projection of \mathbf{M}_{\parallel} onto \mathbf{k} .

The black curve of figure 4.5c is also shifted against the red curve. This is due to the relative position of \mathbf{B}_{AC} and \mathbf{B}_{DC} . Ideally, the DC magnet is situated perpendicular to the AC magnet and central in the AC magnet gap. If, however, the DC magnet is positioned closer to one AC pole than the other it introduces a DC component along the AC magnet that effectively biases the location of the zero AC field transition. This experimental uncertainty is accounted for with a time offset t^{off} in the fit function, equation 4.9.

4.4.3 $S \propto M^2$: the \mathbf{M}_{\parallel} signal

The goal of this chapter is to separate the $S \propto M^2$ (equation 4.4). We expect a signal that is $\propto b \sin(2 \tan^{-1}(|B|_{AC} \sin(t)))$ like the $S(\mathbf{M}_{\parallel})$ signal in figure 4.3b. Unfortunately, it is not the only signal component. As discussed in the last section, a deviation from normal incidence leads to an additional signal contribution $\propto \sin(t)$. Therefore, the data presented in this section is recorded at $\alpha \approx 0^\circ$ within the experimental uncertainty. In section 4.2.2 we discussed that the local maxima of the $S(\mathbf{M}_{\parallel})$ signal correspond to $\mathbf{B}_{AC} = \mathbf{B}_{DC}$. Additionally, we aim to determine b for both probe polarization rotation and ellipticity change measurements. Finally, we will demonstrate that the detection method exhibits

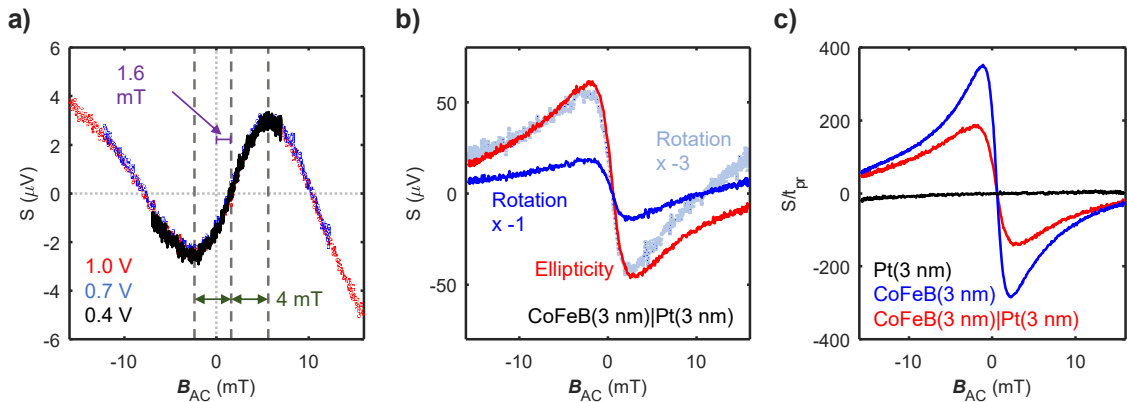


Figure 4.6.: $S(M_{||})$ **a)** Signal recorded on a CoFeB(3 nm)|Pt(3 nm) sample for three different AC fields (control voltage 0.4 V, 0.7 V, and 1 V) in the presence of a DC magnet. The position of the local extrema indicate $|\mathbf{B}_{AC}| = |\mathbf{B}_{DC}|$, as discussed in section 4.2.2. **b)** Signals recorded on another CoFeB(3 nm)|Pt(3 nm) sample (different from panel a) for polarization rotation (blue) and ellipticity change (red) detection. The orientation of the detection waveplate decides the sign of the signal, thus the rotation data is inverted. A scaled copy of the rotation data (light blue) is provided. **c)** The data for the CoFeB(3 nm)|Pt(3 nm) from panel b is compared to a single 3 nm CoFeB layer (blue) and a 3 nm Pt layer (black). The data is normalized for the transmitted probe power. The data in all panels was baseline corrected to make the local maxima symmetric around $S = 0$.

features of a spacial filter in a multilayer sample, as the detection mechanism relies on the existence of a magnetization and is thus insensitive to nonmagnetic sample regions.

Figure 4.6a exhibits data recorded on a CoFeB(3 nm)|Pt(3 nm) sample. The AC magnet is supplied with three different control voltages: 0.4 V, 0.7 V, and 1 V. The same curve is measured over varying ranges, depending on the maximal AC field. At the large AC field ends the curve crosses the zero line (grey vertical dots) again. The curve is shifted by +1.6 mT (central grey dashed line) as seen from the $S = 0$ crossing expected at $\mathbf{B}_{AC} = 0$. Both local maxima (outer grey dashed lines) are equally distant (4 mT) from the $S = 0$ crossing. The equal separation of the local maxima from the central $S = 0$ transition is consistent with the interpretation that the ratio of the AC and DC field determine the angle θ (section 4.2.2). The expected maximum of the $S \propto \sin(2\theta)$ term is at $\theta = 45^\circ$, when $|\mathbf{B}_{AC}| = |\mathbf{B}_{DC}|$. This indicates that $\mathbf{B}_{DC} = 4$ mT at the sample in this measurement. The 1.6 mT shift is likely due to the position of the DC magnet in relation to the AC magnet. A lateral translation of the DC magnet with respect to the AC magnet will add a DC magnetic component along the AC field direction.

Figure 4.6b displays measurements on a CoFeB(3 nm)|Pt(3 nm) sample (different from panel a) for both rotation (blue) and ellipticity (red) probing. The sign of the signal is influenced by the orientation of the analyzing waveplates (figure 4.4). For better comparison the rotation data (blue) is inverted. Indeed, both rotation and ellipticity probe measurements exhibit the same dynamics as seen from the light blue copy of the rotation data, amplified by a factor 3. It follows that b for rotation is 3 times larger than for ellipticity. The baseline mismatch is likely due to the factor 3 multiplication which also amplified the

$S(\mathbf{M}_{\mathbf{k}})$ term.

Finally, we investigate the B-dependent signals that arise from the presence of a magnetization \mathbf{M} in the sample. Figure 4.6c contains the ellipticity data for the CoFeB(3 nm)|Pt(3 nm) sample from panel b (red curve), as well as a signal recorded in the pure component layers: a pure 3 nm CoFeB ferromagnet (blue) and a 3 nm Pt nonmagnetic layer (black). All three curves are normalized for the probe beam transmission through the sample, measured with a power meter. The probe transmission is expected to change with respect to the sample thickness. While the samples containing the ferromagnet (thus have a magnetization \mathbf{M}) exhibit a clear $S(\mathbf{M}_{\parallel})$ signal, the nonmagnetic Pt sample does not. This demonstrates that the detection mechanism indeed depends on the presence of a magnetization in the sample.

It is not surprising that the signal strength and, thus, b depends on extrinsic sample properties such as the metal-film thickness. Ideally, the calibration measurement is conducted in the same experimental condition as the corresponding pump-probe experiment. Since both the pump-probe experiment as well as the calibration measurement experience the same probe beam transmission properties (the influence of the additional Pt layer), these contributions are expected to cancel in the data normalization operation.

4.4.4 Fitting to extract b

The simultaneous and experimentally hardly separable $S(\mathbf{M}_{\parallel})$ and $S(\mathbf{M}_{\mathbf{k}})$ components render a simple peak-to-peak extraction of the scaling factor b virtually impossible. A possible solution to this dilemma is to fit the data with the equation 4.9 developed in section 4.2.3. The implementation details for the fit are found in appendix A. Next to the $S(\mathbf{M}_{\parallel})$ and $S(\mathbf{M}_{\mathbf{k}})$ terms the fit equation also includes a magnetization independent offset $O_{\text{const.}}(\Theta_0)$ that depends on the incident probe polarization direction expressed by Θ_0 . To fit an equation with n variables well, one typically needs a dataset of n distinct measurements. The fit considers 6 parameters ($a, b, B_{AC}, t^{\text{off}}, \alpha$, and Θ_0^{off}) simultaneously for all curves and leaves the offset $O_{\text{const.}}(\Theta_0)$ free to be determined for each curve.

Figure 4.7a displays data measured on a CoFeB(3 nm)|Pt(3 nm) sample for 37 angles Θ_0 . The signal is ~ 0.1 V and exhibits a strong Θ_0 dependence. However, the desired dynamics $\propto B_{AC}$ are hidden. This dataset is fitted as described above, yielding the Θ_0 dependent offset $O_{\text{const.}}(\Theta_0)$, displayed in panel b. This signal is periodic in the initial probe polarization, and thus likely due to slightly mismatched properties of the two $\lambda/2$ waveplates (figure 4.4) leading to periodically imperfect balancing of the photodiodes.

The offsets $O_{\text{const.}}(\Theta_0)$ determined from the fit can be removed from the data, as presented in figure 4.7c. The result are clear magnetic dependent signals ~ 0.1 mV. The dominant oscillatory behavior is expected from the $S(\mathbf{M}_{\parallel})$ component and encouraging. To validate the fit, the red cut through the data in panel c, is compared to the corresponding fit (black) in panel d. $O_{\text{const.}}(\Theta_0)$ was removed from both curves. The fit captures the dynamics of the measurement well, especially considering that the fit result is a compromise of 37 simultaneous fit operations.

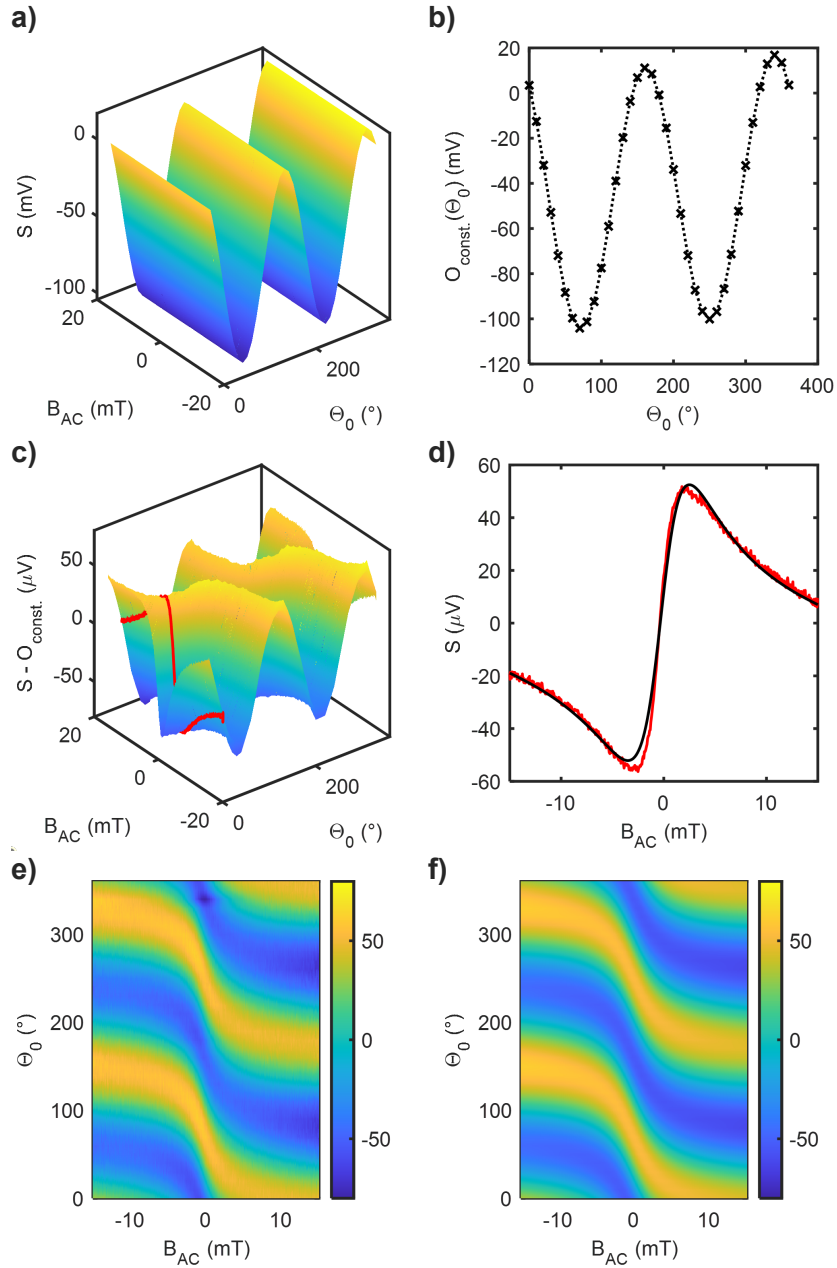


Figure 4.7.: Fitting a dataset **a)** A measurement for 37 angles Θ_0 on a CoFeB(3 nm)|Pt(3 nm) sample. The magnetic field dependent signal is overshadowed by the offset $O_{\text{const.}}(\Theta_0)$. The full dataset is fit simultaneously with equation 4.9, as described in Appendix A. **b)** The fit result for $O_{\text{const.}}(\Theta_0)$. The Signals are ~ 0.1 V. **c)** The desired magnetic dynamics appear when the $O_{\text{const.}}(\Theta_0)$ from panel b are removed from the data in panel a. The offset corrected data are ~ 0.1 mV. The red cut through the data is compared to the fit result (black curve) in panel **d)** Considering that this fit is considering 37 curves simultaneously with shared parameters, the fit result is excellent. If the sample was at perfect normal incidence ($\alpha = 0$) b could be determined as half the peak-to-peak amplitude of this curve. **e)** The entire offset corrected dataset from panel c is presented in top view, for comparison with the fit result surface in panel **f)** This analysis is necessary to determine the factor b needed to calibrate dynamic MLB and MLD signals.

To validate the fit result over the entire dataset, the offset corrected data from panel c is presented in a top down view in panel e. The corresponding fit is presented in panel f. Comparing the data in panel e and f, as well as the two curves in panel d, are considered a good indicator for the fit quality.

Table 4.1.: Fit result corresponding to figure 4.7

Parameter	Result	Uncertainty (%)
a	-1e-04	>100
b	5.387e-05	<0.1
B_{AC}/B_{DC}	5.233	<0.1
t^{off}	-0.0023	<0.1
α	-0.4362°	>100
Θ_0^{off}	-26.6079°	3
$O_{\text{const.}}(\Theta_0)$	~ 0.1 V	<0.01

The fit result uncertainty is extracted from the fit with MATLABs `nlparci` function. The fit result and uncertainty for the data presented in figure 4.7 are displayed in table 4.1. The relatively large value of Θ_0^{off} is expected and related to the measurement of the pump-probe data, presented in chapter 5. Noticeably, both a and α are represented with errors of $> 100\%$. This is understandable, as they both occur exclusively in the same term of the fit equation, and can thus find an infinite number of combinations to represent the strength of the $\mathbf{M}_{\mathbf{k}}$ term. Ideally, one of the two should be removed from the fit function, however we choose to have both for didactical reasons when presenting the material. Especially, as we determined above that the parameter a extracted from this procedure has no physical relevance. The important target of this evaluation, the factor b , is determined with rather high accuracy ($< 0.1\%$ uncertainty).

4.5 Conclusion

In conclusion, we presented an efficient and reliable method to separate MCB and MLB contributions of the magnetization of ferromagnetic thin films. This is a prerequisite to quantify in plane magnetization changes in the pump-probe experiments presented in the next chapter.

We presented a measurement geometry involving the superposition of an AC and a DC magnetic field in the plane of the thin-film sample, saturating the sample magnetization and introducing a time dependence to the magnetization direction. As the $\propto \mathbf{M}^2$ terms of the detection mechanism have a sinusoidal dependence on twice the angle of the probe field polarization and the magnetization, the time dependent magnetization orientation allows the determination of the material constant b .

We demonstrated the origin of the $S(\mathbf{M}_{\mathbf{k}})$ term and the applicability to both polarization rotation and ellipticity change detection schemes. Additionally, we rely on the spatial filter functionality of the detection mechanism, requiring the existence of a magnetization.

We have demonstrated a multi-dimensional fit based extraction technique to reliably determine the sample- and setup-dependent parameter b , which quantifies the strength of the MLB contribution. Thus, we have laid the foundations for the pump-probe investigation of ultrafast magnetic effects in the next chapter. And finally, we have shown that it is possible to detect both in- and out-of-plane magnetization changes simultaneously in a normal incidence, transmission probe experiment. The calibration method presented in this chapter finally brings the MLB and MLD detection effects to table-top optical magnetization studies.

5 THz Frequency Spin Accumulation

The need for smaller and faster electronics requires the use of new physical effects for data storage and handling. The field of spintronics establishes the fundamentals for computation with the electron spin, rather than the electron charge. To utilize the electron spin for computation, it is necessary to transport it through space and across material interfaces. Currently, it is unknown whether the spin accumulation due to spin-orbit coupling persists at THz frequencies. With the aim of THz speed computation, this study investigates whether a speed limit to the necessary effects may be found. It introduces a detection mechanism novel to THz pump-optical probe spectroscopy with which to interrogate THz spin accumulation in thin film metallic samples.

In this chapter we use intense THz electric and magnetic fields to drive spin dynamics in prototypical $F|N$ stacks consisting of a metallic ferromagnetic layer F and a heavy-metal layer N . To detect the spin dynamics, we make use of an optical probe pulse that measures the MLB and MCB effects. We use MLB and MCB to develop a measurement scheme to simultaneously detect all magnetization changes in the sample plane and along the sample normal. Armed with these capabilities, we investigate some questions of THz spintronics. Are the spin-dependent Hall effects active at THz frequencies? Are there signatures of spin accumulation? Is there an inherent speed limit to spin transfer across a material interface?

Parts of this chapter are contained in a manuscript under preparation.

5.1 Motivation

As discussed in section 4.1, studying spintronic effects at THz frequencies is important from a fundamental scientific and an applied viewpoint. Such fundamental spintronic operations are spin current generation, spin transport, spin transfer across an interface and the transfer of magnetic moment from itinerant spins to an existing magnetic order. In this chapter we study these phenomena at THz speeds in metallic thin-film bilayer samples using THz pump – optical transmission probe spectroscopy.

We sufficiently reduce the symmetry of the detection mechanism to cleanly separate the in plane and out-of-plane magnetization response to a THz pump pulse. Specifically, we choose normal incidence of the probe beam onto the sample. Based on the results of the previous chapter, we are sensitive to in and out-of-sample-plane magnetization reorientation as well as in-plane magnetization magnitude changes. Out-of-plane magnetization is probed by the ubiquitous MCB (Faraday) effect. The in-plane magnetization change is probed by the, until now, elusive MLB effect. Such a complete optical determination of the sample magnetization in response to low (kHz) frequency current driven spin-orbit torques has been previously achieved in normal incidence reflection probe MOKE studies [Fan16, Cel19]. Typically, the separation of magnetic and nonmagnetic effects is done by

comparing signals recorded for opposite sample magnetization. The MLB effect is $\propto M^2$ and is even with respect to magnetization reversal, similar to nonmagnetic effects.

We showed in chapter 4 that the MLB has a dependence on the angle θ between probe polarization direction and the sample magnetization, thereby opening a route to disentangle the signals. An appropriate calibration measurement has been demonstrated. In this chapter, we extend this method to transient magnetization changes. We will now introduce the model system and the possible interactions, introduce the measurement principle and finally experimentally disentangle various THz radiation driven magnetization changes, both in and out of the sample plane.

5.2 The probing mechanism

In chapter 4 we have determined that a suitable measurement geometry will produce a change in the probe polarization direction and/or ellipticity which is given by

$$S = -2a\mathbf{u}_\perp \cdot \mathbf{M}_\perp + bM_\parallel^2 \sin(2\theta) \quad (4.4 \text{ revisited})$$

Here, \mathbf{u}_\perp is the sample surface normal unit vector, \mathbf{M}_\perp is the out-of-plane magnetization component (z direction), and \mathbf{M}_\parallel is the in-plane magnetization. Briefly, the first term is the magnetic circular birefringence (MCB). MCB is sensitive to magnetization change along the propagation direction \mathbf{k} of the gate beam, which is parallel to the sample normal vector at normal incidence. The second term is due to magnetic linear birefringence (MLB). MLB is sensitive to magnetization change in the sample plane, perpendicular to \mathbf{k} at normal incidence. The in-plane components is comprised of both a change of magnetization magnitude ΔM_\parallel or a tilt in the plane of the sample $\Delta\theta$ (figure 5.1).

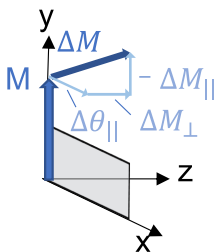


Figure 5.1.: Transient magnetization components The thin film samples in this chapter have an in-plane magnetic anisotropy, keeping the static magnetization \mathbf{M} confined to the sample plane. The action of the THz electric and magnetic fields can transiently alter either the magnetization magnitude ΔM_\parallel or the orientation, both in the sample plane ($\Delta\theta$) and along the sample normal (ΔM_\perp).

Pump induced changes

Continuing from equation 4.4, we can determine the pump-induced signal ΔS from the possible components to $\Delta \mathbf{M}$ for a thin film magnetic sample at normal incidence

$$\Delta S = -2a\mathbf{u}_\perp \cdot \Delta \mathbf{M}_\perp + b \sin(2\theta_0) M_{0\parallel} \cdot \Delta M_\parallel - b M_{0\parallel}^2 \cos(2\theta_0) \Delta\theta_\parallel \quad (5.1)$$

where θ_0 is the angle of the incident probe polarization with the magnetization.

We comment on equation 5.1:

1. We neglected possible pump-induced changes in the MO coupling coefficients a and b . A pump induced change to a can be excluded from simple arguments in our measurement geometry. The THz pump pulse will cause a change $\Delta(a_z \mathbf{M}_z) = \Delta a_z \cdot \mathbf{M}_{0z} + a_{0z} \cdot \Delta \mathbf{M}_z$. The subscript z indicates the direction orthogonal to the sample surface, along the propagation direction of the probe beam (figure 5.1). Since our samples have a strong in-plane anisotropy, $\mathbf{M}_{0z} \approx 0$ and a pump induced change to a can be excluded in our measurement. The pump induced change in b is suppressed by the measurement procedure as well. $\Delta b \cdot \mathbf{M}^2$, is rejected by considering only effects odd in \mathbf{M} .
2. Each term of equation 5.1 yields different information about the pump induced magnetization vector $\Delta \mathbf{M}$ (see above). Thus, disentangling the three terms should provide the vector $\Delta \mathbf{M}$.
3. Equation 5.1 should be understood as spatial average over the probed sample volume (i.e. full thickness) as we measure in a transmission probe geometry. This renders current driven spin accumulations at the interfaces of a single material layer invisible to the detection method. Although the local spin alignment may change, the average spin orientation along the probe path will remain the same.
4. The second term of equation 5.1 exhibits a remarkable spatial filter effect. $\mathbf{M}_{0\parallel} \cdot \Delta \mathbf{M}_{\parallel}$ implies that only regions with nonzero \mathbf{M}_0 contribute to this signal contribution. We can use this feature to overcome the limitation of the last point. To measure the THz induced spin accumulation, we pair a nonmagnetic metal with large spin-orbit coupling (spin current source) with a ferromagnet that acts as a detection layer.

Measured Signals

The challenge now is to disentangle the three terms of equation 5.1. We start by rewriting the equation in three terms T

$$\Delta S = \Delta T_{\perp} + \Delta T_{\mathbf{M}_0} + \Delta T_{\theta} \quad (5.2)$$

ΔT_{\perp} scales with $\Delta \mathbf{M}_{\perp}$, $\Delta T_{\mathbf{M}_0}$ scales with $\Delta \mathbf{M}$ along \mathbf{M}_0 , and ΔT_{θ} scales with $\Delta \theta_{\parallel}$. Disentangling the three terms is achieved by exploiting the different dependencies on θ_0 by performing three measurements with $\theta_0 = -45^\circ, 0^\circ, +45^\circ$

$$\begin{aligned} S(\theta_0 = -45^\circ) &\propto \Delta T_{\perp} - \Delta T_{\mathbf{M}_0} \\ S(\theta_0 = 0^\circ) &\propto \Delta T_{\perp} - \Delta T_{\theta} \\ S(\theta_0 = +45^\circ) &\propto \Delta T_{\perp} + \Delta T_{\mathbf{M}_0} \end{aligned} \quad (5.3)$$

from which the three component $\Delta\mathbf{M}$ can be extracted ($\Delta\theta_{\parallel}$ is an orientational change of \mathbf{M})

$$\begin{aligned}\Delta\mathbf{M}_{\perp} &\propto \Delta T_{\perp} \propto [S(\theta_0 = +45^\circ) + S(\theta_0 = -45^\circ)]/2 \\ \Delta\mathbf{M}_{\parallel} &\propto \Delta T_{M_0} \propto [S(\theta_0 = +45^\circ) - S(\theta_0 = -45^\circ)]/2 \\ \Delta\theta_{\parallel} &\propto \Delta T_{\theta} \propto (S(\theta_0 = 0^\circ) - [S(\theta_0 = +45^\circ) + S(\theta_0 = -45^\circ)]/2)/2\end{aligned}\tag{5.4}$$

Now, having a handle on the three pump induced magnetization changes, we will discuss the sample system and possible interactions that may influence \mathbf{M} .

5.3 Microscopic scenarios of transient $\Delta\mathbf{M}$

Here, we discuss possible microscopic scenarios that lead to changes $\Delta\mathbf{M}$ in the (integrated) sample magnetization. We first consider effects that are linear in the driving THz electromagnetic fields to lowest order, followed by effects that are at least quadratic.

5.3.1 Effects linear in \mathbf{E}_{THz}

The samples investigated in this study are thin-film metallic bilayers composed of a ferromagnet (FM) and a nonmagnetic metal (NM) with large spin-orbit coupling. Charge-to-spin conversion in the NM converts THz speed in-plane currents into THz speed out-of-plane spin currents that cause spin accumulations at the interfaces and may be transferred to the FM layer as well. The FM magnetization will feel both the influence of the injected spins, as well as the THz magnetic field directly. The possible signal contributions that are both magnetic and linear in the THz pump fields are presented in figure 5.2. The signal due to pump induced changes of the magnetization is expressed by equation 5.1. Note that the detection method relies on an intrinsic in plane magnetization $\mathbf{M}_{0\parallel}$ which is provided by the FM layer in our in-plane magnetized thin films. Therefore the detection mechanism itself imposes a spatial filter in the sample: all magnetic signal arise only from areas with an intrinsic magnetization.

Zeeman torque

The direct interaction of \mathbf{B}_{THz} and \mathbf{M} is the Zeeman torque (ZT), schematically drawn in figure 5.2a.

$$\mathbf{T}_Z(t) \propto \mathbf{M}_0 \times \mathbf{B}_{THz}(t)\tag{5.5}$$

which always points out of the plane of the sample for normal incidence pump and in-plane magnetization. Therefore, this effect will manifest as an out-of-plane magnetization

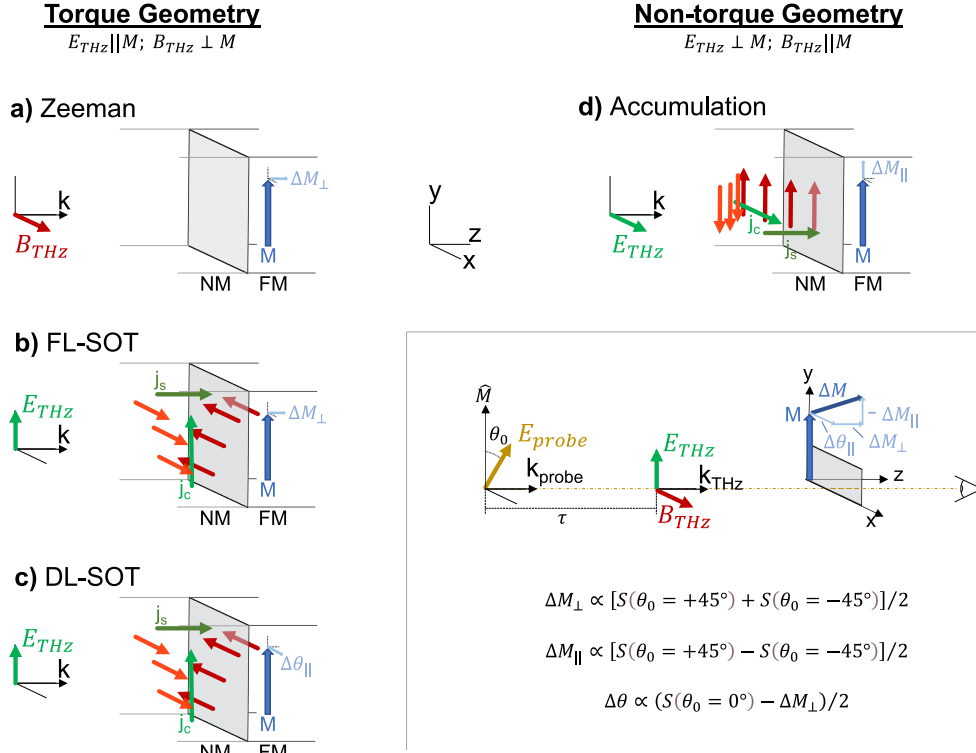


Figure 5.2.: Microscopic ΔM contributions linear in the THz field. The samples are composed metallic thin film bilayers composed of a ferromagnet (FM) and a nonmagnetic metal (NM). Depending on the relative orientation of M_{\parallel} and the THz fields, we distinguish between the *non-torque geometry* ($E_{\text{THz}} \perp M_{\parallel}$) and the *torque geometry* ($E_{\text{THz}} \parallel M_{\parallel}$).

a) The Zeeman Torque is the direct interaction of B_{THz} (red arrow) with the magnetization (blue) $T_Z = M_0 \times B_{\text{THz}}$, causing ΔM_{\perp} . **b)** The field-like spin-orbit torque (FL-SOT) relies on the spin magnetic moment transferred from the NM into the FM layer to produce a Zeeman-like torque $T_{\text{FL-SOT}} = M_0 \times S$, also causing ΔM_{\perp} . **c)** The spin accumulation giving rise to the FL-SOT also gives rise to the damping-like spin-orbit torque (DL-SOT) $T_{\text{DL-SOT}} = M \times (M_0 \times S)$, causing an in-plane orientational change $\Delta \theta_{\parallel}$ of the magnetization. **d)** In the non-torque geometry the spins injected from the NM layer are aligned along the axis of M , modifying the in-plane magnitude of M by ΔM_{\parallel} .

Inset) Disentangling the pump induced changes to the sample (grey) magnetization M (blue) ΔM_{\parallel} , ΔM_{\perp} , and $\Delta \theta_{\parallel}$ (light blue) requires a solid understanding of the angles in the measurement. To measure all magnetization component changes with approximately equal signal strength, we require the angle between E_{THz} and M to be $\approx 30^\circ$. The probe pulse polarization is tilted by θ_0 with respect to the magnetization direction \hat{M} . Signals recorded for $\theta_0 = -45^\circ, 0^\circ, +45^\circ$ can be combined to yield the pump induced magnetization components.

change

$$\Delta M_{\perp} \propto M_0 \times \int_{-\infty}^t dt' B_{\text{THz}}(t') \quad (5.6)$$

and should be detected by MCB. This signal was already shown in previous works, for example by C. Vicario *et al.* [Vic13]. Added benefit for this study: a measurement of $T_Z(t)$ is thus an ideal probe for the field evolution in the sample.

Spin accumulation

In the NM layer, \mathbf{E}_{THz} drives as in plane charge current, which can be converted into a spin current by the spin-dependent Hall effects (section 2.3.4), but also other effects such as the Rashba effect. The spin dependent Hall effects accumulate spins that are oriented perpendicular to both the charge current direction (along \mathbf{E}_{THz}) and the sample surface normal \mathbf{u}_{\perp} . The efficiency of the conversion from charge current \mathbf{j}_c to spin current \mathbf{j}_s^{NM} in the normal metal, as well as the spin direction, are determined by the magnitude and sign of the spin Hall angle α_{SHE}

$$\mathbf{j}_s^{\text{NM}} \propto \alpha_{\text{SHE}}(\mathbf{u}_{\perp} \times \mathbf{j}_c) \propto \alpha_{\text{SHE}}(\mathbf{u}_{\perp} \times \sigma^{\text{NM}} \mathbf{E}_{\text{THz}}) \quad (5.7)$$

Thus the spin accumulation at the interface of the normal metal film is oriented in plane and orthogonal to the charge current direction. Since $\mathbf{E}_{\text{THz}} \perp \mathbf{B}_{\text{THz}}$, thus \mathbf{B}_{THz} and the spin polarity will be oriented in the same line (but not necessarily the same direction, this is decided by α_{SHE}).

The spin moment transferred from the NM to the FM layer can act on the magnitude of $M_{0\parallel}$ if $\mathbf{M} \perp \mathbf{E}_{\text{THz}}$ (*non-torque geometry*). If $\mathbf{M} \parallel \mathbf{E}_{\text{THz}}$ both the spin polarization and \mathbf{B}_{THz} are parallel to \mathbf{M} . The spins co-linear with \mathbf{M} injected into the FM layer will either add or subtract magnetic moment from \mathbf{M} , causing ΔM_{\parallel} (figure 5.2d).

Simultaneously, \mathbf{E}_{THz} will drive a current in the FM. This current will undergo a charge to spin conversion from both the SHE and the anomalous Hall effect (AHE). While the SHE creates a pure spin current, the AHE creates both a charge and a spin current across the F|N interface.

In sum, the spin currents redistribute spin density in the vicinity of the F|N interface. As a consequence, the total magnetic moment of FM may change, giving rise to an MLB signal (see equation 5.1).

Spin-orbit torques

The direct action of \mathbf{B}_{THz} , the ZT, creates an out-of-plane magnetization change ΔM_{\perp} (figure 5.2a) if $\mathbf{M} \parallel \mathbf{E}_{\text{THz}}$ (*torque geometry*). The ZT is not the only effect contributing to ΔM_{\perp} , however. We established that the spin accumulation at the NM interfaces points along the same axis as \mathbf{B}_{THz} . When these carriers cross the interface into the FM the transferred spin magnetic moment S will interact with the magnetization M to cause an out-of-plane field-like spin-orbit torque (FL-SOT), similar to the ZT, of the form (figure 5.2b)

$$\mathbf{T}_{\text{FL-SOT}}(t) \propto \mathbf{M} \times S \quad (5.8)$$

The FL-SOT creates an MCB signal in equation 5.1. Additional to the FL-SOT, there will be a (anti-)damping-like spin-orbit torque (DL-SOT, figure 5.2c). The DL-SOT rotates

the magnetization in the plane of the sample by an angle $\Delta\theta_{||}$, causing an MLB signal in equation 5.1.

$$\mathbf{T}_{\text{DL-SOT}}(t) \propto \mathbf{M} \times (\mathbf{M} \times \mathbf{S}) \quad (5.9)$$

5.3.2 Effects quadratic in \mathbf{E}_{THz}

Ultrafast demagnetization by Joule heating

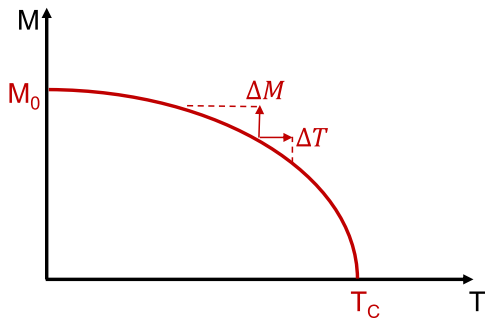


Figure 5.3.: Ultrafast Demagnetization The magnetization has a temperature dependence $M(T)$ that is sketched as a red line. Typical ultrafast demagnetization studies investigate the magnetization response to a sudden jump in temperature ΔT . In contrast, part of the experiments in this chapter investigate the complimentary effect: how does the magnetization respond to a sudden change in magnetization ΔM without accompanying temperature change.

The magnetization is inherently temperature dependent (see chapter 2.2.9), with a typical temperature dependence sketched in figure 5.3. Injecting magnetic moment into a ferromagnet is a textbook experiment: How does the magnet react to a jump in magnetization ΔM without the accompanying change in temperature? This is the complementary experiment to typical ultrafast demagnetization experiments. UDM experiments apply heat to the sample ΔT with a light pulse and study the evolution of the magnetization.

5.3.3 Consequences for setup parameters

Finally, to measure all four effects simultaneously and with similar signal amplitude, the ratio of torque and accumulation geometry signals can be adjusted. The magnetization axis can be rotated in the plane of the sample for a fixed THz polarization. The THz fields will decompose into components parallel and perpendicular to the magnetization, driving all four effects simultaneously. We have found that the larger ZT signal and the smaller Spin Accumulation signal are approximately equal at an angle of $\approx 30^\circ$ between \mathbf{E}_{THz} and \mathbf{M} . Since θ is the angle in between the probe polarization and the magnetization, the orientation of \mathbf{M} defines $\theta = 0$, irrespective of the THz polarization plane.

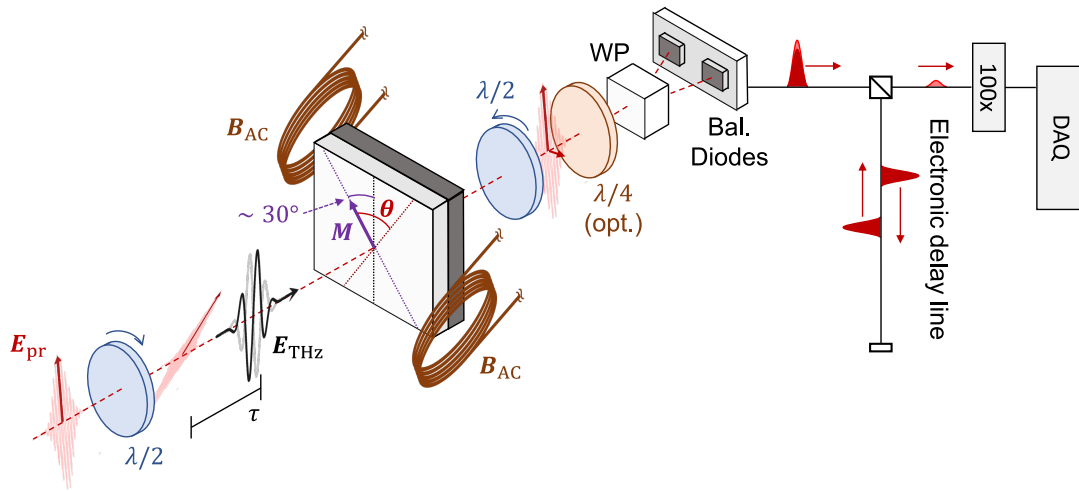


Figure 5.4.: Experimental Setup Schematic The metallic bilayer sample (grey box) is placed in the field of an AC electromagnet (brown coils), operated at 500 Hz, to reverse and saturate the sample magnetization \mathbf{M} (purple arrow) for every THz shot (repetition rate 1 kHz). The magnet is tilted 30° with respect to the THz pulse polarization plane (black dotted line, purple angle). The THz polarity can be flipped (black and grey pulses) as described in the main text. An optical probe pulse (red pulse) interrogates the transient magnetization of the sample a pump-probe delay time τ after the THz pulse. The angle made by the probe polarization direction $\mathbf{E}_{\text{pr}0}$ (red dashed line) and \mathbf{M} (red angle) is θ_0 . The probe polarization plane is controlled with a motorized $\lambda/2$ waveplate (blue disk) and the initial rotation compensated by a second motorized $\lambda/2$ waveplate after the sample. An optional $\lambda/4$ waveplate (orange disk) is inserted with a fixed orientation to measure elliptical probe polarization change instead of polarization rotation. The Wollaston prism (WP) forms an optical bridge with the balanced photodiodes. The polarization change will be reflected in a nonzero signal from the balanced diode. A hard wired electrical interferometer, the electronic delay line, isolates the pump induced signal change. The isolated pump induced change is amplified by two orders of magnitude before being digitized by an NI-PCI 5122 detection card.

5.4 Experiment

5.4.1 Setup

The experiments were performed in a THz pump – optical transmission probe scheme. THz single cycle pulses with a spectrum from 0.1 – 2.5 THz centered at 1 THz were generated from the tilted pulse-front Lithium Niobate source outlined in chapter 3.3.1. The THz power and polarity were controlled with a combination of a motorized *TYDEX HDPE* THz polarizer and a fixed orientation THz polarizer set perpendicular to the original polarization direction, as sketched in figure 3.5b. The initial ~ 1 MV/cm THz field strength was thus reduced to a maximum of ~ 500 kV/cm available. Unless otherwise stated, all data was recorded with the maximum THz field. Motorized polarizer angles $\pm\gamma$ away from the full transmission direction produced THz pulses with equal power but opposite polarity. Appropriate angles γ were found with a THz power meter. The THz spotsize was characterized with the pinhole method and found to be $\approx 1100 \mu\text{m}$, while the samples were $5 \text{ mm} \times 5 \text{ mm}$. The THz radiation thus experienced an extended sample film without modification from the sample edges.

The transient magnetization was probed with linearly polarized pulses (section 2.3.5) from the oscillator pulse train (chapter 3.3.3). The probe pulses were focused to $\approx 60 \mu\text{m}$ and probed the excited sample at the center of the THz spot. To alleviate possible accumulated thermal load on the sample, the oscillator pulse train was blocked in between the arrival of THz pump pulses with an optical chopper (*THORLABS MC2000B*) operating at 1 kHz with a 1:1 blocking blade. The pump and probe pulses were mechanically delayed with a motorized translation stage in fast scan mode, as described in chapter 3.3.

The linear probe pulse polarization could be rotated with a motorized *B. HALLE* broadband $\lambda/2$ waveplate. After the sample, the initial rotation was compensated by another motorized *B. HALLE* broadband $\lambda/2$ waveplate. The additional pump-induced polarization change from the excited sample is detected in an optical bridge setup (chapter 3.3.3). To detect a pump-induced ellipticity change, an additional fixed orientation $\lambda/4$ waveplate could be added between the second motorized waveplate and the Wollaston prism. The polarization change was detected by a pair of balanced photodiodes. The electrical signals from the photodiodes were pre-treated with an electronic delay line (chapter 3.4) before being amplified and recorded in a *NI PCI-5122* digitizer card.

Up to seven samples were mounted simultaneously, together with a piece of z-cut EOS detection quartz, on a long sample finger. A *PI Q521* piezo linear translation stage allowed the samples to be positioned rapidly and reproducibly in the measurement position. This allowed us to measure multiple samples together for direct comparison.

The samples were placed in an alternating external magnetic field that saturated the in-plane sample magnetization in opposite directions for adjacent THz pulses (500 Hz, peak 35 ± 1 mT). As described above, the external magnetic field was rotated away from the fixed THz polarization direction to modify the relative amplitudes of the observed signals.

5.4.2 Time drift correction

All measurements in a sample batch need to adhere to the same time axis to compare the THz light induced magnetic dynamics of different samples and for three different probe polarization angles θ . However, the pump-probe delay drifted significantly on the hour timescale (figure 5.5a). The relative path length of the pump and probe pulses changed due to thermal expansion of optical components or the active components of the laser. The laser was situated in a very temperature and humidity stable clean room environment. However, the relative path length changed by a few hundred micrometers of path difference over the course of hours (figure 5.5b).

The measurement order is presented in figure 5.5a. The innermost loop (I) was the measurement of signals with all four permutations of the sample magnetization orientation (set by the external magnetic field B^\pm) and the THz field polarity (E^\pm). The magnetization was flipped for consecutive THz pulses at 1 kHz rate and the pump-probe trace was sorted apart into two signals with opposite sample magnetization orientation. Ten such traces were recorded for one THz polarity, followed by another ten traces with the opposite pump pulse polarity. Thus, the E and B field modulated signals were recorded quasi- instant-

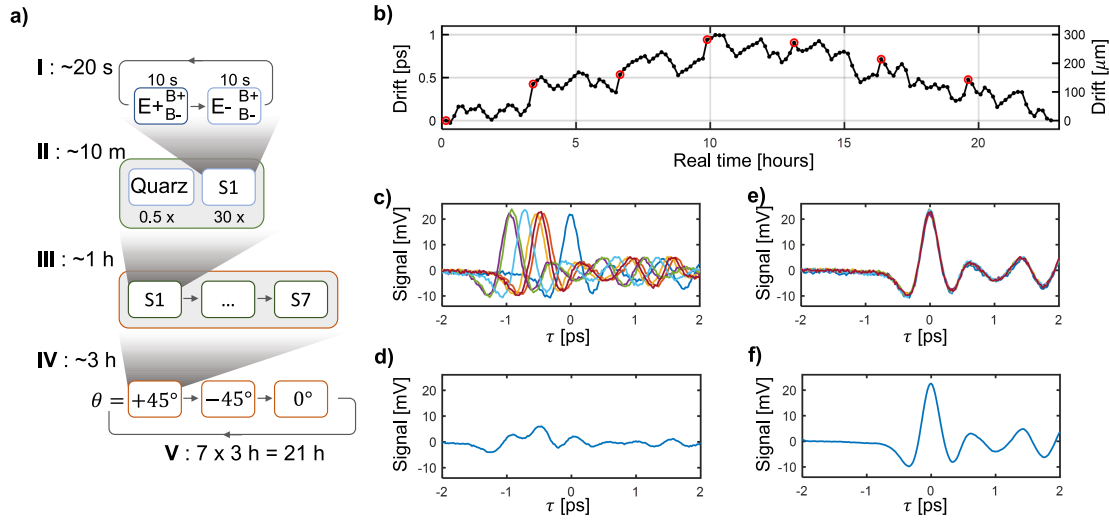


Figure 5.5.: Measurement cycle and delay drift The experiments in this chapter required a direct comparison of up to seven samples, where each sample had to be measured for three probe polarization angles θ each. For this the data must adhere to the same time axis. However, the pump-probe delay τ was affected by thermal drifts of the setup. To compensate the influence of the delay drift, the samples and probe angles were measured in small batches where every measurement was prefaced by a short electro-optic measurement in a quartz detection crystal. The data packages were acquired on times short enough to limit the timing uncertainty to ~ 50 fs. **a)** *The measurement cycle* I) The AC magnet reversed the sample magnetization for every THz pump pulse. Scanning one pump-probe delay curve required ≈ 1 s. The pump-probe delay trace was then separated into two traces, one for each magnetic orientation (B^\pm). The THz pump field polarity (E^\pm) was flipped on every tenth pump-probe trace. Thus traces for all permutations of sample magnetization and pump field polarity were acquired within 20 s. II) To be faster than significant setup drift, the measurement was cut into ≈ 10 minute batches, including 10 pump-probe traces on an EOS crystal (mounted on the same sample finger). III) These 10 minute batches were acquired for all 6-7 samples on the sample finger before IV) repeating the process for the probe polarization angles θ . V) The entire process was repeated for as long as necessary to build the required signal statistics. **b)** *Delay drift correction* An example delay drift curve (black) reconstructed from shape matching the EOS measurements in a measurement. The red circles correspond to data acquired for the same sample and set of measurement parameters. **c)** The time-stamp EOS data for the red circles of panel b, without delay drift correction. **d)** Averaging the data from c without time correction smears out the temporal dynamics. The same signal loss would occur to the associated sample magnetization signals. **e)** Applying the appropriate time shifts to the data visibly overlaps the signals. **f)** Averaging the time corrected data retrieves the correct signal.

neously. (II) This innermost loop was repeated 30 times, together with ten traces of one E-field polarity on the EOS Quartz crystal. The EOS measurement acted as a time stamp signal for the data batch recorded at the same time. The laser drift was small on the 10 minute timescale in between consecutive Quartz time stamp measurements. In the next two loops all samples (III) and all probe angles (IV) were cycled. After 3 hours, at the end of step (IV), all samples and probe angles had been measured once. The process was repeated as many times as necessary to build a good signal to noise ratio (V).

In the data analysis process, the EOS time stamp from all data batches were time shifted onto each other in a two-step process. First, a rough temporal shift was done with a cross-correlation method. This method is limited to integer multiples of the measurement

time step values but can shape match curves with temporal separations larger than half the signal period (> 0.5 ps). To further increase the temporal resolution, the pre-shifted curves were shape matched again with a phase sensitive shape correlation method. This method was not constrained to the measurement time grid but failed for time shifts greater than half the wavelength of the shifted signal. The time-shifts derived from the correlation of the quartz time-stamp measurements of an example measurement is presented in figure 5.5b. Note that the bottom axis is the real time in hours and the left and right axis are delay time shift in picoseconds and the corresponding beam length mismatch in μm . The red circles are all time stamp measurements of the first sample and the first angle θ of the example measurement. Those time stamp data are presented without time drift correction in panel c. Note that the single cycle THz stimulus only lasts for one picosecond, matching the maximal drift over the entire example measurement. If the unshifted data were to be averaged directly (no drift correction) the averaged data would lose most features, as shown in panel d. The time stamps with the correct time shift applied are presented in panel e, with an average in panel f. The time shift procedure is necessary to resolve the temporal dynamics of a THz frequency pump pulse.

An additional benefit of the time marker measurements integrated into the measurement procedure is that measurements from different measurement batches can be related also.

5.4.3 Data pre-treatment

The four permutations of the external parameters (the AC magnetic field B and E_{THz} in figure 5.6a) produce four signals. An example of four such curves (CoFeB|Pt bilayer) are presented in figure 5.6b. The different possible pump induced effects obey symmetries with respect to M (set by B) and E . The signal contributions can be separated by forming sums (even) or differences (odd) of traces with opposite external parameters. Effects that are odd depend on odd orders of the corresponding quantities, while even effects depend on even orders. For the field strengths in this work it is sufficient to consider second order terms at most.

Figure 5.6c displays the *odd in E and odd in B* component

$$S_{\text{odd}E,\text{odd}B} = \frac{(S_{E^+B^+} - S_{E^+B^-}) - (S_{E^-B^+} - S_{E^-B^-})}{4} \quad (5.10)$$

Here, traces with opposite sample magnetization but shared driving field polarity are subtracted first (inner brackets), isolating magnetically dependent signals. The results are subtracted again to become odd in E as well, excluding effects independent of or quadratic in the driving field. This signal component contains effects that are linear in M and E , which are all the effects we are interested in (figure 5.2) except for the DL-SOT. Panel 5.6d contains signals that are *even in E and odd in B* ($\propto E^2, B$), for example UDM. Panel 5.6e contains signals *odd in E and even in B* ($\propto E, B^2$ or independent of B). An important example of a nonmagnetic signal that is linear in the THz field is the electro-optic sampling (EOS) signal recorded as a time-stamp. Signals that are *even in E and*

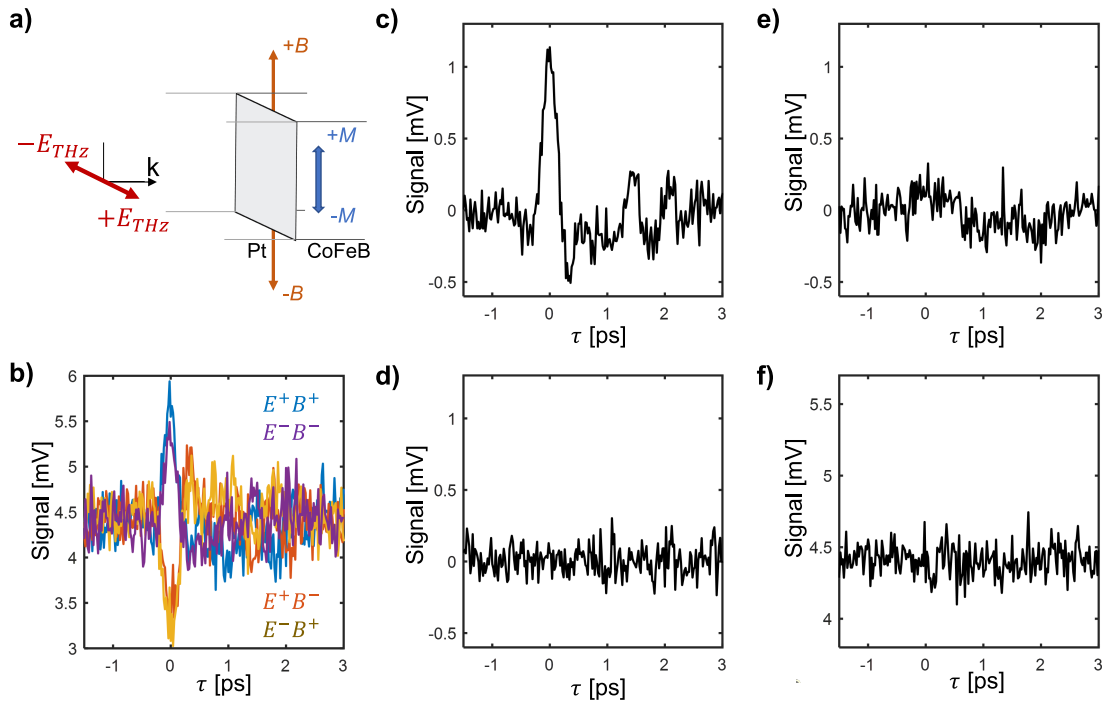


Figure 5.6.: Data pre-treatment, isolating signals by driving field dependence. a) The innermost loop of the measurement (figure 5.5a) quasi-instantaneously records data for four permutations of the THz driving field polarity E^\pm and the external magnetic field direction B^\pm , the latter controlling the sample magnetization M . b) Four signals recorded in a CoFeB|Pt bilayer sample for the permutations of external magnetic field orientation and THz polarity. Depending on the symmetries of the effects, forming the sums and differences of the signal components disentangles different signal contributions for each measurement. c) *Odd in E, odd in B*: This signal component contains signals that are linear in the driving THz fields ($\propto E$) and the magnetization ($\propto M$). The ZT, FL-SOT and spin accumulation signals will appear in this signal contribution. d) *Even in E, odd in B*: Signals in this component are $\propto E^2$ and $\propto M$, like UDM. e) *Odd in E, even in B*: Signals in this component are $\propto E$ and $\propto B^2$ or independent of B , like electro-optic sampling (EOS) of the THz pulse. f) *Even in E, even in B*: Signals in this component are $\propto E^2, B^2$ or independent of E, B . An example of the signals expected here are pump induced modulations of the optical constants in the form of sample transmission changes.

even in B ($\propto E^2, B^2$ or independent of E, B) are contained in panel 5.6f. This last panel would contain nonmagnetic, heat induced modulations of the sample optical properties.

In the following we will consider only those effects linear in the THz driving field and sample magnetization, thus we will investigate the *odd in E and odd in B* components.

5.5 Preliminary results and discussion

From here on out we will consider the signals *odd in E and odd in B*. Unless otherwise stated, all signals are normalized for the probe beam transmittance through the sample T_{pr} , measured with one of the diodes from the balanced photodiode. Normalizing by gate transmittance makes the detection process comparable for different samples. Additionally,

the measurements are normalized for the THz pump transmission t_{THz} , characterized in a broadband THz transmission experiment by O. Gueckstock. The frequency-dependent complex-valued transmission coefficient t_{THz} of the sample can be related to the energy that is deposited by the THz field in the sample at the considered frequency. Normalizing by t_{THz} makes the driving fields inside different samples comparable. Both T_{pr} and t_{THz} can differ depending on layer thicknesses and material compositions.

The samples in this work were grown by Samridh Jaiswal and Maria-Andromachi Syskaki from the group of Professor Mathias Kläui at the Johannes Gutenberg University, Mainz (Germany).

5.5.1 Out-of-plane magnetization change $\Delta\mathbf{M}_{\perp}$

First, we will investigate signals associated with an out-of-plane change of the sample magnetization $\Delta\mathbf{M}_{\perp}$. $S(\Delta\mathbf{M}_{\perp})$ is detected by the MCB effect and thus not dependent on the input probe polarization (section 4.1.1). As outlined above (equations 5.4) we can determine $\Delta\mathbf{M}_{\perp}$ by adding two measurements for $\theta_0 = +45^\circ, -45^\circ$. The in-plane magnetization signal will switch sign and drop out through the summation

$$S(\Delta\mathbf{M}_{\perp}) \propto T_1 \propto \frac{S(\theta_0 = +45^\circ) + S(\theta_0 = -45^\circ)}{2} \quad (5.11)$$

From figure 5.2a,b we know that the two effects expected to produce an $S(\Delta\mathbf{M}_{\perp})$ are the Zeeman torque (ZT) and the field-like spin-orbit torque (FL-SOT).

Separating ZT and FL-SOT

The Zeeman torque, see section 5.3.1, is the direct interaction of the THz magnetic field component perpendicular to the magnetization and the magnetization. The ZT does not flip sign upon sample reversal (F|N \rightarrow N|F). The FL-SOT (see 5.3.1), however, depends on a charge current component in the NM layer, parallel to the FM magnetization direction. The SHE (section 2.3.4) will generate an out-of-plane spin current and accumulate spins of opposite orientation at the NM interfaces. Depending on the layer order, and thus the spin orientation injected into the FM, the FL-SOT is expected to flip sign. For a visual aid refer to the sketches in figure 5.7. Panel a shows the stacking order where ZT (purple arrow on M) and FL-SOT (red arrow on M) act in opposite directions. The reverse stack is presented in panel b where the two torques are expected to cooperate. To compare these two scenarios, two samples of CoFeB(3 nm)|Pt (3 nm) and Pt(3 nm)|CoFeB(3 nm) were grown, where the numbers in parenthesis indicate the layer thickness.

The signals for out-of-plane magnetization change ($S(\Delta\mathbf{M}_{\perp})$) detected by polarization rotation of these two samples are presented in figure 5.7c. Both curves were detected simultaneously, fixing the temporal relationship of the two signals. The FL-SOT component should reverse sign upon sample reversal, while the ZT component is supposed to retain the same sign. Thus, tentatively one could attempt a separation of ZT as the sum of the

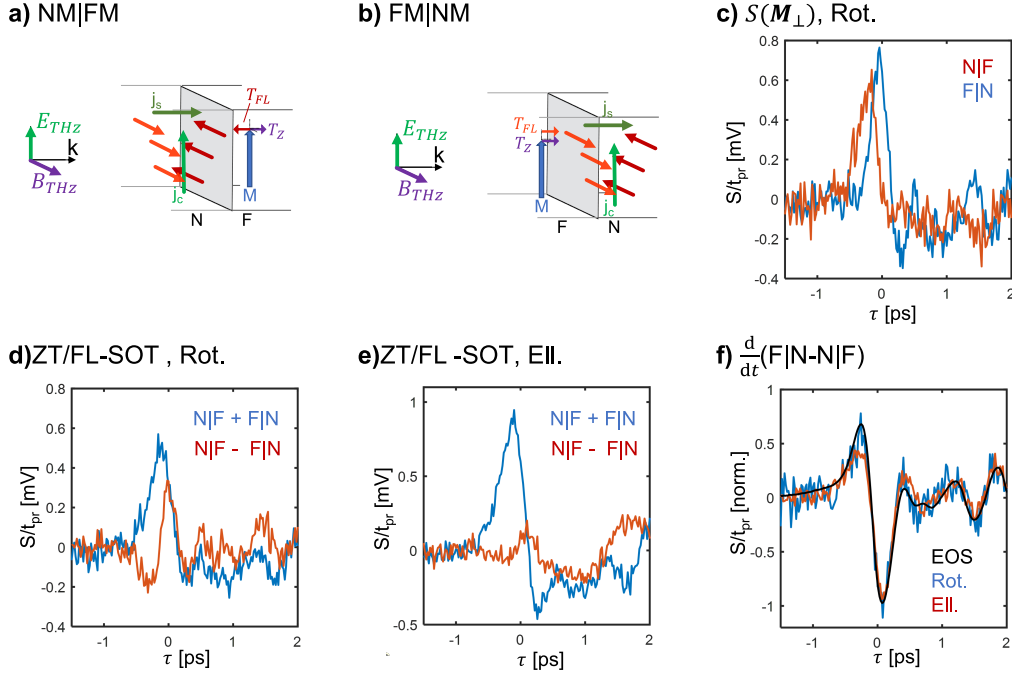


Figure 5.7.: Signals associated with ΔM_{\perp} : ZT and FL-SOT **a)** The sample magnetization \mathbf{M} (blue) experiences a ZT \mathbf{T}_Z due to the interaction with \mathbf{B}_{THz} (both purple) and an FL-SOT \mathbf{T}_{FL} due to the \mathbf{E}_{THz} driven spin injection from the nonmagnetic layer (red). Depending on the spin-Hall angle of the NM α_{SHE} , \mathbf{T}_Z and \mathbf{T}_{FL} may act in opposite directions. **b)** The reverse stacking order sample will experience \mathbf{T}_Z in the same direction as in panel a, while the \mathbf{T}_{FL} component flips when the other spin flavor is injected into the FM layer (orange). **c)** $S(\Delta M_{\perp})$ recorded in F|N = CoFeB(3 nm)|Pt (3 nm) and N|F = Pt(3 nm)|CoFeB(3 nm) samples. Notice that the two traces were measured together, fixing the temporal relationship of both traces. **d)** Exploiting the different behaviors of \mathbf{T}_Z and \mathbf{T}_{FL} , a tentative separation of the two may be done by forming the sum (ZT) and difference (FL-SOT) of the polarization rotation probe $S(\Delta M_{\perp})$ of reversed stacks. See the main text for details. **e)** A similar measurement as in d for ellipticity probe $S(\Delta M_{\perp})$. **f)** To confirm the validity of \mathbf{T}_Z as a sensor for \mathbf{B}_{THz} (equation 5.5) the differentiated \mathbf{T}_Z signals for polarization rotation (blue) and ellipticity (red) probe are compared with the measurement of \mathbf{E}_{THz} by electro-optic sampling (EOS) in 50 μm thick quartz (black). The signals are smoothed before and after the numerical differentiation with gaussian moving average filters of 10 points. The signals (c - e) are normalized by the probe transmittance T_{pr} through the samples.

signals in figure 5.7c, FL-SOT as the difference, provided the ZT signal remains unchanged upon sample reversal.

$$\begin{aligned} S_{\text{ZT}} &= (FM|NM + NM|FM)/2 \\ S_{\text{FL-SOT}} &= (FM|NM - NM|FM)/2 \end{aligned} \quad (5.12)$$

Figure 5.7d presents the extracted ZT (blue) and FL-SOT (red) curves in a polarization rotation measurement. The blue ZT curve indeed behaves like the integral over the THz electric field, while the FL-SOT component astonishingly has the same oscillation period as the driving THz field itself. A similar behavior is observed for the measurement with

ellipticity probe (figure 5.7e).

It must be stressed, that the separation of the ZT and FL-SOT signals by forming the sums and differences of signals from reverse grown samples is tentative (figure 5.7d,e). The analysis is based on the assumption, that the individual signal strength does not vary between the F|N and N|F sample. This assumption is likely valid for the FL-SOT. The FL-SOT is driven by the THz electric field, which is assumed to be constant over the entire sample thickness because the sample is much thinner than the THz wavelength. Thus, the FL-SOT signal likely flips well with the layer order reversal. The ZT is driven by \mathbf{B}_{THz} however. It is expected that the THz magnetic field decays significantly over the sample depth, depending on the layer conductivity. Therefore, the FM layer would experience a stronger \mathbf{B}_{THz} if the FM layer was traversed first. Thus, one should expect that the ZT signals have different magnitudes depending on the layer order, complicating a straightforward signal separation.

In this chapter we will require the temporal dynamics of the ZT signal as an indicator of the time dependent THz magnetic field in the sample. Indeed, we only require the temporal dynamics of the ZT signal to be unmarred by FL-SOT components, irrespective of the magnitude of the effect. As the FL-SOT signal components are expected to flip with identical amplitudes, the sum signal of figures 5.7d,e should indeed be free of FL-SOT influence and dominated by ZT. The difference signal however is likely not the pure FL-SOT signal, but a superposition of FL-SOT and a ZT signal rest originating from the ZT amplitude difference for reversed layer order.

Evidence that the ZT component indeed has the correct temporal shape is presented in figure 5.7f. The ZT is expected to be the integral over the driving magnetic field (equation 5.6). Numerically differentiating the ZT signals for rotation and ellipticity (after smoothing with a 10 point gaussian moving average) yields an excellent match with the THz electric field as detected by electro-optic sampling (EOS) in 50 μm quartz. Notice that both the rotation and ellipticity probe yield the same temporal dynamics of the ZT, confirming the magnetic origin of the signal.

THz field dependence

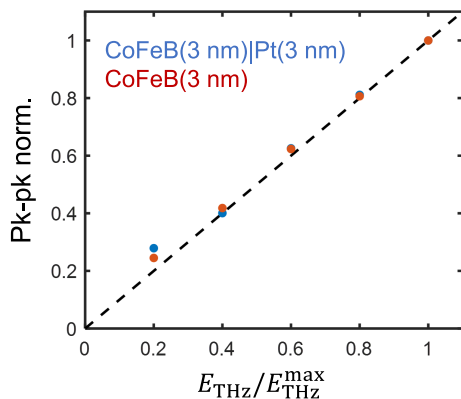


Figure 5.8.: Driving field dependence of $S(\Delta M_{\perp})$ The out-of-plane magnetization signal amplitude scales linearly with the THz driving field. This is consistent both with the Zeeman torque (both in CoFeB and CoFeB|Pt) as well as the FL-SOT (only in CoFeB|Pt). The dashed line is a linear fit to the data. The peak to peak signals were extracted after smoothing the data traces with a 700 fs gaussian moving average filter.

Above, we have attributed $S(\Delta\mathbf{M}_\perp)$ to the Zeeman torque and the FL-SOT. Both contributions are linear in the driving field. Figure 5.8 displays the THz field dependence of $S(\Delta\mathbf{M}_\perp)$ recorded on a CoFeB(3 nm)|Pt(3 nm) [blue] and a CoFeB(3 nm) [red] sample. While the bilayer sample supports both ZT and FL-SOT, the monolayer ferromagnet only supports the ZT. This confirms that the signals *odd in E and odd in B* indeed isolate magnetic effects that are linear in the THz driving field. The peak to peak values were taken from data traces after smoothing with a 35 point gaussian moving average filter.

Outlook: Improved separation of ZT and FL-SOT

As we have established above, the separation of ZT and FL-SOT signal components is marred by the likely layer order dependent ZT amplitude. Here we suggest a few possibilities for future experiments that may confirm the order dependence of the ZT signal and the temporal dynamics of the FL-SOT.

Further insight into the nature of the ZT and FL-SOT components can be gleaned from layer thickness dependent measurements, as ZT is an effect in the bulk F layer and FL-SOT is confined to regions near the F/N interface. Figure 5.9 presents data for CoFeB|Pt bilayers with various layer thickness combinations, measured for both probe polarization rotation and ellipticity change. All data is normalized both for the probe beam transmittance T_{pr} and THz transmission t_{THz} to make both the excitation and detection comparable for different total sample thicknesses. Figure 5.9a,b are thickness variations of the NM layer (CoFeB = 3 nm; Pt = 3, 6, 9 nm) measured in rotation and ellipticity respectively. The signals exhibit no significant NM layer thickness dependence. Figure 5.9c,d are thickness variations of the FM layer (CoFeB = 2, 3, 6, 9 nm; Pt = 3 nm) measured in rotation and ellipticity respectively. The signals exhibit a significant FM layer thickness dependence. The thickness dependent signal change is most evident in panel c, where the character of the signal appears to change around a FM layer thickness of 3 nm.

We interpret the data in figure 5.9 to highlight that the FL-SOT is confined to the F|N interface region while the ZT is a bulk effect. Panels a and b do not exhibit a signal dependence as a function of the NM layer thickness, consistent with the interpretation. The FM layer thickness dependent signals exhibit a clear evolution, however. The signal amplitude decreases with decreasing FM thickness, consistent with a bulk ZT. At lowest FM thicknesses the signal shape changes. We interpret the signal shape change as a signature of the FL-SOT. Indeed, the FL-SOT is an interface effect, considering that the spin-relaxation length of injected spins is on the order of ~ 1 nm [Sei18a]. Therefore, the relative strength of the FL-SOT signal would be strong for thin FM layers, while the ZT signal would dominate at larger FM thicknesses. We suggest repeating this measurement with samples grown in the opposite layer order. Similar to the discussion above, we would expect that the FL-SOT signal would flip sign, the ZT signal would not. This behavior would be evident from the comparison of thickness scans in both stacking orders.

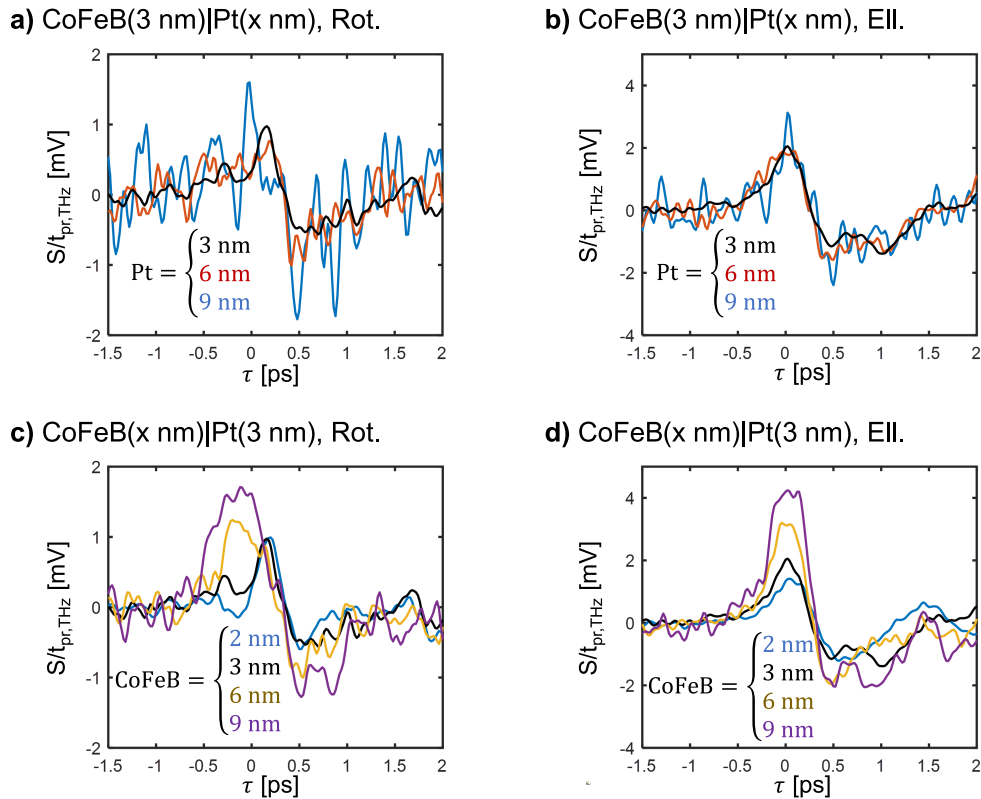


Figure 5.9.: $S(\Delta M_{\perp})$ layer thickness dependence a,b) $CoFeB(3\text{ nm})|Pt(x\text{ nm})$ Changing the Pt layer thickness has no evident influence on the ΔM_{\perp} signal, indicating that any FL-SOT must be due to carriers from a region close to the interface ($<3\text{ nm}$). c,d) $CoFeB(x\text{ nm})|Pt(3\text{ nm})$ Notice that the black curves in c,d are the same data as the black curves in a,b respectively. Changing the FM thickness has an influence on the data. Especially in the rotation probe data of panel c, it appears that the signal changes character above and below $CoFeB = 3\text{ nm}$. All data is normalized by the THz transmission t_{THz} the probe beam transmittance T_{pr} as well as smoothed with a 140 fs gaussian moving average filter. Note, these measurements consider only one layer order, thus we cannot separate the FL-SOT and ZT components as above.

Outlook: Pt vs. W

One could also exploit the spin Hall angle α_{SHE} dependence of the FL-SOT signal to generate signal contrast. Two materials with typically large and opposite α_{SHE} are Pt and W. Thus, comparing FM|NM stacks with NM = Pt, W would likely lead to FL-SOT signals of opposite sign. Preliminary data of such an experiment is presented in figure 5.10. Again, the ZT and FL-SOT components were separated by comparing measurements on reversed stacks, as indicated in equation 5.12. The signals that we attribute to ZT (panel a) indeed share the same dynamics, independent of the NM layer material. The signals that we attribute to the FL-SOT (panel b) exhibit maxima in opposite directions. However, the FL-SOT signals are not inverted copies of one another. This may be understood considering the discussion of the imperfect separation of ZT and FL-SOT signals above. It is likely that the FL-SOT signal is not purely due to the FL-SOT, but contains a ZT component as well. This ZT leakage arises if the ZT signal was stacking order dependent

as discussed above.

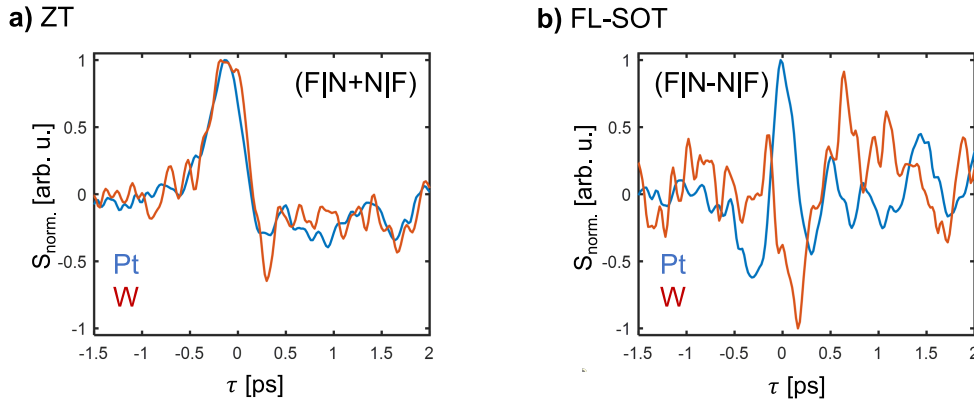


Figure 5.10.: T_Z and T_{FL} for different α_{SHE} The ZT and FL-SOT components separated from reversed sample measurements, as indicated in equation 5.12. **a)** The ZT signal arises from the direct interaction of \mathbf{M} and \mathbf{B}_{THz} and is expected to be independent of the spin-Hall angle α_{SHE} . α_{SHE} is a property of the NM layer material and is expected to have an opposite sign for Pt and W. The signal we associate with ZT (see discussion figure 5.7) appears to be independent of α_{SHE} , an indicator that it contains ZT components only. **b)** The FL-SOT signal is expected to flip according to α_{SHE} . Indeed, the signals for Pt and W caps appear to have lobes in opposite directions. However, they are not exact copies of one another. This is not surprising, considering that the ZT/FL-SOT distinction may be imperfect (see discussion figure 5.7). All data was recorded for polarization rotation probe and smoothed with a 140 fs gaussian moving average filter. All data was normalized to the maximum absolute value peak to retain signal orientation.

Outlook: Modulating the relative THz field strengths

The likely most effective method to separate the ZT and FL-SOT signals would be to rely on the different driving fields of the effects. Since the experiments in this chapter are performed in thin film samples at normal incidence, they fulfill the necessary requirements for the method described in chapter 6. The technique presented in chapter 6 is able to suppress the THz electric field in the sample while doubling the THz magnetic field. Without the THz electric field the $S(\Delta\mathbf{M}_\perp)$ signal contains only the ZT signal, even in bilayer samples. Thus one could directly determine if the ZT signal amplitude is indeed stacking order dependent. Additionally, one would retrieve the 'pure' ZT signal, allowing for a clean extraction of the THz electric field driven FL-SOT signal from the data presented here.

5.5.2 In-plane magnetization change along M_0

While the $S(\Delta\mathbf{M}_\perp)$ signal is a valuable indicator for the THz field evolution in the sample, our predominant interest lies in the $S(\Delta\mathbf{M}_\parallel)$ component. $\Delta\mathbf{M}_\parallel$ is a change of the in-plane magnetization magnitude. Indeed, the ability to probe the in-plane magnetization change optically in a transmission probe was established in the previous chapter. Here we will use the measurement strategy, for the first time, to measure THz driven spin

accumulation and spin injection from a NM into an FM thin film layer. As sketched in figure 5.2d, a component of \mathbf{E}_{THz} perpendicular to \mathbf{M} will accumulate spins aligned colinear with \mathbf{M} at the NM film interfaces, due to the SHE. If the NM and FM layers share a conductive interface, a number of the accumulated spins will be injected into the FM. Essentially, we are performing a textbook spin injection experiment. Spin magnetic moment entering the FM from the HM layer will increase or decrease the magnetization. We will show here that the magnetization adjusts to the additional spin magnetic moment near instantaneously. We will investigate a few different sample geometries to highlight the nature of the signals.

Equations 5.4 state that we can determine $\Delta\mathbf{M}_{\parallel}$ by subtracting two measurements for $\theta_0 = +45^\circ, -45^\circ$.

$$\Delta\mathbf{M}_{\parallel} \propto T_2 \propto \frac{S(\theta_0 = +45^\circ) - S(\theta_0 = -45^\circ)}{2} \quad (5.13)$$

Layer reversal

Figure 5.11a,b show the principle for the observation of THz spin accumulation: the THz electric field component perpendicular to the FM magnetization will drive a charge current in the NM layer. The SHE then generates a spin current with spins oriented parallel (a) or antiparallel (b) to the magnetization. The spins accumulating at the FM|NM interface will penetrate the FM layer if the interface is conducting. We exploit the fact that the SHE accumulates opposite spin flavors at the two sides of the sample and thus the dynamics have an opposite sign for reversed layer order. The injected spin magnetic moment increases (a) or decreases (b) $\Delta\mathbf{M}_{\parallel}$.

Figure 5.11c shows the $\Delta\mathbf{M}_{\parallel}$ signals for polarization rotation probing. The two curves are measured on CoFeB(3 nm)|Pt(3 nm) and Pt(3 nm)|CoFeB(3 nm). The signals are bipolar and have a period of ≈ 1 ps, corresponding to the ≈ 1 THz central frequency of the THz pulse. Notice that the signals are inverted copies with a slight amplitude change. Figure 5.11d shows the same measurement for a probe polarization ellipticity change. However, the traces in panel c are not inverted copies of one another. We investigate the signal mismatch in figure 5.11e,f. To investigate the signal mismatch we form the sums (red) and differences (black) of the data in panels c and d, respectively. For comparison we also present $S(\Delta\mathbf{M}_{\parallel})$ recorded in a pure FM (6 nm CoFeB) layer. The pure FM traces were recorded in a separate measurement from the other data.

The polarization rotation data (figure 5.11c,e) conforms well with the spin accumulation process outlined above. $S(\Delta\mathbf{M}_{\parallel})$ flips with layer order reversal and the sum signal in panel e is a rescaled version of the difference signal, indicating that the original signals have an amplitude mismatch. An amplitude mismatch of the accumulation signals is likely due to slightly different interface properties for the samples. Indeed, these sample structures are utilized in the spintronic terahertz emitter where the interface is known to have a significant influence on the spintronic effects [Gue21]. The spintronic emitter process can be considered the inverse process to the spin accumulation presented here [Sei16].

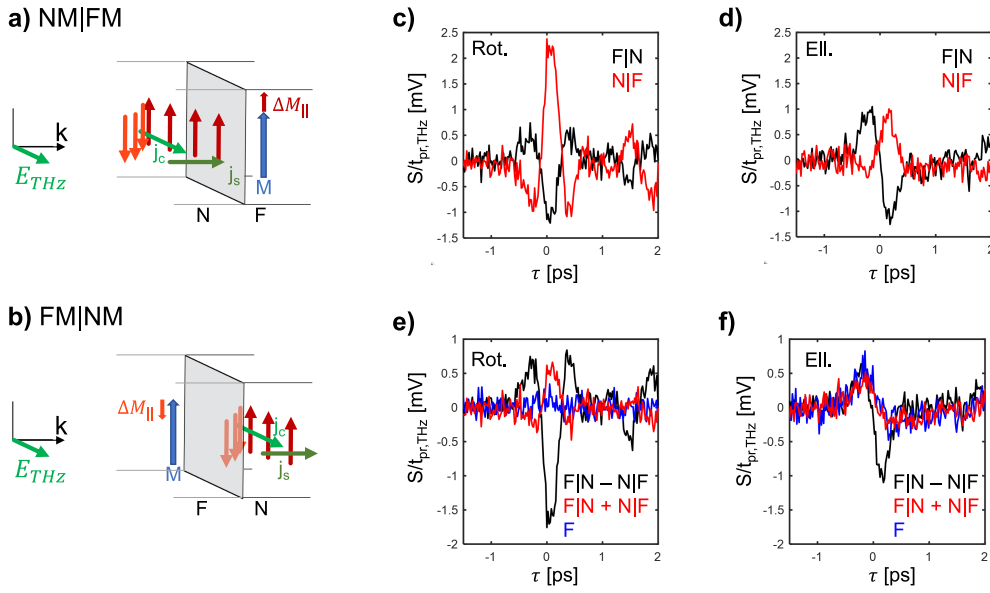


Figure 5.11.: $S(\Delta M_{||})$ under layer reversal **a,b)** Possible mechanism of the spin accumulation signal $S(\Delta M_{||})$. The THz electric field drives a charge current in the plane of the sample (light green arrows) that will be converted into a spin current (dark green arrow) into the depth of the sample. The SHE accumulates oppositely oriented spin populations at both interfaces of the NM layer. Depending on the layer order the FM layer is injected with different spin orientations, adding or subtracting magnetic moment from the magnetization (blue). **c,d)** $S(\Delta M_{||})$ recorded on CoFeB(3 nm)|Pt(3 nm) [red] and Pt(3 nm)|CoFeB(3 nm) [black] samples for rotation and ellipticity probing respectively. The rotation data in panel c displays flipped temporal dynamics with differing amplitudes for the two stacking orders. The ellipticity data in panel d has a similarly flipping component, superimposed with another background signal. **e,f)** To separate the signals in panels c,d into components flipping with the layer order reversal, and those that do not, we form the sums (red) and differences (black). For comparison, we provide the corresponding $S(\Delta M_{||})$ signals from monolayer 6 nm CoFeB (blue). The sum and difference curves in panel e are rescaled versions of one another and the pure FM data is a flat line. This confirms the interpretation of panel c: the spin accumulation signals probed in polarization rotation have opposite sign and different amplitudes for reverse layer orders. The sum and difference signal of panel f are not rescaled copies of one another, however. The sum signal (components that do not flip with layer order) matches the yet unexplained non-zero signal measured from the pure FM layer. This confirms that the deviation from the expected flipping behavior in panel d is due to an additional signal background from the FM layer. All data in this figure is normalized for optical probe transmittance and THz pump transmission.

Interpreting the ellipticity probe data is more challenging, however. In principle the polarization ellipticity change should have the same dynamics as the rotation data, provided it reports on the magnetization dynamics in the same manner. However, comparing the signals in panels c and d of figure 5.11 this is not the case. The sum signal in panel f has different temporal dynamics than the difference signal. This indicates that there is an additional signal component, superimposed with the copy of the spin accumulation signal. Indeed, the sum signal shape matches the $S(\Delta M_{||})$ signal measured in a single FM layer. Removing this background signal from the data in panel c yields the expected symmetric signal flip. Note that all data is normalized for the THz transmission and probe transmittance to make the signals comparable.

The origin of the additional FM signal is unclear, however. Being a *odd in E and odd in B* signal, it should contain only signals $\propto E, E^3$ and $\propto B, B^3$. Additionally, the signal must change sign for $\Delta\theta = 45^\circ$ to survive the signal extraction of equation 5.13. From our current understanding, only in-plane magnetization change probed by MLB fulfills the latter requirement. The current driven spin accumulation due to SHE in the FM layer would only re-distribute spins in the layer, but not alter the total magnetization. The transmission probe, integrating over the entire film thickness, should not be sensitive to such a relocation. Additionally, the signal appears to be similar to the torque-like integral over the driving field, rather than the seemingly field dependent spin accumulation signal that we have been observing from double layers. The rotation probing detection seems insensitive to this additional component as well. Possibly, the rotation and ellipticity probing may have different depth sensitivities in transmission. Determining the origin of this signal is likely a priority for future research. To narrow the field, we propose a measurement with the technique presented in chapter 6 to determine which THz field component (electric or magnetic) is driving the extra signal component.

Additionally, it must be noted that the spin accumulation signals recorded for rotation and ellipticity probe of figure 5.11 appear to have a carrier envelope phase shift with respect to each other. Indeed, this is also observed in the extracted driving fields of figure 5.7. Thus it is likely a consequence of the detection process that is not fully understood yet.

Impact of intermediate layers

A fundamental assumption made when assigning the $S(\Delta\mathbf{M}_{\parallel})$ signal to spin accumulation is that the spin carrying charges indeed originate in the NM layer and are detected in the FM layer. To test this hypothesis we introduce different spacer layers in between the NM and FM layers.

Figure 5.12 shows $S(\Delta\mathbf{M}_{\parallel})$ for various FM|NM interfaces and rotation probing. No signal arises from a pure FM layer (3 nm CoFeB, black) while the CoFeB(3 nm)|Pt(3 nm) bilayer exhibits the same signal as above (blue). All data is normalized for T_{pr} and t_{THz} to make the excitation and detection processes comparable. The conducting Cu spacer in the CoFeB(3 nm)|Cu(2 nm)|Pt(3 nm) sample (red) exhibits a smaller amplitude signal with identical dynamics to the CoFeB(3 nm)|Pt(3 nm) bilayer. The CoFeB(3 nm)|MgO(3 nm)|Pt(3 nm) sample (purple) exhibits no signal, similar to the FM monolayer. The normalization process is responsible for the larger noise level on the MgO spacer sample compared to the pure FM monolayer.

The data in figure 5.12 is consistent with the notion of spin flow from the NM to the FM layer. Pt acts as a spin current source because of its large spin-orbit interaction. Cu is not expected to produce spin currents of its own, but allows for spin transport from Pt to the FM. The signal decrease compared to the bilayer is likely mainly due to some relaxation of the spin polarization during the propagation from Pt to CoFeB. For example, spin flip scattering at the layer interfaces or in the Cu itself may reduce the spin polarization injected into the FM. Alternatively, it is also possible that the Pt|CoFeB interface of the bilayer has a proximity effect in the Pt, causing a magnetization of the NM

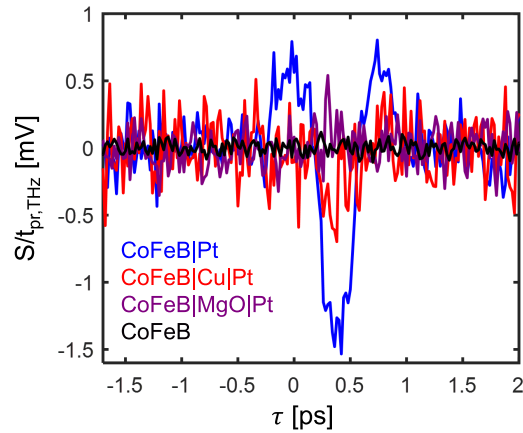


Figure 5.12.: $S(\Delta M_{||})$ for F|I|N stacks with various intermediate layers The importance of electrical contact between the FM and NM layers is investigated by modifying the interface. As expected from the assumed spin accumulation origin of the signal, the pure CoFeB(3 nm)|Pt(3 nm) bilayer exhibits a strong spin accumulation signal (blue), a single CoFeB layer does not (black). An insulating MgO spacer between FM and NM decouples the layers also, leading to no signal (purple). The Cu spacer is conducting, however Cu has no significant spin-Hall effect and does not actively contribute to the spin accumulation. The spin current from the Pt layer is likely partially depolarized at the material interfaces and through spin-flip scattering on its path to the FM, leading to a smaller signal than in the pure bilayer. The data is normalized for THz pump transmission and optical probe transmittance through the sample.

close to the interface. This proximity effect magnetization would contribute to $S(\Delta M_{||})$ in the bilayer, but could not form in the presence of a Cu spacer layer. The MgO spacer is insulating, electrically separating the NM and FM layers. It highlights the importance of spin-polarized charge flow across the NM|FM interface and additionally confirms that no accumulation signals are observed from either NM or FM monolayers. As expected, a pure FM layer does not produce an accumulation signal.

To investigate the importance of the FM|NM interface further figure 5.13 presents $S(\Delta M_{||})$ for bilayers with various layer thickness combinations. The data is normalized for T_{pr} and t_{THz} to make the excitation and detection processes comparable. Additionally, the curves have been smoothed with a 140 fs gaussian moving average filter. Figure 5.13a,b present data for samples with 3 nm CoFeB and 3, 6, or 9 nm Pt measured for rotation and ellipticity probing, respectively. Varying the NM thickness above 3 nm appears to have no influence on the observed dynamics. Figure 5.13c,d display traces recorded for varying FM thicknesses (CoFeB = 2, 3, 6, 9 nm) at constant NM thickness of 3 nm. The thickness dependence of ellipticity probe data (panel d) is more pronounced than in the polarization rotation data (panel c). Notice that the black curve corresponds to CoFeB(3 nm)|Pt(3 nm) in all panels.

The finding that the spin accumulation signal is independent of the NM thickness in figure 5.13a,b is of crucial importance. No NM thickness dependence implies that the spins injected into the FM layer originate from a region < 3 nm from the interface. The spin accumulation is thus an interface effect.

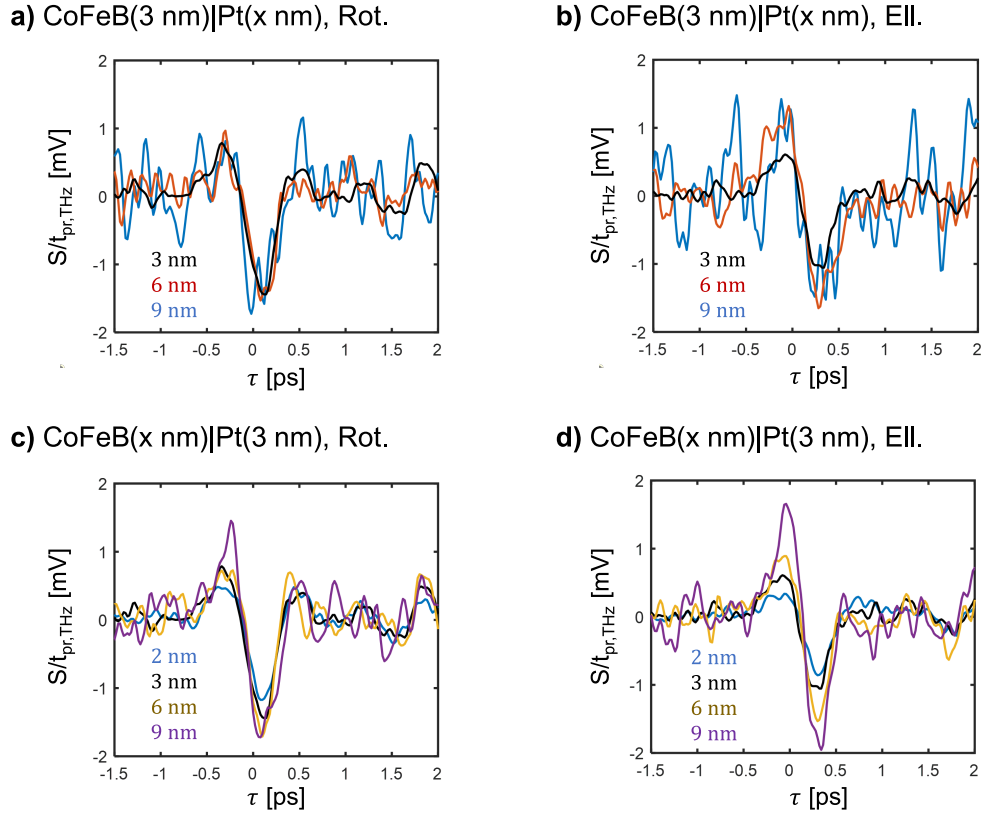


Figure 5.13.: $S(\Delta M_{\parallel})$ for bilayers with various layer thickness combinations All data is normalized for THz pump transmission and optical probe transmittance and smoothed with a 140 fs gaussian moving average filter. **a,b)** $S(\Delta M_{\parallel})$ from bilayers with CoFeB = 3 nm and Pt = 3, 6, 9 nm, for polarization rotation and ellipticity probing respectively. No NM thickness dependence is observed within the noise of the experiment, indicating that the spin accumulation is driven by spins originating $< 3nm$ from the interface. **c,d)** $S(\Delta M_{\parallel})$ from bilayers with CoFeB = 2, 3, 6, 9 nm and Pt = 3 nm, for polarization rotation and ellipticity probing respectively. While the rotation data clearly does not exhibit a FM layer thickness dependence, the ellipticity probe data (d) might. However, considering the noise level on the outlying FM = 9 nm (purple) curve, it is likely that there is no FM thickness dependence after all. This indicates that even 2 nm CoFeB are sufficient to completely absorb the spin magnetic moment injected from the NM layer. Thus, the layer thickness dependence indicates that the spin accumulation is an interface effect.

We assume that a certain THz excitation will transfer a certain number of spins across the NM|FM interface. Normalizing by t_{THz} makes the data in figure 5.13c,d comparable for different sample thicknesses. As the injected spins are not normalized for the total number of spins present in the FM layer we would expect the same signal for the same number of injected spins. This is consistent with panel c, while panel d appears to display a signal varying with the FM thickness.

Dependence on THz field strength

Figure 5.14 shows the THz field dependence of the spin accumulation in a CoFeB|Pt bilayer, confirming a linear dependence. The data represents the signal peak to peak amplitude

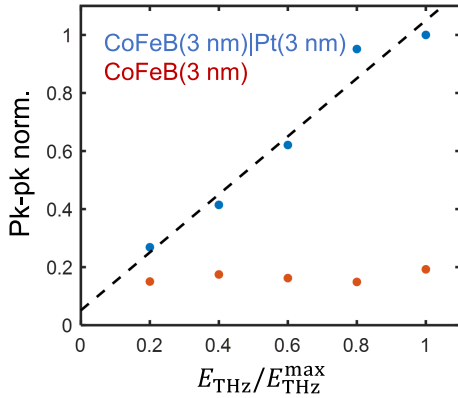


Figure 5.14.: Driving field dependence of $S(\Delta\mathbf{M}_{\parallel})$: The in-plane magnetization signal amplitude scales linearly with the THz driving field in a FM|NM bilayer. The in-plane magnetization is constant in a FM monolayer, however. Both behaviors are consistent with the spin accumulation, which should be visible in FM|NM bilayers but not in monolayers. The FM only data has an offset from zero due to noise on the baseline. The dashed line is a linear fit to the data. The peak to peak signals were extracted after smoothing the data traces with a 700 fs gaussian moving average filter.

after smoothing the data with a 700 fs moving average filter. The dashed line is a linear fit to the data. The spin accumulation is not visible in a FM monolayer, as expected. The FM data offset from zero is ascribed to noise on the signal baseline.

Temporal dynamics of spin accumulation

As mentioned above, the injection of spin magnetic moment into a ferromagnet is a textbook type experiment. Although the spin flow out of the ferromagnet is also possible, we will now consider the fate of electrons flowing from the NM to the FM layer. A spin current pulse injected into a FM will dephase due to the interaction with the magnetization, resulting in a reorientation of the magnetization. A spin accumulation caused by an alternating electric field, such as \mathbf{E}_{THz} , interacts with the magnetization similar to \mathbf{B}_{THz} . \mathbf{B}_{THz} gives rise to a Zeeman torque according to equation 5.6: a signal that accumulates (integrates) the B-field influence over the length of the pulse. In analogy, one would expect a similar behavior from the spin accumulations' influence on the FM magnetization.

Figure 5.15a shows the differentiated ZT signal (black) which equals the THz field evolution within the metal film. The red and blue curves are $S(\Delta\mathbf{M}_{\parallel})$ for FM|NM and NM|FM samples (figure 5.11c), where one is flipped to be directly comparable to the driving field dynamics (blue trace). All three traces are scaled to match in amplitude for comparison. Panel b is the corresponding ellipticity probe measurement.

The data in fig 5.15a is surprising: Contrary to the expected 'torque like' integral shape, the spin accumulation $S(\Delta\mathbf{M}_{\parallel})$ are almost perfect replicas of the driving field, for both sample growth directions. The ellipticity data in panel b is marred by the spurious ellipticity background signal, discussed in the last section (figure 5.11). The underlying signal component biases the spin accumulation signal and causes a mismatch of the $S(\Delta\mathbf{M}_{\parallel})$ and the black THz field trace.

It is very surprising that the spin accumulation (in the nonmagnetic metal) does not have an accumulating effect on the FM layer magnetization. The nearly direct dependence of $S(\Delta\mathbf{M}_{\parallel})$ on the driving field can only be explained by assuming a very rapid decay of the spin population injected into the FM layer. Rapid dephasing would allow the sample

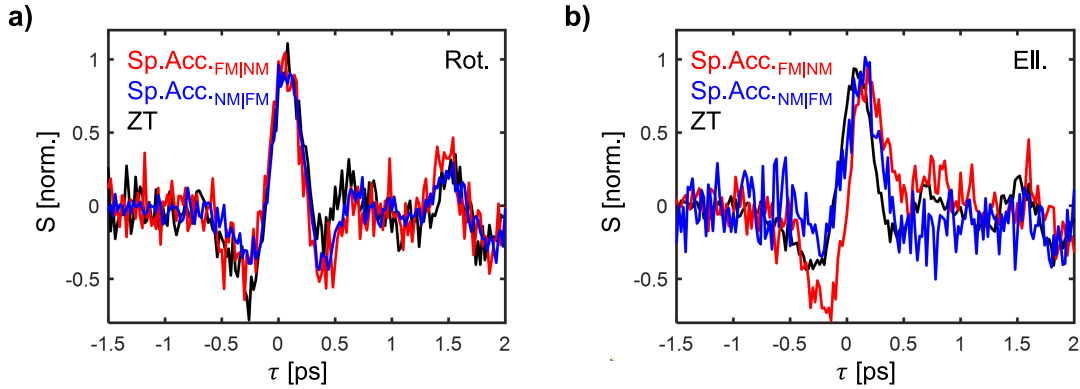


Figure 5.15.: Spin accumulation at THz speeds **a)** The time derivative of $S(\Delta M_{ZT})$ (ZT, black) reveals the time evolution of the THz driving fields in the sample. The spin accumulation $S(\Delta M_{||})$ signal (red) for CoFeB(3 nm)|Pt(3 nm) and (black) Pt(3 nm)|CoFeB(3 nm) evolve with the driving field, without significant delay. The data is measured for polarization rotation probing. One of the two $S(\Delta M_{||})$ was flipped for a better comparison. Other than expected from the analogy to ZT, the spin accumulation is not the integral over the driving field. The data is normalized to match in amplitude. **b)** The spin accumulation $S(\Delta M_{||})$ signal (red) from CoFeB(3 nm)|Pt(3 nm) and (black) Pt(3 nm)|CoFeB(3 nm), for ellipticity probing.

magnetization to follow the driving field more directly, without 'memory' of previously injected spins. From the timing uncertainty and the width of our data we determine a spin dephasing time on the order of ~ 100 fs in the CoFeB layer. This time is in good agreement with the spin-electron relaxation time in CoFeB, which amounts to ≈ 104 fs [Rou21]. It was measured by triggering ultrafast magnetization by optical heating (see figure 5.3).

This finding is plausible: excess spins in a magnet, that is a difference with respect to the instantaneous equilibrium magnetization, can arise from both a temperature increase and spin injection/ejection. When the decay mechanism is dominated by local spin-flip scattering, the decay time is identical for both excitation mechanisms. The measurement confirms that spin accumulation, transport and interaction with a FM magnetization all occur on THz timescales. This is a major result of the thesis.

5.5.3 THz spin accumulation: outlook

Impact of the SHE angle α_{SHE}

Further evidence supporting the mechanism of spin accumulation in the NM layer acting on the FM magnetization is provided by investigating the dependence on the spin Hall angle α_{SHE} of the involved materials. Similar to the treatment of figure 5.10, we chose Pt and W as nonmagnetic layers for their opposite α_{SHE} . Consequently, we expect a sign change of the spin accumulation upon cap material exchange. Alternatively, we expect the same sign signal from oppositely grown samples with different α_{SHE} NM layer.

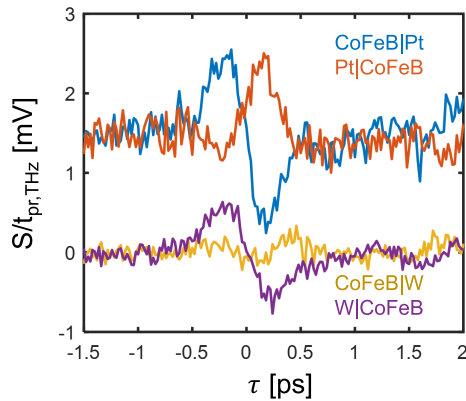


Figure 5.16.: Spin Accumulation dependence on α_{SHE} We interpret the spin accumulation due to SHE in the NM layer as driver of $S(\Delta M_{\parallel})$ the bilayer samples. As the spin accumulation sign depends on the sign of α_{SHE} , we compare bilayers with NM = Pt, W. Pt and W are expected to have opposite spin Hall angles. CoFeB|Pt (blue) and W|CoFeB (purple) clearly show the same sign for reversed stacking order, as expected. CoFeB|W and Pt|CoFeB are not flipped copies of the corresponding other layer order, which may be an indicator of an additional spin current as discussed below. The data is normalized for THz transmission and probe beam transmittance.

Indeed, figure 5.16 shows ellipticity probe data comparing CoFeB(3 nm)|Pt(3 nm) and Pt(3 nm)|CoFeB(3 nm) samples (blue and red, displaced by +1.5) to CoFeB(3 nm)|W(3 nm) and W(3 nm)|CoFeB(3 nm) samples (yellow and purple). As expected, the accumulation sign remains the same for reverse grown samples. The signal amplitude discrepancy between Pt and W capped samples may be due to the different α_{SHE} or the relative strength of the magneto-optical constants. For an investigation of the latter, please refer to the supplementary material of [Sta17].

If observed closely, the data for CoFeB|W (yellow) has a slightly delayed dynamics. This may be due to additional components contributing to the spin movement in the sample and will be discussed below.

Possible spin flow out of the FM

In the last section (figure 5.16) we noticed a mismatch in the data for flipped samples that is not easily explained by the additional ellipticity offset, as it has the dynamics of the spin accumulation itself. This was especially visible in the CoFeB|W sample. As a double check, we performed a measurement with NM = Cu, as Cu has a negligible α_{SHE} . Rotation probe data for CoFeB(3 nm)|Cu(3 nm), blue, and Cu(3 nm)|CoFeB(3 nm), red, are presented in figure 5.17. Instead of the expected flat line, these curves display a small signal with the same time dependence as the accumulation signals above.

While Cu is not expected to produce a spin accumulation in response to the THz current, the FM layer has a strong spin-orbit interaction itself. Indeed, as the THz electric field is expected to be constant across the entire bilayer, a THz charge current will be present inside the FM layer. It is known that CoFeB is host to the SHE, too. An in-plane charge current in the FM layer will thus accumulate spins on the FM|NM layer which are counterpropagating to the spin currents discussed in the rest of the chapter. The detection mechanism would be sensitive to the change of \mathbf{M} , which is losing spins to the FM. It is thus possible that a part of the imbalance in the layer reversal accumulation signals above is due to a superposition with spin flow from the FM layer.

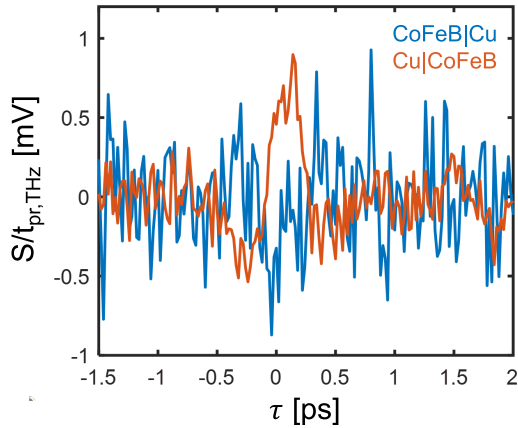


Figure 5.17.: Spin flow from the FM $S(\Delta M_{\parallel})$ measured on CoFeB(3 nm)|Cu(3 nm) and Cu(3 nm)|CoFeB(3 nm) samples. Cu is expected to have a negligible spin-Hall angle and thus should not host a significant SHE. Likely, the observed ΔM_{\parallel} is a spin flow away from the FM layer, due to the SHE or AHE in the CoFeB. Such a spin flow from FM to NM layer would impact all other measurements of $S(\Delta M_{\parallel})$ in this chapter and may explain part of the amplitude discrepancies, especially between opposite spin Hall angle NM materials. The data is normalized for THz transmission and probe beam transmittance.

The spin flow from the FM layer may be investigated in the future by repeating the experiments with an alternate FM layer. The alternate FM layer must have an opposite sign α_{AHE} and α_{SHE} to CoFeB, we suggest $\text{Ni}_{81}\text{Fe}_{19}$ (permalloy).

Number of injected spins

Above, we have presented data that is phenomenologically in line with spin polarized electrons traversing the NM|FM interface due to THz driven spin accumulation in the NM layer and interacting with the FM layer magnetization. Here we will attempt to quantify by how much the magnetization was changed as a fraction $\Delta M_{\parallel}/M_0$. Determining the fractional change of the magnetization, the detection mechanism must be calibrated. The appropriate calibration scheme for the MLB, responsible for probing in-plane magnetization changes, is presented in chapter 4. We will make use of this calibration technique here. The calibration determines the maximum possible signal amplitude (parameter b in the fit equation 4.9) which occurs when the probe angle and the magnetization are at $\theta = 45^\circ$ to one another. At $\theta = 45^\circ$ the second term of equation 4.8 becomes $\propto \sin(2\theta) = 1$.

Importantly, since the calibration is measured in the same setup as the dynamic measurements of this chapter, the calibration already accounts for the sample specific probe beam transmission through the sample. However, the measurement electronics involve a hard-wired delay line and an amplifier in the measurement of $S(\Delta M_{\parallel})$, which are excluded when determining M_0 . To compare the two measurements, the influence of the delay-line and the amplifier was determined by measuring an EOS trace of the THz pulse with both detection schemes, including a signal delay compensation cable to account for the propagation delay in the amplifier (chapter 3.4). It was found that the static calibration signal must be multiplied with a factor ~ 44 to represent M_0 here. Thus, to arrive at a $\Delta M_{\parallel}/M_0$ signal, it is sufficient to divide the signal by $\sim 44 \cdot b$.

Figure 5.18 displays normalized rotation probe (panel a) and ellipticity probe data (panel b). The normalization constants b were extracted from corresponding static measurements, as outlined in chapter 4. It should be noted that the extraction for Pt|CoFeB in rotation probing was particularly challenging and should be taken as an outlier to the analysis

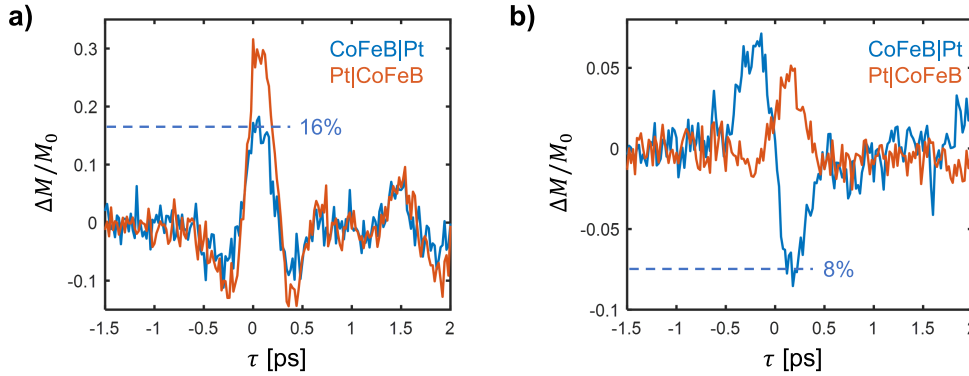


Figure 5.18.: $\Delta M_{||}/M_0$: injected spins as fraction of magnetization **a)** Rotation probe $S(\Delta M_{||})$ from CoFeB(3 nm)|Pt(3 nm) and Pt(3 nm)|CoFeB(3 nm) samples. The data have been normalized with the factor b from a static measurement like those presented in chapter 4, multiplied by the amplifier factor ~ 44 . The extraction of b for the Pt(3 nm)|CoFeB(3 nm) sample (red curve) was particularly challenging and should be considered an outlier. This atypical static value is also responsible for the unexpected same sign for opposite layer directions. Considering the CoFeB(3 nm)|Pt(3 nm) data (blue curve) we find a peak FM magnetization modulation of $\approx 16\%$. **b)** The ellipticity probe measurements corresponding to panel a. Here, the extraction of b is considered to be successful for both traces. Here, the maximum change of the FM magnetization of the CoFeB(3 nm)|Pt(3 nm) sample is found to be $\approx 8\%$.

(red curve, panel a). From a simple consideration, $\Delta M_{||}/M_0$ reflects the number of injected/removed spins from the FM layer, as a fraction of the entire magnetic moment. Thus, if rotation and ellipticity probing probe the same magnetic dynamics, one would expect them to yield the same $\Delta M_{||}/M_0$. However, comparing the maximum amplitude of the CoFeB|Pt curves (blue), we notice that modulation of the magnetization differs by a factor 2. The peak to peak amplitude mismatch is smaller, but still significant. Additionally, a model estimate may confirm if $\Delta M_{||}/M_0 \sim 16\%$ are even physically sensible. Possibly, the calibration method is not sensitive to all magnetic moments in the FM after all.

As the FM|NM interface plays a large role in the process, and a magnetization of the Pt in the interface region is possible, it is not unsurprising that reverse grown stacks yield different magnetization modulations. Additionally, the static calibration is only sensitive to regions of existing, spontaneous magnetization. This may not accurately reflect the situation in the presence of a THz pump pulse. Future research will have to investigate the influence of the interface and disentangle the suspected spin exchange in between the sample layers. Additionally, the different CEP of the signals probed for rotation and ellipticity probing must be understood. We are confident that once these signals are isolated, a consistent normalization of the spin accumulation data is possible.

In-plane magnetization rotation $\Delta\theta_{||}$

According to equation 5.4, the orientation change of the in-plane magnetization $\Delta\theta_{||}$ is given by

$$\Delta\theta_{\parallel} \propto T_{\theta} \propto (S(\theta_0 = 0^\circ) - [S(\theta_0 = +45^\circ) + S(\theta_0 = -45^\circ)]/2)/2. \quad (5.14)$$

According to figure 5.2 we expect the damping-like spin-orbit torque (DL-SOT) in the $\Delta\theta_{\parallel}$ component for in-plane magnetized films. However, the DL-SOT is $\propto M^2$ as seen from equation 5.9. It should thus not appear in the *odd in E and odd in B* signal components we have investigated so far. Instead, we would expect it in the *odd in E and even in B* component, together with other nonmagnetic effects like electro-optic sampling. Disentangling the EOS and DL-SOT signals is left for future work.

5.6 Conclusion

In this chapter we have established a measurement procedure to determine the three THz pump induced component magnetization changes ΔM_{\perp} , ΔM_{\parallel} , and $\Delta\theta_{\parallel}$ in thin film samples for transmission probing at normal incidence. We have offered an overview of likely effects in NM|FM bilayer samples that are likely responsible for the observed effects. We have demonstrated that the signal attributed to ZT indeed exhibits the correct dynamics and have offered routes for further investigation. Especially the layer order dependence of the ZT amplitude warrants further research. We have also seen evidence of a FL-SOT.

Importantly, we have presented phenomenological evidence for THz speed spin accumulation and spin transfer in a NM|FM bilayer. Evidence included the signal behavior under layer reversal, NM material change, interface manipulation and layer thickness variations. We have established that the spin accumulation is an interface effect that relies on a fast relaxation (~ 100 fs) of spins injected into the FM. We have also, while unsuccessful, attempted to normalize the spin accumulation data in terms of the fractional magnetization change in the FM. Possible explanations for the failure of the normalization have been offered. Thus, while many open questions remain, we are confident to have shown THz speed spin accumulation and transfer in NM|FM bilayer samples. Spin accumulation at THz speeds is a necessary requirement for the advance of spintronic devices to THz speed operation.

6 Separated actions of B_{THz} and E_{THz}

As we have encountered in the last chapter, a significant boon of THz radiation pump – optical probe spectroscopy is that the THz light field consists of both an electric (\mathbf{E}_{THz}) and a magnetic field component (\mathbf{B}_{THz}). Both of these fields evolve identically in free space and can interact with the sample, potentially coupling to different subsystems. This presents an additional challenge for the study of materials, however. It may not be entirely certain a priori which THz field component is responsible for the observed dynamics.

In this chapter, we present a strategy to distinguish the effects of \mathbf{E}_{THz} and \mathbf{B}_{THz} in magnetic thin film samples. We demonstrate that locating a conductive mirror surface behind the thin film sample will modify the amplitude ratio of the two light fields in a narrow region in front of the sample. The superposition of the incident and reflected electric field form a standing wave node (zero field) at the mirror surface, while the magnetic field forms an antinode with twice the initial magnetic field amplitude. For short THz pulses with a broad frequency spectrum, the region of optimal operation is confined close to the mirror, requiring samples much thinner than $\lambda_{\text{THz}}/4$ that do not disturb the THz radiation significantly. Comparing measurements with and without a mirror enables an attribution of the driving field for the observed dynamics.

In this study we employ the Zeeman torque ($\propto \mathbf{B}_{\text{THz}}$, section 2.3.2) and the demagnetization ($\propto \mathbf{E}_{\text{THz}}^2$, section 2.3.1) in a 6 nm thin $\text{Co}_{20}\text{Fe}_{60}\text{B}_{20}$ film as probes of \mathbf{B}_{THz} and \mathbf{E}_{THz} , respectively. We demonstrate the effectiveness of the THz field amplitude ratio modulation and thus provide new functionality to THz pump – optical probe experiments.

Parts of this chapter are contained in a manuscript in preparation.

6.1 Motivation

The THz electric and magnetic fields evolve simultaneously and act on a sample in tandem. Here they can, for example, excite infrared-active phonons and magnons, couple to an existing magnetic order and drive currents. THz pump pulses provide a spectrally broad stimulus for many such resonances in diverse material systems. The resulting dynamics typically manifest in a transient birefringence or an isotropic sample transmissivity change that can be probed with a suitable probe pulse (section 2.3.5).

Fundamentally, the THz B-field couples to magnetic dipole moments (MD) via the Zeeman interaction (section 2.3.2). Perturbing the magnetic lattice can excite long wavelength spin waves, known as magnons (section 2.2.8). The THz E-field, on the other hand, couples to electric dipoles (ED) and can excite long wavelength lattice vibrations (phonons, section 2.2.8) and drive charge currents (section 2.3.1) in the sample. In some cases, the character of an observed resonance may be yet undetermined. Here we present a strategy to modulate the relative amplitudes of the THz electric and magnetic fields. Comparing two measurements with different $|E|_{\text{THz}}/|B|_{\text{THz}}$ ratios, we separate the simultaneous action of

the two light fields in the sample. Thus, we demonstrate an effective experimental scheme able to determine the character of resonances in THz pump, optical probe studies. This is very relevant for the study of spintronic materials without inversion symmetry such as multiferroics.

6.2 Principle

Fundamentally, the scheme presented here makes use of the superposition of waves incident on, and reflected from a mirror surface, in a region very close to the mirror. Such a superposition will exhibit a different E- and B-field amplitude ratio than the freely propagating wave. In a transparent material with real-valued refractive index, the time- and space-varying fields $E(z, t)$ and $B(z, t)$ of a plane wave co-propagate in phase and with mutually perpendicular polarization (fig 6.1a). The electric and magnetic field vectors \mathbf{E} and \mathbf{B} are mutually orthogonal and obey (section 2.4.1)

$$\mathbf{B} \propto \frac{1}{\omega}(\mathbf{k} \times \mathbf{E}) \quad (6.1)$$

where \mathbf{k} and ω are the wavevector and frequency of the monochromatic wave, respectively.

A perfectly conducting metallic mirror with 100% reflectivity will have a Fresnel reflection coefficient $r = -1$ over a broad range of frequencies [Hec16]. This Fresnel reflection coefficient of -1 indicates that the reflected electric field wave will have gained a phase jump of 180° (Eulers' formula $e^{i\pi} = -1$ [Con96]), a polarity flip, while retaining the full amplitude. Thus, the superposition of forward and backward propagating electric fields will form a standing wave node at the mirror surface (figure 6.1b). A very thin sample placed in a standing wave node will not experience the THz electric field \mathbf{E}_{THz} .

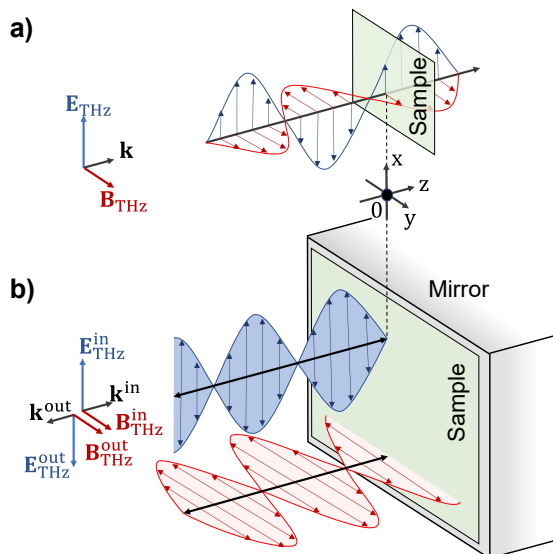


Figure 6.1.: Modulating $\mathbf{E}_{\text{THz}}/\mathbf{B}_{\text{THz}}$ **a)** The *propagating wave (PW) geometry*: A propagating EM wave consists of an electric (blue) and a magnetic (red) field that are in phase when propagating in free space. The relationship between \mathbf{E}_{THz} , \mathbf{B}_{THz} , and the wavevector \mathbf{k} is given by equation 6.1. A sample (green) will experience both fields equally. **b)** The *standing wave (SW) geometry*: A conducting mirror ($r \approx -1$) reflects the wave, flipping the \mathbf{E}_{THz} polarity in the process. The electric field forms a standing wave node at the mirror ($E(0, t) = 0$) while magnetic field forms an antinode with twice the initial amplitude ($|B(0, t)| = 2|\mathbf{B}_{\text{THz}}|$). A thin film ($d < \lambda/4$) sample in close proximity to the mirror experiences a modulated ratio $|E|_{\text{THz}}/|B|_{\text{THz}}$.

The THz magnetic field (\mathbf{B}_{THz}) incident and reflected waves superimpose constructively, however. While the electric field undergoes a polarity flip ($\mathbf{E}_{\text{THz}} \rightarrow -\mathbf{E}_{\text{THz}}$) during the reflection, and the propagation direction of a reflected wave is also opposite to that of the initial wave ($\mathbf{k} \rightarrow -\mathbf{k}$), the B field direction remains the same ($\mathbf{B}_{\text{THz}} \rightarrow \mathbf{B}_{\text{THz}}$), see figure 6.1b. Therefore, the THz B-field superimposes constructively and forms a standing wave, with a quarter-wavelength shift with respect to the electric field standing wave. Directly at the perfectly conducting mirror, where the THz electric field amplitude is suppressed, the amplitude of the THz B field doubles. These ideal values are strongly dependent on the mirror quality and the sample itself. The perfect electric field cancellation and magnetic field doubling require 100% reflection. Additionally, the sample should not disturb the incoming wave, imposing severe restrictions on the sample. Imperfect conditions would manifest in an imperfect electric field extinction and a magnetic field amplification by < 2 .

For monochromatic plane waves these standing waves will have many nodes spaced with half a wavelength. The broadband THz pulses used in this work will not form such an extended standing wave, however. Every frequency component has a unique node spacing and the superposition of many such waves ‘smears out’ the nodes and antinodes. The only shared node and antinode for a few cycle pulse are at the mirror surface, constraining the location for a sample (figure 6.2). To experience the cancellation of the forward and backward propagating fields, the sample must be much thinner than $\lambda/4$ of the THz pump wave. The sample must also be significantly thinner than the THz field decay length, to ensure a constant field within the sample.

The mirror-induced modification of the field amplitudes can be used to selectively excite only the MD interactions of a sample in the presence of the mirror. We call this the *standing wave* (SW) geometry (figures 6.1a and 6.2a). Alternatively, the regular combination of both MD and ED effects are observed without a mirror. We call this the *propagating wave* (PW) geometry (figures 6.1b and 6.2b). In a transmission probe experiment, the mirror material must be chosen such that it is transparent for the probe wavelength.

To probe the action of both the electric and magnetic fields of the light pulse separately, a simple thin film ferromagnet in the x-y-plane, magnetized along the $\hat{\mathbf{x}}$ direction ($\mathbf{M}_{(x,0)}$), is ideal. The THz pump light propagates along the $\hat{\mathbf{z}}$ direction. The THz B-field oscillates in the $\hat{\mathbf{y}}$ direction ($B(z,t) = \mathbf{B}_{\text{THz}}(t) = \mathbf{B}(t)\hat{\mathbf{y}}$) and causes a Zeeman Torque \mathbf{T}_z out-of-plane, in the $\hat{\mathbf{z}}$ direction, (section 2.3.2) of the form [Vic13]

$$\Delta\mathbf{M}_{\text{ZT}}(t) \propto \mathbf{M}_{(x,0)} \times \hat{\mathbf{y}} \int_{-\infty}^t dt' B(0,t') \quad (6.2)$$

where the integral captures the accumulated effect of the B-field evolution in the sample. The effect is linearly dependent (odd) on the driving magnetic field. At the same time, the THz electric field $E(z,t)$ excites a current in the sample (section 2.3.1). This current possibly excites a spectrum of magnons through resistive heating, leading to an ultrafast decrease of the in-plane magnetization (ultrafast demagnetization, $\Delta\mathbf{M}_{\text{UDM}}$)

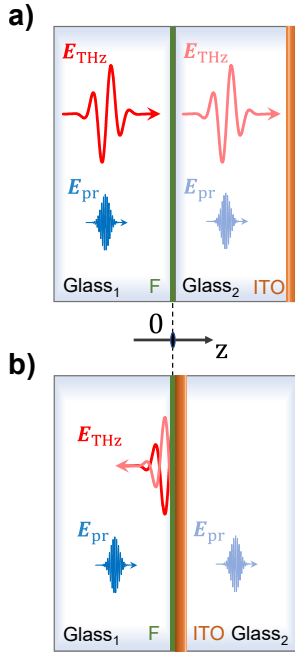


Figure 6.2.: Experimental implementation of the PW and SW geometries of figure 6.1 The experimental realization requires a thin ferromagnetic (F) sample (green) grown on an identical glass substrate (Glass₁) and a THz mirror (ITO, brown) on a glass substrate (Glass₂). **a)** The *propagating wave (PW) geometry*: The sample F is brought into mechanical contact with the glass substrate of the mirror. Both \mathbf{E}_{THz} and \mathbf{E}_{pr} can traverse the interface. The reflection of \mathbf{E}_{THz} in the mirror surface returns to the sample delayed, outside of the measurement window. **b)** The *standing wave (SW) geometry*: The sample F is brought into mechanical contact with the ITO mirror. While \mathbf{E}_{pr} traverses the mirror unperturbed, \mathbf{E}_{THz} is reflected with $r \approx -1$. \mathbf{E}_{THz} reverses polarity upon reflection and the superposition of both pulses creates an electric field standing wave node ($\mathbf{E}_{\text{THz}} \rightarrow 0$) at the mirror surface.

$$\Delta \mathbf{M}_{\text{UDM}}(t) \propto \mathbf{M}_0 \int_{-\infty}^t dt' E^2(0, t') \quad (6.3)$$

that depends on the deposited total energy. The effect is quadratically dependent (even) on the driving electric field. It should be noted that the exact mechanism of ultrafast demagnetization is a complex subject [Fä18, Kum20, Tao19, Bü18]. Here we choose a macroscopic model explanation as we only intend to highlight the $\propto E^2$ nature of the effect.

6.3 Experiment

Similar to the experiment presented in chapter 5, the samples were pumped with broadband THz pulses (1 kHz repetition rate, 0.1 – 2.5 THz) centered at 1 THz from a tilted pulse front Lithium Niobate source (description, pulse shape and spectrum in chapter 3.3). The THz E-field polarity was controlled with a combination of motorized and fixed polarizers as shown in figure 3.5b, reducing the maximal available THz field to ~ 500 kV/cm. The THz field amplitude was further controlled with the motorized THz polarizer, similar to chapter 5.

The sample was placed inside an external magnetic field \mathbf{B}_{AC} that alternated at ≈ 500 Hz, orienting the sample magnetization in opposite directions for consecutive THz pump pulses. The maximum magnetic field of ≈ 70 mT was applied at an angle $\alpha \approx 15.5^\circ$ to the sample plane, which was kept at normal incidence to the pump and probe pulses. The magnetic field decomposed into a component $\mathbf{B}_{\text{AC},\parallel}$ parallel and a component $\mathbf{B}_{\text{AC},\perp}$ perpendicular to the sample plane. The in-plane component was sufficient to saturate the sample in-

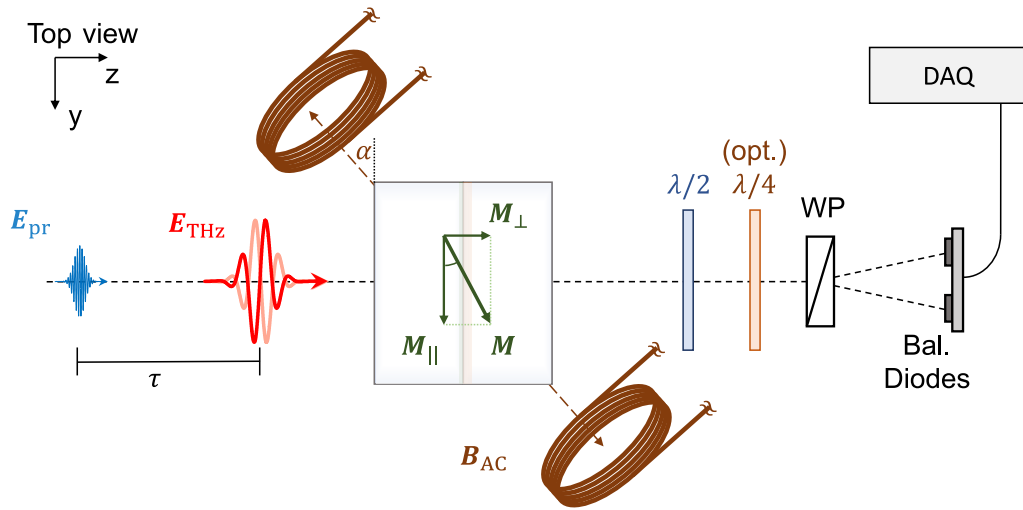


Figure 6.3.: Experiment The sample stacks (figure 6.2) are mounted on a motorized sample figure for direct comparison. The samples are placed in an AC electromagnet (brown coils) positioned in the y - z -plane, rotated by an angle $\alpha \approx 15.5^\circ$ to pull the magnetization \mathbf{M} out of the sample against the magnetic anisotropy, achieving an out-of-plane magnetization tilt. The out-of-plane magnetization component M_{\perp} is probed directly by a linearly polarized optical probe pulse (blue) from the oscillators' 80 MHz pulse train via the MCB effect. Separated by a temporal pump-probe delay τ , a THz pulse (red) from a Lithium Niobate THz source excites the sample. The THz pulse polarity (two shades of red) is controlled via a set of motorized polarizers. The THz magnetic field (not shown) creates a Zeeman torque on the in-plane M_{\parallel} component, creating a transient ΔM_{\perp} along the probe propagation. ΔM_{\perp} is detected via the MCB effect as well. The probe light is conditioned with a $\lambda/2$ and an optional $\lambda/4$ waveplate to detect the pump induced polarization rotation and ellipticity change, respectively. A Wollaston prism (WP) separates the probe light into two orthogonally polarized light beams that are detected on a set of balanced photodiodes. The electrical pulses from the photodiodes are treated with the electronic delay line (figure 3.6) before detection in a digitizer card (DAQ).

plane magnetization. The out-of-plane component of the external field worked against the in-plane magnetic anisotropy, pulling the saturated sample magnetization slightly out of the sample plane. This was necessary to observe the magnetization magnitude changes from ΔM_{UDM} with the MCB effect (see section 4.1). The MCB is only sensitive to ΔM_{\perp} along the probe propagation direction, that is along the sample normal.

The pump-induced dynamics were interrogated with 25 fs duration, 1 nJ pulses centered at 790 nm from the 80 MHz oscillator pulse train, as described in section 3.3.3. The probe pulse was mechanically delayed with respect to the THz pump pulse. The signal-carrying probe pulse was treated to isolate the pump-induced modulation (see figure 3.6) and amplified by a factor ≈ 100 , before digitizing with an *NATIONAL INSTRUMENTS NI PCI-5122* card.

The THz-beam focus diameter was $\approx 1100 \mu\text{m}$ while the probe beam was much smaller at $\sim 60 \mu\text{m}$. Therefore, the interrogated sample region was considered uniformly excited. The beams were characterized with the pinhole method and appropriately calibrated power meters.

The sample was a 6 nm $\text{Co}_{20}\text{Fe}_{60}\text{B}_{20}$ film deposited on a 500 μm glass substrate with a 4 nm MgO cap, grown by Samridh Jaiswal and Maria-Andromachi Syskaki from the group of Professor Mathias Kläui at the Johannes Gutenberg University, Mainz (Germany). The thin film sample was inherently in-plane magnetized. The mirror coatings were either indium tin oxide (ITO, ≈ 65 nm, sheet resistance 23.27 Ω/sq measured with four-point probe) or aluminium doped zinc oxide (AZO, ≈ 850 nm as inferred from [Ton18], sheet resistance 18.45 Ω/sq measured with four-point probe) on thick (1-2 mm) glass substrates. Both ITO and AZO are excellent conductors and mirrors for THz radiation but transparent for the probe pulse.

The standing wave (SW) and propagating wave (PW) geometries, outlined above, were implemented with two combinations of the sample and the mirror. Two 5×5 mm snippets of sample and mirror were brought into contact in two different orientations (figure 6.2) within a mechanical sample finger vice. The sample was brought into contact with either the mirror or the substrate side of the mirror. The sample and mirror sides were brought into contact to form the SW geometry. The PW geometry had the mirror substrate in contact with the sample. It was important to join both the flakes in each case to provide a symmetrical environment for the probe pulse around the sample layer. In the PW geometry, the additional path length of $2 \times$ the mirror substrate thickness removed the reflected THz pump pulse from the observed time window.

The mechanical vice sample finger, from chapter 5, consisted of a base and a cover slide connected by screws, all manufactured from nonmagnetic metals. The sample vice ensured a good mechanical contact between sample and mirror pieces. Rubber spacers on one side of the sample stack compensated for a possible slight unevenness of the sample vice and ensured a tight fit of sample and mirror substrates. The air gap in between the samples is estimated to be ~ 1 μm as inferred from optical transmission spectra. The optical transmission was measured with a spectrometer and the transmission spectrum compared to a simulation, similar to [Pas20]. The sample finger was mounted on a *PHYSIK INSTRUMENTE Q-521* piezo translation stage.

The measurement sequence was similar to that presented in chapter 5 and figure 5.5. \mathbf{B}_{AC} , and thus \mathbf{M} , was reversed for consecutive THz shots along one pump-probe trace. The THz polarity was flipped every five to ten pump-probe traces. The PW and SW geometries were averaged in batches of 20 minutes each. The external parameters were varied on the timescale of half a minute and thus measured quasi-simultaneously during the 20-minute integration time per sample. These 20-minute measurements were sorted and averaged, producing a set of averaged curves for each cycle of the measurement. These individual measurements were grouped for each sample and time-drift corrected with a numerical THz-shape-matching algorithm. Since the Zeeman torque signal was comparatively large, dominating the recorded signal, it was a suitable marker for the time-drift correction. The drift-time-corrected sample batches were again averaged to receive four pump-probe traces for the permutations of external parameters with good signal to noise ratio. Example result curves are presented in figure 6.4a.

6.4 Data and Discussion

Magnetization dependent signals

Four pump-probe traces were recorded nearly simultaneously for all permutations of THz electric (E) field polarity and external AC magnetic field (B) direction: $S_{E^+B^+}$, $S_{E^+B^-}$, $S_{E^-B^+}$, $S_{E^-B^-}$. Example signals for the four combinations are presented in figure 6.4a. To isolate the magnetic signals, curves recorded for the same THz E-field polarity but opposite sample magnetization were subtracted from each other.

$$\begin{aligned} S_{B^+-B^-}^{E^+} &= \frac{S_{E^+B^+} - S_{E^+B^-}}{2} \\ S_{B^+-B^-}^{E^-} &= \frac{S_{E^-B^+} - S_{E^-B^-}}{2} \end{aligned} \quad (6.4)$$

Typical magnetic dependent signals are presented in figure 6.4b.

Zeeman torque and ultrafast demagnetization

To distinguish the effects driven by the THz E and B fields, we separated the Zeeman torque ($\propto \mathbf{B}_{\text{THz}}$) and the ultrafast demagnetization ($\propto \mathbf{E}_{\text{THz}}^2$) signals. As mentioned above, the Zeeman Torque is odd in the driving field polarity

$$\Delta \mathbf{M}_{\text{ZT}} \propto \frac{S_{B^+-B^-}^{E^+} - S_{B^+-B^-}^{E^-}}{2} \quad (6.5)$$

while the ultrafast demagnetization is even in the driving field

$$\Delta \mathbf{M}_{\text{UDM}} \propto \frac{S_{B^+-B^-}^{E^+} + S_{B^+-B^-}^{E^-}}{2} \quad (6.6)$$

The separation of $S(\Delta \mathbf{M}_{\text{ZT}})$ and $S(\Delta \mathbf{M}_{\text{UDM}})$ as sums and differences of magnetic signals with opposite driving field requires that the two \mathbf{E}_{THz} polarities are of equal magnitude. Small deviations in the magnitude of opposite polarities of the THz field strength are possible within the measurement uncertainty of the THz power meter, used to determine the positions of the motorized THz polarizer (figure 3.5). To compensate for such a mismatch, one of the magnetic signals in figure 6.4b was scaled by the ratio of the integrated signals for both E field polarities (dashed line). We will see that the signal is dominated by the $\propto E$ component, thus this procedure is justified.

$S(\Delta \mathbf{M}_{\text{ZT}})$ and $S(\Delta \mathbf{M}_{\text{UDM}})$ are displayed in figure 6.4c. The torque curve (blue) has the expected (equation 6.2) shape of the integrated driving field (dashed red line). The driving field was derived from electro-optic sampling (EOS) in 50 μm Quartz, presented in figure 3.4a. $S(\Delta \mathbf{M}_{\text{UDM}})$ is a step-like signal (grey), multiplied by a factor 10 for better

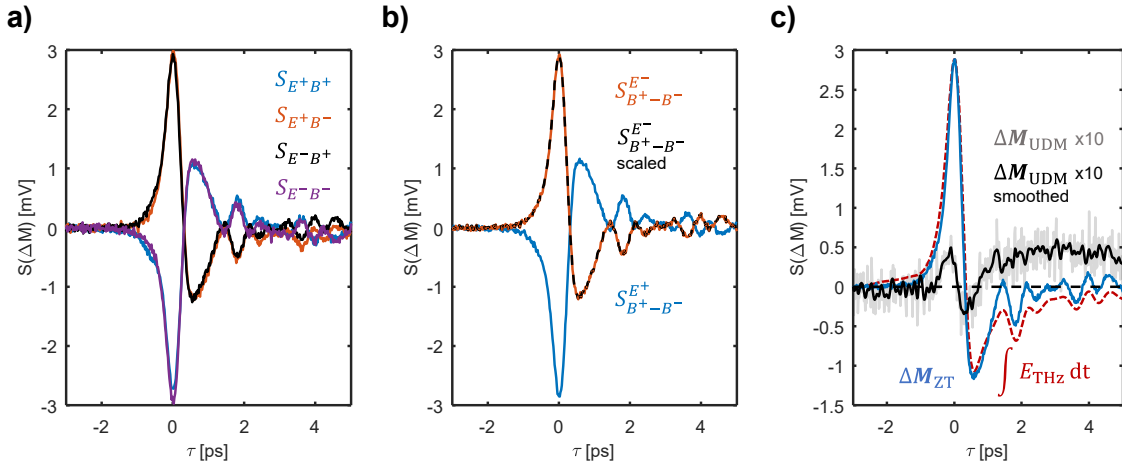


Figure 6.4.: Data and signals The E_{THz} and B_{THz} probes, ultrafast demagnetization $\propto E_{\text{THz}}^2$ and Zeeman torque $\propto B_{\text{THz}}$ respectively, can be disentangled depending on their symmetry with respect to the driving field polarity and the sample magnetization. The sample magnetization is controlled with the external AC magnetic field B_{AC} . **a)** Typical signals recorded for the four permutations of the external parameters. Note that the THz electric and magnetic fields change polarity together. **b)** Only the magnetic response of the sample, extracted by subtracting curves with shared driving field polarity but opposite sample magnetization. Slight amplitude mismatches of the THz field polarity amplitudes are corrected by the ratio of the integral over the respective signal spectra (dashed line). **c)** To extract $S(\Delta M_{\text{UDM}})$ (black) and $S(\Delta M_{\text{ZT}})$ (blue) we take advantage of the field dependence and take the sum and difference of the curves in panel b. ΔM_{ZT} (blue) exhibits the expected dynamics, compared to the integral over the THz electric field (red dashes) characterized with EOS in $50 \mu\text{m}$ quartz, presented in figure 3.4a. ΔM_{UDM} (grey) is a comparatively small signal and presented amplified by a factor 10. For clarity, the data is smoothed with a 320 fs gaussian moving average filter (black). ΔM_{UDM} exhibits the expected step-like behavior for data $\tau < -1$ ps and $\tau > 2$ ps. Around $\tau = 0$ the data is superimposed with a signal that matches the ΔM_{ZT} signal shape. This is likely cross-talk between the two channels due to the ~ 2 orders of magnitude signal difference. The stray component is minimized by the scaling procedure in panel b, it is thus likely due to a mismatch in the two driving field polarities.

visibility. To highlight the curve shape, the black curve is $S(\Delta M_{\text{UDM}})$ smoothed with a 320 fs gaussian moving average filter. Some crosstalk from $S(\Delta M_{\text{ZT}})$ into the $S(\Delta M_{\text{UDM}})$ is especially visible at $\tau = 0$. As this signal can be minimized with the rescaling of the magnetic signals in panel b, it is likely that it arises from electric field amplitude mismatches. As $S(\Delta M_{\text{ZT}})$ and $S(\Delta M_{\text{UDM}})$ are almost two orders of magnitude different, even a small leakage signal becomes significant. The stray oscillatory torque response is superimposed with the expected step-like function and needs to be excluded in the data analysis procedure.

As a double check of the magnetic origin of the signals we present a comparison of the rotation and ellipticity measurements of $S(\Delta M_{\text{ZT}})$ (figure 6.5a) and $S(\Delta M_{\text{UDM}})$ (figure 6.5b). The polarization rotation and ellipticity changes both reflect the magnetic dynamics, albeit with different proportionality constants given by the magneto-optical constants of the material. The ellipticity data of both panels is scaled by a factor 0.65 to match the amplitude of the rotation signals. The rotation signal is flipped (-1) as the sign depends on the choice of the waveplate orientation (figure 6.3) in front of the Wollaston prism.

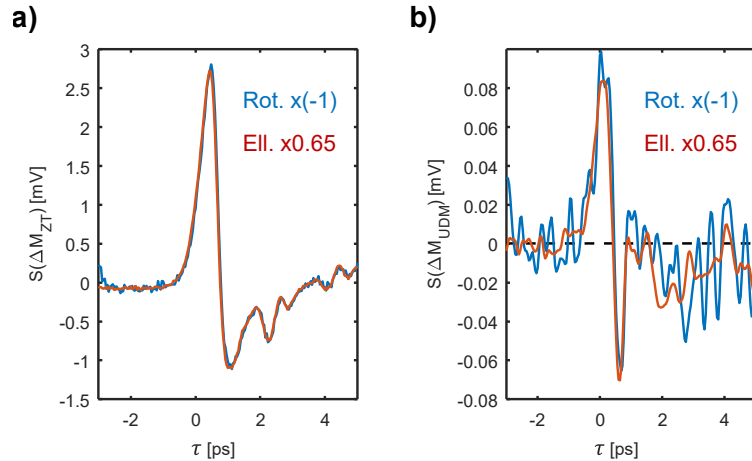


Figure 6.5.: Polarization rotation and ellipticity change **a)** The ΔM_{ZT} component detected in rotation (blue) and ellipticity (red) exhibit the same dynamics. The sign of the signal is determined by the choice of waveplate orientation in the experiment, thus the rotation data can be flipped. The ellipticity data is scaled by 0.65 for direct comparison. **b)** The ΔM_{UDM} signals are equally scaled and exhibit well matching behavior for rotation and ellipticity probing as well. This behavior confirms that the signals are indeed of magnetic origin.

Evidently, the magnetic dynamics captured are identical. The shape of the torque also matches the data presented in figure 6.4c.

Impact of THz mirror

Figure 6.6a compares the Zeeman Torque signal without a mirror (PW, red) to the signal with a mirror (SW, blue), measured at maximum THz pump field. The amplitudes of the ZT signals are doubled in the SW geometry as expected from the doubled B-field amplitude. The linear dependence of the Zeeman torque on the driving field is presented in fig. 6.6b. The datapoints are the integrated spectra of the ZT time traces like those from panel a. The dashed lines are linear guides to the eye emphasizing the doubling of the THz B-field in the presence of the mirror. The inset presents the SW/PW amplitude ratio for multiple THz field strengths. An average (black dashed line) of 1.97 ± 0.06 is reasonably close to the ideal factor 2 and confirms the validity of our approach as well as the highly metallic mirror operation at ≈ 1 THz. The color code for PW and SW geometries is upheld for the entire figure 6.6.

Figure 6.6c exhibits the smoothed (compare fig. 6.4c) $S(\Delta M_{UDM})$ for the SW and PW geometries measured at maximum THz pump fields. The stray torque background components exhibit an increase in the presence of a mirror. Comparing data $\tau < -1$ ps and $\tau > 2$ ps, the UDM step is evidently present in the PW geometry but not clearly visible underneath the stray torque component in the SW geometry. These observations align well with the expectations that the mirror should double the magnetic field and significantly reduce the electric field in the sample.

Figure 6.6d shows a THz electric field dependence of $S(\Delta M_{UDM})$. To extract the $S(\Delta M_{UDM})$

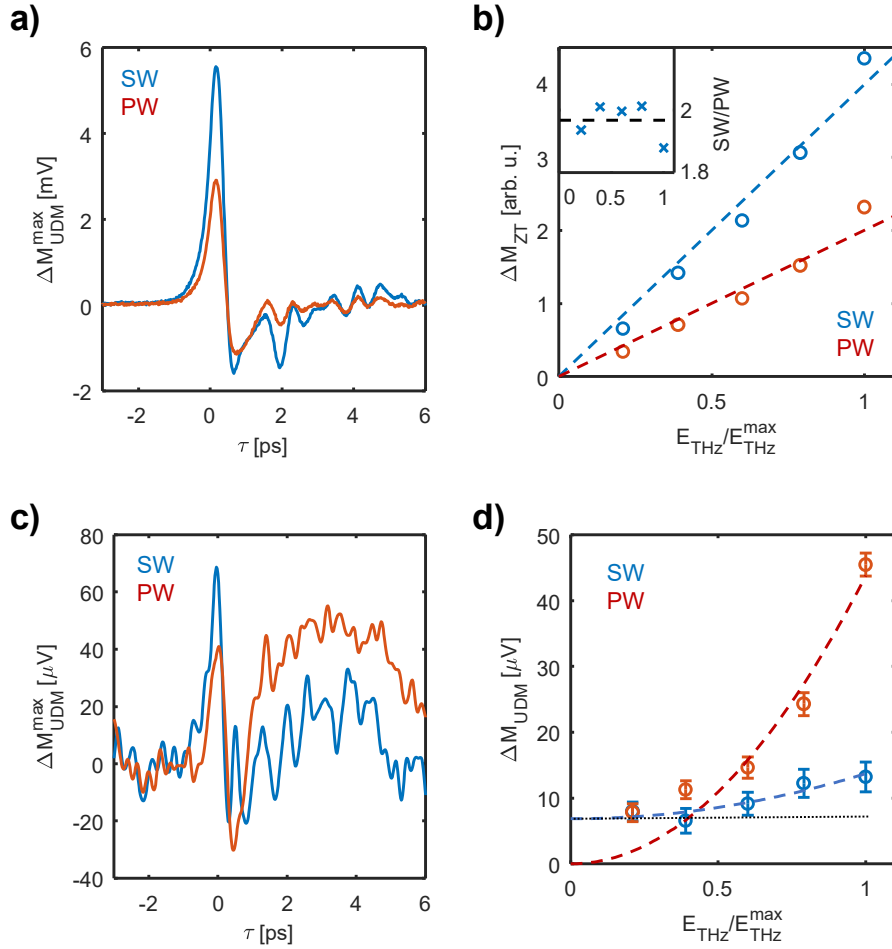


Figure 6.6.: Separating the action of E_{THz} and B_{THz} The data separation strategy in figure 6.4 yields $S(\Delta M_{\text{UDM}})$ and $S(\Delta M_{\text{ZT}})$. **a)** Typical $S(\Delta M_{\text{ZT}})$ for the standing wave (blue) and traveling wave (red) geometries. The data was recorded at maximal THz field strength. The SW signal is approximately twice the PW geometry signal. **b)** The $S(\Delta M_{\text{ZT}})$ signals are condensed to single datapoints by integrating over their spectrum. $S(\Delta M_{\text{ZT}})$ is presented for five field strengths each in both the SW (blue) and the PW (red) geometries. The dashed lines are linear guides to the eye with a factor 2 difference in the slope. **b inset)** The ratio of SW and PW $S(\Delta M_{\text{ZT}})$ components versus field. The average value (dashed line) was found to be 1.97 ± 0.06 , indicating highly metallic mirror operation at ≈ 1 THz. **c)** Typical $S(\Delta M_{\text{UDM}})$ for the standing wave (blue) and traveling wave (red) geometries. The data was recorded at maximum THz field strength. Both signals are affected by the ZT signal leakage (compare to panel a), that reflect the ZT amplitude enhancement in the SW geometry. Comparing signals for $\tau < -1$ ps and $\tau > 2$ ps the PW geometry exhibits a clear step while the SW geometry signal does not. The average of the data $\tau < -1$ ps is subtracted from the average of the data $\tau > 2$ ps to extract datapoints. The stray torque signal in the SW geometry produces a non-zero baseline for the extracted values. **d)** The field dependence of the SW and PW geometry $S(\Delta M_{\text{UDM}})$ reveals a strong signal suppression by the mirror. The dashed black dotted line is a guide to the eye, capturing the ZT signal background (as discussed in c). While the SW geometry exhibits a small field strength dependence, the PW geometry signals are clearly $\propto E^2$ above the noise floor (dotted line). The dashed lines are $\propto E^2$ guides to the eye. However, the signal increase in the SW geometry may also be due to the $\propto E$ nature of the ZT signal that causes the background.

step magnitude, unsmoothed data is averaged separately for $\tau < -1$ ps and $\tau > 2$ ps and the difference plotted. The blue symbols correspond to the SW geometry, where the THz E-field should be suppressed. Indeed, the SW data exhibits comparatively little dependence on the driving field. The non-zero signal offset (black dotted line) is due to the stray torque component discussed in the context of figure 6.6c. The error bars are the combined standard deviations of the averaged data per datapoint, thereby taking into account the added uncertainty from the stray torque signal. The red symbols correspond to the signal in the PW geometry. The signal exhibits a clear quadratic dependence on the driving field. The dashed lines are $\propto E^2$ guides to the eye. At low fields $S(\Delta\mathbf{M}_{\text{UDM}})$ is likely smaller than the baseline from the stray torque signal. Although the blue dashed guide to the eye suggests a quadratic electric field behavior of the SW geometry signal, it is equally likely that the field dependent increase arises due to the $\propto E$ dependence of the stray torque signal.

Figure 6.6 clearly demonstrates that we successfully separate the $\propto E$ and $\propto E^2$ signals linked to the THz magnetic and electric fields respectively. The presence of a mirror indeed increases the THz magnetic field in the sample by a factor ≈ 2 while largely suppressing the THz electric field in the sample.

6.5 Outlook and Conclusion

Future improvements

Most noticeably, this measurement suffers from the large disparity of $S(\Delta\mathbf{M}_{\text{ZT}})$ and $S(\Delta\mathbf{M}_{\text{UDM}})$ amplitude. The magnitude of $S(\Delta\mathbf{M}_{\text{UDM}})$ is mostly limited by the MCB effect itself. The MCB effect, responsible for probing the magnetization, is sensitive to the out-of-plane magnetization change in the sample. While the Zeeman torque tilts an in-plane magnetization out-of-plane and is thus easily detected by the MCB effect, the ultrafast demagnetization only creates a magnitude change of the out-of-plane magnetization component. To increase $S(\Delta\mathbf{M}_{\text{UDM}})$ one needs to increase the out-of-plane magnetization component, either with a stronger magnet or by growing films with out-of-plane magnetic anisotropy. However, typical thin-film samples only exhibit such an out-of-plane anisotropy if they are embedded in layers of different materials. These additional layers may give rise to other pump induced signals, similar to those in chapter 5. These additional effects complicate the clear separation of THz electric and magnetic field driven effects achieved in this work.

Alternatively, it would be fruitful to tilt the sample to non-normal probe incidence such that part of the in-plane magnetization was projected onto the propagation direction of the probe pulse. A sample tilt is strongly limited by the spatial confinements of the experiment, however, and cannot reach significant tilt angles in this work. Finally, it would be possible to probe the in-plane magnetization directly in a reflection probe MOKE measurement.

Alternate application

Additionally the discrimination of \mathbf{E}_{THz} and \mathbf{B}_{THz} driven effects in the sample, the local increase of the THz B field may be useful for studies of the magnetic interactions. For example, the presence of a mirror would lower the energy requirements of THz driven magnetic switching experiments while additionally suppressing the E-field induced demagnetization.

It may also be used as an extension to the measurements in chapter 5 to specifically disentangle the \mathbf{E}_{THz} driven spin-orbit torques from the \mathbf{B}_{THz} driven Zeeman torque.

Conclusion

In conclusion, we demonstrate that the presence of a mirror in contact with the sample indeed suppresses the \mathbf{E}_{THz} close to the mirror while doubling the \mathbf{B}_{THz} . The simultaneous detection of the Zeeman Torque and the ultrafast demagnetization in a suitable sample are presented as evidence and disentangled by their driving field dependence. The sample, a 6 nm thick CoFeB thin film, fulfills the requirements for good wave superposition at the mirror surface: it perturbs the THz-electric field only weakly as it is both much thinner than the THz penetration depth and $\lambda/4$ of the pump wavelength. The mirror materials ITO and AZO perform as excellent conductive THz mirrors while being transparent to the probe spectrum. The introduction of a mirror is an effective addition to THz pump-optical probe studies of complex, thin film materials and may even aid THz light induced magnetic switching experiments.

7 Optical suppression of THz writing in antiferromagnetic CuMnAs

Antiferromagnets (AFM) are a very promising alternative to ferromagnets for high-speed data storage applications. FMs and AFMs are magnetically ordered solids, capable of encoding information in the orientation of the magnetic order parameter, the magnetization \mathbf{M} or Néel vector \mathbf{L} respectively. Recently, THz light induced reorientation of the Néel vector \mathbf{L} in antiferromagnetic CuMnAs was demonstrated, raising hopes for future AFM magnetic storage. However, the intrinsically wide beam waist of THz frequency writing pulses ($\approx 1100 \mu\text{m}$) is too unspecific for memory applications with nanometer bit sizes. Here, we present a spatially selective optical suppression of the THz write operation without measurable influence on the previously set orientation of \mathbf{L} . The optical pump pulse photoexcites the semiconducting substrate, providing a transient conductive channel and electrical short for the THz write current in the AFM. The optical powers necessary to excite the substrate are far below the threshold for pure optical AFM resistance modulation. A model relating the substrate excitation to the effective reduction of the THz writing current in the AFM (similar to an ‘optical-gate transistor’) is presented. The orientation of \mathbf{L} is readily and non-destructively interrogated with electrical anisotropic magnetoresistance (AMR, section 2.3.5) measurements. The demonstrated concept has high technological relevance.

Parts of this chapter are under review at Phys. Rev. Appl. and the revised manuscript has been submitted.

7.1 Introduction

Recently, the first spintronic memory devices have reached the market [Gar18, Liu19]. Here, spintronic principles are utilized to influence the magnetization \mathbf{M} of a ferromagnetic layer. The orientation of the magnetic layer encodes the binary ‘0’ and ‘1’ states (figure 7.1). However, data encoded in the magnetic orientation of ferromagnets (FM) has an intrinsic rate limiting factor: the reorientation of the magnetization requires angular momentum exchange with the lattice [Bai20]. This limits the maximum FM memory switch rate to GHz frequencies [Sto06].

Benefits of antiferromagnets

Antiferromagnets (AFM) are magnetically ordered alternatives with potential for magnetic storage. The antiferromagnetic order parameter, the Néel vector \mathbf{L} , may be used to encode data in orthogonal orientations (figure 7.1). The two AFM magnetic sublattices (indicated as red and blue arrows) require equal and opposite angular momentum change for a reorientation of \mathbf{L} . Therefore, switching speed limiting angular momentum exchange

with the lattice is not required [Mae18, Bai20]. Additionally, antiferromagnets typically support direct coherent excitations of the magnetic lattice (zone-center magnons) in the THz range [Kam10].

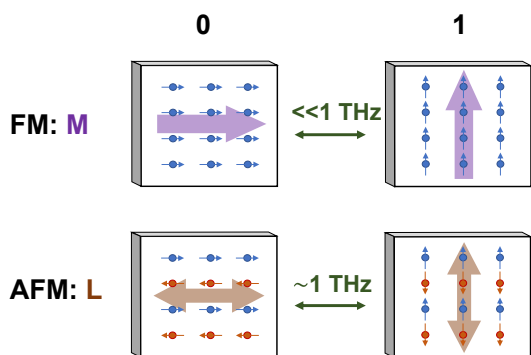


Figure 7.1.: Magnetic data encoding Binary data (0/1) can be encoded in the orientation of the magnetic order parameter in magnetically ordered solids (fat arrows). Typically, ferromagnets (FM) are used because the magnetization \mathbf{M} is easily accessible with external magnetic fields. Model antiferromagnets (AFM) have a magnetic order oriented along the Néel vector \mathbf{L} , while the magnetic sublattices (red, blue) cancel macroscopically, $M = 0$. AFM have both technological advantages and disadvantages. Most important for this study: the nominally equal and opposite AFM magnetic sublattices conserve angular momentum among themselves, allowing \mathbf{L} to reorient on THz timescales, while the FM magnetization is limited to GHz frequencies.

The perfect macroscopic cancellation of the sublattice magnetizations enable AFM to resist large magnetic fields (e.g. CuMnAs resists ~ 60 T) [Son18, Kaš20]. Therefore, without a stray magnetic field the packing density of magnetic bits is higher compared to crosstalk affected FM devices. However, without a stray field, manipulation of the magnetic order is challenging [Wan20b]. Several theoretical and experimental works have found evidence of a current generated, sublattice dependent staggered field in suitable crystal structures (CuMnAs, Mn_2Au) [Gom10, Ole18, Roy16, Wad16]. Such a staggered field creates equal and opposite torques on the opposed magnetic sublattices and thus rotates \mathbf{L} . However, heating the AFM leads to an incoherent switching process which must not involve the rotation of \mathbf{L} [Son18, Chi19, Dan21, God18, Jun16].

Electrical resistance modulation

Experimentally we detect an electrical resistance change due to anisotropic magnetoresistance (AMR, section 2.3.5), depending on the relative orientation of \mathbf{L} and the probe current direction [Wad16, Fin14]. The resistance change associated with current induced orientational change of \mathbf{L} has been seen both for trains of low frequency electrical current pulses [Wie12, Wad18, God18], as well as for pulse trains of THz radiation [Ole18]. Notably, the resistance change observed in [Ole18] accumulates with every THz writing pulse and therefore behaves like a multistate memory with potential for neuromorphic computation. However, the AFM domain structure is also observed to shatter at too large write currents [Jan20], changing the observed sample resistance without a rotation of \mathbf{L} . Similarly, heating the sample optically to its Néel temperature (when the antiferromagnetic order breaks down) has been demonstrated to produce comparable resistance changes [Kaš20]. The pump induced resistance states persist for multiple seconds at room temperature and much longer at lower temperature [Kaš20, MW19].

Note, however, that the exact resistance modulation mechanism is irrelevant for the validity of our findings. The study presented here only requires a charge current modified magnetic order in the AFM layer. Thus, we shall refer to a *THz current induced resistance modulation* relating to the experimental observable when presenting the data.

Optical control over currents in the AFM

Optical gating of THz radiation driven resistance modulation in AFMs may have technological relevance. In the following, we will present a scheme for functionalizing the sample substrate for ‘optical-gate transistor’ type gating of the THz write current, conceptually similar to the work in chapter 6. Optically exciting quasi-free electrons and holes in the semiconductor substrate [Ulb11, LH12, Shi08] will provide an electrical short for the write current in the AFM layer. Exciting carriers in a semiconductor with structured light profiles has been used to form and control transient metamaterials on semiconductors before [Oka10, Kam14]. We will see that the photoexcited substrate has potential for optical control of the THz write current in an AFM.

Free space optics are intrinsically limited to focus diameters of half the wavelength [Hec16]. For tight packed, nanometer sized, magnetic recording structures the typical THz focus ($\approx 1100 \mu\text{m}$) is too large. On the other hand, optical radiation with wavelengths of hundreds of nanometers can be structured with $\lambda_{\text{opt}}/2 = 200 \text{ nm}$ resolution. The finer resolution of structured optical beams may be useful to constrain the action of spatially broad THz pulses.

Here we will demonstrate that the optically excited carriers in the substrate indeed influence the THz writing process. Samples grown on semiconductors (GaAs, GaP) with different bandgaps will allow us to control how much optical energy is absorbed in the substrate. Additionally, optical radiation can be utilized to heat the AFM directly. We will investigate whether optical heating will modulate the magnetic anisotropy and enhance THz induced resistance modulation. Additionally, we will inspect if the AFM resistance state changes as a result of heating only the AFM.

7.2 CuMnAs samples

Generally, we investigate thin films of CuMnAs grown on semiconducting substrates and pattern etched into crosses. The same sample structure was used in both low frequency electrical, and THz frequency radiation driven experiments [Ole18]. The samples for this work were prepared by collaborators at the academy of sciences of the Czech Republic, K. Olejník, V. Novák and Z. Kašpar.

CuMnAs structure

Tetragonal phase CuMnAs is a member of the high temperature I-Mn-V Antiferromagnets with a $P4/nmm$ space group [Wad15]. It is a metallic antiferromagnet [Sid20] with rela-

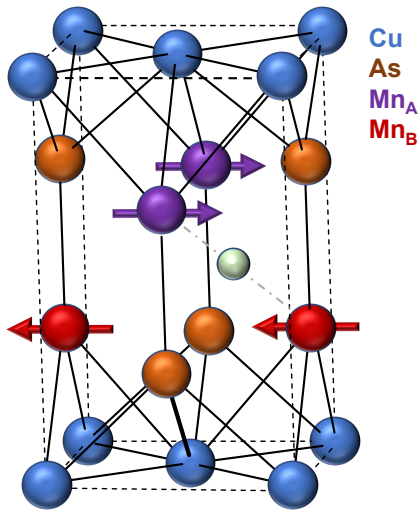


Figure 7.2.: CuMnAs structure Tetragonal phase CuMnAs is a model antiferromagnet where the magnetic Mn atoms form the two magnetic sublattices $\mathbf{M}_{a,b}$ (purple and red). The crystal structure is inversion symmetric about an interstitial site (green), while the Mn atoms are embedded in locally inversion symmetry broken environments. This very special inversion symmetry configuration allows for the appearance of staggered fields to reorient the magnetic order parameter \mathbf{L} . Redrawn from [Wad16]

tively high Néel temperature of $\approx 480\text{K}$ [Wad15] that allows for confident manipulation of the Néel vector $\mathbf{L} = \mathbf{M}_A - \mathbf{M}_B$ at room temperature. $\mathbf{M}_{A,B}$ are the sublattice magnetizations that are equal and opposite and cancel completely, leaving no macroscopic stray field $\mathbf{M} = \mathbf{M}_A + \mathbf{M}_B = 0$.

The crystal structure is presented in figure 7.2. Note that the crystal is inversion symmetric around an interstitial site (marked green) and that both magnetic sublattices form inversion partners. Importantly, the magnetic Mn atoms are in an environment of locally broken inversion symmetry. These special symmetry properties are prerequisites for a potential current induced staggered field switching [Wad16]. Bulk crystals (thickness > 10 nm) exhibit biaxial anisotropy in the ab plane, which is the plane that the bottom layer of Cu atoms of figure 7.2 lie in [Wad15].

The ab plane lattice constant of 3.820 angstrom matches the half diagonal of the GaP unit cell [Wad15], suggesting strain free growth on a typical semiconducting substrate. Indeed, CuMnAs is compatible with GaP, GaAs, and even Si [Kaš20, Ole17, Kri20], which is a promising prerequisite for efficient technological integration.

CuMnAs THz conductivity

The CuMnAs layers studied in this chapter have a thickness of 50 nm and a slightly differing sheet conductance depending on the semiconducting substrate. DC electrical characterization found sheet conductances of 40 mS on GaAs and 50 mS on GaP. To confirm the conductivity at THz frequencies our collaborator K. Geishendorf at Charles University, Prague has performed a THz transmission experiment on an unpatterned, 20 nm thick sheet of CuMnAs grown on GaP. The complex-valued conductivity measured for 0 - 2 THz was inferred with the Tinkham formula (figure 7.3) [Nád21]. A Drude model fit $\sigma(\omega) = \sigma(\omega = 0)/(1 - i\omega\tau_{el})$ yielded $\sigma(\omega = 0) = 7.5 \times 10^5$ S/m and electron scattering time $\tau_{el} = 4.1$ fs. The measured conductivity corresponds to a sheet conductance of approximately 40 mS in a 50 nm thick film on GaP and confirms the validity of the DC measured values at THz frequencies. The short scattering time likely benefits the efficient

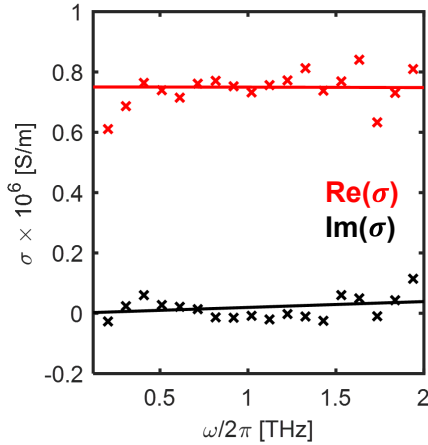


Figure 7.3.: THz conductivity THz conductivity of an unpatterned, 20 nm thick sheet of CuMnAs grown on GaP. The data was inferred from THz transmission data with the Tinkham formula [Nád21] and fitted with a Drude model, yielding $\sigma(\omega = 0) = 7.5 \times 10^5$ S/m and electron scattering time $\tau_{el} = 4.1$ fs in the frequency range of 0-2 THz. Measured by our collaborator K. Geishendorf at Charles University, Prague.

interaction of spin polarized electrons with the sublattice magnetization.

Sample design

Two different semiconductor substrate materials were chosen for their differing optical bandgap of 1.43 eV (GaAs)[Pan69, Bla82, Hei97] and 2.26 eV (GaP) [Pan69]. 50 nm of CuMnAs were deposited on a 500 μm thick semiconductor substrate (figure 7.4a). Additionally, a 5 nm Cr wetting layer and another 80 nm Au are grown on top to function as electrode material. The three layers are etched into a cross shape as shown in figure 7.4b. The Au contact pads (yellow) have lateral dimensions of 330 μm and 210 μm and are tapered on the inner third of the length. They serve both for electrical contacting and as antennas, amplifying the THz electric field in the cross center region by up to a factor ~ 20 (the antenna effect and the THz field distribution in the sample are discussed in [Ole18]). The center region of the cross (figure 7.4b, red circle and blow-up) is cleared of Au to be a region of uncapped CuMnAs. The side length of the central square region was varied from 2 μm – 4 μm . The lateral dimensions of this central region are referred to as device size in the following discussion.

Electrical contacts are necessary for the DC AMR detection scheme to determine the orientation of \mathbf{L} , as explained in section 3.4. For efficient integration into the measurement apparatus the samples were mounted and micro-bonded on contacted, standardized PCB boards by the sample growers.

Previous resistance modulation studies in similar samples

Earlier THz speed switching experiments performed by K. Olejník and T.S. Seifert have demonstrated THz radiation driven switching with identical samples and experimental set-up as is presented in this work [Ole18]. The authors interpreted the signals as THz current staggered field switching, however, the signal relaxation observed after THz excitation is more in line with a signal dominated by incoherent switching (domain fragmentation). Figure 7.5a shows the resistance signal build up as a function of applied THz pulses and

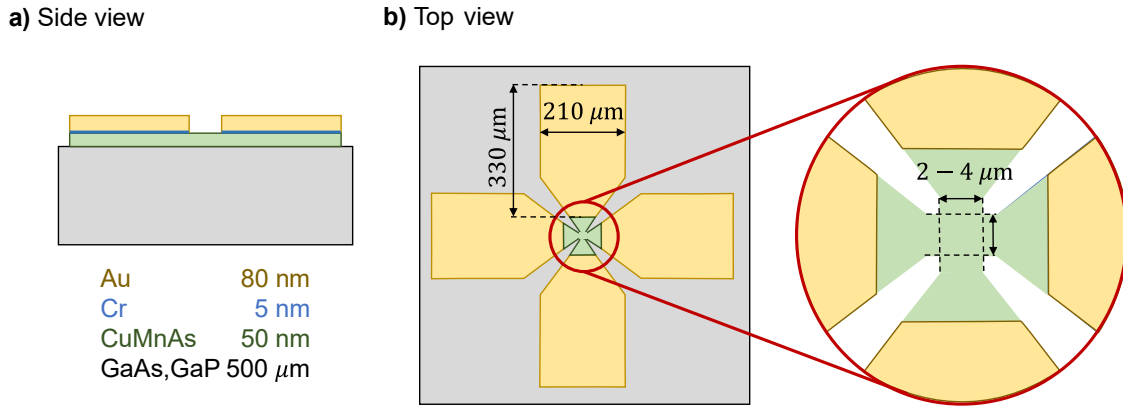


Figure 7.4.: **CuMnAs samples** **a)** Side view of the sample stack. 50 nm of the AFM CuMnAs (green) are grown on 500 μm thick, semiconducting substrates. The substrates are either GaAs or GaP. 5 nm Cr (blue) are deposited on the CuMnAs as a wetting layer before adding 80 nm Au (yellow) for the manufacture of electrical contacts. **b)** Top view of the sample. The sample structure is etched out of the sample stack. The Gold contact pads (yellow) are 210 μm by 33 μm with a taper in the last third of the length. In the center region, the Au and Cr layers are removed, leaving only the CuMnAs layer (green). **Blow-up** The center CuMnAs region is formed into a square of side lengths between 2 and 4 μm . This is the *device size* as the central region undergoes the switching operation. Electrical contacts for the DC readout scheme are bonded to the Au contact pads.

is reproduced from [Ole18] with permission from the authors. It is clearly seen that the current driven by a single THz pulse ($2.9 \times 10^9 \text{ A/m}^2$, 2 μm device on GaAs) induces a significant resistance change already. Figure 7.5b indicates how the two different THz polarity directions induce write currents through the cross structure of the device. \mathbf{L} will orient perpendicular to the current flow direction in the staggered field switching picture.

On the other hand, in slightly different CuMnAs samples, Kašpar *et al.* have observed that optical frequency excitation is sufficient to shatter the CuMnAs domain structure, resulting in a similar signal and decay [Kaš20]. However, they required significant optical powers to heat the AFM to its Néel temperature. T. Janda *et al.* [Jan20] observed in a separate work with yet another sample geometry that applying too strong low frequency writing currents ($1.3 \times 10^{11} \text{ A/m}^2$) will fracture the domain structure. This shows that the current densities in the sample needed for THz pulse excitation are very close to the domain shattering limit, especially considering the highly nonlinear power dependence of the THz switching effect [Ole18].

7.3 Experiment

The experiments in this chapter were performed in a THz and optical pump - electrical read-out scheme. In principle, a THz frequency light pulse induced a charge current in the AFM along the THz polarization direction. An optional, additional optical pump pulse excited the semiconducting substrate a certain pulse-pulse delay time τ later, illuminating both the AFM and the semiconducting substrate. A constant current AMR read-out scheme

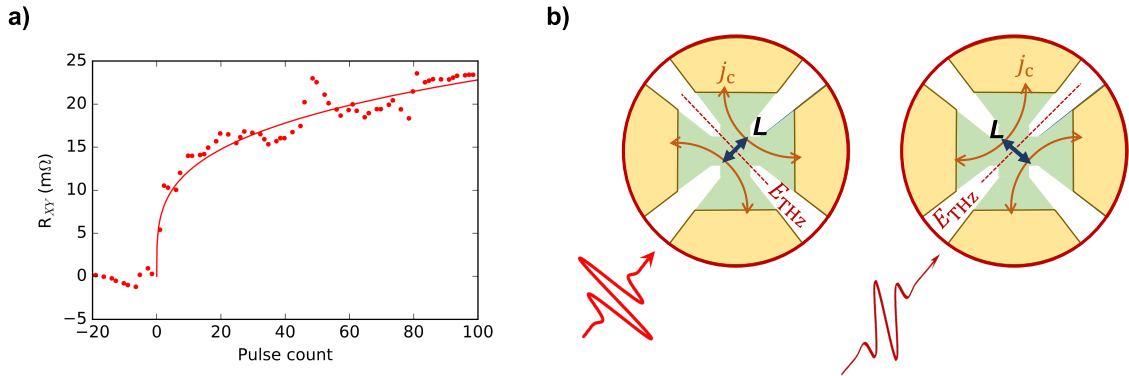


Figure 7.5.: THz speed staggered field AFM switching **a)** Shot-by-shot increase of the CuMnAs resistance due to the arrival of THz light pulses. Data reproduced from [Ole18] with permission from T. S. Seifert. **b)** The large circular cutouts are the same blow-up sketches as in figure 7.4 and are redrawn from the concept sketches in [Ole18]. The THz pulse (dark red) induces a charge current j_c along the polarization direction (dark red dashed line) which flows between the Au contact pads (curved arrows). The Néel vector (L , blue) is oriented orthogonal to the current direction.

continuously interrogated the orientation of L . The experimental concept is shown in figure 7.6 and the setup is described in great detail in section 3.3 and figure 3.3.

All experiments were performed at room temperature and under ambient conditions. THz currents in the sample were driven by two mutually orthogonal polarized THz pulses (figure 3.4) from a 1 kHz pulse train ($\pm 45^\circ$ to the original THz polarization direction, red circle and red/brown dotted lines in figure 7.6), similar to the measurement in [Ole18]. Each illumination phase was followed by a relaxation phase where the THz beam was shuttered with a motorized mechanical beam block. The beam block was placed behind the generation crystal, ensuring a constant heat load on the generation crystal. The THz pulse was focused on to the sample with a parabolic mirror to a spotsize of $\approx 1100 \mu\text{m}$ ($1/e$ diameter), with maximum THz fields of $\sim 0.5 \text{ MV/cm}$ (figure 3.5a) [Saj15]. The THz power was controlled by varying the laser pump power supplied to the Lithium Niobate THz source.

The sample state was interrogated continuously with a transverse electrical resistance measurement (contacts and circuits, figure 7.6). A constant current I_x of 0.5 mA per μm device center size was applied to one bar of the cross structure with a *KEITHLEY* constant current source. The voltage across the perpendicular contact pair U_y was measured with a *KEITHLEY* multimeter. The detection integrated the sample response for 0.5 ms per sample at a rate of 5 Hz. The detection process averaged the response over the entire AFM cross center region. The observable of the measurement was the transverse resistance $R_{xy} = U_y/I_x$, which corresponds to the AMR signal (equation 2.38).

An optical ('gating') pulse of either 400 nm or 800 nm wavelength (3.1 eV and 1.55 eV photon energy), with motorized power control and at a motorized pulse-pulse delay τ (up to $\pm 1 \text{ ns}$) with the THz excitation pulse was focused through a hole in the parabolic mirror

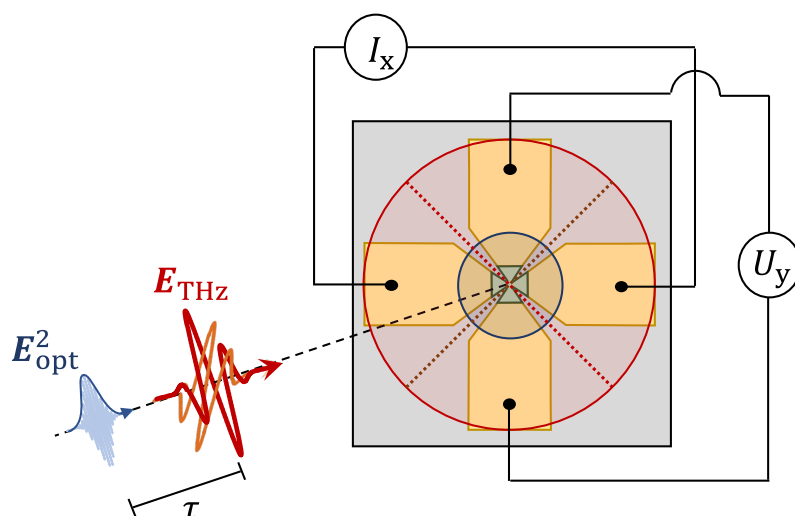


Figure 7.6.: THz pump - electrical probe The CuMnAs sample (green) is supplied with Au contact pads (yellow) and etched into a cross shape (figure 7.4). The Au contact pads are required for the AMR based electrical readout scheme. A constant current source I_x supplies a constant current to one leg of the cross. A Voltmeter detects the voltage U_y in the orthogonal cross leg. The observable of the measurement is the transverse resistance $R_{xy} = U_y/I_x$. The orientation of \mathbf{L} in the AFM will modulate the read-out voltage due to AMR (section 2.3.5). In the staggered field picture, the orientation of \mathbf{L} is set by the direction of \mathbf{E}_{THz} that is oriented along either of the dotted lines. The direction (polarization) of \mathbf{E}_{THz} is set with a motorized THz polarizer, oriented at $\pm 45^\circ$ to the initial THz polarization direction. A motorized mechanical shutter is used to block the THz pump radiation and observing the sample relaxation. An optional optical pump pulse (blue pulse with envelope) of either 400 or 800nm wavelength, delayed by the pulse-pulse delay τ with respect to the THz pump pulse, can excite carriers in the substrate material and protect the sample from the writing operation. The optical spot on the sample (blue circle) is much smaller than the THz spot (red circle) on the sample.

on to the sample to form spotsizes of $\approx 60 \mu\text{m}$ and $\approx 85 \mu\text{m}$ ($1/e$ diameter), respectively. It should be noted that only the 800 nm spotsize was determined with the pinhole method. The direct determination of the 400 nm spot size with the pinhole method was impossible because the maximal power was too weak. As discussed in section 3.3.2 we estimated the 400 nm spot diameter to be $\sqrt{2}/2$ times the 800 nm spot diameter from gaussian and nonlinear optics arguments.

Focal spot diameters and optical power

Estimating the 3.1 eV optical beam spot diameter (see section 3.3.2) has direct consequences for the presentation of the data. In the discussion below we will compare the sample response under the influence of the different optical pump pulse wavelengths (photon energies), that each have an associated focal spot diameter. Typically, one would specify the beam strength in terms of fluence, that is pulse energy per unit area, to compare the two beams fairly. However, if one spot diameter (= illuminated area) is more uncertain than the other, presenting data in terms of absolute fluence may suggest a false sense of comparability. Two methods to avoid this issue are either: normalize the fluence

values to the individual maximum value, or quote the beam strength in terms of power or pulse energy. Here we choose to present the data in terms of optical power, clearly separating the discussion of beam strength signal dependencies from the signal dependence on the optical photon energy (wavelength).

The focused beam diameters on the sample ($\approx 60 \mu\text{m}$, $\approx 85 \mu\text{m}$) are larger than the $2 \mu\text{m}$ - $4 \mu\text{m}$ AFM devices studied in this chapter, thus the devices experience only the center of the lateral beam profile. If one were to consider fluences, it would be prudent to specify the $1/e$ spot diameters as this definition determines the peak fluence at the center of a gaussian beam. The $1/e$ spot diameters are expressed as $2b$, where b is the radius of the gaussian beam profile at $1/e$ of the peak intensity.

7.4 Data and discussion

7.4.1 Data analysis procedure

We will inspect example data on the different timescales in figure 7.7 and follow the analysis procedure step by step. Figure 7.7 displays a delay scan between the THz excitation of $P_{\text{THz}} = 105 \mu\text{W}$ and an 800 nm , $P_{\text{opt}} = 2 \mu\text{W}$ gating pulse on a $3 \mu\text{m}$ device grown on GaAs.

Figure 7.7a shows the *modulation cycle*, the base unit of a measurement. The switching cycle is separated into four phases by the dashed vertical lines. The purple data line represents the continuous transverse resistance R_{xy} measurement vs. lab time (minutes). In the first segment, continuous THz excitation of one polarization direction ('THz on'), reduce the resistance. The state relaxes, in the next segment, when the shutter is closed ('THz off'). THz light polarized orthogonal to the first THz polarization state increases the resistance ('THz on, second direction'). Followed by another sample relaxation ('THz off'). The signal shape for this measurement cycle is identical for both GHz and THz excitation as observed by Olejník *et al.* [Ole18].

Figure 7.7b presents a larger time window. Four consecutive *modulation cycles* are measured for each set of external parameters. Data for real time $t < 612 \text{ s}$ (purple) shows four modulation cycles measured when the optical gating (800nm , 1.55 eV) occurred after the THz writing pulse arrived (pulse-pulse delay $\tau = -240 \text{ ps}$). Data for $t > 612 \text{ s}$ (green) shows data for four modulation cycles at the overlap of the optical gating pulse with the write pulse ($\tau = 0 \text{ ps}$). Data (indicated in black) are selected for both top and bottom resistance states and averaged (dashed lines). The difference of the top and bottom averages for each switching cycle is the *resistance modulation* ΔR . The signal adjusts to the new external parameters within the first cycle, thus, the first modulation cycle per set of four is ignored, the other three form a *datapoint*.

Figure 7.7c: more data around the excerpt presented in panel b, measured continuously in lab time t . The color coded data regions indicate measurement blocks of four modulation cycles per set of external parameters. The measurement presented in figure 7.7 is a pump-

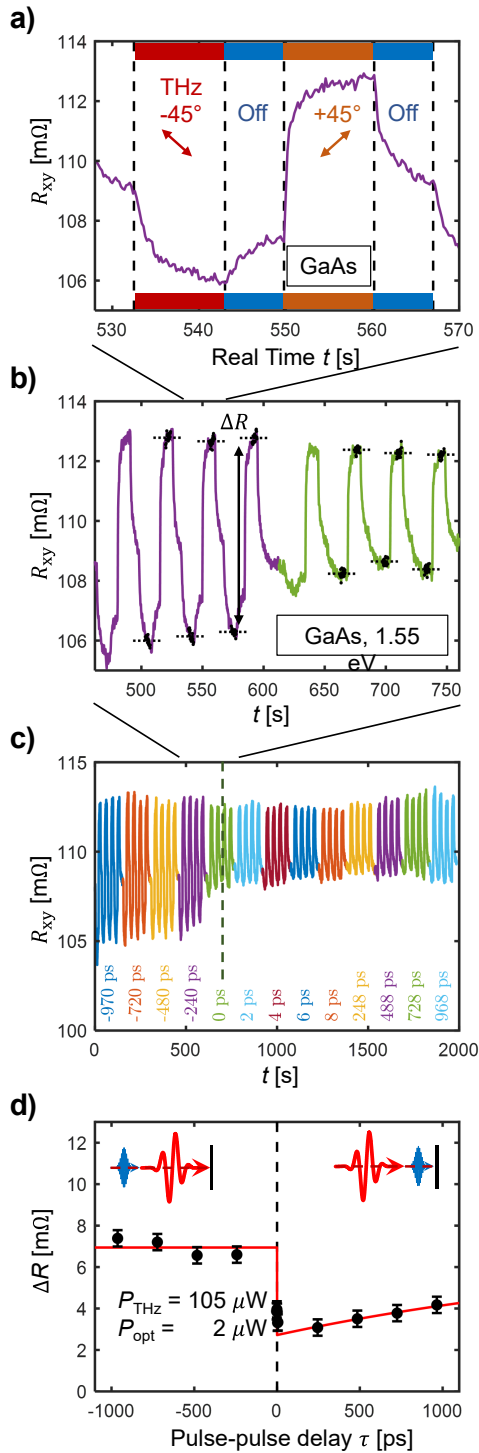


Figure 7.7.: Data analysis procedure The electrical detection continuously interrogates the transversal sample resistance R_{xy} , while the sample is driven into two magnetic orientation by alternating THz pulse polarization direction. The THz power is held constant at $P_{\text{THz}} = 105 \mu\text{W}$. **a)** The principle unit of such a switching cycle contains two phases (red/orange) where the continuous illumination with many THz pulses of orthogonal polarization (double arrows) orient the magnetic orientation in the sample. Following the excitation phase, the THz beam is shuttered (blue, 'off') and the magnetization relaxes again. Four such switching cycles are recorded for each set of external parameters. Note that the bottom axis is laboratory time, in seconds. **b)** Two sets of four switching cycles (color coded) are presented for a CuMnAs sample on GaAs, illuminated with $P_{\text{opt}} = 2 \mu\text{W}$ above-bandgap photon energy 1.55 eV. The data $t < 612$ s (purple) corresponds to the situation where the THz pulse leads the optical pulse by 240 ps. The data $t > 612$ s (green) is recorded for the THz and optical pulses arriving at the same time ($\tau = 0$). Multiple points are selected and averaged for each switched state (black dots, dashed average lines) and the resistance modulation ΔR is calculated for each of the last three switching cycles per set of four. The first state is affected by the starting conditions and thus omitted. **c)** The data of panel b within the context of the entire pulse-pulse delay scan. The pulse-pulse delay τ for each set of four switching cycles is indicated in the same color code while the continuous resistance measurement is plotted against laboratory time t . **d)** The average of the three ΔR of each set of four switching cycles is plotted against pulse pulse delay τ . The errorbars are calculated from the standard deviation of all ΔR for $\tau < 0$ to consider both short and longer range signal drifts. The two sketches indicated whether the THz pulse (red) or the optical pulse (blue) lead, with the pulse-pulse overlap indicated by the vertical dashed line. The red curve is a mono-exponential fit to the data with a decay time of 2.3 ns. This is discussed in section 7.4.2.

probe delay scan on a non-equidistant pulse-pulse delay time τ axis indicated above the data (matching color code). For $\tau < 0$, when the THz writing pulse arrives before the heating pulse, no large amplitude variation is observed. After $\tau = 0$, the signal amplitude (ΔR) reduces drastically and then slowly recovers.

In figure 7.7d the last three ΔR for each set of four in panel c are averaged to create a datapoint each. The standard deviation of all ΔR for $\tau < 0$ is presented as an estimate of the measurement uncertainty, capturing both short and longer term signal variations. Note that the lower axis is now in pulse-pulse delay time τ . The dashed vertical line indicates the temporal overlap of pump and gate pulse ($\tau = 0$). At $\tau < 0$ the THz pulse precedes the gating pulse, as indicated in the sketch. At $\tau > 0$ the heating pulse acts on the sample before the writing pulse arrives. The red curve is a mono-exponential fit to the data with a decay time of 2.3 ns. This data will be discussed below.

7.4.2 Role of the optical pump

The optical frequency pump pulse has many options to affect the measurement. Optically heating the AFM might soften the anisotropy and ease the THz resistance modulation. However, optically heating the AFM beyond the Néel temperature will destroy the magnetic order and cause a domain fracturing with accompanying sample resistance change [Kaš20]. A photon energy larger than the bandgap can also excite the semiconducting substrate (*above-gap excitation*), promoting valence band carriers into the conduction band and making the substrate transiently conducting. To investigate these possibilities and their effect on the resistance modulation, we present experimental data measured for different permutations of semiconductor substrates (different bandgap) and optical photon energy.

Results

Figure 7.7d, above, shows above bandgap excitation (1.55 eV) of a 3 μm CuMnAs device grown on GaAs (bandgap 1.43 eV). The THz excitation is held constant at $P_{THz} = 105 \mu\text{W}$ and the optical power at $P_{opt} = 2 \mu\text{W}$. For $\tau < 0$ the THz induced resistance modulation occurs before the arrival of the optical gating pulse and the signal exhibits no delay dependence. However, a step-like resistance modulation drop occurs at $\tau = 0$, recovering for $\tau > 0$ when the gating pulse precedes the THz writing pulse. The gating pulse induced change in ΔR is clearly larger than the measurement uncertainty. The ΔR recovery for $\tau > 0$ can be fitted with a function composed of a step and a mono-exponential decay (red line), yielding a time constant of 2.3 ns. The datapoints are the mean ΔR per last three switching cycles as described above. The error bars are the standard deviation of data ΔR for $\tau < 0$.

Above bandgap excitation of a 2 μm sample, grown on the larger bandgap (2.25 eV) semiconductor GaP, is achieved with a frequency doubled (400 nm) optical pump with photon energy $\hbar\omega = 3.1 \text{ eV}$.

Figure 7.8a shows multiple pulse-pulse delay scans with constant THz pump power ($P_{THz} = 590 \mu\text{W}$) and multiple optical pump powers P_{opt} ranging from 0 μW to 70 μW . Again, the datapoints are the mean ΔR of the last last three switching cycles per set as described above. The error bars are the standard deviation of data $\tau < 0$. Notably, at $P_{opt} = 0 \mu\text{W}$ the system exhibits no delay dependence within the error bars. Complete suppression of

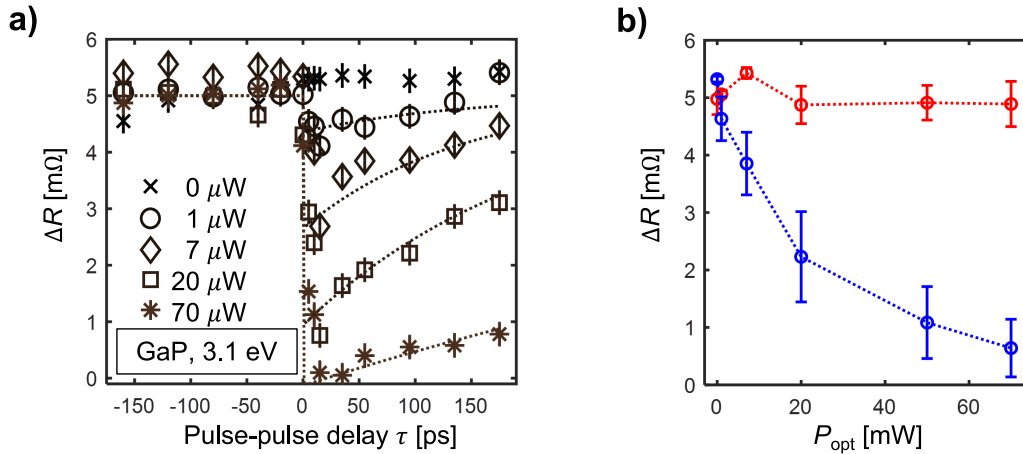


Figure 7.8.: CuMnAs on GaP Data for a 2 μm CuMnAs sample, grown on the larger bandgap (2.25 eV) semiconductor GaP. **a)** ΔR as a function of pulse-pulse delay τ for various powers of the optical pump beam from 0 μW to 70 μW , with constant $P_{\text{THz}} = 590 \mu\text{W}$. The optical beam was frequency doubled to 3.1 eV for substrate excitation. The errorbars are given by the standard deviation of all ΔR for $\tau < 0$. The dashed lines indicate mono-exponential fits to the data (main text). Notice, that at $P_{\text{opt}} > 0$ the shape of the curve is identical to that in figure 7.7d. **b)** Averages of the two data regions $\tau < 0$ (red) and $\tau > 0$ (blue) of panel a as a function of optical pump power. The average of data $\tau > 0$ exhibits a clear dependence on P_{opt} while the data $\tau < 0$ does not.

the resistance modulation is achieved for $P_{\text{opt}} = 70 \mu\text{W}$ at $\tau \approx 20$ ps. Again, a mono-exponential fit is applied to every curve, yielding a range of relaxation times from 140 ps to 800 ps. Figure 7.8b highlights the delay dependent signal change as a function of gate power. The red symbols are the average and standard deviation of all data points $\tau < 0$ presented in panel a, with no dependence on the optical pump power. The blue symbols are the average and standard deviation of all data $\tau > 0$ in panel a, when the gate pulse precedes the THz pulse, and exhibit a strong nonlinear dependence on the gate power.

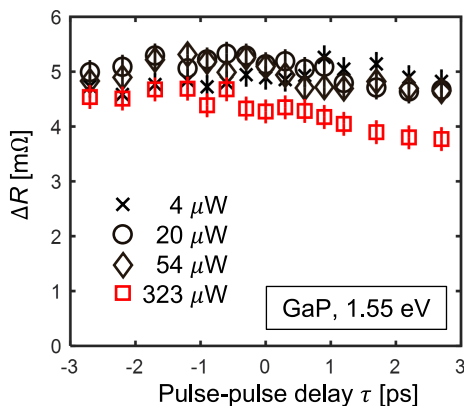


Figure 7.9.: Below substrate bandgap pumping on GaP The same sample as in figure 7.8a is illuminated with 800 nm optical light (1.55 eV) to avoid excitation of the substrate. Pulse-pulse delay scans are presented, with the optical powers indicated in the legend. The errorbars are the standard deviation of ΔR for $\tau < 0$. Note that the red squares indicate an optical power five times larger than that needed for complete suppression of the resistance modulation in figure 7.8a. The slight τ dependence of the red squares data may be due to two photon absorption in the semi-conducting substrate.

In figure 7.9, the experiment is repeated with below-bandgap, 800 nm (1.55 eV), optical pump photon energy on the same 2 μm sample. The sample resistance is modulated at a constant THz power of $P_{THz} = 590 \mu\text{W}$. As the substrate should not absorb below-bandgap photons, this measurement is expected to reveal the effect of heating only the AFM layer. Pulse-pulse delay scans for four different optical powers are presented. No large step like changes of ΔR are observed at $\tau = 0$. Note that the largest optical power (red symbols) is five times larger than the power that led to complete modulation suppression, in the same sample, with above bandgap excitation (figure 7.8a). While the data for the largest optical power exhibits a small ΔR decrease after $\tau = 0$, no clear increase of the resistance modulation signal is observed. The datapoints are the mean ΔR of the last three switching cycles per set of four, the error bars are the standard deviation of ΔR at $\tau < 0$.

Discussion

We initially set out to determine whether

- exciting the substrate can modulate the THz resistance modulation,
- optical heating of the AFM can reduce the magnetic anisotropy and ease resistance modulation,
- the AFM state itself is perturbed by the optical pump beam.

It is of general importance to the interpretation of this data that the lasers 1 kHz repetition rate allows for a complete thermalization (ns timescale) of the sample before the arrival of the next THz and optical radiation pulse pair (ms timescale). The long detection integration time (0.5 ms) probes a quasi-equilibrium state of the sample with a rate of 5 Hz and the signal buildup during THz irradiation is the accumulated effect of many pulses from the THz pulse train.

Above-bandgap pump photon energy. The optical excitation of the substrate produces a very clear pulse-pulse delay dependent signal. Signals for both 1.55 eV excitation of GaAs (1.43 eV bandgap) in figure 7.7d and 3.1 eV excitation of GaP (2.25 eV bandgap) in figure 7.8a exhibit constant signal levels for $\tau < 0$, step-like signal decrease at $\tau = 0$, and subsequent signal recovery. This signal shape is consistent with the interpretation of a substrate excitation: the transient substrate conductivity influences the THz current only if the substrate is photoexcited before the arrival of the THz pulse. Additionally, the modification of the THz current depends on the excitation density of the substrate and will decrease as the photoexcited carriers relax or diffuse. The τ -dependent resistance modulation can be fitted well by a combination of a step function and a mono-exponential decay (red lines in figure 7.7d, dashed lines in figure 7.8a).

As evident from figure 7.8b, the THz writing effect is not influenced by a conductivity change of the substrate after THz writing has already occurred (red symbols). However, it depends strongly on the excitation density of the substrate when THz pulse arrives (blue symbols). For a sufficiently large excitation of the substrate ($P_{opt} = 70 \mu\text{W}$, figure 7.8a) the resistance modulation can even be completely suppressed. We attribute this to

the conductivity of the substrate creating an electric shortcut for the THz induced writing current in the AFM. Alternatively, one can interpret the resistance modulation suppression as a consequence of the THz electric field (in the AFM) being suppressed by the existence of an adjacent conductivity, similar to the results in chapter 6. Note that this mechanism is expected to work for any (THz or lower frequency) current driven resistance modulation mechanism in the AFM. The transient electrical short concept is captured in a model in the next section, quantifying the THz writing current change as a function of optical power.

Evidence that the observed resistance modulation suppression is indeed related to the excitation of carriers in the substrate is provided by the relaxation times obtained for the mono-exponential fits. In general, the carrier recombination time in semiconductors depends sensitively on material parameters like the surface quality, defect density and compensation doping [See04]. The sample on GaAs (figure 7.7d) exhibits a relaxation time of 2.3 ns. This relaxation time falls into the typical range of carrier relaxation times in GaAs ranging from hundreds of picoseconds to nanoseconds [Nie19, Cad17, Ten09]. The excitation density dependent recombination times in GaP (figure 7.8a) span a range of 140 ps to 800 ps, in good agreement with values for photo-excited GaP [Alb17, Wah18, Lin15, Col13] and typical values observed in other large-gap semiconductors like ZnTe and 6H-SiC [Rub14, Saj14]. It should be noted that the resistance modulation has a strong nonlinear dependence on the THz electric field [Ole18] which likely influences the observed carrier relaxation times. Therefore, these relaxation times should be treated as order of magnitude estimates, in agreement with typical values for the material.

In terms of the 'optical-gate-transistor', the substrate excitation time determines the duration of the THz write protection and can be tuned with standard semiconductor methods like impurity concentration and growth temperature [Har93, Koz14]. Importantly, the photoexcited substrates relax completely until the next pair of pump pulses arrives (1 ms later).

Additionally, one may consider that the signal onset is not instantaneous either, although the τ resolution of the measurements presented here does not emphasize this. The optical pump pulse duration and the time required for the photoexcited carriers to form a Drude-type conductivity lead to a signal buildup around τ_0 . The formation of a Drude-type conductivity, depending on the excitation conditions, typically requires $\sim 50 - 100$ fs [Hub01, May14].

Below-bandgap pump photon energy. When the semiconductor bandgap is chosen to be larger than the gate photon energy, the radiation is only absorbed in the AFM layer. Corresponding resistance modulation data as a function of both gate beam power and pulse-pulse delay is presented in figure 7.9. If optically heating the AFM would soften the magnetic anisotropy, one could expect an increase in resistance modulation when the sample is pre-heated with the optical pulse ($\tau > 0$) compared to when the THz pulse arrives first ($\tau < 0$). However, we do not observe a τ -dependent signal increase.

Since we are considering saturated resistance states, we are sensitive to the total amount of affected domains. Possibly, the expected anisotropy softening does not motivate more

domains to switch in total, but rather influences how many domains a single THz pulse is able to alter. A possibility for future experiments is to detect and compare only the influence of a single THz shot.

Contrary to the expectation, a slight decrease of the resistance modulation is observed for $\tau > 0$ and at the highest optical powers in figure 7.9. This is likely due to a minor substrate excitation by nonlinear two photon absorption in the substrate. Indeed, one can estimate from the two-photon absorption coefficient of GaP [Wah18, Nat85, Gri19] that the highest optical power should excite the substrate slightly.

Optical excitation of the AFM. Considering that the effect of the optical pulse has decayed completely before the arrival of the next THz pulse allows us to draw conclusions on the integrity of the resistance state when gate power is absorbed by the AFM layer directly.

All data $\tau < 0$ (figures 7.7d, 7.8a, 7.9), when the THz resistance modulation is followed by a heating pulse, provide evidence that the resistance state is unperturbed by optical excitation. If the optical pulse would undo the action of the THz pulse immediately before, the ΔR for $\tau < 0$ would decrease depending on the optical power (see figure 7.8b, red data). Additional evidence is presented in figure 7.9 where the influence of the substrate is removed. The optical deposition of energy in the AFM layer did not alter the resistance state independent of pulse order, aside from a possible two photon absorption process at very large powers. In fact, tentatively considering the measured 800 nm spot diameter (85 μm) and the estimated 400 nm spot diameter (60 μm), the highest power below-bandgap data (red, figure 7.9) was exposed to a larger fluence than the fluence needed for complete suppression of the resistance modulation in figure 7.8a.

It can be concluded that the AFM resistance state is robust against pure optical excitation, within the range of optical power applied in this chapter. We estimate a deposition of 50 pJ/ μm^3 per pulse, increasing the sample temperature by a few tens of Kelvin by comparison with [Kaš20]. In contrast, an order of magnitude more energy per shot has been shown to alter the AFM resistance state directly [Kaš20], suggesting that the mechanism described here is confined to a relatively small power window.

Substrate excitation and the electrical measurement. Finally, the current based detection mechanism should be affected in the presence of a conducting substrate as well.

The probe current is expected to experience the same transient shunt resistance as the THz write current. However, the electrical short is present for only a few ns while the current flows constantly (different from the THz current pulse). The detection mechanism averages over 0.5 ms, thus the extremely short modulation duration of the read-out current is not expected to influence the signal.

The measurement presented in figure 7.7b,c reveals another interesting feature: the transverse resistance signal R_{xy} exhibits a different offset for $\tau < 0$ and $\tau > 0$. This behavior may originate from slightly broken spatial symmetries of the fabricated sample (non-orthogonal contacts), an asymmetric THz pump beam cross-section and an anisotropic CuMnAs conductivity [Kri20]. In consequence, both the excitation and detection process

is spatially non-symmetric, even without the optical gate pulse, leading to asymmetric signals from orthogonal currents. On top, there may be some slowly relaxing (tens of minutes) signal components of the THz resistance modulation [Kaš20]. However, the resistance modulation ΔR is very insensitive to the baseline shifts.

7.4.3 Two resistor model

The influence of the heating pulse is to excite quasi-free electrons and holes in the semi-conducting substrate. These conduction band electrons create a transient loss channel and rescale the THz write current in the AFM layer. In a simple picture, the AFM and the transiently excited substrate layer form a current divider.

The model

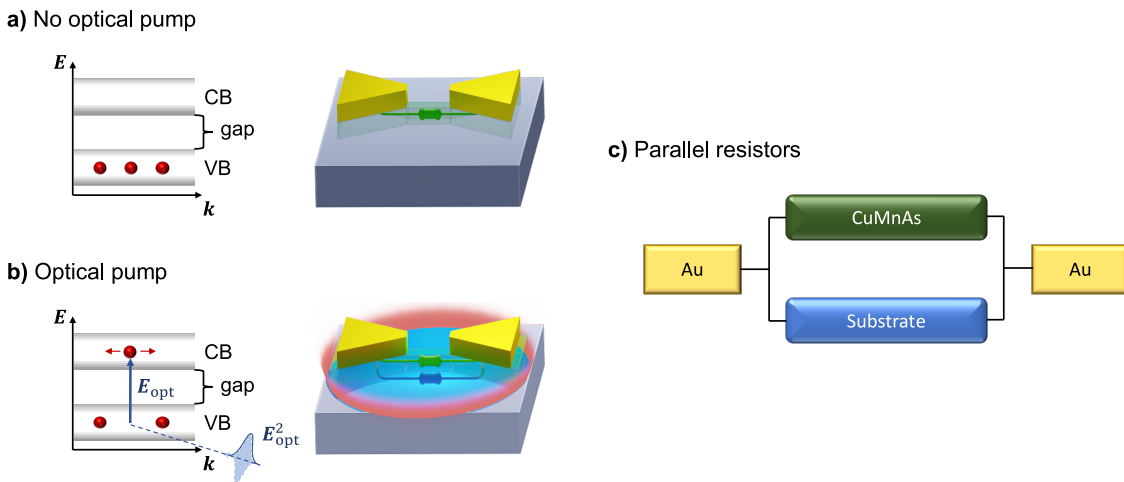


Figure 7.10.: Optical switching suppression **a)** Sketch of an unexcited semiconductor band-structure where the electrons (red) remain stationary in the valence band (VB). The bandgap separates the VB from the conduction band (CB). The 3D sketch of the sample geometry has one bar of the cross structure removed for clarity. In a simple picture, the THz writing current flows from the yellow gold contacts through the CuMnAs layer, indicated by a green resistor. **b)** When photons of energy E_{opt} greater than the bandgap excite the semiconducting substrate, they promote electrons from the VB into the CB. The semiconducting substrate becomes conductive for the lifetime of the excited electrons and provides an electrical 'shunt resistance' (blue resistor). **c)** The model circuit of the parallel resistances, a typical current divider.

Typically, the semiconducting substrate behaves like an insulator with no electrons in the conduction band. This situation is sketched in figure 7.10a, together with a 3D sketch of the sample. One bar of the cross structure is omitted for clarity. The THz current in the AFM is represented by the green resistor connecting the yellow Au contact pads. Upon photoexcitation (figure 7.10b) electron-hole pairs are excited in the semiconductor, populating the conduction band. The current flowing in the transiently conducting substrate is represented by the blue resistor.

The substrate resistance drops (conductivity increases) proportional to the excitation density of the semiconductor and the two conduction channels behave like parallel resistances and form a classical current divider (figure 7.10c). In consequence, the THz write current in the AFM layer is reduced by a factor C that depends on the ratio of the two conductances: both the AFM conductance G_{AFM} and the transient substrate conductance $\Delta G_{\text{S}}(P_{\text{opt}}, \tau)$.

We consider the AFM thin film as an infinitely extended layer sandwiched in between two half-spaces of substrate (S) and air (A). To relate the incident THz field to the field inside the AFM, we calculate a substrate conductivity dependent transmission coefficient with the Tinkham formula [Nád21, Neu18].

$$t(\Delta G_{\text{S}}) = \frac{E_{\text{AFM}}(\Delta G)}{E_{\text{inc}}} = \frac{2n_{\text{A}}}{n_{\text{A}} + n_{\text{S}} + Z_0 G_{\text{AFM}} + Z_0 G_{\text{S}}} \quad (7.1)$$

with the free-space impedance $Z_0 \approx 377 \Omega$, and the refractive indices for air and unexcited substrate, n_{A} and n_{S} .

The use of the Tinkham formula is justified because the THz field is approximately constant over the AFM thickness and the excited region. Since the calculation requires some of the following equations, the estimate of the THz skin depth in relation to the expected thickness of the transient conducting substrate layer will be presented in appendix B. The THz skin depth is found to be $> 1 \mu\text{m}$, larger than the combination of AFM thickness (50 nm) and gate penetration depths of 750 nm (1.55 eV, GaAs) and 116 nm (3.1 eV, GaP).

At a constant incident THz field, the transmission coefficient depends on the transient conductance of the photoexcited substrate $\Delta G_{\text{S}}(P_{\text{opt}}, \tau)$, determined by optical gate power and pulse-pulse delay. Neglecting charge recombination (i.e. the situation directly after excitation, $\tau \approx 0$) the transient substrate conductance is related to the number of optically excited photons $N_{\text{opt}}(P_{\text{opt}})$ absorbed per gate pulse and substrate area, depending on the optical power P_{opt}

$$\Delta G_{\text{S}}(P) = e\mu N_{\text{opt}}(P_{\text{opt}}) = e\mu \left(\frac{PT}{f\epsilon \cdot \pi 2b^2/4} \right)_{\text{opt}} \quad (7.2)$$

where μ is the mobility of photogenerated electron-hole pairs in the substrate and e the electron charge. $2b_{\text{opt}}$ is the optical beam focus $1/e$ diameter (b is the radius of the gaussian beam at $1/e$ of the maximum intensity), ϵ_{opt} the photon energy, and f the 1 kHz laser repetition rate. The optical beam transmission T_{opt} through the AFM layer is calculated from the Airy formula, as described in appendix B, with the refractive index values of the individual sample layers from table 7.1.

However, the expression for $\Delta G_{\text{S}}(P)$ contains multiple parameters that carry uncertainties. Experimentally, the beam waist $2b_{\text{opt}}$ has a certain uncertainty. Additionally, the carrier mobility μ is taken from literature rather than measured for the samples at hand. To capture the essential physics, we reduce equation 7.2 to a single proportionality constant $B = e\mu T_{\text{opt}} / (f\epsilon \cdot \pi b^2)_{\text{opt}}$

$$\Delta G_S(P) = B \cdot P_{\text{opt}} \quad (7.3)$$

Finally, these considerations can be combined to define a proportionality constant to relate the THz E field in the sample for an excited and unexcited substrate $E_{\text{AFM}}(\Delta G_S) = C \cdot E_{\text{AFM}}$

$$C = \frac{E_{\text{AFM}}(\Delta G_S)}{E_{\text{AFM}}(0)} = \frac{t(\Delta G_S)}{t(0)} \approx \frac{1}{1 + \Delta G_S / \Delta G_{\text{AFM}}} \quad (7.4)$$

Where the last approximation considers that $Z_0 G_{\text{AFM}} \approx 15$ is much larger than $n_A + n_S \approx 4.6$. As the data shows, the direct gate photon influence on the AFM layer is negligible. This model can now be employed to fit experimental data.

Comparing model and data

To apply the model to measured values of C , the proportionality constant $E_{\text{AFM}}(\Delta G_S) = C \cdot E_{\text{AFM}}$ is reformulated in terms of optical power ($P \propto E^2$). C^2 describes the effective power equivalent to the photoinduced reduction of the THz write current in the AFM, $P_{\text{THz}}^{\text{eff}}(\Delta G_S)$, in relation to the total current available without optical excitation $P_{\text{THz}}(0)$

$$C^2 = \frac{P_{\text{THz}}^{\text{eff}}(\Delta G_S)}{P_{\text{THz}}(0)} \quad (7.5)$$

To calculate C^2 , two measurements were performed on devices grown on GaAs and GaP with appropriate gate photon energy for substrate excitation.

Let us first discuss a 4 μm device on a GaAs substrate, interrogated at a fixed pulse-pulse delay $\tau = 15$ ps (optical leading THz). Figure 7.11a depicts the modulation amplitude ΔR as a function of THz power (red data and axis). ΔR exhibits a strong nonlinear dependence on the THz pump power, as expected from [Ole18]. For later data extraction, the THz power vs. ΔR curve is fitted with $P_{\text{THz}} = a_1 \cdot \Delta R^{a_2} + a_3$ with fit parameters a_1, a_2, a_3 (red line). In a second measurement (black data) the THz power is held constant at $P_{\text{THz}} = 426 \mu\text{W}$ and the sample is illuminated with P_{opt} above bandgap (1.55 eV) radiation. $P_{\text{opt}} \approx 1.8 \mu\text{W}$ are sufficient to quench the resistance modulation almost completely. The factor C^2 is extracted from the data with an assignment policy indicated by the blue arrows in panel a, relating ΔR for P_{opt} to an effective $P_{\text{THz}}^{\text{eff}}(\Delta G_S)$ with the THz power fit. The result is displayed as blue circles in panel b. The uncertainties were estimated from the uncertainties of the optical power dependence (black, panel a) and the THz power fit (red, panel a), neglecting the smaller THz power uncertainty.

The strongly nonlinear nature of the THz writing mechanism is evident as 70% of the maximum THz power correspond to almost complete resistance modulation suppression (data panel b at $P_{\text{opt}} \approx 1.8 \mu\text{W}$ with $C^2 \approx 0.7$, comparison a and b). The red curve in panel b is the result of a fit with the model, described above, fitted to the data with values

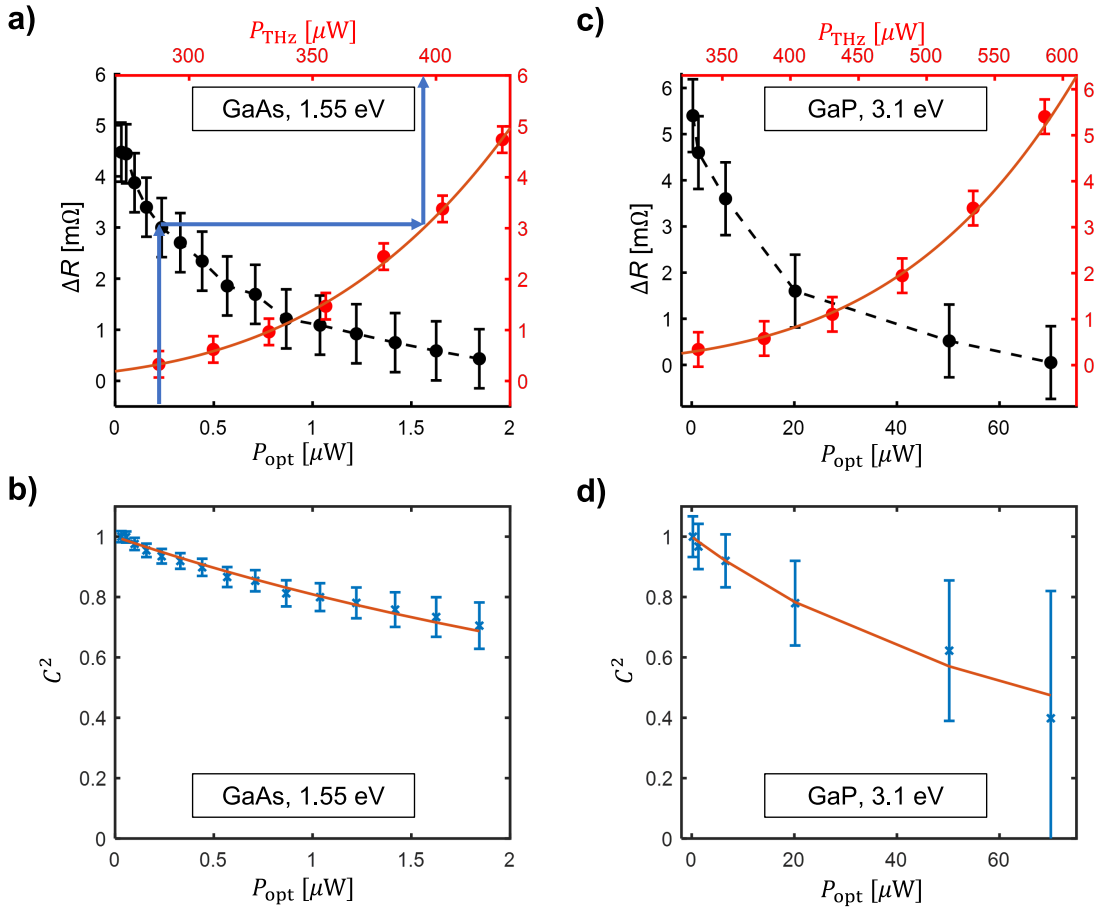


Figure 7.11.: Applying the model a) CuMnAs on GaAs with 1.55 eV above bandgap optical pump. The resistance modulation ΔR has a nonlinear dependence on the THz power (red points versus top axis) that is fitted with a function of the form $P_{\text{THz}} = a_1(\Delta R)^{a_2} + a_3$ with fit parameters a_1, a_2 and a_3 . To observe the influence of exciting the substrate, the THz power is held constant at $P_{\text{THz}} = 426 \mu\text{W}$ while the optical power is increased (black points) until the resistance modulation is nearly suppressed. C^2 expresses the rescaling of the THz current in the AFM by matching the resistance modulation ΔR achieved for a certain P_{opt} to a corresponding P_{THz} that would achieve the same ΔR . This mapping is indicated by the blue arrows. **b)** C^2 extracted from the data in panel a (blue circles) compared to the fitted model result for the values in table 7.1 and fit parameter B . The uncertainty of the black data in panel a was propagated with the fit to the red THz data, neglecting the uncertainty of the THz data itself. Notice that ΔR is quenched almost completely for 70% ($C^2 \approx 0.7$) the maximal THz power, highlighting the nonlinear behavior of the resistance modulation with respect to the THz power. **c) + d)** The corresponding analysis for CuMnAs on GaP with 3.1 eV above-bandgap optical pump.

from table 7.1 and fit parameter B (equation 7.3).

The same experiment and analysis was performed for a $2 \mu\text{m}$ device on GaP with above bandgap gate photon energy 3.1 eV at a pulse-pulse delay of $\tau = 35$ ps (optical leading THz), shown in figure 7.11c. For the gate power dependence, the THz power was held constant at $P_{\text{THz}} = 590 \mu\text{W}$. The THz power scan is fitted like before and the values C^2 extracted (blue symbols panel d). Again, the red curve in panel d is the result of a fit with the model, using values from table 7.1 and the fit parameter B (equation 7.3).

Table 7.1.: Values required to apply the model, figure 7.11. T_{opt} and $2b$ for GaP are estimates derived from other values in the table, as described in the main text.

Parameter	unit	GaAs	GaP	Source
n_S @ 1 THz		3.6	3.3	[Heb04, Gri90, Vod08]
Bandgap	eV	1.43	2.26	[Pan69, Bla82]
Gate photon energy ϵ_{opt}	eV	1.55	3.1	
$n_S(\epsilon_{\text{opt}})$		3.68+0.09i	4.20+0.27i	[Asp83]
$n_{\text{AFM}}(\epsilon_{\text{opt}})$		3.7+2.0i	2.5+2.2i	[Vei18]
T_{opt}	%	14	2.7	
G_{AFM}	mS	40	50	[Ole18], fig. 7.3
$2b_{\text{opt}}$	μm	85	60	

The fit results $B = 8500$ S/W (GaAs) and $B = 570$ S/W (GaP) from the fit of C^2 as a function of P_{opt} capture the simultaneous uncertainty of the carrier mobility μ , the estimated optical transmission T_{opt} and the beam waist at the sample $2b$. Using the measured beam diameter of $2b = 85 \mu\text{m}$ for 1.55 eV photon energy on GaAs, together with the relevant parameters of table 7.1, we calculate a mobility of $\mu = 5300 \text{ cm}^2/(\text{Vs})$ for the photoexcited electrons and holes in the semiconductor. This value corresponds well to typical electron mobilities in photoexcited undoped GaAs [Alb17, Mag20, Hey06, Rod75, Sti70, Bla82].

The same analysis for $B = 570$ S/W obtained for 3.1 eV photoexcitation of GaP, together with the estimated value $2b = 60 \mu\text{m}$, yields $\mu = 1800 \text{ cm}^2/(\text{Vs})$, which is at odds with the upper bound in literature ($\mu = 400 \text{ cm}^2/(\text{Vs})$) reported for photoexcitation of undoped GaP [Alb17, Rod75, Wah18, Cas69, Kao83]. Note, however, that both $2b$ and T_{opt} are estimates in the case of 3.1 eV excitation, possibly with significant uncertainties of the order of 50%. We therefore consider the carrier mobility extracted for a GaP substrate as reasonable.

Thus, considering the AFM and the photoexcited substrate layer as parallel conductances is supported by the result of the model fits.

7.4.4 Tentative comparison to existing technology

The optical control over the THz write current in the AFM, similar to an ‘optical-gate transistor’, may be of relevance for future AFM based data storage applications.

While the THz write spot is large, the optical excitation can be spatially structured on the nanometer scale to protect the illuminated regions from THz current writing. The spatial selectivity is constrained by how well the optical radiation can be focused. Indeed, there are already data storage technologies (heat assisted magnetic recording, HAMR) that rely on the optical heating of a, magnetically hard, ferromagnetic recording medium. Thus, laser diodes with appropriate power and focal spots for substrate excitation are already

available [Zho18, Cha09].

Importantly, we do not claim that all-optical THz speed AFM memory is demonstrated in this work. Especially the lifetime of the AFM state here is incompatible with long term magnetic storage, as the AFM states decay naturally within minutes. Currently, one could only imagine AFM memories close to processors where more volatile memory is typically employed, and even then there still are significant technological challenges. However, the gating method presented here has the potential to become relevant as a component of AFM memory in the future. The write current suppression is independent of the storage medium and relies only on the presence of laser light of sufficient power and photon energy to excite the substrate. We will now compare the energy requirement to protect a 50×50 nm area ('bit') from THz writing, with the sample conditions of this study, to the energy required to allow magnetic writing of a similar bit in HAMR.

In HAMR, the storage medium is a ferromagnetic surface with large magnetic anisotropy that is exposed to a large-area writing magnetic field (similar to the broad THz pump spot of this work) not strong enough to overcome the magnetic anisotropy. The optical power from a solid-state laser diode, focused with a nanoantenna to dimensions like 50×50 nm, softens the magnetic anisotropy by heating the ferromagnetic medium directly [Cha09]. This softened area is subsequently switched by the applied magnetic field while the surrounding area remains in its previous magnetization state. The size of the bit is determined by the spatial extent of the heating pulse and the speed at which the FM layer cools, 'freezing' the set state.

We estimate, with values from Ref. [Zho18], that 33 pJ of power per bit area of 50×50 nm are deposited for anisotropy softening in the geometry of Ref. [Cha09]. Our experiment requires only ≈ 0.5 fJ for the protection of the same size area. The temporal protection duration, and thus the write rate, is limited by the carrier lifetime in the substrate, which can readily be tuned by industry standard methods like doping [See04].

Although we observe a drastic decrease in the energy required per bit for AFM protection compared to HAMR, the energy savings are likely not significant. While HAMR only softens individual bits when writing data, the entire area around the bit of interest must be protected from the writing pulse when gating optically. Thus, quasi the entire area of the THz pump spot must be illuminated save the bit intended to switch, increasing the power demand per writing operation significantly. However, the necessary technology for optical gating is currently available.

7.5 Conclusion

In this chapter, we have demonstrated the functional integration of AFM and semiconductor properties into an 'optical-gate transistor' like scheme, with complete optical suppression of the THz write current in the AFM material. Significantly, the photoinduced bypass channel suppresses any THz current driven resistance modulation, irrespective of the debated signal origin. We therefore offer no additional insights into the nature of the AFM resistance modulation effect. However, we observe a complete suppression of

the THz resistance modulation for an order of magnitude less optical energy than that required for the direct optical resistance modulation observed by [Kaš20].

A model, successfully capturing the influence of the photoexcited substrate on the THz write current with the scaling factor C , expresses the write suppression in a parallel conductance scheme. This model successfully captures the drastically different optical powers needed for THz write suppression in CuMnAs on GaP and GaAs. In both cases, the write protection duration is dependent on the substrate carrier recombination time, which can be tuned with standard semiconductor methods.

Contrary to expectations, we find no evidence that the AFM magnetic anisotropy is modified by ultrafast optical gating. This is advantageous, as it indicates that the optical power range necessary for complete quenching of the THz resistance modulation does not destroy the AFM state, an important prerequisite for potential future AFM memory application. Indeed, the optical gating of the THz write operation has potential application for low power masking of high density antiferromagnetic memories with feature sizes of 200 nm, determined by the limits of free space optics.

8 Summary

The work presented in this thesis extends the experimental possibilities of nonlinear THz spectroscopy with normal incidence transmission magneto-optical probing. These improvements are put to immediate use, demonstrating optical gating of THz resistance modulation in antiferromagnets and investigating spintronic effects at THz frequencies, respectively.

The workhorse of this study is a tilted pulse front Lithium Niobate source (chapter 3), producing THz pump pulses from the output of an amplified laser system. The transient sample magnetization was probed either optically, or with a contacted electrical measurement. In chapter 7 an additional optical pump beam was added.

Advancing the magneto-optical probe

Magneto-optic (MO) effects are widely employed to determine the sample magnetization optically, both with probe light reflected from or transmitted through the sample. However, detecting all vector components of the sample magnetization typically requires multiple measurements with significant changes to the setup or involved data analysis. Experiments overcoming these limitations have been demonstrated in reflection geometry, offering access to all components of the vector magnetization by changing only the incident probe polarization [Fan16, Cel19]. However, a similar experiment for transmission probing was unavailable until now.

In chapter 4 we show that the combination of magnetic circular birefringence (MCB) and magnetic linear birefringence (MLB) enables the simultaneous determination of in- and out-of-sample-plane magnetization components in magnetic thin films, interrogated optically at normal incidence and in transmission. This experimental geometry significantly reduces the complexity of the measurement. While the MCB has no dependence on the angle between probe polarization and the in-plane magnetization θ , the MLB is $\propto \sin(2\theta)$. Measuring the magnetically saturated sample response as a function of θ reveals the maximum MLB signal amplitude, encoded in the MLB coefficient b . A multi-parameter fit reliably extracted b from measurement data. The MLB coefficient b serves as a reference to normalize pump-induced MLB signals.

Investigating spintronic principles at THz speeds

In chapter 5, the combined measurement of MCB and MLB was put to use, studying spintronic effects at THz frequencies. Thin film multilayers, composed of ferromagnets (FM) and nonmagnetic heavy metals (NM), were investigated at normal incidence and in transmission geometry, allowing for a clean separation of the vector components of the pump induced transient magnetization. A NM layer with large spin-orbit coupling, like Pt, converted THz electric field driven charge currents in the sample plane into spin currents

flowing into the depth of the sample. The spin magnetic moment injected into the FM layer altered both the magnitude and orientation of the magnetization. Additionally, the direct interaction of the THz magnetic field with the FM magnetization was observed in the form of a Zeeman torque.

In principle, the NM layer served as a spin current source while the FM magnetization detected spin magnetic moment transferred across the FM|NM interface. In-plane and out-of-the-sample-plane magnetization components were recorded simultaneously with MLB and MCB, respectively, and separated by comparing measurements with different initial probe polarizations.

In our experiment, the MCB effect was sensitive to the out-of-sample plane magnetization change and, thus, primarily sensitive to torques on the magnetization. The Zeeman torque (ZT) signal was isolated and provided a measurement of the THz field evolution in the sample. Evidence for a field like spin orbit torque (FL-SOT) was found as well. While the signal symmetry under layer reversal conformed with FL-SOT, the FL-SOT signal did not have the expected ZT-like time evolution. The ZT signal is the accumulated effect of the THz magnetic field on the sample, with a 'memory' lasting for the entire pulse duration. However, the FL-SOT signal did not accumulate in the same fashion, suggesting that the spins injected into the FM relax within the measurement uncertainty of ~ 100 fs.

A spin injection into the FM requires a spin accumulation at the NM|FM interface. A component of the injected spin magnetic moment was oriented along the FM magnetization, changing the magnetization magnitude. The MLB signal was sensitive to this change in magnetization magnitude, revealing that the spin accumulation and injection process are indeed active at THz frequencies. This is a major result of the thesis, nurturing hope for THz frequency spintronic applications.

Furthermore, the spin transfer across the interface was confirmed with interlaced conducting and insulating layers. A comparison to the THz field evolution in the sample additionally revealed that the spin accumulation signal involved spins close to the interface, relaxing within ~ 100 fs of entering the FM layer.

It was also attempted to quantify the amount of injected spins from the MLB coefficient found in chapter 4. However, the obtained result did not match for polarization rotation and ellipticity probing, as would have been expected. Furthermore, another, yet unexplained, signal component was superimposed on the spin accumulation signals obtained for ellipticity probing of the spin accumulation but could not be resolved in for polarization rotation probing. Further investigation of these findings, together with isolating the damping-like spin-orbit torque signal, is left for future research.

Modifying the THz pump fields in the sample

Nonlinear THz spectroscopy was augmented in chapter 6, adding the ability to modify the amplitude ratio of the electric and magnetic THz fields in thin film samples. This has profound consequences, for example for the study of material resonances in the THz frequency range, revealing if the observed signals originate from the THz electric or magnetic

field.

To modify the amplitude ratio of the THz magnetic and electric fields in the sample, the THz pump beam was reflected from a near-perfect conductor in contact with the sample. Upon reflection from a perfect conductor with Fresnel reflection coefficient $r \approx -1$ the THz electric field polarity flips, forming a standing wave node in front of the mirror even for broad band THz pulses. At the same time, the THz magnetic field was shown to superimpose and form an anti-node, doubling the available THz magnetic field in the sample. However, the samples must be much thinner than $\lambda_{\text{THz}}/4$ and should not affect the THz pump beam for a good superposition of incident and reflected THz light.

The effectiveness of this pump field modulation was demonstrated with THz pump - optical probe measurements on a 6 nm thick ferromagnetic sample. The Zeeman torque and the ultrafast demagnetization effect were taken as respective indicators for the THz magnetic and electric fields in the sample. The two effects were separated by driving field reversal, the Zeeman torque depending linearly and the demagnetization quadratically on the THz field. The effect of the THz electric field was significantly suppressed while the magnetic field was found to increase by 1.97 ± 0.06 , in good agreement with the predicted factor 2. This increase of the THz magnetic field in the sample may benefit future THz magnetic switching studies.

Suppressing the action of E_{THz} in an antiferromagnet

Finally, chapter 7 added optical gating functionality, akin to an 'optical-gate transistor', to the previously demonstrated THz electric field driven resistance modulation in antiferromagnetic CuMnAs [Ole18]. Optically exciting the semiconducting substrate provided a conducting bypass channel for the THz writing current, reducing the effective THz writing current in the AFM. Indeed, considering the results in chapter 6, the conducting substrate acts like a THz mirror, quenching the THz electric field in the thin film AFM sample. A simple model has been presented that captures the relevant physics successfully, even for a change in substrate material.

Various combinations of pump photon energy (1.55 eV, 3.1 eV) and substrate bandgap (1.43 eV, 2.25 eV) showed that, within a certain power window, photoexciting the substrate can quench the strongly nonlinear resistance modulation process completely. The optical power required for complete signal suppression did not perturb the magnetic order in the AFM itself and the protection lasted as long as the substrates remained excited. The carrier recombination rates in semiconductors are easily modified with standard semiconductor methods. Thus, optically gating the THz current in the AFM provides an important functionality to potential future AFM based memories: optical address-ability.

In summary, this thesis adds significant functionality to THz pump-optical probe experiments, pathing the way for future studies of THz magnetic dynamics and THz spintronics. Additionally, it demonstrates THz frequency spin accumulation and spin transfer, necessary for THz spintronic applications.

A Appendix: Fit procedure to extract b

Chapter 4 describes the determination of the MCB and MLB coefficients a, b for measurements on thin film ferromagnets. As described in the same chapter, the measured signals

$$S \propto -2a\mathbf{u}_\perp \cdot \mathbf{M}_\perp + bM_\parallel^2 \sin(2\theta) \quad (4.4 \text{ revisited})$$

can be fit by the equation

$$\begin{aligned} S_F(\Theta_0) = & -2a|B_{AC}| \sin(t + t^{\text{off}}) \tan(\alpha) \\ & + b \sin\left(2 \tan^{-1}\left[|B|_{AC} \sin(t + t^{\text{off}})\right] + \Theta_0 + \Theta_0^{\text{off}}\right) \\ & + O_{\text{const.}}(\Theta_0) \end{aligned} \quad (4.9 \text{ revisited})$$

to a data set of curves measured for multiple $\mathbf{E}_{\text{pr}0}$ orientations Θ_0 . The origin of this fit function is described in section 4.2. The constant offset $O_{\text{const.}}(\Theta_0)$ is left as a free parameter for all $S(\Theta_0)$. The other fit parameters $a, b, B_{AC}, t^{\text{off}}, \alpha, \Theta_0^{\text{off}}$, and Θ_0 are shared parameters in the fit. The extracted factor b is relevant for the data analysis in chapter 5.

Data fitting was implemented in MATLAB R2020a. In general, the data was conditioned to give all parameters approximately the same value range. This was especially important as $a, b \sim 10^{-5}$ while $B_{AC}/B_{DC} \approx 5-20$. All fit parameters except for the unbalancing offset $O_{\text{const.}}(\Theta_0)$ were constrained within rough uncertainty ranges. The constraints imposed on the fit parameters were derived from measurement uncertainty (α : $(-3)^\circ-3^\circ, \Theta_0^{\text{off}}$: $25^\circ-35^\circ$), physical necessity ($|B_{AC}|$ must be positive) or a loose interval (a : $(-0.01)-0.01$, b : $(-0.01)-0.01$, t^{off} : $(-0.2)-0.2$). The fit result was compared visually to the data to ensure good convergence (figure 4.7). The 95% confidence intervals of the fitted parameters were extracted with the MATLAB inbuilt function `nlparci()` from the residuals and Jacobian generated by the fit function.

The fit procedure involves two steps, first a fit of only the $\Theta_0 = 0^\circ$ curve to determine starting values for the simultaneous fit of all curves. In the next step the entire data set was fitted simultaneously.

The 0° curve was prefit with the inbuilt `fit()` function. This unconstrained ‘**NonlinearLeastSquares**’ fit with the ‘**Trust-Region**’ algorithm and ‘**LAR**’ (=least absolute residuals) robustness settings generated starting values for the simultaneous fit of multiple curves $S(\Theta_0)$. The generated starting conditions were checked against the parameter boundary conditions and only applied to the multi-curve fit when they fell into the acceptable region. Rejected starting parameters were replaced by the inbuilt starting value generation of the multi-curve fit.

At its heart, the multi-curve fit is a `nsqnonlin()` nonlinear least squares fit, with MATLABs' own 'trust-region-reflective' algorithm. This nonlinear least squares fit was simultaneously applied to multiple curves, sharing most parameters among all curves and leaving $O_{\text{const.}}(\Theta_0)$ free for each curve. To fit with a number of shared parameters the `lsqmultinonlin()` wrapper written by Dr. Bessam Z. Al-Jewad and publicly available on the MathWorks File Exchange (<https://de.mathworks.com/matlabcentral/fileexchange/68727-lsqmultinonlin>, downloaded 5.3.2021) was implemented with minor alterations.

B Appendix: Auxiliary calculations for THz writing suppression

The model of chapter 7 requires some estimates of material properties. First, we require the transmission coefficients for the optical pump beam traversing the CuMnAs layer and exciting the semiconducting substrate. Then, the Tinkham formula requires that the THz electric field is approximately constant over the depth of the sample. To show this we will estimate the skin depths of the materials.

Optical pump reflection and transmission coefficients

T is the optical pump intensity transmittance through the AFM layer into the substrate. To take all reflection echoes in the AFM into account, T is calculated with the Airy formula

$$T = \frac{\text{Re } n_s}{\text{Re } n_A} t_{\text{opt}}^2 = \frac{\text{Re } n_s}{\text{Re } n_A} \left(\frac{t_{12} t_{23} e^{\frac{2\pi i n_2 d}{\lambda}}}{1 + r_{12} r_{23} e^{\frac{4\pi i n_2 d}{\lambda}}} \right) \quad (\text{B.1})$$

with Fresnel reflection and transmission coefficients r, t at normal incidence of the interfaces between the layers 1) air, 2) CuMnAs, and 3) substrate. The AFM thickness $d = 50$ nm and all other parameters are found in table 7.1.

Even though the gate does not obviously modify the state of the AFM on GaP (figure 7.9), it is nonetheless absorbed. The absorptance A_{opt} is given by $A_{\text{opt}} = 1 - T_{\text{opt}} - R_{\text{opt}}$ with

$$R_{\text{opt}} = \left| \left(\frac{r_{12} + r_{23} e^{\frac{2\pi i n_2 d}{\lambda}}}{1 + r_{12} r_{23} e^{\frac{4\pi i n_2 d}{\lambda}}} \right) \right|^2 \quad (\text{B.2})$$

Skin depths

The Tinkham formula assumes that the skin depth of the THz radiation is larger than the combination of AFM layer thickness and the region of excited substrate underneath. To roughly estimate the THz skin depth δ at 1 THz we use [Abo20, Aza05]

$$\delta(\omega) = \sqrt{\frac{2c}{Z_0 \omega \sigma(\omega)}} \quad (\text{B.3})$$

with $Z_0 = 377\Omega$, $\omega = 2\pi \cdot 1$ THz, and c the speed of light in vacuum. With a conductivity $\sigma(\omega) \approx 8 \times 10^5$ S/m it yields a skin depth of approximately 560 nm in CuMnAs, much

longer than the 50 nm layer thickness.

To estimate the penetration depth in the semiconducting substrates while taking into account the pump induced change to the substrate conductivity we express it in terms of the models' proportionality constant C

$$\Delta\sigma_S = \frac{G_{\text{AFM}} \left(\frac{1}{C} - 1 \right)}{\delta_s^{\text{opt}}} \quad (\text{B.4})$$

where G_{AFM} is chosen appropriately to the substrate material. $\delta_s^{\text{opt}} = 750$ nm and 116 nm are the optical penetration depths in GaAs (800 nm) and GaP (400 nm). With the experimentally extracted C values for the highest optical powers from figure 7.11b,d, we obtain a THz skin depth of 4.9 μm and 1.0 μm for GaAs and GaP. The use of the Tinkham formula is therefore justified, considering the 1 THz wavelength of 300 μm .

Bibliography

- [Abo20] A. Abohmra, H. Abbas, M. Al-Hasan, I. B. Mabrouk, A. Alomainy, M. A. Imran, & Q. H. Abbasi. *Terahertz Antenna Array Based on a Hybrid Perovskite Structure*. IEEE Open Journal of Antennas and Propagation **1**, (2020) 464.
- [Alb17] B. G. Alberding, W. R. Thurber, & E. J. Heilweil. *Direct comparison of time-resolved terahertz spectroscopy and Hall Van der Pauw methods for measurement of carrier conductivity and mobility in bulk semiconductors*. Journal of the Optical Society of America B **34**, 7, (2017) 1392.
- [Ash05] N. W. Ashcroft & D. N. Mermin. *Festkörperphysik*. Oldenbourg, 2005.
- [Asp83] D. E. Aspnes & A. A. Studna. *Dielectric functions and optical parameters of Si, Ge, GaP, GaAs, GaSb, InP, InAs, and InSb from 1.5 to 6.0 eV*. Physical Review B **27**, 2, (1983) 985.
- [Avc19] C. O. Avci, G. S. D. Beach, & P. Gambardella. *Effects of transition metal spacers on spin-orbit torques, spin Hall magnetoresistance, and magnetic anisotropy of Pt/Co bilayers*. Physical Review B **100**, 23, (2019) 235454.
- [Aza05] A. K. Azad & W. Zhang. *Resonant terahertz transmission in subwavelength metallic hole arrays of sub-skin-depth thickness*. Optics Letters **30**, 21, (2005) 2945.
- [Azz87] R. M. A. Azzam & N. M. Bashara. *Ellipsometry and polarized light*. North-Holland Sole distributors for the USA and Canada, Elsevier Science Pub. Co, Amsterdam New York, 1987.
- [Bü18] K. Bühlmann, R. Gort, G. Salvatella, S. Däster, A. Fognini, T. Bähler, C. Dornes, C. A. F. Vaz, A. Vaterlaus, & Y. Acremann. *Ultrafast demagnetization in iron: Separating effects by their nonlinearity*. Structural Dynamics **5**, 4, (2018) 044502.
- [Bai16] S. Baiert, M. Hohenleutner, T. Kampfrath, A. K. Zvezdin, A. V. Kimel, R. Huber, & R. V. Mikhaylovskiy. *Nonlinear spin control by terahertz-driven anisotropy fields*. Nature Photonics **10**, 11, (2016) 715.
- [Bai20] H. Bai, X. Zhou, Y. Zhou, X. Chen, Y. You, F. Pan, & C. Song. *Functional antiferromagnets for potential applications on high-density storage and high frequency*. Journal of Applied Physics **128**, 21, (2020) 210901.
- [Bea96] E. Beaurepaire, J.-C. Merle, A. Daunois, & J.-Y. Bigot. *Ultrafast Spin Dynamics in Ferromagnetic Nickel*. Physical Review Letters **76**, 22, (1996) 4250.

- [Bla82] J. S. Blakemore. *Semiconducting and other major properties of gallium arsenide*. Journal of Applied Physics **53**, 10, (1982) R123.
- [Boy08] R. Boyd. *Nonlinear optics*. Academic Press, Amsterdam Boston, 2008.
- [Bra92] T. Brabec, C. Spielmann, P. F. Curley, & F. Krausz. *Kerr lens mode locking*. Optics Letters **17**, 18, (1992) 1292.
- [Bru12] E. Bruendermann, H.-W. Huebers, & M. F. Kimmitt. *Terahertz Techniques*. Springer-Verlag GmbH, 2012.
- [Buc09] M. Buchmeier, R. Schreiber, D. E. Bürgler, & C. M. Schneider. *Thickness dependence of linear and quadratic magneto-optical Kerr effects in ultrathin Fe(001) films*. Physical Review B **79**, 6, (2009) 064402.
- [Buc19] F. Buchali, K. Schuh, R. Dischler, M. Chagnon, V. Aref, H. Buelow, Q. Hu, F. Pulka, M. Frascolla, E. Alhammadi, A. Samhan, I. Younis, M. El-Zonkoli, & P. Winzer. *1.3-Tb/s single-channel and 50.8-Tb/s WDM transmission over field-deployed fiber*. In *45th European Conference on Optical Communication (ECOC 2019)*. Institution of Engineering and Technology, 2019 .
- [Cad17] F. Cadiz, D. Lagarde, P. Renucci, D. Paget, T. Amand, H. Carrère, A. C. H. Rowe, & S. Arscott. *Spin and recombination dynamics of excitons and free electrons in p-type GaAs: Effect of carrier density*. Applied Physics Letters **110**, 8, (2017) 082101.
- [Cas69] H. C. Casey, F. Ermanis, & K. B. Wolfstirn. *Variation of Electrical Properties with Zn Concentration in GaP*. Journal of Applied Physics **40**, 7, (1969) 2945.
- [Cel19] H. Celik, H. Kannan, T. Wang, A. R. Mellnik, X. Fan, X. Zhou, R. Barri, D. C. Ralph, M. F. Doty, V. O. Lorenz, & J. Q. Xiao. *Vector-Resolved Magneto-optic Kerr Effect Measurements of Spin-Orbit Torque*. IEEE Transactions on Magnetism **55**, 1, (2019) 1.
- [Cha09] W. A. Challener, C. Peng, A. V. Itagi, D. Karns, W. Peng, Y. Peng, X. Yang, X. Zhu, N. J. Gokemeijer, Y.-T. Hsia, G. Ju, R. E. Rottmayer, M. A. Seigler, & E. C. Gage. *Heat-assisted magnetic recording by a near-field transducer with efficient optical energy transfer*. Nature Photonics **3**, 4, (2009) 220.
- [Che07] J. Chen, Y. Chen, H. Zhao, G. J. Bastiaans, & X.-C. Zhang. *Absorption coefficients of selected explosives and related compounds in the range of 0.1-2.8 THz*. Optics Express **15**, 19, (2007) 12060.
- [Che19] J. Chen, U. Bovensiepen, A. Eschenlohr, T. Müller, P. Elliott, E. Gross, J. Dewhurst, & S. Sharma. *Competing Spin Transfer and Dissipation*

-
- atCo/Cu(001)Interfaces on Femtosecond Timescales*. Physical Review Letters **122**, 6, (2019) 067202.
- [Chi19] C. Chiang, S. Huang, D. Qu, P. Wu, & C. Chien. *Absence of Evidence of Electrical Switching of the Antiferromagnetic Néel Vector*. Physical Review Letters **123**, 22, (2019) 227203.
- [Chu07] E. M. Chudnovsky. *Theory of Spin Hall Effect: Extension of the Drude Model*. Physical Review Letters **99**, 20, (2007) 206601.
- [Col13] C. M. Collier, B. Born, X. Jin, & J. F. Holzman. *Ultrafast charge-carrier and phonon dynamics in GaP*. Applied Physics Letters **103**, 7, (2013) 072106.
- [Com12] E. D. Commins. *Electron Spin and Its History*. Annual Review of Nuclear and Particle Science **62**, 1, (2012) 133.
- [Con96] J. Conway. *The book of numbers*. Springer New York, New York, NY, 1996.
- [Cos16] A. Cosentino. *Terahertz and Cultural Heritage Science: Examination of Art and Archaeology*. Technologies **4**, 1, (2016) 6.
- [dA11] J. A. del Alamo. *Nanometre-scale electronics with III-V compound semiconductors*. Nature **479**, 7373, (2011) 317.
- [Dan21] T. Danegger, M. Berritta, K. Carva, S. Selzer, U. Ritzmann, P. M. Oppeneer, & U. Nowak. *Ultrafast coherent all-optical switching of an antiferromagnet with the inverse Faraday effect*. Physical Review B **104**, 6, (2021) L060413.
- [Das18] S. Das, L. Avraham, Y. Telepinsky, V. Mor, M. Schultz, & L. Klein. *Magnetization switching of multi-state magnetic structures with current-induced torques*. Scientific Reports **8**, 1, (2018) 15160.
- [Dem13] W. Demtröder. *Experimentalphysik 2*. Springer Berlin Heidelberg, 2013.
- [Dem16] W. Demtröder. *Experimentalphysik 3*. Springer-Verlag GmbH, 2016.
- [Dew18] J. K. Dewhurst, S. Shallcross, E. K. U. Gross, & S. Sharma. *Substrate-Controlled Ultrafast Spin Injection and Demagnetization*. Physical Review Applied **10**, 4, (2018) 044065.
- [Dey21] P. Dey & J. N. Roy. *Spintronics*. Springer Singapore, 2021.
- [Din01] H. F. Ding, S. Pütter, H. P. Oepen, & J. Kirschner. *Spin-reorientation transition in thin films studied by the component-resolved Kerr effect*. Physical Review B **63**, 13, (2001) 134425.

- [Fä18] M. Fähnle. *Review of Ultrafast Demagnetization After Femtosecond Laser Pulses: A Complex Interaction of Light with Quantum Matter*. American Journal of Modern Physics **7**, 2, (2018) 68.
- [Fan14] X. Fan, H. Celik, J. Wu, C. Ni, K.-J. Lee, V. O. Lorenz, & J. Q. Xiao. *Quantifying interface and bulk contributions to spin-orbit torque in magnetic bilayers*. Nature Communications **5**, 1, (2014) 3042.
- [Fan16] X. Fan, A. R. Mellnik, W. Wang, N. Reynolds, T. Wang, H. Celik, V. O. Lorenz, D. C. Ralph, & J. Q. Xiao. *All-optical vector measurement of spin-orbit-induced torques using both polar and quadratic magneto-optic Kerr effects*. Applied Physics Letters **109**, 12, (2016) 122406.
- [Fin14] I. Fina, X. Marti, D. Yi, J. Liu, J. H. Chu, C. Rayan-Serrao, S. Suresha, A. B. Shick, J. Železný, T. Jungwirth, J. Fontcuberta, & R. Ramesh. *Anisotropic magnetoresistance in an antiferromagnetic semiconductor*. Nature Communications **5**, 1, (2014) 4671.
- [Fit05] A. J. Fitzgerald, B. E. Cole, & P. F. Taday. *Nondestructive Analysis of Tablet Coating Thicknesses Using Terahertz Pulsed Imaging*. Journal of Pharmaceutical Sciences **94**, 1, (2005) 177.
- [Fue19] J. A. Fueleop, S. Tzortzakis, & T. Kampfrath. *Laser-Driven Strong-Field Terahertz Sources*. Advanced Optical Materials **8**, 3, (2019) 1900681.
- [Gal99] G. Gallot & D. Grischkowsky. *Electro-optic detection of terahertz radiation*. Journal of the Optical Society of America B **16**, 8, (1999) 1204.
- [Gam11] P. Gambardella & I. M. Miron. *Current-induced spin-orbit torques*. Philosophical Transactions of the Royal Society A: Mathematical, Physical and Engineering Sciences **369**, 1948, (2011) 3175.
- [Gar18] K. Garello, F. Yasin, S. Couet, L. Souriau, J. Swerts, S. Rao, S. V. Beek, W. Kim, E. Liu, S. Kundu, D. Tsvetanova, K. Croes, N. Jossart, E. Grimaldi, M. Baumgartner, D. Crotti, A. Fumemont, P. Gambardella, & G. Kar. *SOT-MRAM 300MM Integration for Low Power and Ultrafast Embedded Memories*. In *2018 IEEE Symposium on VLSI Circuits*. IEEE, 2018 .
- [Ger02] T. Gerrits, H. A. M. van den Berg, J. Hohlfeld, L. Bär, & T. Rasing. *Ultrafast precessional magnetization reversal by picosecond magnetic field pulse shaping*. Nature **418**, 6897, (2002) 509.
- [Gha20] Y. Ghasempour, R. Shrestha, A. Charous, E. Knightly, & D. M. Mittleman. *Single-shot link discovery for terahertz wireless networks*. Nature Communications **11**, 1, (2020) 2017.

-
- [Gha21] Y. Ghasempour, Y. Amarasinghe, C.-Y. Yeh, E. Knightly, & D. M. Mittleman. *Line-of-sight and non-line-of-sight links for dispersive terahertz wireless networks*. APL Photonics **6**, 4, (2021) 041304.
- [God18] J. Godinho, H. Reichlová, D. Kriegner, V. Novák, K. Olejník, Z. Kašpar, Z. Šobáň, P. Wadley, R. P. Campion, R. M. Otxoa, P. E. Roy, J. Železný, T. Jungwirth, & J. Wunderlich. *Electrically induced and detected Néel vector reversal in a collinear antiferromagnet*. Nature Communications **9**, 1, (2018) 4686.
- [Gom10] H. V. Gomonay & V. M. Loktev. *Spin transfer and current-induced switching in antiferromagnets*. Physical Review B **81**, 14, (2010) 144427.
- [Gri90] D. Grischkowsky, S. Keiding, M. van Exter, & C. Fattinger. *Far-infrared time-domain spectroscopy with terahertz beams of dielectrics and semiconductors*. Journal of the Optical Society of America B **7**, 10, (1990) 2006.
- [Gri19] G. Grinblat, M. P. Nielsen, P. Dichtl, Y. Li, R. F. Oulton, & S. A. Maier. *Ultrafast sub-30-fs all-optical switching based on gallium phosphide*. Science Advances **5**, 6, (2019) eaaw3262.
- [Gue21] O. Gueckstock, L. Nádvorník, M. Gradhand, T. S. Seifert, G. Bierhance, R. Rouzegar, M. Wolf, M. Vafaei, J. Cramer, M. A. Syskaki, G. Woltersdorf, I. Mertig, G. Jakob, M. Kläui, & T. Kampfrath. *Terahertz Spin-to-Charge Conversion by Interfacial Skew Scattering in Metallic Bilayers*. Advanced Materials **33**, 9, (2021) 2006281.
- [Gui20] F. S. M. Guimarães, J. Bouaziz, M. dos Santos Dias, & S. Lounis. *Spin-orbit torques and their associated effective fields from gigahertz to terahertz*. Communications Physics **3**, 1, (2020) 19.
- [Ham17] P. Hamm, M. Meuwly, S. L. Johnson, P. Beaud, & U. Staub. *Perspective: THz-driven nuclear dynamics from solids to molecules*. Structural Dynamics **4**, 6, (2017) 061601.
- [Han08] P. Haney, R. Duine, A. Núñez, & A. MacDonald. *Current-induced torques in magnetic metals: Beyond spin-transfer*. Journal of Magnetism and Magnetic Materials **320**, 7, (2008) 1300.
- [Har93] E. S. Harmon, M. R. Melloch, J. M. Woodall, D. D. Nolte, N. Otsuka, & C. L. Chang. *Carrier lifetime versus anneal in low temperature growth GaAs*. Applied Physics Letters **63**, 16, (1993) 2248.
- [Heb02] J. Hebling, G. Almasi, I. Kozma, & J. Kuhl. *Velocity matching by pulse front tilting for large area THz-pulse generation*. Optics Express **10**, 21, (2002) 1161.

- [Heb04] J. Hebling, A. Stepanov, G. Almasi, B. Bartal, & J. Kuhl. *Tunable THz pulse generation by optical rectification of ultrashort laser pulses with tilted pulse fronts*. Applied Physics B: Lasers and Optics **78**, 5, (2004) 593.
- [Heb08] J. Hebling, K.-L. Yeh, M. C. Hoffmann, B. Bartal, & K. A. Nelson. *Generation of high-power terahertz pulses by tilted-pulse-front excitation and their application possibilities*. Journal of the Optical Society of America B **25**, 7, (2008) B6.
- [Hec16] E. Hecht. *Optics, Global Edition*. Pearson Education Limited, 2016.
- [Hei27] W. Heitler & F. London. *Wechselwirkung neutraler Atome und homoeopolare Bindung nach der Quantenmechanik*. Zeitschrift fuer Physik **44**, 6-7, (1927) 455.
- [Hei97] R. Heitz, M. Veit, N. N. Ledentsov, A. Hoffmann, D. Bimberg, V. M. Ustinov, P. S. Kop'ev, & Z. I. Alferov. *Energy relaxation by multiphonon processes in InAs/GaAs quantum dots*. Physical Review B **56**, 16, (1997) 10435.
- [Hey06] J. N. Heyman, D. Bell, & T. Khumalo. *Terahertz photo-Hall measurements of carrier mobility in GaAs and InP*. Applied Physics Letters **88**, 16, (2006) 162104.
- [Hir18] A. Hirohata, Y. Baba, B. A. Murphy, B. Ng, Y. Yao, K. Nagao, & J. young Kim. *Magneto-optical detection of spin accumulation under the influence of mechanical rotation*. Scientific Reports **8**, 1, (2018) 1974.
- [Hof09] M. C. Hoffmann, J. Hebling, H. Y. Hwang, K.-L. Yeh, & K. A. Nelson. *THz-pump/THz-probe spectroscopy of semiconductors at high field strengths [Invited]*. Journal of the Optical Society of America B **26**, 9, (2009) A29.
- [Hub01] R. Huber, F. Tauser, A. Brodschelm, M. Bichler, G. Abstreiter, & A. Leitenstorfer. *How many-particle interactions develop after ultrafast excitation of an electron-hole plasma*. Nature **414**, 6861, (2001) 286.
- [Ign21] D. O. Ignatyeva, G. A. Knyazev, A. N. Kalish, A. I. Chernov, & V. I. Belotelov. *Vector magneto-optical magnetometer based on resonant all-dielectric gratings with highly anisotropic iron garnet films*. Journal of Physics D: Applied Physics **54**, 29, (2021) 295001.
- [Jan20] T. Janda, J. Godinho, T. Ostatnicky, E. Pfitzner, G. Ulrich, A. Hoehl, S. Reimers, Z. Šobán, T. Metzger, H. Reichlová, V. Novák, R. P. Champion, J. Heberle, P. Wadley, K. W. Edmonds, O. J. Amin, J. S. Chauhan, S. S. Dhese, F. Maccherozzi, R. M. Otxoa, P. E. Roy, K. Olejník, P. Němec, T. Jungwirth, B. Kaestner, & J. Wunderlich. *Magneto-Seebeck microscopy of domain switching in collinear antiferromagnet CuMnAs*. Physical Review Materials **4**, 9, (2020) 094413.

-
- [Jed01] F. J. Jedema, A. T. Filip, & B. J. van Wees. *Electrical spin injection and accumulation at room temperature in an all-metal mesoscopic spin valve*. Nature **410**, 6826, (2001) 345.
- [Jhu20] K. Jhuria, J. Hohlfeld, A. Pattabi, E. Martin, A. Y. A. Córdova, X. Shi, R. L. Conte, S. Petit-Watelot, J. C. Rojas-Sanchez, G. Malinowski, S. Mangin, A. Lemaître, M. Hehn, J. Bokor, R. B. Wilson, & J. Gorchon. *Spin-orbit torque switching of a ferromagnet with picosecond electrical pulses*. Nature Electronics **3**, 11, (2020) 680.
- [Jun16] T. Jungwirth, X. Marti, P. Wadley, & J. Wunderlich. *Antiferromagnetic spintronics*. Nature Nanotechnology **11**, 3, (2016) 231.
- [Jun18] M. B. Jungfleisch, W. Zhang, & A. Hoffmann. *Perspectives of antiferromagnetic spintronics*. Physics Letters A **382**, 13, (2018) 865.
- [Kal08] A. M. Kalashnikova, A. V. Kimel, R. V. Pisarev, V. N. Gridnev, P. A. Usachev, A. Kirilyuk, & T. Rasing. *Impulsive excitation of coherent magnons and phonons by subpicosecond laser pulses in the weak ferromagnet FeBO₃*. Physical Review B **78**, 10, (2008) 104301.
- [Kam02] T. Kampfrath, R. G. Ulbrich, F. Leuenberger, M. Münzenberg, B. Sass, & W. Felsch. *Ultrafast magneto-optical response of iron thin films*. Physical Review B **65**, 10, (2002) 104429.
- [Kam06] T. Kampfrath. *Charge-Carrier Dynamics in Solids and Gases Observed by Time-Resolved Terahertz Spectroscopy*. Dissertation, Freie Universität Berlin (2006).
- [Kam10] T. Kampfrath, A. Sell, G. Klatt, A. Pashkin, S. Mährlein, T. Dekorsy, M. Wolf, M. Fiebig, A. Leitenstorfer, & R. Huber. *Coherent terahertz control of antiferromagnetic spin waves*. Nature Photonics **5**, 1, (2010) 31.
- [Kam13] T. Kampfrath, K. Tanaka, & K. A. Nelson. *Resonant and nonresonant control over matter and light by intense terahertz transients*. Nature Photonics **7**, 9, (2013) 680.
- [Kam14] N. Kamaraju, A. Rubano, L. Jian, S. Saha, T. Venkatesan, J. Nötzold, R. K. Campen, M. Wolf, & T. Kampfrath. *Subcycle control of terahertz waveform polarization using all-optically induced transient metamaterials*. Light: Science & Applications **3**, 2, (2014) e155.
- [Kao83] Y. C. Kao & O. Eknayan. *Electron and hole carrier mobilities for liquid phase epitaxially grown GaP in the temperature range 200–550 K*. Journal of Applied Physics **54**, 5, (1983) 2468.

- [Kaš20] Z. Kašpar, M. Surýnek, J. Zubáč, F. Krizek, V. Novák, R. P. Campion, M. S. Wörnle, P. Gambardella, X. Marti, P. Němec, K. W. Edmonds, S. Reimers, O. J. Amin, F. Maccherozzi, S. S. Dhesi, P. Wadley, J. Wunderlich, K. Olejník, & T. Jungwirth. *Quenching of an antiferromagnet into high resistivity states using electrical or ultrashort optical pulses*. *Nature Electronics* **4**, 1, (2020) 30.
- [Kaw04] K. Kawase. *Terahertz Imaging For Drug Detection And Large-Scale Integrated Circuit Inspection*. *Optics and Photonics News* **15**, 10, (2004) 34.
- [Kei16] S. Keiber, S. Sederberg, A. Schwarz, M. Trubetskov, V. Pervak, F. Krausz, & N. Karpowicz. *Electro-optic sampling of near-infrared waveforms*. *Nature Photonics* **10**, 3, (2016) 159.
- [Kit04] C. Kittel. *Introduction to Solid State Physics*. WILEY, 2004.
- [Koz14] V. A. Kozlov, F. Y. Soldatenkov, V. G. Danilchenko, V. I. Korolkov, & I. L. Shulpina. *Defect engineering for carrier lifetime control in high voltage GaAs power diodes*. In *25th Annual SEMI Advanced Semiconductor Manufacturing Conference (ASMC 2014)*. IEEE, 2014 .
- [Koz19] M. Kozina, M. Fechner, P. Marsik, T. van Driel, J. M. Glowina, C. Bernhard, M. Radovic, D. Zhu, S. Bonetti, U. Staub, & M. C. Hoffmann. *Terahertz-driven phonon upconversion in SrTiO₃*. *Nature Physics* **15**, 4, (2019) 387.
- [Kri20] F. Krizek, Z. Kašpar, A. Vetushka, D. Kriegner, E. M. Fiordaliso, J. Michalicka, O. Man, J. Zubáč, M. Brajer, V. A. Hills, K. W. Edmonds, P. Wadley, R. P. Campion, K. Olejník, T. Jungwirth, & V. Novák. *Molecular beam epitaxy of CuMnAs*. *Physical Review Materials* **4**, 1, (2020) 014409.
- [Kum20] I. Kumberg, E. Golias, N. Pontius, R. Hosseinifar, K. Frischmuth, I. Gelen, T. Shinwari, S. Thakur, C. Schüßler-Langeheine, P. M. Oppeneer, & W. Kuch. *Accelerating the laser-induced demagnetization of a ferromagnetic film by anti-ferromagnetic order in an adjacent layer*. *Physical Review B* **102**, 21, (2020) 214418.
- [Kus11] T. Kuschel, H. Bardenhagen, H. Wilkens, R. Schubert, J. Hamrle, J. Pištora, & J. Wollschläger. *Vectorial magnetometry using magneto-optic Kerr effect including first- and second-order contributions for thin ferromagnetic films*. *Journal of Physics D: Applied Physics* **44**, 26, (2011) 265003.
- [Lam14] C.-H. Lambert, S. Mangin, B. S. D. C. S. Varaprasad, Y. K. Takahashi, M. Hehn, M. Cinchetti, G. Malinowski, K. Hono, Y. Fainman, M. Aeschlimann, & E. E. Fullerton. *All-optical control of ferromagnetic thin films and nanostructures*. *Science* **345**, 6202, (2014) 1337.
- [Lee11] O. J. Lee, D. C. Ralph, & R. A. Buhrman. *Spin-torque-driven ballistic preces-*

- sional switching with 50 ps impulses.* Applied Physics Letters **99**, 10, (2011) 102507.
- [Les16] E. Lesne, Y. Fu, S. Oyarzun, J. C. Rojas-Sánchez, D. C. Vaz, H. Naganuma, G. Sicoli, J.-P. Attané, M. Jamet, E. Jacquet, J.-M. George, A. Barthélémy, H. Jaffrès, A. Fert, M. Bibes, & L. Vila. *Highly efficient and tunable spin-to-charge conversion through Rashba coupling at oxide interfaces.* Nature Materials **15**, 12, (2016) 1261.
- [LH12] J. Lloyd-Hughes & T.-I. Jeon. *A Review of the Terahertz Conductivity of Bulk and Nano-Materials.* Journal of Infrared, Millimeter, and Terahertz Waves **33**, 9, (2012) 871.
- [Lin15] G. Lin, Q. Zhang, X. Lin, D. Zhao, R. Jia, N. Gao, Z. Zuo, X. Xu, & D. Liu. *Enhanced photoluminescence of gallium phosphide by surface plasmon resonances of metallic nanoparticles.* RSC Advances **5**, 60, (2015) 48275.
- [Liu11] L. Liu, T. Moriyama, D. C. Ralph, & R. A. Buhrman. *Spin-Torque Ferromagnetic Resonance Induced by the Spin Hall Effect.* Physical Review Letters **106**, 3, (2011) 036601.
- [Liu12] L. Liu, C.-F. Pai, Y. Li, H. W. Tseng, D. C. Ralph, & R. A. Buhrman. *Spin-Torque Switching with the Giant Spin Hall Effect of Tantalum.* Science **336**, 6081, (2012) 555.
- [Liu19] Y. Liu & G. Yu. *MRAM gets closer to the core.* Nature Electronics **2**, 12, (2019) 555.
- [Mae06] S. Maekawa (Hg.). *Concepts in Spin Electronics.* Oxford University Press, 2006.
- [Mae17] S. F. Maehrlein, M. Wolf, & K. Franke. *Nonlinear Terahertz Phononics: A Novel Route to Controlling Matter.* Dissertation, Freie Universität Berlin (2017).
- [Mae18] S. F. Maehrlein, I. Radu, P. Maldonado, A. Paarmann, M. Gensch, A. M. Kalashnikova, R. V. Pisarev, M. Wolf, P. M. Oppeneer, J. Barker, & T. Kampfrath. *Dissecting spin-phonon equilibration in ferrimagnetic insulators by ultrafast lattice excitation.* Science Advances **4**, 7, (2018) eaar5164.
- [Mag20] T. J. Magnanelli & E. J. Heilweil. *Carrier mobility of silicon by sub-bandgap time-resolved terahertz spectroscopy.* Optics Express **28**, 5, (2020) 7221.
- [Man09] A. Manchon & S. Zhang. *Theory of spin torque due to spin-orbit coupling.* Physical Review B **79**, 9, (2009) 094422.
- [Man18] A. Manzoor, M. A. Khan, & W. Kuch. *Correlation between ferromagnetic*

- resonance and densification of RE substituted polycrystalline ferrites*. *Ceramics International* **44**, 11, (2018) 13328.
- [Man19] A. Manchon, J. Železný, I. Miron, T. Jungwirth, J. Sinova, A. Thiaville, K. Garello, & P. Gambardella. *Current-induced spin-orbit torques in ferromagnetic and antiferromagnetic systems*. *Reviews of Modern Physics* **91**, 3, (2019) 035004.
- [Mar14a] I. L. Markov. *Limits on fundamental limits to computation*. *Nature* **512**, 7513, (2014) 147.
- [Mar14b] X. Marti, I. Fina, C. Frontera, J. Liu, P. Wadley, Q. He, R. J. Paull, J. D. Clarkson, J. Kudrnovský, I. Turek, J. Kuneš, D. Yi, J.-H. Chu, C. T. Nelson, L. You, E. Arenholz, S. Salahuddin, J. Fontcuberta, T. Jungwirth, & R. Ramesh. *Room-temperature antiferromagnetic memory resistor*. *Nature Materials* **13**, 4, (2014) 367.
- [May14] B. Mayer, C. Schmidt, J. Bühler, D. V. Seletskiy, D. Brida, A. Pashkin, & A. Leitenstorfer. *Sub-cycle slicing of phase-locked and intense mid-infrared transients*. *New Journal of Physics* **16**, 6, (2014) 063033.
- [McG75] T. McGuire & R. Potter. *Anisotropic magnetoresistance in ferromagnetic 3d alloys*. *IEEE Transactions on Magnetics* **11**, 4, (1975) 1018.
- [Mey17] U. Meyer, G. Haack, C. Groth, & X. Waintal. *Control of the Oscillatory Inter-layer Exchange Interaction with Terahertz Radiation*. *Physical Review Letters* **118**, 9, (2017) 097701.
- [Mil10] P. W. Milonni & J. H. Eberly. *Laser Physics*. John Wiley & Sons, Inc., 2010.
- [Mon15] M. Montazeri, P. Upadhyaya, M. C. Onbasli, G. Yu, K. L. Wong, M. Lang, Y. Fan, X. Li, P. K. Amiri, R. N. Schwartz, C. A. Ross, & K. L. Wang. *Magneto-optical investigation of spin-orbit torques in metallic and insulating magnetic heterostructures*. *Nature Communications* **6**, 1, (2015) 8958.
- [Mot29] N. F. Mott. *The scattering of fast electrons by atomic nuclei*. *Proceedings of the Royal Society of London. Series A, Containing Papers of a Mathematical and Physical Character* **124**, 794, (1929) 425.
- [MW19] T. Matalla-Wagner, M.-F. Rath, D. Graulich, J.-M. Schmalhorst, G. Reiss, & M. Meinert. *Electrical Néel-Order Switching in Magnetron-Sputtered CuMnAs Thin Films*. *Physical Review Applied* **12**, 6, (2019) 064003.
- [Nád21] L. Nádvorník, M. Borchert, L. Brandt, R. Schlitz, K. A. de Mare, K. Výborný, I. Mertig, G. Jakob, M. Kläui, S. T. Goennenwein, M. Wolf, G. Woltersdorf, & T. Kampfrath. *Broadband Terahertz Probes of Anisotropic Magnetoresistance*

-
- Disentangle Extrinsic and Intrinsic Contributions.* Physical Review X **11**, 2, (2021) 021030.
- [Naf19] Naftaly, Vieweg, & Deninger. *Industrial Applications of Terahertz Sensing: State of Play.* Sensors **19**, 19, (2019) 4203.
- [Nag10] N. Nagaosa, J. Sinova, S. Onoda, A. H. MacDonald, & N. P. Ong. *Anomalous Hall effect.* Reviews of Modern Physics **82**, 2, (2010) 1539.
- [Nat85] V. Nathan, S. S. Mitra, & A. H. Guenther. *Review of multiphoton absorption in crystalline solids.* Journal of the Optical Society of America B **2**, 2, (1985) 294.
- [Neu18] J. Neu, K. P. Regan, J. R. Swierk, & C. A. Schmuttenmaer. *Applicability of the thin-film approximation in terahertz photoconductivity measurements.* Applied Physics Letters **113**, 23, (2018) 233901.
- [Nie19] M. Niemeyer, P. Kleinschmidt, A. W. Walker, L. E. Mundt, C. Timm, R. Lang, T. Hannappel, & D. Lackner. *Measurement of the non-radiative minority recombination lifetime and the effective radiative recombination coefficient in GaAs.* AIP Advances **9**, 4, (2019) 045034.
- [Nol09] W. Nolting & A. Ramakanth. *Quantum Theory of Magnetism.* Springer Berlin Heidelberg, 2009.
- [Nol15] W. Nolting. *Grundkurs Theoretische Physik 5/2.* Springer Berlin Heidelberg, 2015.
- [Oka10] T. Okada, K. Ooi, Y. Nakata, K. Fujita, K. Tanaka, & K. Tanaka. *Direct creation of a photoinduced metallic structure and its optical properties in the terahertz frequency region.* Optics Letters **35**, 10, (2010) 1719.
- [Ole17] K. Olejník, V. Schuler, X. Marti, V. Novák, Z. Kašpar, P. Wadley, R. P. Campion, K. W. Edmonds, B. L. Gallagher, J. Garces, M. Baumgartner, P. Gambardella, & T. Jungwirth. *Antiferromagnetic CuMnAs multi-level memory cell with microelectronic compatibility.* Nature Communications **8**, 1, (2017) 15434.
- [Ole18] K. Olejník, T. Seifert, Z. Kašpar, V. Novák, P. Wadley, R. P. Campion, M. Baumgartner, P. Gambardella, P. Němec, J. Wunderlich, J. Sinova, P. Kužel, M. Müller, T. Kampfrath, & T. Jungwirth. *Terahertz electrical writing speed in an antiferromagnetic memory.* Science Advances **4**, 3, (2018) eaar3566.
- [Pan69] M. B. Panish & H. C. Casey. *Temperature Dependence of the Energy Gap in GaAs and GaP.* Journal of Applied Physics **40**, 1, (1969) 163.
- [Pas20] N. C. Passler, M. Jeannin, & A. Paarmann. *Layer-resolved absorption of light*

- in arbitrarily anisotropic heterostructures*. Physical Review B **101**, 16, (2020) 165425.
- [Pol18] D. Polley, M. Pancaldi, M. Hudl, P. Vavassori, S. Urazhdin, & S. Bonetti. *THz-driven demagnetization with perpendicular magnetic anisotropy: towards ultrafast ballistic switching*. Journal of Physics D: Applied Physics **51**, 8, (2018) 084001.
- [Pyr19] T. Pyragius, H. M. Florez, & T. Fernholz. *Voigt-effect-based three-dimensional vector magnetometer*. Physical Review A **100**, 2, (2019) 023416.
- [Qin15] H. J. Qin, K. Zakeri, A. Ernst, L. M. Sandratskii, P. Buczek, A. Marmodoro, T. H. Chuang, Y. Zhang, & J. Kirschner. *Long-living terahertz magnons in ultrathin metallic ferromagnets*. Nature Communications **6**, 1, (2015) 6126.
- [Rab07] K. M. Rabe, C. H. Ahn, & J.-M. Triscone. *Physics of Ferroelectrics*. Springer Berlin Heidelberg, 2007.
- [Rad11] I. Radu, K. Vahaplar, C. Stamm, T. Kachel, N. Pontius, H. A. Dürr, T. A. Ostler, J. Barker, R. F. L. Evans, R. W. Chantrell, A. Tsukamoto, A. Itoh, A. Kirilyuk, T. Rasing, & A. V. Kimel. *Transient ferromagnetic-like state mediating ultrafast reversal of antiferromagnetically coupled spins*. Nature **472**, 7342, (2011) 205.
- [Ral08] D. Ralph & M. Stiles. *Spin transfer torques*. Journal of Magnetism and Magnetic Materials **320**, 7, (2008) 1190.
- [Rod75] D. Rode. *Chapter 1 Low-Field Electron Transport*. In *Semiconductors and Semimetals*. Elsevier, 1975 1–89.
- [Rog16] A. E. Rogachev, P. M. Vetoshko, N. A. Gusev, M. A. Kozhaev, A. R. Prokopov, V. V. Popov, D. V. Dodonov, A. G. Shumilov, A. N. Shaposhnikov, V. N. Berzhansky, A. K. Zvezdin, & V. I. Belotelov. *Vector magneto-optical sensor based on transparent magnetic films with cubic crystallographic symmetry*. Applied Physics Letters **109**, 16, (2016) 162403.
- [Rou21] R. Rouzegar, L. Brandt, L. Nadvornik, D. A. Reiss, A. L. Chekhov, O. Gueckstock, C. In, M. Wolf, T. S. Seifert, P. W. Brouwer, G. Woltersdorf, & T. Kampfrath. *Laser-induced terahertz spin transport in magnetic nanostructures arises from the same force as ultrafast demagnetization* (2021).
- [Roy16] P. E. Roy, R. M. Otxoa, & J. Wunderlich. *Robust picosecond writing of a layered antiferromagnet by staggered spin-orbit fields*. Physical Review B **94**, 1, (2016) 014439.
- [Rub14] A. Rubano, M. Wolf, & T. Kampfrath. *Terahertz conductivity and ultrafast*

- dynamics of photoinduced charge carriers in intrinsic 3C and 6H silicon carbide.* Applied Physics Letters **105**, 3, (2014) 032104.
- [Rul05] C. Rullière (Hg.). *Femtosecond Laser Pulses*. Springer New York, 2005.
- [Sai17] V. Saidl, P. Němec, P. Wadley, V. Hills, R. P. Champion, V. Novák, K. W. Edmonds, F. Maccherozzi, S. S. Dhesi, B. L. Gallagher, F. Trojánek, J. Kuneš, J. Železný, P. Malý, & T. Jungwirth. *Optical determination of the Néel vector in a CuMnAs thin-film antiferromagnet.* Nature Photonics **11**, 2, (2017) 91.
- [Saj14] M. Sajadi, M. Wolf, & T. Kampfrath. *Terahertz field enhancement via coherent superposition of the pulse sequences after a single optical-rectification crystal.* Applied Physics Letters **104**, 9, (2014) 091118.
- [Saj15] M. Sajadi, M. Wolf, & T. Kampfrath. *Terahertz-field-induced optical birefringence in common window and substrate materials.* Optics Express **23**, 22, (2015) 28985.
- [Saj17] M. Sajadi, M. Wolf, & T. Kampfrath. *Transient birefringence of liquids induced by terahertz electric-field torque on permanent molecular dipoles.* Nature Communications **8**, 1, (2017) 14963.
- [See04] K. Seeger. *Semiconductor Physics*. Springer Berlin Heidelberg, 2004.
- [Sei16] T. Seifert, S. Jaiswal, U. Martens, J. Hannegan, L. Braun, P. Maldonado, F. Freimuth, A. Kronenberg, J. Henrizi, I. Radu, E. Beaurepaire, Y. Mokrousov, P. M. Oppeneer, M. Jourdan, G. Jakob, D. Turchinovich, L. M. Hayden, M. Wolf, M. Münzenberg, M. Kläui, & T. Kampfrath. *Efficient metallic spintronic emitters of ultrabroadband terahertz radiation.* Nature Photonics **10**, 7, (2016) 483.
- [Sei18a] T. S. Seifert, S. Jaiswal, J. Barker, S. T. Weber, I. Razdolski, J. Cramer, O. Gueckstock, S. F. Maehrlein, L. Nadvornik, S. Watanabe, C. Ciccarelli, A. Melnikov, G. Jakob, M. Münzenberg, S. T. B. Goennenwein, G. Woltersdorf, B. Rethfeld, P. W. Brouwer, M. Wolf, M. Kläui, & T. Kampfrath. *Femtosecond formation dynamics of the spin Seebeck effect revealed by terahertz spectroscopy.* Nature Communications **9**, 1, (2018) 2899.
- [Sei18b] T. S. Seifert, T. Kampfrath, & M. Wolf. *Spintronics with Terahertz Radiation: Probing and driving spins at highest frequencies.* Dissertation, Freie Universität Berlin (2018).
- [Sha04] J. Shan & T. F. Heinz. *Terahertz Radiation from Semiconductors.* In *Topics in Applied Physics*. Springer Berlin Heidelberg, 2004 1–56.
- [Sha18] M. Shalaby, A. Donges, K. Carva, R. Allenspach, P. M. Oppeneer, U. Nowak,

- & C. P. Hauri. *Coherent and incoherent ultrafast magnetization dynamics in 3d ferromagnets driven by extreme terahertz fields*. Physical Review B **98**, 1, (2018) 014405.
- [Shi08] Y. Shi, Q. li Zhou, C. Zhang, & B. Jin. *Ultrafast high-field carrier transport in GaAs measured by femtosecond pump-terahertz probe spectroscopy*. Applied Physics Letters **93**, 12, (2008) 121115.
- [Sho19] Y. A. Shokr, O. Sandig, M. Erkovan, B. Zhang, M. Bernien, A. A. Ünal, F. Kronast, U. Parlak, J. Vogel, & W. Kuch. *Steering of magnetic domain walls by single ultrashort laser pulses*. Physical Review B **99**, 21, (2019) 214404.
- [Sid20] S. A. Siddiqui, J. Sklenar, K. Kang, M. J. Gilbert, A. Schleife, N. Mason, & A. Hoffmann. *Metallic antiferromagnets*. Journal of Applied Physics **128**, 4, (2020) 040904.
- [Sin15] J. Sinova, S. O. Valenzuela, J. Wunderlich, C. Back, & T. Jungwirth. *Spin Hall effects*. Reviews of Modern Physics **87**, 4, (2015) 1213.
- [SM13] C. Seco-Martorell, V. López-Domínguez, G. Arauz-Garofalo, A. Redo-Sanchez, J. Palacios, & J. Tejada. *Goya's artwork imaging with Terahertz waves*. Optics Express **21**, 15, (2013) 17800.
- [Son18] C. Song, Y. You, X. Chen, X. Zhou, Y. Wang, & F. Pan. *How to manipulate magnetic states of antiferromagnets*. Nanotechnology **29**, 11, (2018) 112001.
- [Sta17] C. Stamm, C. Murer, M. Berritta, J. Feng, M. Gabureac, P. Oppeneer, & P. Gambardella. *Magneto-Optical Detection of the Spin Hall Effect in Pt and W Thin Films*. Physical Review Letters **119**, 8, (2017) 087203.
- [Sti70] G. Stillman, C. Wolfe, & J. Dimmock. *Hall coefficient factor for polar mode scattering in n-type GaAs*. Journal of Physics and Chemistry of Solids **31**, 6, (1970) 1199.
- [Sto06] J. Stoehr & H. C. Siegmann. *Magnetism*. Springer-Verlag GmbH, 2006.
- [Str85] D. Strickland & G. Mourou. *Compression of amplified chirped optical pulses*. Optics Communications **56**, 3, (1985) 219.
- [Sun05] Q. Sun & X. C. Xie. *Definition of the spin current: The angular spin current and its physical consequences*. Physical Review B **72**, 24, (2005) 245305.
- [Tak08] S. Takahashi & S. Maekawa. *Spin current, spin accumulation and spin Hall effect*. Science and Technology of Advanced Materials **9**, 1, (2008) 014105.
- [Tao19] Z. Tao, P. Tengdin, W. You, C. Chen, X. Shi, D. Zusin, Y. Zhang, C. Gentry,

- A. Blonsky, M. Keller, P. Oppeneer, H. C. Kapteyn, & M. M. Murnane. *The nature of non-equilibrium ultrafast demagnetization in ferromagnetic nickel*. In H. Wang (Hg.), *Eleventh International Conference on Information Optics and Photonics (CIOP 2019)*. SPIE, 2019 .
- [Ten09] L. H. Teng, K. Chen, J. H. Wen, W. Z. Lin, & T. S. Lai. *Density dependence of electron-spin polarization and relaxation in intrinsic GaAs at room temperature*. *Journal of Physics D: Applied Physics* **42**, 13, (2009) 135111.
- [Ton18] K. N. Tonny, R. Rafique, A. Sharmin, M. S. Bashar, & Z. H. Mahmood. *Electrical, optical and structural properties of transparent conducting Al doped ZnO (AZO) deposited by sol-gel spin coating*. *AIP Advances* **8**, 6, (2018) 065307.
- [Tsa18] T.-Y. Tsai, T.-Y. Chen, C.-T. Wu, H.-I. Chan, & C.-F. Pai. *Spin-orbit torque magnetometry by wide-field magneto-optical Kerr effect*. *Scientific Reports* **8**, 1, (2018) 5613.
- [Tud04] I. Tudosa, C. Stamm, A. B. Kashuba, F. King, H. C. Siegmann, J. Stöhr, G. Ju, B. Lu, & D. Weller. *The ultimate speed of magnetic switching in granular recording media*. *Nature* **428**, 6985, (2004) 831.
- [Ulb11] R. Ulbricht, E. Hendry, J. Shan, T. F. Heinz, & M. Bonn. *Carrier dynamics in semiconductors studied with time-resolved terahertz spectroscopy*. *Reviews of Modern Physics* **83**, 2, (2011) 543.
- [Urs16] N. O. Urs, B. Mozooni, P. Mazalski, M. Kustov, P. Hayes, S. Deldar, E. Quandt, & J. McCord. *Advanced magneto-optical microscopy: Imaging from picoseconds to centimeters - imaging spin waves and temperature distributions (invited)*. *AIP Advances* **6**, 5, (2016) 055605.
- [Vei18] M. Veis, J. Minár, G. Steciuk, L. Palatinus, C. Rinaldi, M. Cantoni, D. Kriegner, K. K. Tikuišis, J. Hamrle, M. Zahradník, R. Antoš, J. Železný, L. Šmejkal, X. Marti, P. Wadley, R. P. Campion, C. Frontera, K. Uhlířová, T. Duchoň, P. Kužel, V. Novák, T. Jungwirth, & K. Výborný. *Band structure of CuMnAs probed by optical and photoemission spectroscopy*. *Physical Review B* **97**, 12, (2018) 125109.
- [vH18] A. von Hoegen, R. Mankowsky, M. Fechner, M. Först, & A. Cavalleri. *Probing the interatomic potential of solids with strong-field nonlinear phononics*. *Nature* **555**, 7694, (2018) 79.
- [Vic13] C. Vicario, C. Ruchert, F. Ardana-Lamas, P. M. Derlet, B. Tudu, J. Luning, & C. P. Hauri. *Off-resonant magnetization dynamics phase-locked to an intense phase-stable terahertz transient*. *Nature Photonics* **7**, 9, (2013) 720.

- [Vod08] K. L. Vodopyanov & Y. H. Avetisyan. *Optical terahertz wave generation in a planar GaAs waveguide*. Optics Letters **33**, 20, (2008) 2314.
- [Wad15] P. Wadley, V. Hills, M. R. Shahedkhah, K. W. Edmonds, R. P. Champion, V. Novák, B. Ouladdiaf, D. Khalyavin, S. Langridge, V. Saidl, P. Nemeč, A. W. Rushforth, B. L. Gallagher, S. S. Dhesi, F. Maccherozzi, J. Železný, & T. Jungwirth. *Antiferromagnetic structure in tetragonal CuMnAs thin films*. Scientific Reports **5**, 1, (2015) 17079.
- [Wad16] P. Wadley, B. Howells, J. Zelezny, C. Andrews, V. Hills, R. P. Champion, V. Novak, K. Olejnik, F. Maccherozzi, S. S. Dhesi, S. Y. Martin, T. Wagner, J. Wunderlich, F. Freimuth, Y. Mokrousov, J. Kune, J. S. Chauhan, M. J. Grzybowski, A. W. Rushforth, K. W. Edmonds, B. L. Gallagher, & T. Jungwirth. *Electrical switching of an antiferromagnet*. Science **351**, 6273, (2016) 587.
- [Wad18] P. Wadley, S. Reimers, M. J. Grzybowski, C. Andrews, M. Wang, J. S. Chauhan, B. L. Gallagher, R. P. Champion, K. W. Edmonds, S. S. Dhesi, F. Maccherozzi, V. Novak, J. Wunderlich, & T. Jungwirth. *Current polarity-dependent manipulation of antiferromagnetic domains*. Nature Nanotechnology **13**, 5, (2018) 362.
- [Wah18] J. K. Wahlstrand & E. J. Heilweil. *Contactless THz-based bulk semiconductor mobility measurements using two-photon excitation*. Optics Express **26**, 23, (2018) 29848.
- [Wan04] B. Wang, J. Wang, J. Wang, & D. Y. Xing. *Spin current carried by magnons*. Physical Review B **69**, 17, (2004) 174403.
- [Wan20a] C. Wang & Y. Liu. *Ultrafast optical manipulation of magnetic order in ferromagnetic materials*. Nano Convergence **7**, 1, (2020) 35.
- [Wan20b] M. Wang, C. Andrews, S. Reimers, O. J. Amin, P. Wadley, R. P. Champion, S. F. Poole, J. Felton, K. W. Edmonds, B. L. Gallagher, A. W. Rushforth, O. Makarovskiy, K. Gas, M. Sawicki, D. Kriegner, J. Zubáč, K. Olejník, V. Novák, T. Jungwirth, M. Shahrokhvand, U. Zeitler, S. S. Dhesi, & F. Maccherozzi. *Spin flop and crystalline anisotropic magnetoresistance in CuMnAs*. Physical Review B **101**, 9, (2020) 094429.
- [Wer11] D. Werner. *Funktionalanalysis*. Springer, Berlin New York, 2011.
- [Wie12] S. Wienholdt, D. Hinzke, & U. Nowak. *THz Switching of Antiferromagnets and Ferrimagnets*. Physical Review Letters **108**, 24, (2012) 247207.
- [Wil17] R. B. Wilson, Y. Yang, J. Gorchon, C.-H. Lambert, S. Salahuddin, & J. Bokor. *Electric current induced ultrafast demagnetization*. Physical Review B **96**, 4, (2017) 045105.

- [Xin21] Y. Xing & T. S. Rappaport. *Terahertz Wireless Communications: Co-sharing for Terrestrial and Satellite Systems above 100 GHz*. IEEE Communications Letters (2021) 1–1.
- [Yan16] H. Yang, Y. Li, & W. E. Bailey. *Large spin pumping effect in antisymmetric precession of Ni79Fe21/Ru/Ni79Fe21*. Applied Physics Letters **108**, 24, (2016) 242404.
- [Yan20] H. Yan, Z. Feng, P. Qin, X. Zhou, H. Guo, X. Wang, H. Chen, X. Zhang, H. Wu, C. Jiang, & Z. Liu. *Electric-Field-Controlled Antiferromagnetic Spintronic Devices*. Advanced Materials **32**, 12, (2020) 1905603.
- [Yos20] S. Yoshii, R. Ohshima, Y. Ando, T. Shinjo, & M. Shiraishi. *Detection of ferromagnetic resonance from 1 nm-thick Co*. Scientific Reports **10**, 1, (2020) 15764.
- [You20] B. You & J.-Y. Lu. *Optical Gas Sensors Using Terahertz Waves in the Layered Media*. In *Gas Sensors*. IntechOpen, 2020 .
- [Žel18] J. Železný, P. Wadley, K. Olejník, A. Hoffmann, & H. Ohno. *Spin transport and spin torque in antiferromagnetic devices*. Nature Physics **14**, 3, (2018) 220.
- [Zha19] D. Zhao, H. Hu, R. Haselsberger, R. A. Marcus, M.-E. Michel-Beyerle, Y. M. Lam, J.-X. Zhu, C. L. o vorakiat, M. C. Beard, & E. E. M. Chia. *Monitoring Electron–Phonon Interactions in Lead Halide Perovskites Using Time-Resolved THz Spectroscopy*. ACS Nano **13**, 8, (2019) 8826.
- [Zha20] H. Zhao, Y. Tan, L. Zhang, R. Zhang, M. Shalaby, C. Zhang, Y. Zhao, & X.-C. Zhang. *Ultrafast hydrogen bond dynamics of liquid water revealed by terahertz-induced transient birefringence*. Light: Science & Applications **9**, 1, (2020) 136.
- [Zho18] C. Zhong, P. Flanigan, N. Abadía, F. Bello, B. D. Jennings, G. Atcheson, J. Li, J.-Y. Zheng, J. J. Wang, R. Hobbs, D. McCloskey, & J. F. Donegan. *Effective heat dissipation in an adiabatic near-field transducer for HAMR*. Optics Express **26**, 15, (2018) 18842.
- [Zho19] X. Zhou, X. Chen, J. Zhang, F. Li, G. Shi, Y. Sun, M. Saleem, Y. You, F. Pan, & C. Song. *From Fieldlike Torque to Antidamping Torque in Antiferromagnetic Mn2Au*. Physical Review Applied **11**, 5, (2019) 054030.
- [Zie96] J. Zielbauer & M. Wegener. *Ultrafast optical pump THz-probe spectroscopy on silicon*. Applied Physics Letters **68**, 9, (1996) 1223.
- [Zve97] A. K. Zvezdin & V. A. Kotov. *Modern magneto-optics and magneto-optical materials*. Institute of Physics Pub, Bristol Philadelphia, Pa, 1997.

List of Publications

Publications within this thesis

J. J. F. Heitz, L. Nádvorník, V. Balos, Y. Behovits, A. L. Chekhov, T. S. Seifert, K. Olejník, Z. Kašpar, K. Geishendorf, V. Novák, R. P. Campion, M. Wolf, T. Jungwirth, T. Kampfrath. *Optically Gated Terahertz-Field-Driven Switching of Antiferromagnetic CuMnAs*. Physical Review Applied **16**, (2021) 064047.

Other Publications

A. L. Chekhov, Y. Behovits, J. J. F. Heitz, C. Denker, D. A. Reiss, M. Wolf, M. Weinelt, P. W. Brouwer, M. Münzenberg, T. Kampfrath. *Ultrafast Demagnetization of Iron Induced by Optical vs Terahertz Pulses*. Physical Review X **11**, (2021) 041055

Academic curriculum vitae

Johan Julius Frederick Heitz

14199 Berlin

Der Lebenslauf ist in der Online-Version aus Gründen des Datenschutzes nicht enthalten.

Acknowledgments

I would like to thank everyone that was part of my scientific and non-scientific life in the last years. All of you made this time very special. In particular, I would like to thank the following people:

First and foremost, the biggest thanks go to Professor *Tobias Kampfrath*! Thank you, Tobi, for all the guidance and support throughout this PhD. I took a lot from both our personal and professional discussions. Especially your seemingly unerring scientific intuition and ability to explain complex issues in simple concepts helped me across road-blocks more than once.

Many thanks to Professor *Wolfgang Kuch* as well. Thank you for being my second supervisor and giving me the chance to present this work in your group seminar multiple times.

Similarly, I would like to thank *Alexander Paarmann* and *Ines Bressel* for providing both personal and professional counsel, both in and outside of the IMPRS. You two are amazing people. Also, I would like to thank the IMPRS for giving me access to very helpful soft-skills seminars over the years.

Lukáš Nádvorník, I really enjoyed sharing an office and working with you! Conversations with you are always enjoyable and I hope you can continue to live out those many different interests that you have, even with the pressures of having your own group.

Thanks for many fruitful discussions and a lot of proof reading go to *Tom Seifert* as well. Discussions with you have been invaluable to the understanding of the project.

Yannic Behovits, from shared beamtimes to proof-reading and taking over the laser so expertly - thank you very much! Your arrival was a game changer for me.

Without samples, there is no research. Thus I would like to thank our collaborators *Samridh Jaiswal* and *Maria-Andromachi Syskaki* (Johannes Gutenberg University, Mainz) as well as *Zdeněk Kašpar*, *Kamil Olejník*, and *Vít Novák* (Czech Academy of Sciences, Prague). You did amazing work!

Marcel Krenz, *Reinhard Franke*, *Albrecht Ropers*, *Sven Kubala*, *Daniel Wegkamp*, *Jörg Wagatha* and *Harald Kirsch*, thank you for your friendship and expert technical support. Without your input, this thesis would not have happened. You were always helpful, night and day problem solvers and taught me a lot about the technical aspects beyond standard laboratory work. In fact, you made me feel like an honorary member of the tech crew at times. I sincerely hope the garden gatherings and Christmas goose dinners continue in future!

Manuel Krüger, *Marietta Wissmann*, and *Angela Ziebarth*, thank you for keeping the worldly side of university life in check. I cannot count how many times you managed to find last minute solutions for bureaucratic nightmares and deadlines almost missed. Additionally, you have been great support in the more challenging situations of the last few years.

Big thanks go to the other current and former THz group members as well! *Oliver Gückstock, Alexander Chekhov, Genaro Bierhance, Reza Rouzegar, Chihun In, Ilie-Elian Radu, Bruno Rosinus Serrano, Martin Borchert, and Patrick Müller*, you made this time truly enjoyable and I hope we will stay in contact in the future. I am really grateful for all the happy memories with each and every one of you as well as the the comradeship of the group.

Sebastian Mährlein, thank you so much for teaching me about the laser system and helping me get started in the lab. I did my best to take care of it while it was my charge!

Vasilis Balos, I really enjoyed working with you over the years. I don't know anyone else as good in soldiering on with a smile as you!

Big thanks go to the other PhD students at FHI, the PhD net and the Fellow students of the IMPRS for the great times we had. From PhD events to a conference we organized ourselves, you people are a great bunch!

Dr. Wessendorf, you gave me the tools to construct the bridge over the biggest rift of this journey, thank you very much!

I would like to thank *Peter Wiechert, Ulrike Möller, Chad Felt* and *Prof. Daniele Faccio* for the many opportunities and solid foundations you have given me. I consider myself extremely fortunate to have learned from you.

Mike, it's a privilege to explore the world on two wheels with you.

Nic, Lisa, Lewis, Dan, Alex, Killian and *Kristina*, thank you for being there, even after so many years!

Anke and *Wolfgang*, thank you for all the support! I could not ask for a better set of alternate parents.

My quasi-brother *Tim*, I am sure there are many more adventures down the road for us. *Lisa*, I consider myself extremely lucky to have you as a friend.

Importantly, I would like to thank my family! Thank you *dad* for inspiring the choice of physics. Thanks, *mom*, for your never ending trust and support in all endeavors. Thanks to my *siblings* for sticking together. And thanks to the *grandparents* for all the love and seasoned perspective. You all made returning to Berlin the absolutely correct choice!

Finally, *Julia*, thank you for your love, patience and support. You help me remember what is actually important in life!

Selbstständigkeitserklärung

Ich erkläre gegenüber der Freien Universität Berlin, dass ich die vorliegende Dissertation selbstständig und ohne Benutzung anderer als der angegebenen Quellen und Hilfsmittel angefertigt habe. Die vorliegende Arbeit ist frei von Plagiaten. Alle Ausführungen, die wörtlich oder inhaltlich aus anderen Schriften entnommen sind, habe ich als solche kenntlich gemacht. Diese Dissertation wurde in gleicher oder ähnlicher Form noch in keinem früheren Promotionsverfahren eingereicht.

Mit einer Prüfung meiner Arbeit durch ein Plagiatsprüfungsprogramm erkläre ich mich einverstanden

Berlin, den

Johan Julius Frederick Heitz